Structure, Abundances, and Reddening of the Magellanic Clouds from its Variable Stars

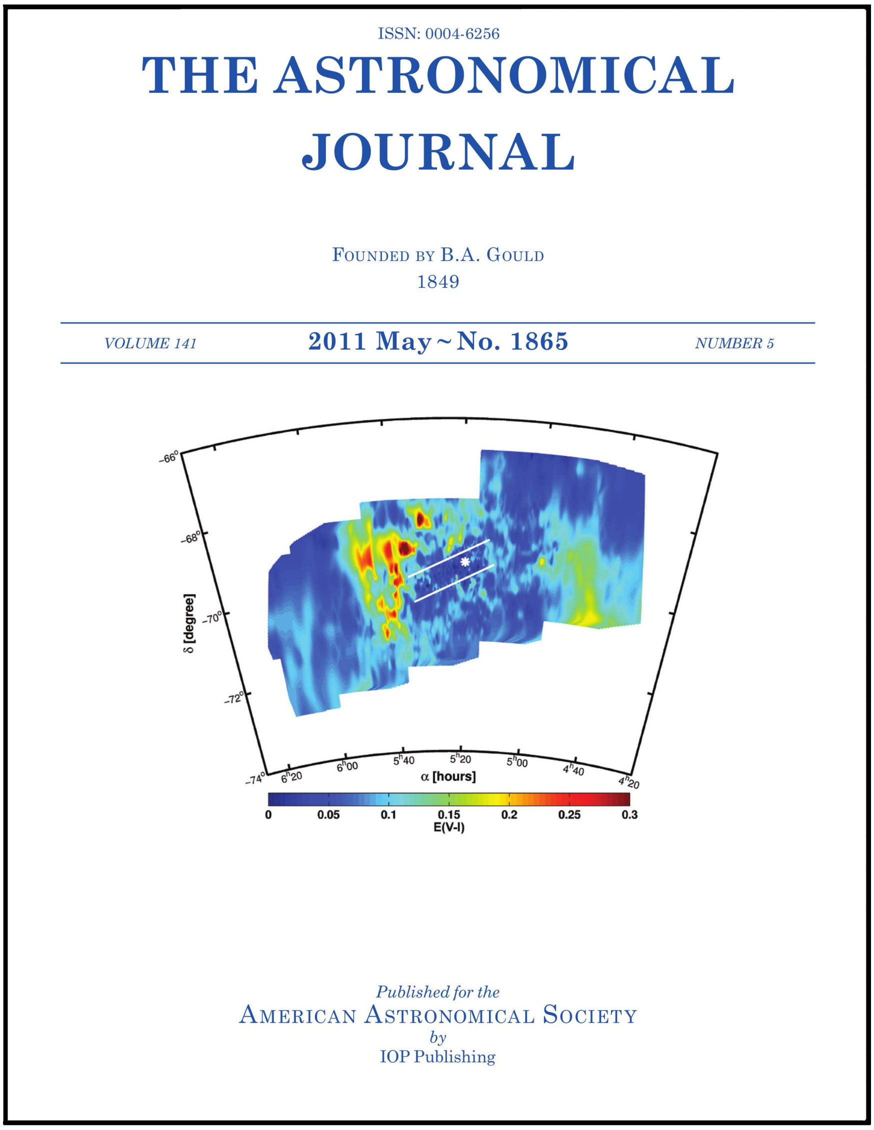

ISSN: 0004-6256

THE ASTRONOMICAL JOURNAL

FOUNDED BY B.A. GOULD
1849

VOLUME 141 **2011 May ~ No. 1865** *NUMBER 5*

Published for the
AMERICAN ASTRONOMICAL SOCIETY
by
IOP Publishing

Raoul Haschke

Dissertation
submitted to the
Combined Faculties of the Natural Sciences and Mathematics
of the Ruperto-Carola-University of Heidelberg, Germany
for the degree of
Doctor of Natural Sciences

Put forward by
Raoul Haschke
born in: Frankfurt am Main, Germany
Oral examination: 2^{nd} May, 2012

Structure, Abundances, and Reddening of the Magellanic Clouds from its Variable Stars

Referees: Prof. Dr. E. K. Grebel
Prof. Dr. N. Christlieb

ABSTRACT

Structure, Abundances, and Reddening of the Magellanic Clouds from its variable stars

Using the data obtained by the Optical Gravitational Lensing Experiment (OGLE) we investigate the properties of the old population of the Magellanic Clouds (MCs) using the variable RR Lyrae stars and of the young population traced by Cepheids.

With our own reddening estimates, we deduce distances to the RR Lyrae stars and Cepheids. These distances are used to determine structural parameters, such as scale height, position angle and inclination of the Large Magellanic Cloud (LMC) and Small Magellanic Cloud (SMC). The depth extent of the SMC is significantly higher than for the LMC. For the SMC a quite different orientation of the young Cepheids is found in comparison to the old RR Lyrae stars. One of the most interesting results is the off-center bar of the LMC, which extends for up to ~ 5 kpc in both populations out of the disk.

We determine metallicities for single RR Lyrae stars and the metallicity distribution functions reveal significant differences between the LMC and SMC. The mean metallicity of the SMC is ~ 0.2 dex lower. This leads to the conclusion of a different early enrichment history of the MCs.

Investigating RR Lyrae stars in the OGLE field towards the Galactic bulge, we obtain reddening estimates, metallicities and distances to the bulge and to a small part of the Sagittarius stream. The stream has a significantly lower metallicity and seems to be inclined.

Performing a spectroscopic analysis of individual element abundances of nine very metal-poor candidate RR Lyrae stars, we find the most metal-poor star ($[Fe/H] = -2.7$ dex) yet detected in the MCs. The other very metal-poor stars have abundances leading to the conclusion that a build-up of the Galactic halo from a merger with a MC-type galaxy is plausible.

ZUSAMMENFASSUNG

Struktur, Elementhäufigkeiten und Verfärbung der Magellanischen Wolken von ihren variablen Sternen

Mit Hilfe von Daten des Optical Gravitational Lensing Experiment werden die Eigenschaften der Magellanischen Wolken untersucht. Für die alte Population werden RR Lyrae Sternen genutzt und für die junge Population Cepheiden.

Die Messung der Entfernungen von RR Lyrae Sternen und Cepheiden werden mit unseren eigenen Verfärbungskarten korrigiert. Mit diesen Entfernungen errechnen wir die Skalenhöhe, der Positionswinkel und die Inklination der Großen und Kleinen Magellanischen Wolke (G/KMW). Die Skalenhöhe der KMW ist signifikant höher als die der GMW. Die jungen Cepheiden der KMW haben eine andere Orientierung als die alten RR Lyrae Sterne. Eines der interessantesten Resultate ist der versetzte Balken der GMW, welcher, in beiden Populationen, bis zu ~ 5 kpc aus der Scheibe herausragt.

Die Metallizitätsverteilungfunktion wird aus Metallizitäten einzelner RR Lyrae Sterne bestimmt und zeigt signifikante Unterschiede zwischen GMW and KMW. Die mittlere Metallizität der KMW ist um ~ 0.2 dex niedriger. Dies ist ein Hinweis auf eine unterschiedliche Anreicherungsgeschichte der frühen Wolken.

Die Untersuchung der RR Lyrae Sterne in den OGLE Feldern des Galaktischen Bulge erlaubt es Verfärbungen, Metallizitäten und Entfernungen zu RR Lyrae Sternen im Bulge und in einem kleinen Teil des Sagittarius Stroms zu bestimmen. Der Strom hat eine signifikant niedrigere Metallizität und scheint geneigt zu sein.

Mit Hilfe einer spectroskopischen Analyse von individuellen Elementhäufigkeiten von neun möglichen metallarmen RR Lyrae Sternen, finden wir den bisher metallärmsten Stern ($[Fe/H] = -2.7$ dex) in den Magellanischen Wolken überhaupt. Die Elementhäufigkeiten der anderen Sterne ermöglichen die Schlußfolgerung, dass der Galaktische Halo durch die Akkretion einer Galaxie von Magellanischem Typus entstanden sein könnte.

Für meine Eltern und für Katharina,
ohne Euch hätte ich dies nicht geschafft.

"Handle so,
dass die Maxime deines Willens
jederzeit zugleich
als Prinzip einer allgemeinen Gesetzgebung gelten könne."

Immanuel Kant
§ 7 Grundgesetz der reinen praktischen Vernunft in der Kritik der praktischen Vernunft

Contents

"There’s an old saying. Fortune favors the bold.
Well, I guess we’re about to find out."
Benjamin Sisko - Star Trek: Deep Space Nine (Sacrifice of Angels)

1

Introduction

This thesis compiles work on several different topics, which can be illustrated by a house with several levels. Each level is needed to build the next on top of it. However every level has interesting patterns of its own, which are worth investigating and which are different from all the other levels. The central theme or the fundament of this construct in our case are the Magellanic Clouds (MCs) and the variable RR Lyrae stars. Therefore their history and their most important properties are described in this chapter. Furthermore I will present a more detailed introduction for each level/topic as we enter them. This should allow you (as the reader) to gain a better understanding of the characteristics of each level you will visit.

1.1 Magellanic Clouds

The MCs are the largest galaxies orbiting our Milky Way (MW). Visible only from the southern hemisphere, they were first described by the Persian astronomer Abd al-Rahman al-Sufi in 964 AD in his *Book of fixed stars*. He named the object al-Baqar al-Abyad or the “White Bull”. For the ‘general European astronomical community’the MCs were unknown until Ferdinand Magellan described them while circumnavigating the world for the first time. However, the name ‘Magellanic Cloud’was introduced much later and until the 18th century they were known as ‘Large Cloud’and ‘Small Cloud’.

The sizes and proximity of the MCs give us the opportunity to study them in great detail. However, many questions remain unanswered. To solve some of the open questions I dedicate my PhD thesis to the further exploration of these objects, especially because some of the parameters of the MCs are used to infer other astronomical scales. Even though the distances to the clouds are not yet settled, beyond doubt, they are used as one of the essential steps defining the cosmological distance ladder (Freedman et al. 2001). But there are also other unresolved questions. MC-type galaxy are not commonly found as satellites of other spiral galaxies (Liu et al. 2011), which is in agreement with SPH-simulations performed by Libeskind et al. (2007). This rarity might be giving us hints towards the formation history of the MW and its satellite galaxies. Models indicate that the MCs might be on their first passage around the MW, as proposed by Besla et al. (2007) using the proper motion data of Kallivayalil et al. (2006b,a). If the MCs are infalling galaxies the chemical building blocks might have been different from our own Galaxy. The old and metal-poor stars as tracers of the early star formation history (SFH) could have a different chemical composition in the MCs than in the halo of the MW, which consists mainly of old stars. This would lead to a different metallicity distribution function (MDF) of the MCs compared with the MW as well as with the other MW satellite galaxies.

There are many other issues to investigate , but I would like to start with ordering the different results found during the last 100 years of research on the MCs, when astronomers realized that our Galaxy might not be the sole constituent of the universe.

I will start with one of the most important parameters – the distance. The ‘Great Debate’of Shapley and Curtis in 1920 (Hoskin 1976) was the climax of the discussion of whether the Galaxy was the only object in the universe or whether island universes existed (this term had already been introduced by Kant in 1755). In 1908 Leavitt had proposed Cepheids as distance indicators and confirmed their calibration in Leavitt & Pickering (1912). The discovery of Cepheids in the Andromeda galaxy and in NGC 6822 by Hubble (1925a,b) solved the question in favor of the island universes. These discoveries made it possible to think about galaxies as independent objects and therefore to determine realistic distances.

The distances to the MCs had already been investigated at that time. The different methods, however, revealed very different results. The distances found for the Large Magellanic Cloud (LMC) ranged from 15 kpc using O-stars (Wilson 1924), 30.7 kpc, derived by Lundmark (1924) utilizing O-stars and a star cluster, to the Cepheid distance of 34.5 kpc (Shapley 1924). The great difficulty of distance determination at that time is illustrated by the distance of 0.95 kpc obtained by Perrine (1927) using Cepheids and star clusters.

During the 1930s and 1940s only minor work was done on the MCs, but Shapley (1953) investigated globular clusters (GCs) and restarted the discussion by proposing that the MCs should have double the distance than believed before. Thackeray & Wesselink (1953) were the first to use variable RR Lyrae stars as distance indicators for the MCs. They found both Clouds to be at the same distance of 44 kpc and revised this value to 55 kpc in Thackeray & Wesselink (1955). The equal distances of both MCs were confirmed by de Vaucouleurs (1955c) using Cepheids and Novae and determining a distance of 56.2 kpc. These values are already close to today’s mean distance determinations for the MCs. In 1968 Sandage & Tammann disentangeled the distance moduli for LMC and Small Magellanic Cloud (SMC), obtaining a difference of 11 kpc between the two objects. The methods and distance determinations have been refined since those days, but the distances have not changed dramatically. Reviewing the most recent distances, Alves (2004) found a mean distance modulus for the LMC of $m - M = 18.50 \pm 0.02$ mag (50.1 kpc). In the review of Walker (2011) a mean value of $m - M = 18.48 \pm 0.05$ mag (49.7 kpc) was determined.

Johnson (1961) suggested that the SMC might have a large line-of-sight depth and Mathewson et al. (1986) established that the SMC has a great depth extent of more than 30 kpc. Even though this value might be too large (cf. Crowl et al. 2001; Subramanian & Subramaniam 2009, hereafter S09), it complicates the determination of a mean distance. Westerlund (1997) stated a mean value of $m-M = 18.90$ mag (60.3 kpc), averaging over several different measurements and methods. Newer estimates using a variety of different distance indicators, such as Cepheids, tip of the red giant branch (RGB), red clump (RC) or RR Lyrae stars, result in (mean) distances between 18.85 mag $\leq m - M \leq$ 19.11 mag.

The mean distances to the MCs may now have been determined to an acceptable precision, but the uncertainty on their not-so-well-determined three-dimensional structure, especially of the old population, always adds additional uncertainties. Nikolaev et al. (2004) used more than 2000 Cepheids, observed by the MACHO survey (Alcock et al. 2000), to determine distances and structural parameters of the LMC. Even though they show three-dimensional maps, Nikolaev et al. (2004) do not deduce scale-height estimates for the LMC. They only state that the bar of the LMC seems to be located about 0.5 kpc closer to the observer than the main disk. In Subramaniam (2003, 2004) and Subramaniam & Subramanian (2009b) the question of the location of the bar is raised again using red giants and RR Lyrae stars, but with the opposite conclusion, which “rules out” (Subramaniam & Subramanian 2009b) that the bar is located in front of the LMC.

Using pulsating red giants from the second phase of the Optical Gravitational Lensing Experiment

(OGLE II) data set, Lah et al. (2005) divided the MCs into equally sized fields on the sky. For each field they evaluated the mean distance. The differences between the mean distances of the different fields are 2.4 kpc for the LMC and 3.2 kpc for the SMC, which they regard as a lower limit for the scale height. However, due to averaging over all distances within the fields, the scale height might be considerably higher than these values. Another estimate using RC stars by S09 led to a depth of 4.17 ± 0.97 kpc for the LMC and 4.90 ± 1.23 kpc for the SMC, respectively. The newest estimate of the SMC depth utilizes RR Lyrae stars and Kapakos et al. (2011) found a value of 4.13 ± 0.27 kpc. Instead of using individual stars to determine the scale height of a system the distribution of clusters can be used as a proxy. In Crowl et al. (2001) the clusters give a depth of the SMC between 6 kpc and 12 kpc, while the clusters analyzed in Glatt et al. (2008a) lead to a depth of approximately 10 kpc.

Most of these investigations have used mean reddening estimates from, e.g., RC stars. These estimates do not take internal differential reddening effects into account and might therefore have led to misinterpretations of the data. Additionally, most of these studies bin the data and determine mean distances with standard deviations. Therefore it is possible that smaller features were overlooked or averaged out. We improve the presentation of the data in this respect. For this purpose we develop new methods to gain a better insight into the reddening estimate for each individual star and use them on unbinned datasets.

Before describing the structural parameters in detail we go for a short excursion into the morphology of the MCs. Even though most people consider the LMC as an irregular galaxy, some consider it to be a barred spiral of type *SB(s)m* (de Vaucouleurs et al. 1991). Nonetheless, the LMC differs from normal spiral galaxies in terms of not having spiral denisty waves and of showing solid-body rotation just like other massive galaxies. Its “bar” appears to be distinct from the bar features observed in massive spiral galaxies. Following de Vaucouleurs et al., the LMC is often called the prototype of Magellanic spirals, which are kinematically quite different form the “normal” spirals int he classical Hubble scheme. In Westerlund (1997) the LMC is characterized as a circular disk galaxy with an overlaid bar feature. Whether the bar is aligned with the disk is still under debate (e.g., Subramaniam & Subramanian 2009b, and above) and is one of the important questions discussed in this thesis. For the SMC the morphology is even harder to determine. In 1961 Johnson described a spiral pattern and de Vaucouleurs & Freeman (1972) concluded that the SMC is a rotating galaxy with a spiral structure. However, the great depth extent and the asymmetry of the SMC, due to the very different distribution of old and young stars (Zaritsky et al. 2000), makes it rather difficult to assign it to a morphological class. Today the SMC is most often described as an irregular dwarf galaxy (e.g., Wilcots 2009) or as the prototype of Magellanic irregulars.

Photographic plates with a limiting magnitude of 16 mag were used by de Vaucouleurs (1955a) to determine an inclination angle i of 65° and a position angle Θ of 160° for the LMC. Since many authors have determined the structural parameters of the LMC, I will only mention some of those made within the last decade. It is clear that, for the LMC, the structural parameters have converged and the different methods do not result in large discrepancies. The global shape of the LMC, as estimated by van der Marel (2001) from surface density maps of asymptotic giant branch (AGB) stars and RGB stars, is shown in Figure 1.1. For the inclination angle, different studies find values between $i = 23.5° \pm 0.4°$ (Koerwer 2009) and $i = 34° \pm 6°$ (van der Marel & Cioni 2001). The position angle is mostly in agreement with the value of $\Theta = 122.5° \pm 8.3°$ (e.g., van der Marel 2001; Pejcha & Stanek 2009; Subramaniam & Subramanian 2009a), however some studies deduce a position angle around $\Theta = 154° \pm 3°$ (Nikolaev et al. 2004; Koerwer 2009).

For the SMC, an inclination angle i of 30° and a position angle Θ of 45° have been determined already by de Vaucouleurs (1955b). These values are based on the brightest stars of the SMC, with a magnitude limit of 16 mag, and do not take the old population into account. Newer estimates of the structural parameters, using young Cepheids, found an inclination angle of $i = 68° \pm 2°$ and a position

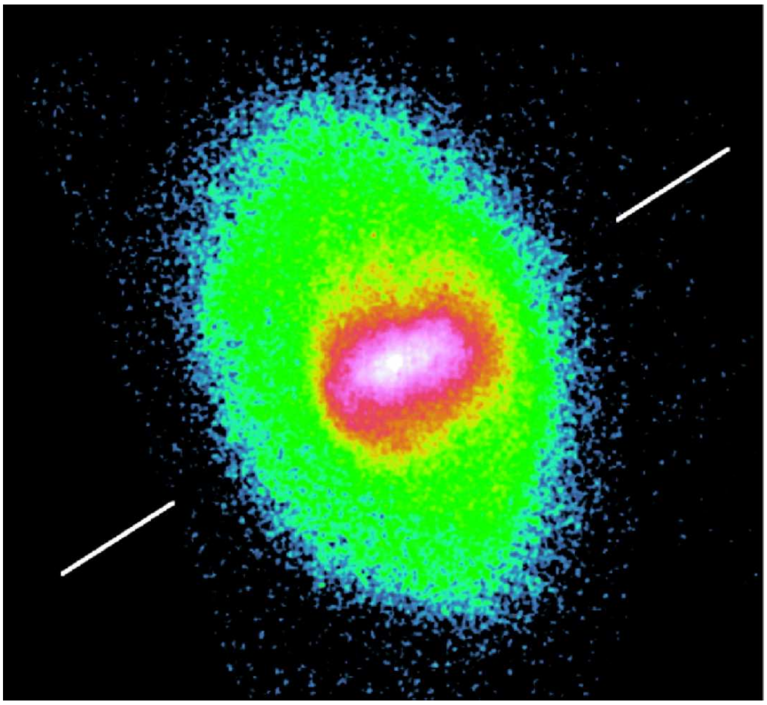

Figure 1.1: Surface number density distribution of AGB and RGB stars within the LMC. It was deprojected using the parameters determined in van der Marel & Cioni (2001). Figure taken from van der Marel (2001).

angle of Θ = 238° ± 7° (Groenewegen & Oudmaijer 2000). However, Zaritsky et al. (2000) showed that the young population is much more extended than the old stars and has a different orientation. For the RR Lyrae stars of the SMC, Subramanian & Subramaniam (2012) found $i = 0.4°$ and Θ = 66°.

The different orientation of the old and young populations of the SMC is based on the SFH of the clouds. The LMC had very intensive star formation in the first few Gigayears (Gyr) after its formation. While Harris & Zaritsky (2009) found that only very little star formation was going on from 12 Gyr to 5 Gyr ago and then got re-ignitied and continued until today, Rubele et al. (2012) showed that the star formation was continuous with only minor contributions in the last three Gyrs. For the SMC Harris & Zaritsky (2004) found that star formation was active until 8.4 Gyr ago, went into a very quiet phase and restarted again about 3 Gyr ago. These results are in contradiction to Noël & Gallart (2007) and Sabbi et al. (2009), who found that the SMC star formation had a very quiet early phase followed by several bursts of star formation 0.3 Gyr, 3-4 Gyr and 6 Gyr ago. In recent times both MCs underwent several bursts of star formation, which happend at very similar times. These results are indicative of very close interactions of the MCs with each other in the last several Gyr. The long period of quiescence in both Clouds and the distinct times of early star formation are tempting to draw the conclusions that the MCs have not always been together.

The interactions of the LMC and SMC have perturbed the shape and in particular the gaseous component of both galaxies and led to the formation of the Magellanic bridge and Magellanic stream, respectively. The bridge, first discovered by Hindman et al. (1963), connects both Clouds with each other and contains mainly metal-poor H I gas. Irwin et al. (1985) were the first to find stars within the bridge, which are believed to have formed in-situ and are very young with ages below 300 Myrs (Harris 2007). Furthermore, the LMC has an elongated shape (e.g., Caldwell & Coulson 1986; van der Marel 2001) and indications of warps have been found (e.g., Olsen & Salyk 2002; Nikolaev et al. 2004). The Magellanic stream is a gas-only feature that contains of a trailing and a leading arm and spans around 200° on the sky (Nidever et al. 2010). In contrast to the bridge, the stream is emanating from the interaction of the MCs with the MW.

Until a few years ago a very different scenario was favored. It seemed that the MCs had orbited the MW for at least the last 10 Gyr, most probably together (e.g., Westerlund 1997). With *HST* data Kallivayalil et al. (2006b,a) showed that the proper motion of what might be considerably larger than measured before. These results were used by Besla et al. (2007) to propose a new model for the MCs, where both Clouds are infalling (or at least have highly eccentric orbits) and are on their first passage around the MW. In Piatek et al. (2008) the *HST* data are reexamined to test for systematic errors in the the work of Kallivayalil et al. (2006a). Their results are consistent with each other. Ground-based proper motions taken by Costa et al. (2009, 2011) and Vieira et al. (2010) reveal smaller values, however with larger errors. These newer estimates are more consistent with a bound scenario. Furthermore, several models of the MCs have been proposed in recent years, using the different proper motion results in the literature. These models, which also have to take the Magellanic Stream into account, lead to very different scenarios. Růžička et al. (2010) can explain the features of the MCs only with a bound scenario, while Besla et al. (2010) show that a first infall could produce the stream in its actual shape, even though the times of highest star formation activity in the model are not compatible with the observations.

The question of the origin of the MCs will not be answered by the current proper-motion measurements. Other measures are therefore required. A direct probe of the properties of the old stellar population is a feasible way to disentangle some of the unsolved questions about the history of the MCs. The MDFs and metallicity evolution of the Clouds could, in particular, give insights into their evolutionary history. The most straightforward way of investigating old populations are GC systems. These star clusters are usually very old and therefore probe the early evolutionary stages of a galaxy. While several old GCs are present in the LMC and some of them have already been spectroscopically investigated by Johnson et al. (2006) and Mucciarelli et al. (2009, 2010), only one GC (NGC121) is present in the SMC. Furthermore, NGC121 is several Gyr younger than the oldest stars in the SMC (Glatt et al. 2008b) and therefore more metal-rich, with [Fe/H] = −1.46 dex. To investigate the old population with field stars is complicated by the fact that their age determination is in general not easy.

Several investigations have used RGB stars within both Clouds to determine abundances of stars with ages spanning the whole age range of ages larger than 1 Gyr. In Gallart et al. (2008) and Carrera et al. (2008b, 2011) several hundred LMC RGB stars were spectroscopically investigated and metallicities were determined through measurements of the Ca II triplet. These authors found that the mean metallicity decreases towards the outskirts, which is mainly caused by the lower number of stars with ages below 1 Gyr. CMD fitting, however, revealed only a handful of old and metal-poor stars within the sample of the observed stars. Carrera et al. (2008a) looked at RGB stars of the SMC and found a similar result of a metallicity gradient, caused by an age gradient. With a different sample of SMC RGB stars, De Propris et al. (2010) found hints for a second bump in the MDF of the SMC, indicative of a very intensive episode of star formation during the formation of the Magellanic Stream. No hint for any kind of metallicity gradient or bump was found by Parisi et al. (2010) with field RGB stars of the SMC. These investigations of the SMC contained only a minority of old stars in their sample. To infer more details about the early history of the MCs, a different tracer that is purely old and easily recognizable is needed.

Gratton et al. (2004) and Borissova et al. (2004, 2006) have performed low resolution spectroscopic measurements of RR Lyrae stars in the LMC. These stars have ages of at least 9 Gyr (Sarajedini et al. 2006) and are therefore consistently old. By investigating the Ca K line of over 100 RR Lyrae stars within the bar and central regions, Gratton et al. and Borissova et al. found a broad metallicity distribution, with a range of $-2.3\,\mathrm{dex} < [\mathrm{Fe/H}] < -0.6\,\mathrm{dex}$. The mean metallicity in each analysis was found to be around $[\mathrm{Fe/H}] \simeq -1.50\,\mathrm{dex}$. Using the results of OGLE, several investigations on the metallicities of RR Lyrae stars using their photometric properties have been conducted. For the LMC, Feast et al. (2010, from now on FAW10) used the OGLE III (Udalski et al. 2008a,b) survey to determine a mean metallicity of

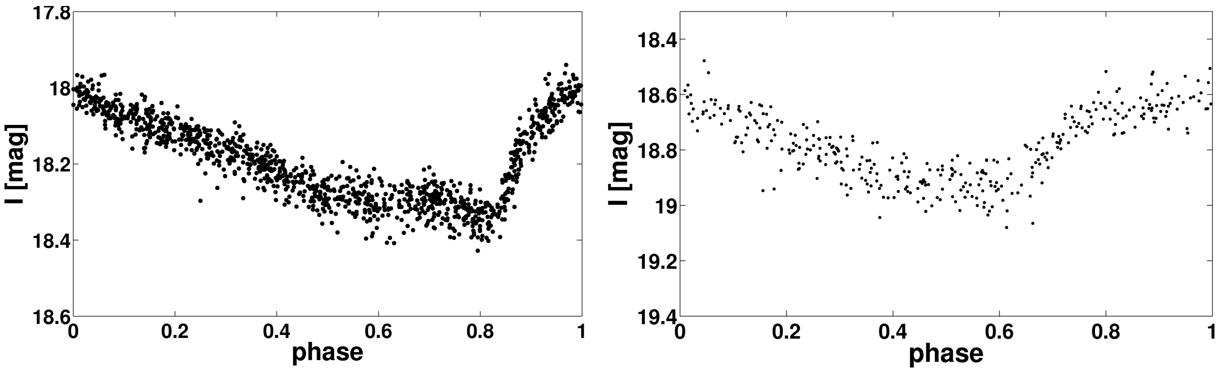

Figure 1.2: Example lightcurves of RR Lyrae stars of type ab (left panel) and type c (right panel). The lightcurves are taken from the OGLE III data (Soszyński et al. 2008) of the LMC.

$[\mathrm{Fe/H}] = -1.218 \pm 0.004$ dex with a small gradient of 0.01 ± 0.002 dex kpc^{-1} from the central parts to the outer fields. From OGLE II data, Deb & Singh (2010, from now on DS10) analyzed 352 RR Lyrae stars of the SMC. The mean metallicity is significantly lower, at $[\mathrm{Fe/H}] = -1.56 \pm 0.25$ dex. Kapakos et al. (2011) determined photometric metallicities for 100 RR Lyrae stars of the SMC using OGLE III data and found a mean value of $[\mathrm{Fe/H}] = -1.62 \pm 0.41$ dex.

RR Lyrae stars appear to be ideal tracers for the old field star population. Therefore I would like to discuss them in further detail.

1.2 RR Lyrae stars

The variability of the star RR Lyrae was discovered by Williamina Fleming in 1898 and published in the *Harvard Second Catalogue of Variable Stars* by Pickering (1903). At the time, variable stars were classified into three different groups depending on the shape of their lightcurves (see Kiess 1913 for a description of the classes). As the allocation to one of the groups was not so obvious for the RR Lyrae stars, they were sometimes treated as *cluster variables* (e.g., Kiess 1913) or as Cepheids (e.g., Shapley 1916). In 1924 Hertzsprung introduced a new class of variables of type RR Lyrae.

Schwarzschild (1940) recognized that the different periods and shapes of the lightcurves of the RR Lyrae stars were connected to the pulsational properties of the stars. At that time the RR Lyrae stars were divided into type a, b and c (Bailey 1902) based on their lightcurve shapes. The shape of the lightcurve changes steadily from a nearly sinusoidal shape to a highly asymetric shape with a long descending phase and a strong increase in magnitude, see Figure 1.2 for examples of the lightcurves. Later it was found that type a and b pulsate in the fundamental mode, while type c are first overtone pulsators. The RR Lyrae stars are therefore nowadays divided into two groups of type ab and type c.

The pulsation of the RR Lyrae stars is driven by the so-called κ-mechanism (Baker & Kippenhahn 1962). A layer of partially ionized helium is exited by the radiation coming from the interior of the star. The ionization of He^{+} to He^{++} sets electrons free and the opacity of the layer increases. The radiation becomes trapped inside the helium layer and the pressure increases until the radiation pushes the upper layer to the outside. Due to the pressure the temperature decreases and the ionization of the layer is reversed. Therefore the opacity shrinks, the radiation can move through the star more easily and the radiation pressure decreases. This is the moment when gravitional forces take over and the layer contracts back into the star. When the layer has fallen back far enough the ionization of the helium layer starts again and the next cycle begins (see Figure 1.3). Several effects prevent most stars from pulsating. If the partially ionized helium layer is located too deep inside the star the pressure is not strong enough

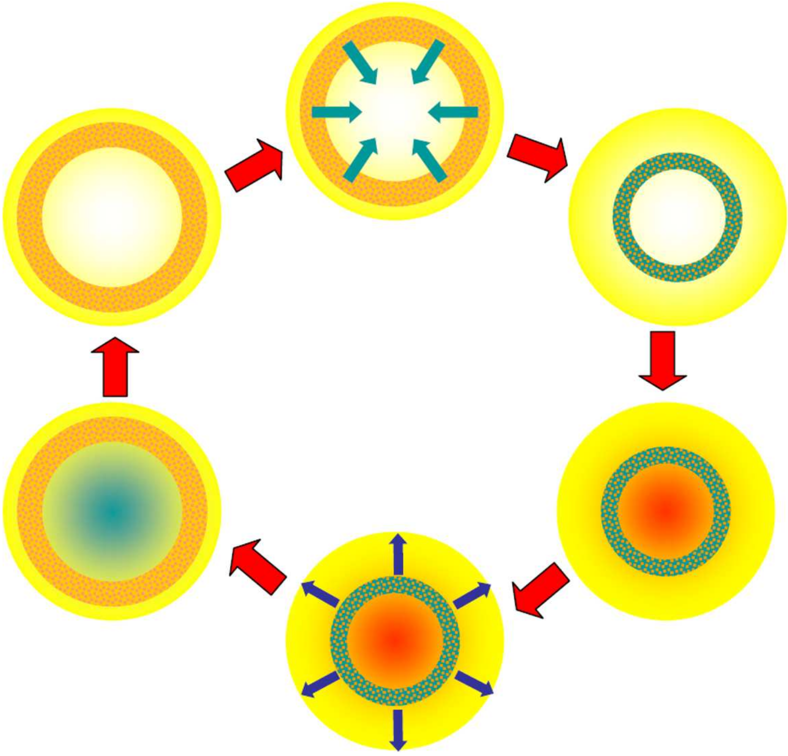

Figure 1.3: The pulsation cycle of a typical variable star. The partially ionized helium layer (green ring) traps the radiation, the layers below the helium heat up (red interior). The helium layer is pushed outside, the radiation can escape, the star cools (blue central region) and the helium is reionized (orange ring). The layer falls back into its former configuration, where it starts to heat again. The proportions of this figure are obviously not to scale. Figure courtesy of Stefan Jordan

to move the outer layers, if the partially ionized layer is too close to the surface the density of the gas is too low and the effect is negligible as well. Additionally some stars are dominated by convection in their outer layers. The layers are therefore well mixed and the layer of partly ionized helium necessary for pulsations to develop cannot exist. All these factors lead to the observation that pulsation caused by the κ-mechanism is only observed in the instability strip (Cox & Olsen 1963), where the effective temperature of the star is between 5500 K and 7500 K (Figure 1.4).

As mentioned before some stars pulsate in overtone modes. The exact reason for the different pulsation modes are nor yet entirely understood, but Christy (1966) explained these overtone pulsations as the additional influence of a partly ionized layer of hydrogen. The physical principles are the same as for the partly ionized helium layer, the hydrogen layer is just located closer to the star's surface. In overtone pulsators the physical properties (temperature, metallicity, density, etc.) are just adequate to have both layers being ionized at the same time. Observations show that type c stars are in general hotter and have shorter periods. This agrees with the models (e.g., Bono et al. 1997) which predict that hotter RR Lyrae stars are more unstable towards overtone pulsations.

Another important feature of RR Lyrae stars is the Blažko effect, an effect that is still not fully understood. In 1907 Blažko reported modulations in the amplitude and phase of variable stars for the first time. These modulations were later confirmed by Shapley (1916) investigating the star RR Lyrae. The reason for the additional modulation of the pulsation has been subject to speculation for more than a century. Even though the number of possibilities accounting for the underlying physical processes have steadily been eliminated, the final solution has still not been found. But the number of stars exhibiting

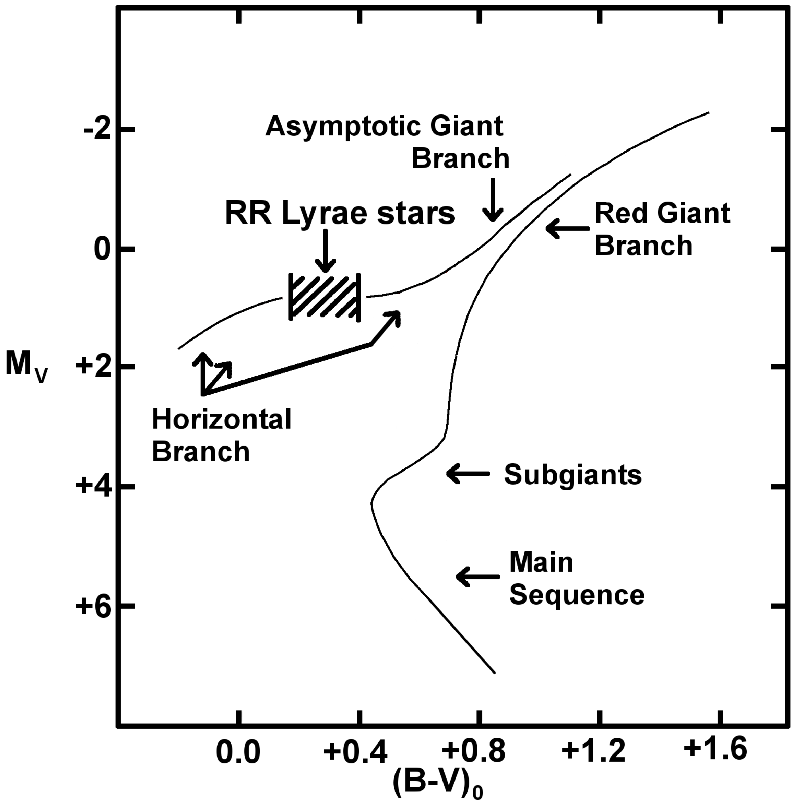

Figure 1.4: Evolutionary track of RR Lyrae stars. Progenitors of RR Lyrae stars have masses around 0.7 $M_\odot$ and are rather metal-poor. After finishing hydrogen-core burning the stars enter the giant-branch stage. With the ignition of helium they move to the asymptotic giant branch and go through the RR Lyrae phase. While they are in the instability strip the RR Lyrae stars pulsate with periods between 0.2 days and 1.1 days and have typical temperatures between 6100 K and 7400 K. Their mean absolute magnitudes are very stable around 0.6 mag, dependening on the metallicity, and these type of stars are therefore used as standard candles. Values and figure are taken from Smith (2004) and slightly modified.

the Blažko effect is believed to be as high as 50% (e.g Jurcsik et al. 2009). Usually most authors find that the fundamental pulsators show the Blažko effect more often than the first overtone pulsators (e.g., Benkő et al. 2006). However, Arellano Ferro et al. (2011) show that in the GC M53 the frequency of type c pulsators with Blažko modulations is nearly double that of the type ab. Kolenberg (2011) summarized the most recent models for the Blažko effect. The observation with the space telescopes *CoRoT* and *Kepler* allowed RR Lyrae stars to be observed with unreached precision thus far. The favoured models to explain the Blažko effect are either pulsation due to non-radial pulsational modes (e.g., Olech et al. 2000) or models that treat the modulations similar to the theory of electronic signal transmission (Benkő et al. 2011).

The first distance estimate of an RR Lyrae star was carried out in 1938 by Joy on W Canum Venaticorum. Thackeray & Wesselink (1953) conducted the first distance estimates of the MCs using RR Lyrae stars. These authors used the relation between the luminosity of a star and its period (e.g., Sandage 1958). Subsequently, Arp (1955) and Preston (1959) discovered that it is possible to relate the period of an RR Lyrae star to its metallicity. In Sandage et al. (1981) a general description of absolute magnitude in dependence of the metallicity was introduced. Therefore it was a great improvement, when the determination of the metallicity of a RR Lyrae star by using a photometric method became possible and therefore large datasets could be chemically investigated.

Adam (1978) and Simon & Lee (1981) showed that the parameters from a Fourier decomposition of a Cepheid lightcurve are related to several stellar parameters and extended this work to RR Lyrae stars in Simon & Teays (1981) and Simon (1985). The different orders of the Fourier phase ϕ_n are related to one another by $\phi_{ij} = \phi_i - i\phi_j$. An interdependency between the Fourier parameter ϕ_{31}, the period and the metallicity of RR Lyrae stars was found by Simon (1988) and Kovács & Zsoldos (1995), while Jurcsik & Kovács (1996) introduced the formula

$$[\mathrm{Fe/H}] \quad = \quad -5.038 - 5.394\,P + 1.345\,\phi_{31} \tag{1.1}$$

This formula is based on the metallicity scale calibrated for RR Lyrae stars by Jurcsik (1995, from now on J95).

The Fourier decomposition of the lightcurve of a variable star is usually done by a multi-order fit of the form

$$V = A_0 + \sum_{k=1}^{N} A_k \sin(k\omega t + \phi_k) \tag{1.2}$$

where V is the observed V band magnitude, $A_{0/k}$ is the amplitude, ϕ_k the phase, ω the angular frequency, and t the specific time at which a data point was measured. N is the order to which the Fourier series is developed, which in most cases is between four and six. The values for the Fourier amplitude and phase depend linearly on the shape of the decomposed lightcurve (Stellingwerf & Dickens 1987). The skewness of the lightcurve, which is a measure of the time while the star gets dimmer in comparison to the time while the magnitude of star is rising again, is related to the amplitude. The Fourier phase parameters depend on the acuteness of the lightcurve. The acuteness is a measure for the time of the lightcurve spent below the average luminosity compared to the time above average luminosity. No physical explanation has been found, why the Fourier phase ϕ_{31} is related to the metallicity (Simon & Clement 1993), it is an empirical result based purely on observational evidence. However, Sandage (2004) showed that the distribution of RR Lyrae stars in a log P vs. [Fe/H] diagram, which appears unordered at first view, can be ordered by introducing fiducial lines of constant Fourier parameters ϕ_{31}. This follows the same structure as for the period-metallicity relation found by Arp (1955) and Preston (1959). For this relation the amplitude, color or rise time (time from minimum to maximum light) is used as a second parameter. Sandage (2004) showed that ϕ_{31} is preferable to the other parameters, because the relation is much tighter and the uncertainties are therefore lower. Some investigations, such as Clement & Shelton (1999) and Bono et al. (2007), found that the period-amplitude relation depends only weakly on metallicity but instead on the Oosterhoff type. Based on these results Smith et al. (2011) point out that the relation between the period, amplitude and the metallicity might not be reliable. In absence of other reliable estimators, they state however that these relations are still useful.

Before summarizing the different metallicity-luminosity relations found in the recent literature, we take a short excursion into the period distribution of RR Lyrae stars within GCs and the history of the Oosterhoff-types.

Grosse & Schorr (1932) found first indications that the RR Lyrae stars within GCs have similar mean periods, but that these mean periods differ from one GC to another. In 1939 and 1944 Oosterhoff defined two groups of clusters. In these groups of clusters the fundamental mode pulsators of the RR Lyrae stars have mean periods of around 0.55 days and 0.65 days. In the so-called ‘Oosterhoff-gap’, with periods between these two values, only very few MW GCs are present. More recent investigations of the GC systems within the satellite galaxies (see e.g., Mackey & Gilmore 2004 for a compilation of properties of several clusters) and their RR Lyrae stars have revealed that the RR Lyrae stars are preferentially located inside the ‘Oosterhoff-gap’(Figure 1.5). These very different properties of the RR Lyrae stars within MW GCs in comparison with the objects located within the satellite galaxies, together with the different chemical abundances of the intermediate metallicity clusters (Geisler et al. 2007), are taken as

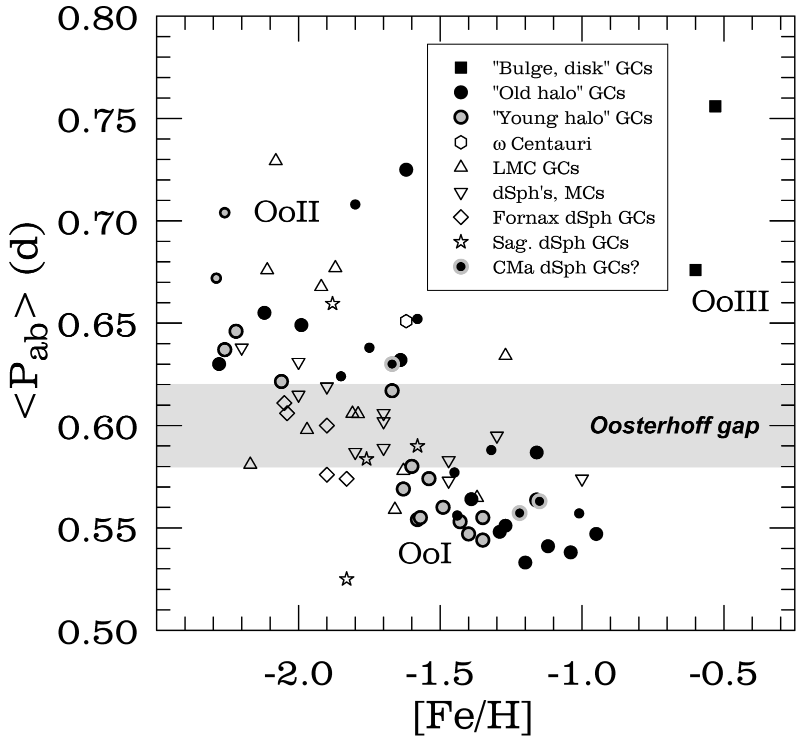

Figure 1.5: Oosterhoff types of GCs within the MW and its satellite galaxies. The MW GCs are located in two groups, while the RR Lyrae stars within the satellite galaxies are preferentially located in the 'Oosterhoff-gap'. Figure taken from Smith et al. (2011).

an indication that the hierarchical build-up of the MW (halo) from present-day type dwarf spheroidal galaxies (dSphs) as well as from LMC like irregular galaxies is unlikely (Catelan 2009; Smith et al. 2011).

The first relation between the absolute magnitude and the metallicity was introduced by Sandage et al. (1981). Since then many different relations have been found, most being of the form $M = a + b[\mathrm{Fe/H}]$. To calibrate the absolute magnitudes of the RR Lyrae stars, several different methods are used. The most popular methods are statistical parallaxes, the Baade-Wesselink method and main-sequence fitting. The Baade-Wesselink method (Baade 1926; Wesselink 1946) uses spectroscopic information to measure the pulsation curve of a variable star and to determine the difference between the minima and maxima in radius. The color differences throughout a pulsation cycle of the star are used to determine the ratios between the star's radii at different times. Using both pieces of information together, it is possible to solve for the radius of the star. Together with the temperature the absolute magnitude can be determined, and hence the distance. For a more detailed description of this method, see e.g., Smith (2004). In Sandage & Tammann (2006) the different relations for the absolute magnitude M_V-metallicity relation have been summarized and the interested reader is referred to the review for details on the different relations. However, the different relations lead to significant differences in the absolute magnitudes of the stars and therefore in their distances. At a metallicity of $[\mathrm{Fe/H}] = -1.5$ dex the absolute magnitudes of the different calibrations vary between 0.47 mag (Carretta et al. 2000a) and 0.68 mag (Fernley et al. 1998), which translates into a distance difference of about 5 kpc at the distance of the LMC. Parallax measurements of five RR Lyrae stars with *HST* conducted by Benedict et al. (2011) confirmed that the M_V-metallicity relation by Clementini et al. (2003) and Gratton et al. (2004) leads to the best agreement with the data. Several authors such as Catelan et al. (2004), Sandage & Tammann (2006) and Bono et al. (2007), have introduced relations with an additional quadratic term of the metallicity ($M = a +$

b[Fe/H] + c[Fe/H]^2). However, the observations do not clearly show whether these quadratic equations lead to better fits of the data (e.g., Benedict et al. 2011).

1.3 The Optical Gravitational Lensing Experiment - OGLE

In 1992 the OGLE (Optical Gravitational Lensing Experiment) experiment started its first phase of observations of the MCs and the Galactic bulge region using the 1 m Swope telescope of Las Campanas Observatory, Chile (Udalski et al. 1992). This telescope was replaced by a 1.3 m telescope owned by the OGLE collaboration at Las Campanas in 1995, with which the second phase of the OGLE experiment was performed. The CCD camera of the first two phases had a field of view of $15' \times 15'$ and 2048×2048 pixels (Udalski et al. 1997). Data were taken preferentially in the I band and additionally in the V and B bands until 2001, when the third phase of OGLE was started. The eight CCDs of the OGLE III camera, each with 2048×4096 pixels, took data until 2009. With a total of 8192×8192 pixels, this camera covered a total area of $35' \times 35'$ per exposure (Udalski 2003b). In the Galactic bulge region 92 square degrees were monitored, in the LMC nearly 40 square degrees, while 14 square degrees were observed in the SMC using V and I band filters. Altogether photometric data of high precision were obtained and are now provided for 340 million stars in the Galactic bulge, 35 million stars in the LMC and 6.2 million stars in the SMC[1] (Udalski et al. 2008a,b; Szymański et al. 2011). The point source catalogues are divided into 267 fields for the bulge, 116 fields for the LMC and 40 fields for the SMC. The 41st SMC field targets the massive Galactic GC 47 Tuc and is ignored in our study.

In addition to the full photometric catalogue, subsets of interesting objects such as RR Lyrae stars or Cepheids have also been compiled by the OGLE collaboration. For the LMC, OGLE III provides data for 17693 RR Lyrae stars of type ab (Soszyński et al. 2008) and 1849 classical Cepheids (Soszyński et al. 2009), which all pulsate in the fundamental mode and are distributed over the entire area of the LMC covered by OGLE. In Soszyński et al. (2010b) the data for 2626 classical SMC Cepheids are presented, while Soszyński et al. (2010a) published the data for 1933 SMC RR Lyrae stars of type ab. All of these stars are also pulsating in the fundamental mode and cover the entire OGLE field of the SMC. For the Galactic bulge Soszyński et al. (2011) found 11756 RR Lyrae stars of type ab. Only 21 fundamental mode classical Cepheids are present in the OGLE III bulge field (Soszynski et al. 2011).

For each star, the period (with individual uncertainties) and mean magnitudes in the V and I bands are provided. For the I band measurements the resulting amplitude of the lightcurve is given. Furthermore, the OGLE III collaboration calculates the amplitude parameters R_{21} and R_{31}, which represent the skewness, as well as phase paremeters ϕ_{21} and ϕ_{31}, corresponding to the acuteness of the lightcurve (Stellingwerf & Dickens 1987), via Fourier decomposition (Simon & Lee 1981; Simon & Clement 1993; Kovács & Zsoldos 1995).

1.4 Why do we look for old stars in the Magellanic Clouds?

As mentioned at the beginning of this chapter, the understanding of the MW as a galaxy being rather ordinary among many others is less than 100 years old (Hubble 1925a,b). Since then many different theories of the formation and evolution of the universe in general and of our own galaxy in particular have been developed. The Big Bang theory (Lemaître 1931) and dark matter (postulated first by Zwicky 1933) are the foundation for our present understanding of the universe and the basis of the large simulations of structure formation in the universe (e.g., Springel et al. 2005). These dark matter simulations are also used to infer constraints about the formation and evolution of our Galaxy (e.g., Guedes et al. 2011).

---

[1] The catalogues are available from `http://ogle.astrouw.edu.pl/`

From now on, I would like to concentrate on the MW and its satellite galaxies, rather than on the evolution of the universe as a whole. The idea of the MW being a spiral galaxy is amazingly old (Alexander 1852). Eggen et al. (1962) introduced a formation model, where the MW was formed from an enormous, instantaneously collapsing gas cloud, first forming the Galactic halo. The gas then settled down to form a disk of stars and gas. Investigating galaxy clusters, Gunn & Gott (1972) proposed that intracluster gas might fall into the galaxies after the initial galaxy formation. Using observational evidence, Searle & Zinn (1978) found that the halo build-up of the MW did not happen from a single gas infall event, but rather in several episodes. Many different simulations tried to match these results (e.g., Gunn 1977; Dekel et al. 1980). Later, evidence was found for an hierarchical galaxy formation scenario, where smaller constituents were formed first and then merged to form the early MW. Ibata et al. (1994) found a stellar stream in Sagittarius (Sgr), which was later identified as a dSph being currently disrupted by the MW. Hernquist & Mihos (1995) and Johnston et al. (1996)were among the first, who gave theoretical evidence for the build-up of the Galaxy by its satellites.

The accretion of satellite galaxies has considerable implications for the disk of a spiral galaxy (Quinn & Goodman 1986). The rather undisturbed shapes of most disks lead to the conclusion that most of the spiral galaxies have accreted less than 10% of their mass in the last 5 Gyr (Navarro et al. 1994). Therefore the stars that were accreted during the merger events and that are still present in our Galaxy should preferentially be old.

The formation scenario for the MW halo is still under debate. It is well known that most halo stars are rather metal-poor, but it is not yet clearly solved where these stars originate from. Dissolving GCs could have contributed a significant amount of stars to the halo, with Martell et al. (2011) finding that at least 17% of all halo stars may have this origin. The accretion of satellite galaxies also contributes to the halo stellar content. Some investigations, for instance by Bell et al. (2008), found that the substructure present in the MW halo is consistent with a halo that is purely made of accretion debris of satellite galaxies. In contrast, Catelan (2009) and Smith et al. (2011) conclude from investigating RR Lyrae stars within GCs that no major contribution was made by satellite galaxies to the Galactic halo. Investigations of the SDSS fields by Carollo et al. (2007) revealed that the halo is not homogeneous, but rather divided into an inner and an outer halo component with rather different metallicities and velocities that lead to a counter-rotation of both components with respect to each other. How these two distinct constituents of the halo would have formed is still an unsolved problem and still under intensive debate (e.g., Schönrich et al. 2011).

In recent years it has been suggested that it is unlikely that the majority of the halo has been formed from the disruption and accretion of smaller dSphs. Instead, simulations suggest that in the early history of the MW, a merger with at least one MC-type galaxy took place (e.g., Robertson et al. 2005). In their model the accretion happened ~ 9 Gyr ago, after an intensive star formation in the dwarf irregular galaxy. Therefore the stellar contribution from the dwarf galaxy to the halo, which was born before the merger, would be observable today as, for instance, RR Lyrae stars. In order to compare the MW halo components, which might have been accreted from the merger, with the MC components from the same era, we have to make sure to observe purely old populations. This is achieved by choosing RR Lyrae stars as tracers for our investigations.

Investigating the halo of M31, Richardson et al. (2009) found that the mean metallicity of its halo is significantly higher than the mean metallicity of the MW halo. In 2008 Font et al. compared the observed substructure of the M31 halo with the structural parameters of simulated halos and found good agreement with an accretion event of an dwarf irregular. Simulations of the observed metallicity and surface brightness distribution by Gilbert et al. (2009) show that this merger event might have happened a few Gyr ago. In the simulations the disk of M31 gets heated and disturbed and some of the stars of the disk moved to the halo. This could explains the higher mean metallicity, as well as the higher mean metallicity of the accreted satellite galaxy. The simulations indicate that the substructure is still visible for M31, because the merger event happend much later as for the MW, where no substructure from a MC-type merger event has been observed yet. There is also evidence that other some spiral galaxies outside of the Local Group have experienced recent accretion due to merger events with satellite galaxies (Ibata et al. 2009).

1.5 Motivation for and structure of this thesis

The structure of this thesis can be divided into two main topics. We would like to gain a deeper understanding for the three-dimensional structure and the structural parameters of both MCs. In addition, we are also very much interested in the early history of the MCs and hope to draw some conclusions about the similarities or differences of the MCs' evolution compared to the evolution of the MW halo and the dSphs orbiting our Galaxy.

The data from the third phase of the OGLE survey allow us to compare the young and old stellar populations with a coherent set of observations. When starting this thesis, our first aim was to derive distances in order to determine three-dimensional maps for all available RR Lyrae stars of type ab and for all Cepheids pulsating in the fundamental mode present in the OGLE field of the MCs. This turned out to be more difficult than anticipated, because, in contrast to the OGLE II data release, no information about the reddening was given by the OGLE collaboration. We therefore had to perform some intermediate steps, which themselves yield in very interesting and important results. These are also presented in this thesis.

At the time the thesis work was started, the reddening maps presented in the literature were either not detailed enough (e.g., Schlegel et al. 1998, from now on SFD98) or the maps were just presented as figures without tables (e.g., Subramaniam & Subramanian 2009b). Therefore, we started this thesis by producing **extinction maps of both MCs** using two different stellar tracers and approaches, namely RC stars and RR Lyrae stars. The analysis and results are presented in Chapter 2. We further compare our extinction maps to many of the available reddening maps of the MCs. In order to allow others to access the extinction values easily, we make the extinctions maps available via the Virtual Observatory[2].

The next steps towards deriving the 3D maps of the RR Lyrae stars are determinations of the metallicities for the old populations of the MCs. As shown in Section 1.2 the absolute magnitude depends on the metallicity of the star, which can be calculated using the period and the Fourier decomposition parameters of the lightcurve. We realized that these results are not only an intermediate step towards the 3D-maps, but in fact give insights into the early chemical enrichment of the MCs, which is a very interesting topic by itself. In Chapter 3, the **metallicity distribution functions of the MCs** are presented and the implications for the early history and the origin of the MCs are discussed.

After performing these two steps we are able to compute **three-dimensional maps of the LMC**. In Chapter 4, the structural parameters scale height, inclination, and position angle are determined for the old RR Lyrae stars as well as for the young Cepheids present in the OGLE III field of the LMC. In particular, the unsolved question of the location and orientation of the bar is intensively investigated.

The different orientation and depth extent of the Cepheids and RR Lyrae stars in the SMC is a result of the recent interaction with the LMC. The **three-dimensional maps of the SMC** and the structural parameters scale height, inclination, and position angle for both stellar populations are presented in Chapter 5. We perform an analysis of the similarities and differences between the young and old population. In particular, the depth extent of the SMC is studied, which is still under debate and for which a variety of values have been published in the literature.

The OGLE collaboration observed not only fields towards the MCs, but also close to the Galactic bulge. Behind the bulge the fields cover a small portion of the leading arm of the Sgr stream. In Chap-

---

[2] `http://dc.zah.uni-heidelberg.de/mcx`

ter 6, we investigate the **reddening map** of the RR Lyrae stars located towards the OGLE fields of the bulge. The Fourier decomposition parameters of the lightcurve are used to find **metallicity distribution functions as well as three-dimensional maps of the Galactic bulge region** and the part of the Galaxy where we expect the **Sagittarius stream** to be located.

The Chapters 2 to 6 of this thesis present the first part of this thesis. Even though the number of pages of this first part easily exceeds the second part, the number of hours spent on the two parts is comparable. This can be explained by the fact that we were using pre-reduced data in the first part, while, for the second part, we had to learn from scratch how to handle the spectroscopic data that are used there.

The acquisition of the spectroscopic data was not as easy as expected. We applied three times for observation time on the VLT/X-Shooter, but our application was rejected every time. Finally we were able to observe four nights (split into two runs) with the MagE spectrograph mounted on the Magellan 6.5 m telescope in Las Campanas, Chile. The **analysis of the medium-resolution spectra of very metal-poor RR Lyrae star candidates** is presented in Chapter 7. The candidates were taken from the analysis presented in Chapter 3. We had hoped to extend the calibration of the relation for the photometric metallicities from the Fourier decomposition of the lightcurve (Smolec 2005) to lower values. It turned out that the data quality was not good enough to do this. However, for the first time, direct chemical abundance measurements of ten different elements were performed for RR Lyrae stars in the MCs. Furthermore we confirm the most metal-poor star found to date in the MCs with a metallicity of $[\mathrm{Fe/H}] = -2.7$ dex. We discuss these findings within the framework of the current models of galaxy formation in ΛCDM and the merger history of the MW (halo).

All chapters presented in this thesis have been or will be published in individual papers. The status of these papers (as of February 20, 2012) is mentioned at the beginning of each chapter. Similarities between the papers and the chapters are unavoidable.

In the last chapter, Chapter 8, the different results are summarized and discussed in a comprehensive manner. This allows an outlook on the further prospectives of this work and what steps should be taken next.

"It is possible to commit no errors and still lose. That is not a weakness. That is life."
Jean Luc Picard - Star Trek: The Next Generation (Peak Performance)

2

New optical reddening maps of the Large and Small Magellanic Clouds

We present new reddening maps of the Small and Large Magellanic Cloud based on the data of the third phase of the Optical Gravitational Lensing Experiment (OGLE III). We have used two different methods to derive optical reddening maps. We adopt a theoretical mean unreddened colour for the red clump in the SMC and LMC, respectively. We subdivide the photometric data for both Clouds into subfields and calculate the difference between the observed red clump position and the theoretical value for each field, which provides us with the reddening value in $(V - I)$. Furthermore reddening values are obtained for 13490 LMC RR Lyrae ab and 1529 SMC RR Lyrae ab stars covering the whole OGLE III region of the MCs. The observed colours $(V - I)$ of the RR Lyrae stars are compared with the colour from the absolute magnitudes. The absolute magnitude of each RR Lyrae star is computed using its period and metallicity derived from Fourier decomposition of its lightcurve.

In general we find a low and uniform reddening distribution in both Magellanic Clouds. The red clump method indicates a mean reddening of the LMC of $E(V - I) = 0.09 \pm 0.07$ mag, while for the SMC $E(V - I) = 0.04 \pm 0.06$ mag is obtained. With RR Lyrae stars a median value of $E(V - I) = 0.11 \pm 0.06$ mag for the LMC and $E(V - I) = 0.07 \pm 0.06$ mag for the SMC is found. The LMC shows very low reddening in the bar region, whereas the reddening in the star-forming leading edge and 30 Doradus is considerably higher. In the SMC three pronounced regions with higher reddening are visible. Two are located along the bar, while the highest reddening is found in the star-forming wing of the SMC. In general the regions with higher reddening are in good spatial agreement with infrared reddening maps as well as with reddening estimations of other studies. The position-dependent reddening values from the red clump method are available via the German Astrophysical Virtual Observatory interface at `http://dc.zah.uni-heidelberg.de/mcx`

This chapter is based on Haschke, Grebel, & Duffau (2011)

2.1 Introduction

The gas rich and star-forming SMC and LMC are the most massive galaxies orbiting the MW. They are used in many ways as benchmarks, for instance, for studies of star formation at lower metallicity (e.g. Cignoni et al. 2009; Glatt et al. 2008b; Sabbi et al. 2009) and as calibrators for the cosmological distance scale (Freedman et al. 2001). Large optical and infrared imaging surveys of the MCs, such as OGLE (Udalski et al. 1992, 2008b,a), the Magellanic Clouds Photometric Survey (MCPS, Zaritsky et al. 1997), the Massive Compact Halo Objects (MACHO) survey (e.g. Alcock et al. 2000; Cook et al. 1992), the Expérience pour la Recherche d'Objets Sombres (EROS, Aubourg et al. 1993) or the Two Micron All Sky Survey (2MASS, Skrutskie et al. 2006), have been completed in recent years. These surveys provide invaluable information about the stellar content of the MCs . But for interpreting the data of these surveys, for deriving star formation histories and for stellar population studies in general the knowledge of the reddening is crucial.

Reddening is caused by gas and dust located between the emitting object and the observer. This leads to dimmer observed magnitudes and redder colours than emitted by the object. The magnitude of absorption and scattering depends on the grain sizes of the dust and on the wavelength of the passing light. For different wavelengths the absorption by dust has a differing effectiveness. The resulting change of the observed colour of the star is defined as $\mathrm{E}(\lambda_1 - \lambda_2) = (\lambda_1 - \lambda_2)_{\mathrm{obs}} - (\lambda_1 - \lambda_2)_{\mathrm{intrinsic}}$ and is quoted in the literature as colour excess, selective extinction or reddening. The total extinction A_λ can be calculated by adopting an extinction law. Using stars from the local neighbourhood Cardelli et al. (1989) found that an extinction law can be introduced that depends on just one parameter: $\mathrm{R_V} = \mathrm{A_V}/\mathrm{E(B-V)}$, which has a typical value of $\mathrm{R_V} = 3.1$. Gordon et al. (2003) tested various lines of sight to test the local extinction laws for more distant fields in the Galaxy, in the LMC and the SMC. They found that for some fields the law is indistinguishable from the result by Cardelli et al. (1989), but many fields show considerable differences from the local extinction law. This is explained by the different environments probed by the authors. However, Gordon et al. (2003, their Figure 10) show that for the visual wavelength range, which is of interest in our current study, the differences in the extinction laws are quite small. For the visible wavelength range Zagury (2007) confirms that the MCs have a similar extinction law as the Galaxy, while he suggests that for regions with deviations other explanations than a differing reddening law might also be valid. Even though the dust content of the Galaxy is far from being understood these studies show that at optical wavelength adopting the extinction law by Cardelli et al. (1989) is generally a valid assumption.

Reddening maps of the MCs have been obtained by several groups. With infrared data from the 2MASS Dobashi et al. (2008, 2009, herafter D08 and D09) explored the dust content of the LMC and SMC, which can be translated into and compared with reddening maps. The optical data of the MCPS were analysed fitting photometric model predictions of stellar luminosity, effective temperatures and extinctions to apparent U, B, V and I magnitudes for the stars in the MCs. In Zaritsky (1999) an extinction map is constructed by finding the best match between the theoretical values and the observations for a fraction of the LMC field. The whole dataset of the MCPS results in wide area reddening maps of the MCs that are presented in Zaritsky et al. (2002, 2004, hereafter Z02 for the SMC and Z04 for the LMC).

For OGLE II (see Section 1.3) reddening maps from estimates based on RC stars (Udalski et al. 1999a,b) were provided. A similar technique was adopted by Subramaniam (2005, hereafter S05) and S09. They measured the position and apparent shift of the RC in the CMD with respect to the theoretically unreddened values to analyse the spatial distribution of the reddening in the V- and I-band of the LMC covered by the OGLE II and the OGLE III surveys.

Sturch (1966) introduced a completely different approach of measuring reddening values. He proposed to use the difference between the observed colour and the intrinsic colour of RR Lyrae stars as an indicator for the reddening towards these stars. RR Lyraes are standard candles with distinct relations to calculate absolute magnitudes from the observable parameters apparent magnitude, period and metallic-

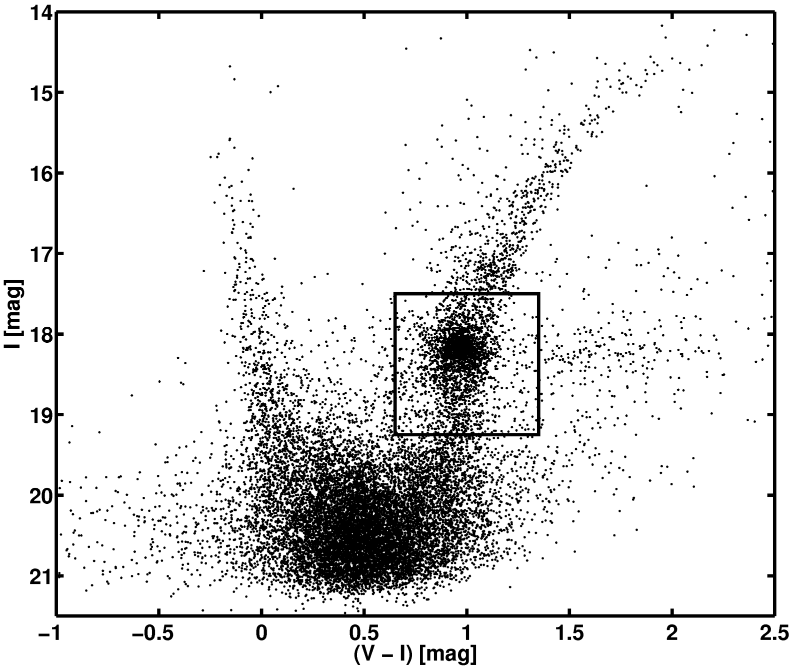

Figure 2.1: A typical CMD of a LMC subfield. This field is located at $RA = 81°32'$ and $DEC = -69°33'$ with a projected size of $9'\times9'$. It contains 18268 stars. 2661 stars are in our RC selection box, represented by the continuous line.

ity. These can be used to obtain the intrinsic colour. Pejcha & Stanek (2009, herafter PS09) used this technique for RR Lyrae stars observed by OGLE III to derive a reddening map of the LMC. For their computations they assume that that all RR Lyrae stars share a common metallicity.

Here we present new optical reddening maps for the MCs derived via two different methods. In Section 1.3 we present the data. In Section 2.2 we describe the RC method and the resulting reddening maps of the MCs. We use the method of measuring the RC, introduced by Wozniak & Stanek (1996), in small subfields of the MCs to determine new reddening estimates for both Clouds. As mentioned earlier, in OGLE II the reddening was derived using the RC method (S05 and Udalski et al. (1999a)), while OGLE III leaves this task to the user. Since S09 sample the OGLE III area with a grid of constant subfield size and then apply the RC method in each subfield, some fields are not sufficiently populated to yield a reddening value. The individual reddening values of S09 are not available in tabular form. Using an adjusting field size we are able to circumvent the undersampling problem.

In Section 2.3 we present the method and results for the RR Lyrae reddening. We calculate the absolute magnitudes of the RR Lyrae taking their metallicity into account, which we obtain from Fourier decomposition of their light curves.

The discussion of the reliability of our reddening determinations and the comparison to other reddening maps are presented in Section 2.4. Section 2.5 summarises all results.

2.2 Reddening based on the red clump

2.2.1 Method

Our goal is to infer a reddening map for both Clouds using the mean position of the RC in a CMD.

For this purpose we define a selection box in colour-magnitude space. All stars between $17.50 \leq \mathrm{I} \leq 19.25$ mag and $0.65 \leq (\mathrm{V}-\mathrm{I}) \leq 1.35$ mag are taken into account for the determination of the mean

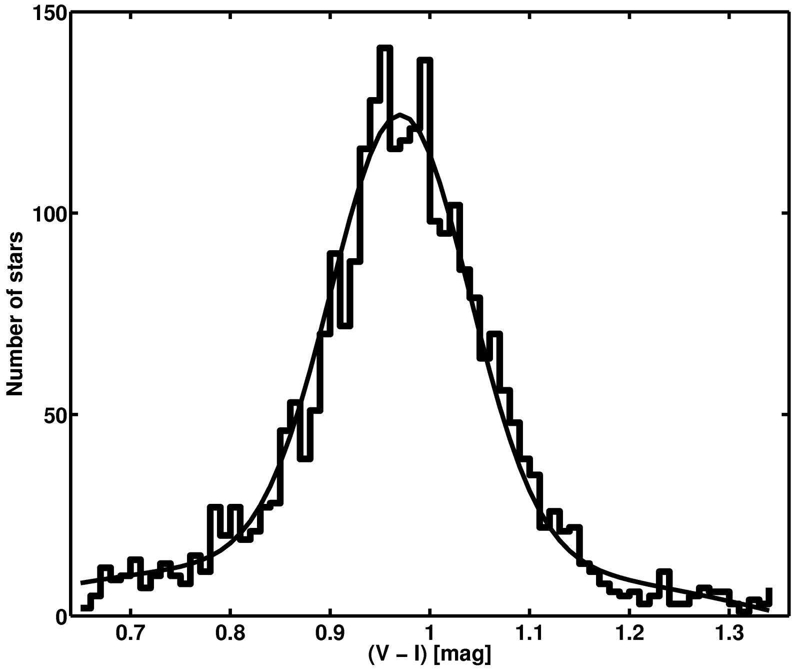

Figure 2.2: Histogram distribution of the RC stars in one of the examined fields, which is centred on RA = 81°32′ and DEC = −69°33′., The solid line represents the fit to the distribution and the χ^2 of the fit in this field is 1.06. We find a mean colour of (V − I) = 0.97 mag for the 2661 stars.

locus of the RC in the LMC fields (see Figure 2.1). These boundaries correspond to the selection box used by S05 (S09 adopts the methods and specifications of S05). For the SMC the limits in colour are chosen as in the LMC, but due to the greater distance, the box is shifted by 0.3 mag towards fainter I-band magnitudes.

To find an adequate number of stars the size of each field has to be carefully chosen. With a low number of stars the uncertainty in determining the mean colour would increase, while too large a number of stars prevents a map with details on smaller scales. We want to define a grid that allows us to obtain reddening information on scales as small as possible across the OGLE III field. Due to the density differences between the central parts and the outskirts of the Clouds we have to adjust the subfield sizes in dependence of the absolute number of stars in a given area. Our angular resolution is therefore variable and only driven by the available number of stars as listed in Table 2.1.

The individual fields of the SMC and LMC defined by the OGLE collaboration are large and contain many more stars than needed to find a significant RC in the colour-magnitude diagram. Therefore our first step for both galaxies is to divide each OGLE field in three, nearly quadratic, subfields. Due to the very different numbers of stars in these subfields we make further subdivisions dependent on the stellar density. If the total number of stars in the selection box in a subfield exceeds a certain threshold, this field is divided further, taking care that the number of RC stars per field does not drop below a few hundred stars. If a quadratic subfield of 36′ × 36′ contains for example more than 40,000 RC stars this field is cut into 64 equally sized fields with an average size of 4.5′ × 4.5′. For different stellar densities Table 2.1 lists the number of stars of the quadratic subfield in the first column, while the number of equally sized subfields and the dimensions of the finally evaluated fields are given in the second and third column, respectively.

In total we divide the LMC into 3174 subfields, while the SMC reddening is examined in 693 subfields. The number of RC stars in each examined subfield varies in the LMC from 260 to 4046, with an average number of 1257 RC stars in each field. For the SMC the least populated field has 477 RC stars,

Table 2.1: Sizes of the finally examined subfields in dependence of the number of stars in the evaluated OGLE III field.

# of Stars	# of subfields	size [arcmin]
> 40,000	64	4.5 × 4.5
> 12,000	16	9 × 9
≧ 3,000	4	18 × 18
< 3,000	1	36 × 36

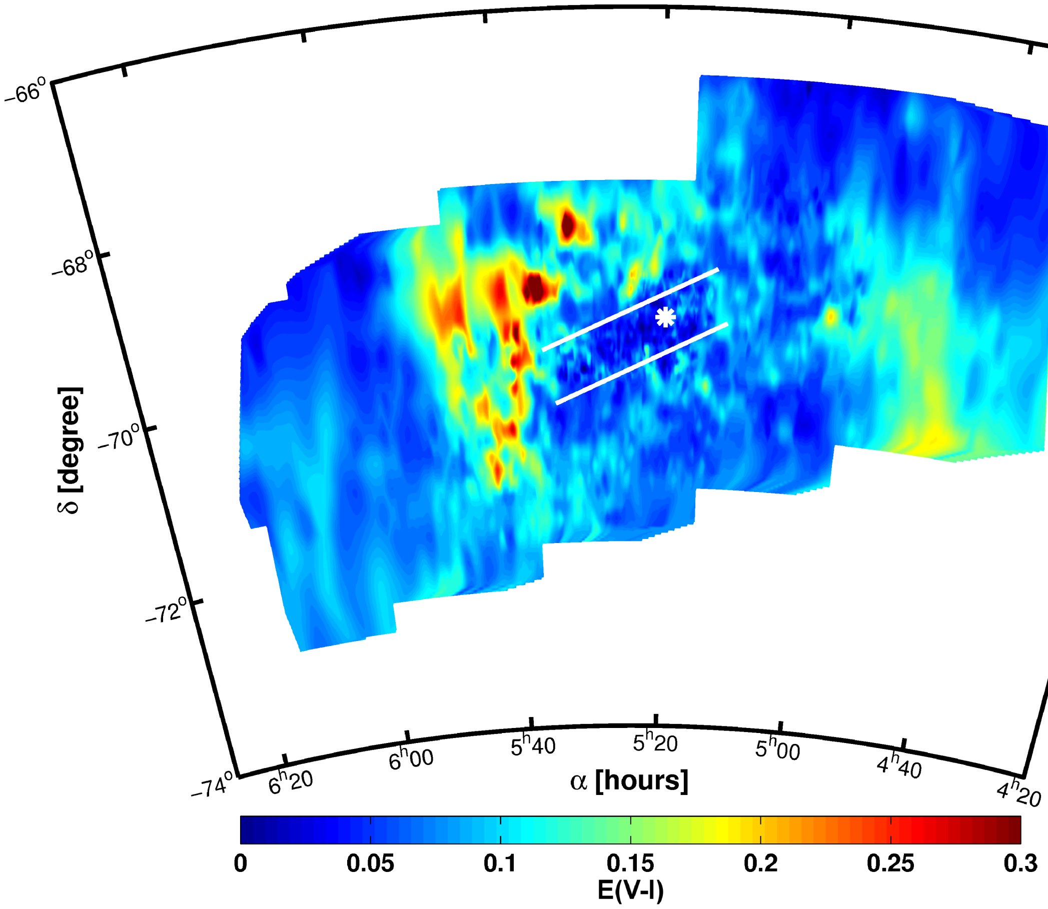

Figure 2.3: LMC reddening distribution. This contour map shows high reddening values in red and low reddening in blue. In the bar region of the LMC, marked with two diagonal white lines, the reddening is very low. Only along the leading edge of the LMC we find comparatively high reddening with values up to $E(V-I) = 0.43$ mag. The white star represents the optical centre of the LMC ($\mathrm{RA} = 5^{\mathrm{h}}19^{\mathrm{m}}38^{\mathrm{s}}$ and $\mathrm{DEC} = -69^{\circ}27'5''.2$) found by de Vaucouleurs & Freeman (1972). Reddening values in 30 Doradus and the leading edge are only lower limits due to high differential reddening

.

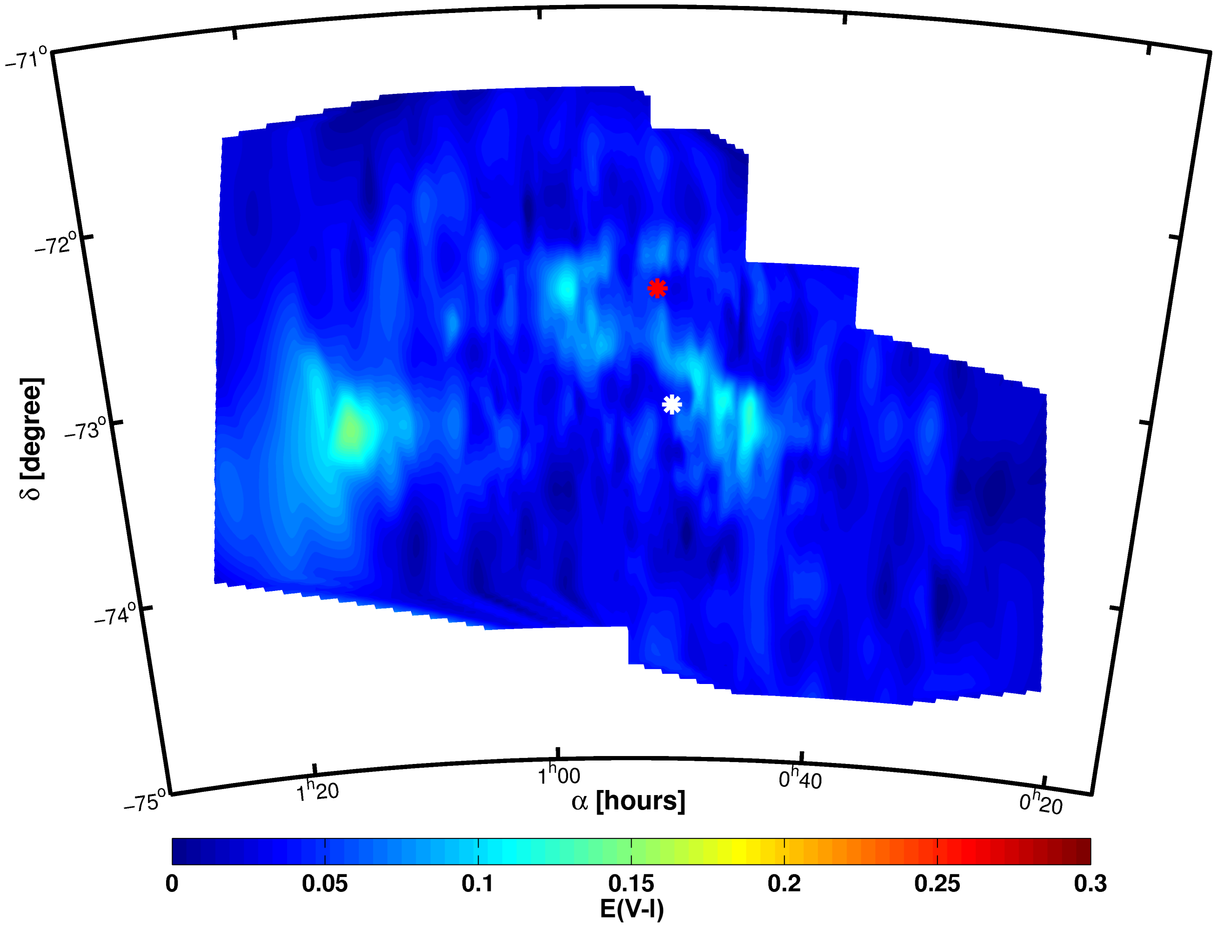

Figure 2.4: SMC reddening distribution. As before in Figure 2.3 low reddening is coded in blue and high reddening in red. The overall reddening is quite low with values around $E(V-I)_{mean} = 0.04$ mag. The highest reddening is found along the bar and the wing (RA = $1^{h}15^{m}$ and DEC = $-73°10'$) of the SMC. The red star represents the kinematical centre found by Piatek et al. (2008), while the white star shows the centre found from K- and M-dwarfs by Gonidakis et al. (2009, from now on G09).

while the population reaches its maximum at 3635. On average 1318 RC stars are located in each field.

In theory all RC stars have a well-defined mean colour $(V-I)_0$. This colour only depends on the mean metallicity and the age of the population. Girardi & Salaris (2001) examined theoretical RC colours in dependence of metallicity and computed mean values for $(V-I)_0$. For the LMC we adopt $(V-I)_0 = 0.92$ mag ($z = 0.004$) from the work by Olsen & Salyk (2002), who inspected RC stars to test for a warp in the LMC. For the SMC, due to the lower metallicity ($z \sim 0.0025$; Cole 1998; Glatt et al. 2008a), $(V-I)_0 = 0.89$ mag is used. In Udalski et al. (1998) a similar value for the unreddened RC of the SMC was used.

Due to reddening effects by interstellar dust and gas the mean colour of the clump is shifted redwards, which we denote as $(V-I)_{obs}$. By calculating the difference between the theoretical value and the observed colour of the field the reddening can be obtained with $E(V-I) = (V-I)_{obs} - (V-I)_0$.

To find the mean colour of the RC the histogram of the RC colour distribution (Figure 2.2) is fitted with a Gaussian plus a second order polynomial. The maximum of this function is assumed to be the mean colour of the clump. Different effects contribute to a broadening of the peak, such as the intrinsic scatter around the mean locus, photometric errors, the range of ages, differential reddening, the presence

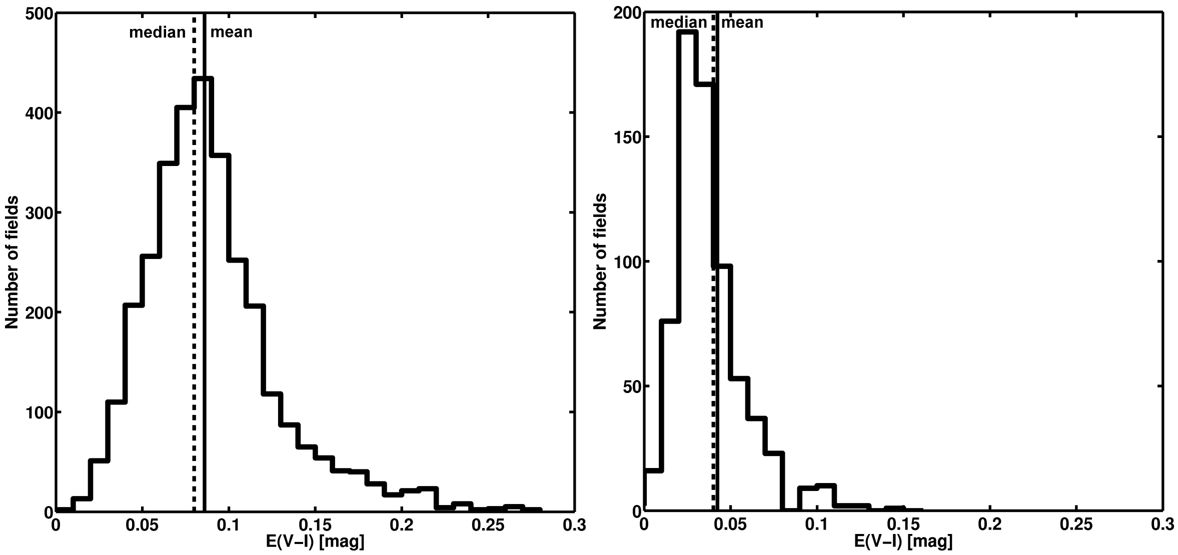

Figure 2.5: The distribution of reddening E(V − I) based on RC stars for the LMC (top) and SMC (bottom) is shown. The median and the mean reddening are very similar. We find that the mean reddening values match the peak of the reddening distributions very well.

of binaries or differences in metallicity as well as contributions of red giants and red horizontal branch stars.

The mean reduced χ^2_{mean} of the fits is 1.03 for the LMC, indicating that a Gaussian provides a good approximation to the data. Fields with a reduced $\chi^2 \geq 3$ were removed from the sample and then inspected by eye to check whether the mean location of the RC was correctly identified. Only 4 of the 3174 subfields in the LMC needed further inspection. For the SMC 34 out of 693 fields had a reduced $\chi^2 \geq 3$, while the χ^2_{mean} is 1.52. The deviant LMC and SMC subfields are mostly affected by a strong RGB, which leads to a second bump in the histogram. The small displacements of the mean colour are taken into consideration in the calculation of the uncertainties and hence no fields were rejected.

2.2.2 Results for the LMC

The unreddened value $(\mathrm{V}-\mathrm{I})_0$ was subtracted from the estimated mean RC colours of each of the 3174 subfields in the LMC. The difference corresponds to the mean reddening value E(V − I). These reddening values are plotted in spatially resolved contour maps (Figures 2.3 and 2.4).

In the LMC we find a mean reddening of $\mathrm{E(V-I)} = 0.09$ mag and a median value of $\mathrm{E(V-I)} = 0.08$ mag (see Figure 2.5). In the central regions, which correspond to the bar, the reddening is quite low. Towards the leading edge of the LMC the reddening increases and reaches its highest values with $\mathrm{E(V-I)} = 0.43$ mag close to the centre of 30 Doradus. Its centre is located at RA = $5^{\mathrm{h}}38^{\mathrm{m}}$ and DEC = $-69^\circ 06'$ (Høg et al. 2000). In the southwestern part of the observed field (RA $\sim 4^{\mathrm{h}}45^{\mathrm{m}}$ and DEC $\sim -70^\circ 20'$) there is a second area with higher reddening visible. There is only one field with a negative reddening in the dataset. But within the uncertainties this value is consistent with zero.

The uncertainty of the reddening values is determined by calculating the σ of the gaussian distribution of the stars within the selection box. This represents the broadening of the RC due to metallicity effects, binaries and differential reddening. For the LMC the mean 1σ error is 0.07 mag. The photometric errors of the observed magnitude of the stars are low due to the large number of repeat observations in the OGLE III survey. This leads to a very precise photometry with an average uncertainty of $\sigma = 0.08$ mag for each star. Each field contains a large number of stars, therefore this error can be neglected.

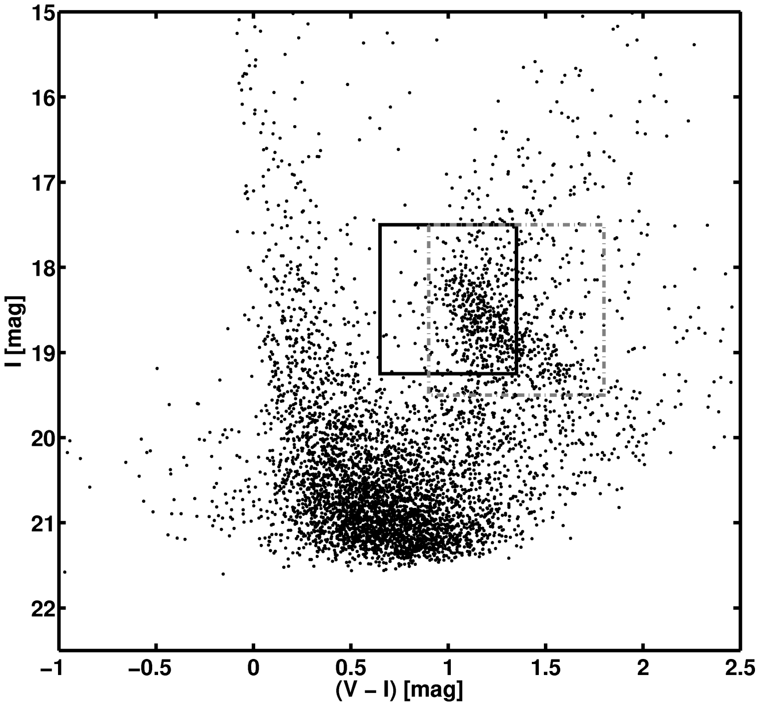

Figure 2.6: CMD of the LMC subfield with the highest reddening. This field is located in 30 Doradus at RA = 5^h35^m and DEC = $-69°10'$ with a projected size of $9' \times 9'$. The CMD contains 4386 stars, while 275 stars are in our original selection box, represented by the continuous line. The dashed grey line shows the boundaries of the new box for the RC.

Since the central regions contain many more stars than the outskirts of the LMC, the subfields for the determination of the reddening are much smaller than in the outer regions. Therefore, a lot more substructure can be seen here in the reddening map in Figure 2.3.

Regions with high reddening

A minor fraction of 2% of the LMC fields show considerable reddening with values of $E(V - I) > 0.2$ mag. These 60 fields are inspected by eye and only 23 fields with reddening values of $E(V - I) \geq 0.25$ mag suffer from a very extended RC, which is caused by differential reddening (Figure 2.6). The reddening results in these regions are reanalysed by shifting the RC box to $0.9 \leq V - I \leq 1.8$ mag and $17.5 \leq I \leq 19.5$ mag and refitting the distribution of stars as described above. The results are shown in Table 2.2. While the peak of the reddening distribution of the field is only marginally shifted, we find a considerable amount of differential reddening for most of the fields. This differential reddening does not follow a Gaussian distribution, but instead typically shows a rapid rise from low reddening to the peak of the distribution, whereas there is a much more shallow and much wider tail towards higher reddening. To determine an estimate for the width of the distribution we calculate the mean of each distribution. To each side of the mean of the RC we include 34.1% of all stars and determine the colour of the star just outside this border (vertical lines in Figure 2.7). This corresponds to a width of 1σ.

Differential Reddening

For every subfield the mean reddening of all RC stars is measured. Therefore we do not take into account that the dust content may not be evenly distributed within a given subfield. By including 34.1% of all

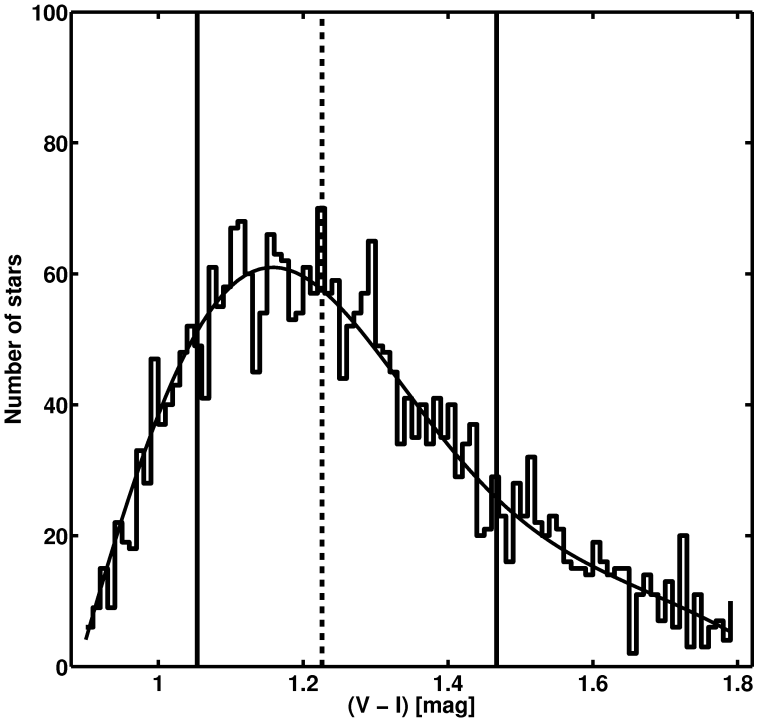

Figure 2.7: Distribution of reddening for a highly reddened field in the LMC. The two vertical lines show the width that includes 68.2% of all stars closest to the mean reddening (dashed line) and is considered as the 1σ width of the distribution here.

stars on both sides from the maximum, we define the 1σ width of the distribution, which we use as a measure of the amount of differential reddening.

Figure 2.8 shows the distribution of differential reddening in the LMC. The regions with high reddening from Figure 2.3 are prominent in the differential reddening map as well. Another region with a considerable spread of the distribution is the bar. Interestingly, the region of increased reddening in the southwestern part of the LMC does not show up as having higher differential reddening.

2.2.3 Results for the SMC

On average the SMC is less reddened than the LMC. For the 693 fields evaluated in the SMC we find the mean and median value to be E(V − I) = 0.04 mag (see Figure 2.4 and 2.5). Three main concentrations of higher reddening are revealed in Figure 2.4. Two of the concentrations are found at RA = 0^h45^m and DEC = −73°10′ and at RA = 0^h58^m and DEC = −72°30′, which coincides with the southwest part and the northern part of the bar, respectively. The overall density of stars is enhanced in these regions. The third area with high reddening is the well known wing of the SMC (RA = 1^h15^m and DEC = −73°10′). In this region the reddening reaches its maximum with a value of 0.16 mag. In all regions with high reddening multiple H II regions are located (Livanou et al. 2007). The lowest calculated reddening is 0.00 mag. The uncertainty is calculated in the same manner as for the LMC. The same error sources are present and the photometry is as good as for the LMC. We find a mean 1σ uncertainty of 0.06 mag.

We measure the differential reddening of the SMC in the same manner as for the LMC. For most fields the differential reddening is quite low and only the bar and the wing show considerable differential reddening.

Data access

We are making the coordinates of the subfields and the derived RC reddening values for both LMC and SMC available via the German Astrophysical Virtual Observatory (GAVO) (`http://dc.zah.uni-heidelberg.de/mcx`). Using the transformation relations published by SFD98 the webpage has the capability to calculate extinctions for 19 different filters in four photometric systems.

Table 2.2: The fields with reddening values of $E(V-I) \geq 0.25$. These fields are reanalysed using a wider RC box and the 1-sigma intervals are calculated.

α	δ	fieldsize	$E(V-I)_{\text{old}}$	$E(V-I)_{\text{new}}$
82.717	-68.428	9×9	0.26	$0.26^{-0.10}_{+0.14}$
82.856	-68.428	9×9	0.35	$0.35^{-0.17}_{+0.19}$
82.995	-68.428	9×9	0.43	$0.52^{-0.40}_{+0.14}$
83.659	-69.174	9×9	0.26	$0.25^{-0.11}_{+0.18}$
83.802	-69.174	9×9	0.31	$0.41^{-0.22}_{+0.24}$
83.802	-69.020	9×9	0.25	$0.26^{-0.10}_{+0.31}$
83.839	-69.172	9×9	0.38	$0.53^{-0.33}_{+0.15}$
83.839	-69.018	9×9	0.34	$0.34^{-0.15}_{+0.27}$
83.982	-69.172	9×9	0.38	$0.43^{-0.21}_{+0.20}$
83.982	-69.018	9×9	0.33	$0.37^{-0.17}_{+0.25}$
84.125	-69.172	9×9	0.28	$0.30^{-0.14}_{+0.16}$
84.125	-69.018	9×9	0.34	$0.38^{-0.17}_{+0.18}$
84.268	-69.172	9×9	0.32	$0.39^{-0.20}_{+0.25}$
84.268	-69.018	9×9	0.26	$0.27^{-0.12}_{+0.23}$
85.055	-69.095	18×18	0.27	$0.27^{-0.13}_{+0.30}$
84.687	-69.918	9×9	0.27	$0.26^{-0.13}_{+0.25}$
84.687	-69.611	9×9	0.32	$0.32^{-0.16}_{+0.21}$
84.834	-69.918	9×9	0.28	$0.28^{-0.13}_{+0.30}$
84.981	-69.611	9×9	0.26	$0.27^{-0.13}_{+0.31}$
84.824	-70.201	9×9	0.26	$0.31^{-0.17}_{+0.31}$
84.975	-70.661	9×9	0.28	$0.27^{-0.13}_{+0.19}$
85.605	-71.099	9×9	0.25	$0.25^{-0.10}_{+0.14}$
86.397	-69.401	18×18	0.25	$0.24^{-0.11}_{+0.31}$

Use of the RC reddening data

The reddening maps from the RC stars cover the complete area of the OGLE III survey. They average the reddening within distinct subfields. For all stars in such a field this value can be used as a reliable indication for the average reddening that these stars are experiencing.

Since RC stars are quite red and cool they may not be the first choice for the dereddening of very young and hot stars (see Grebel & Roberts (1995) who discuss the dependence of heterochromatic extinction on stellar parameters such as temperature and Z02, who discuss variations in reddening maps in dependence of stellar population age). Furthermore the reddening in regions with high dust and gas densities, such as star forming regions, might differ significantly with depth. Our method is not able to account for differential reddening along the line of sight, but averages along the sight line, similar as the SFD98 maps do for our MW.

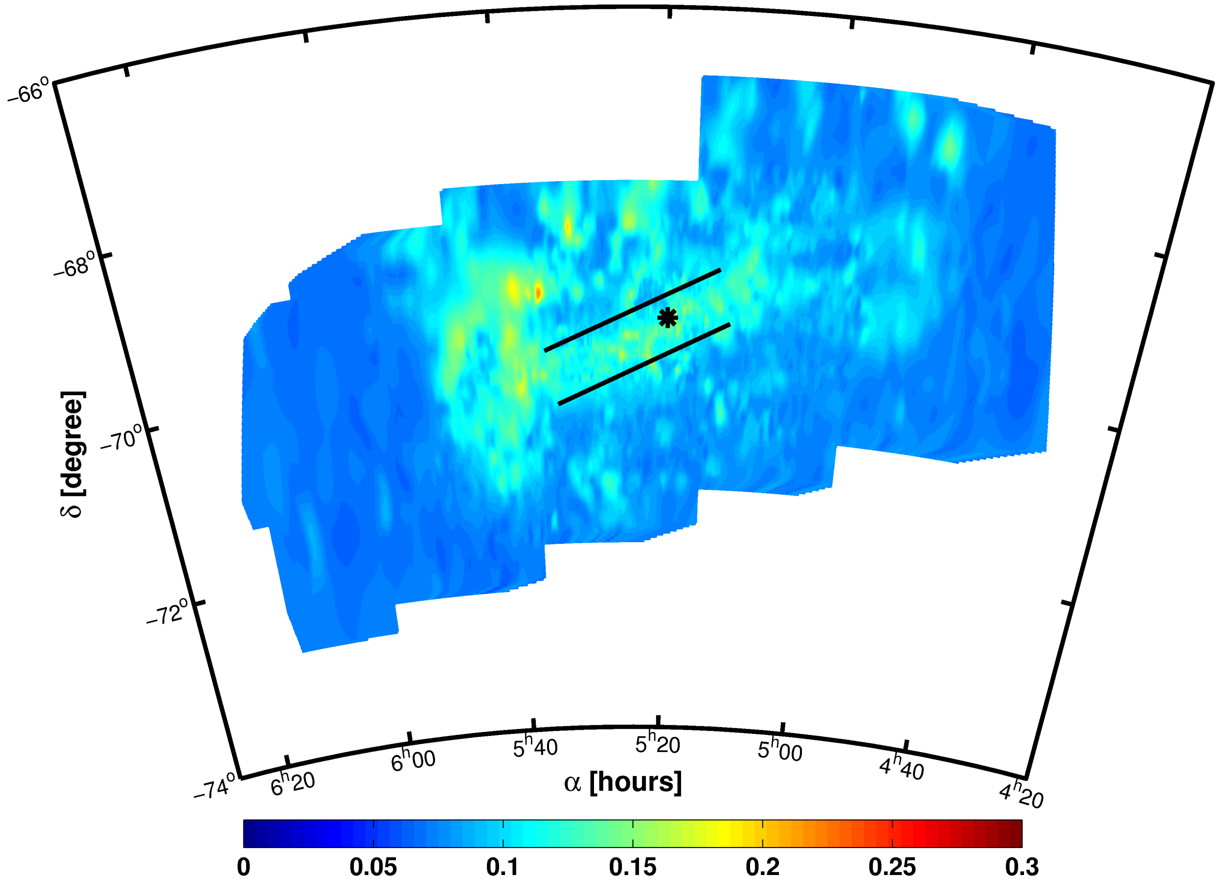

Figure 2.8: Distribution of differential reddening for the LMC. The differential reddening is high in regions with high reddening, as 30 Doradus, and in densely populated regions, as the bar.

Our RC reddening maps are thus useful for applications in which the bulk properties of stellar populations in the MCs are studied. They are also useful for applications where objects are studied whose properties make the derivation of individual reddening difficult (e.g. individual RC stars or individual RGB stars). In studies of individual stellar objects (instead of entire stellar populations), users of the reddening maps should be aware of the afore mentioned caveats of using average (as opposed to individual) reddening values.

2.3 Reddening based on RR Lyrae ab stars

2.3.1 Method

RR Lyrae stars provide an independent means of deriving reddening values. For the MCs the OGLE collaboration presents lightcurves and photometry of RR Lyrae covering most of the main bodies of these galaxies (Soszyński et al. 2009, 2010a). PS09 used these data to infer a reddening map of the LMC. They assumed one single metallicity for all RR Lyrae stars in the LMC, −1.39 dex (Cohen & Meléndez 2005), which results in a theoretical intrinsic colour of $(V - I) = 0.48$, with a mean period of 0.57 days for all RR Lyrae in the LMC. However, the spectroscopic studies of RR Lyrae stars in the LMC by Borissova et al. (e.g. 2009) show that a range of metallicities is present. Moreover, Guldenschuh et al. (2005) showed in their work that the metallicity of the RR Lyrae is negligible only if the colour is measured during minimum light. The OGLE collaboration on the other hand has released mean magnitudes. Hence

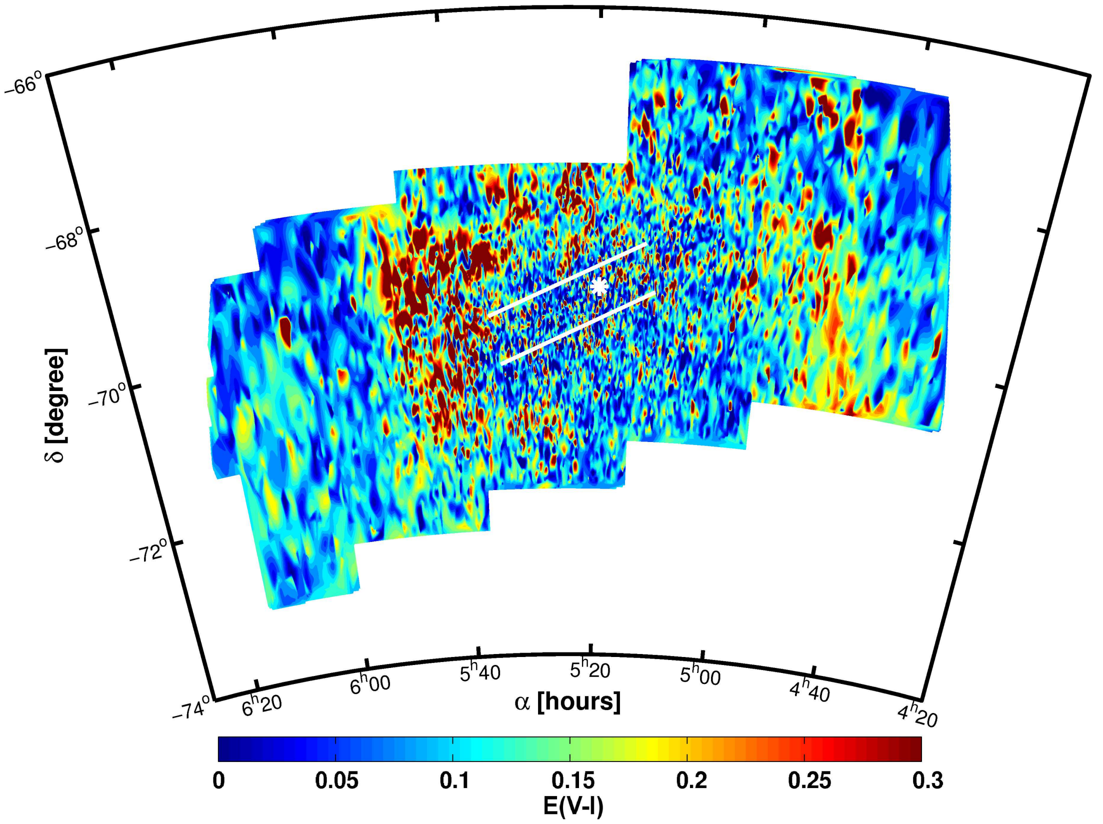

Figure 2.9: A reddening map for the LMC based on individual RR Lyrae stars, taking their metallicity into account. The map reveals large differences between stars that are in projection very close to each other on the sky. These small-scale variations appear to be due to differences in the line-of-sight extinction.

we decided to extend the work of PS09 by calculating the theoretical value of the colour taking the metallicity of each single star into account.

Using the photometric method established by Kovács & Zsoldos (1995); Jurcsik & Kovács (1996); Kovács & Jurcsik (1996) we use the Fourier coefficient ϕ_{31} and the period to calculate the metallicity [Fe/H] of each RR Lyrae star of type ab. This metallicity is independent of reddening. As shown in the studies quoted above, the V-band light curve of the RR Lyrae stars can be decomposed with a Fourier series. The phase parameters can be used to calculate the property $\phi_{31} = \phi_3 - 3\phi_1$. It was shown in the studies cited above that the metallicity can be determined with the knowledge of ϕ_{31} and the period. Since the light curve properties are different in different photometric bands a separate calibration of ϕ_{31} and the period has to be carried out if the data are not taken in the V-band. This is relevant for the OGLE data, where the light curves are best sampled in the I-band. Smolec (2005) provides a relation valid when ϕ_{31} is computed from the I-band instead of V-band magnitudes. We use Smolec's relation to infer the metallicities of the RR Lyrae from OGLE's I-band ϕ_{31}. Then we use the metallicity dependent relations for the V- and I-band, found by Catelan et al. (2004) by theoretical modelling of lightcurves, to infer the absolute colour $(V-I)_0$ of each star. Further details on the results for the RR Lyrae ab metallicities are presented in a separate paper (Chapter 3).

The measurements of the RR Lyrae have the same photometric uncertainties as the RC stars: $\sigma = 0.08$ mag. For the observed colour this is the only source of uncertainty taken into account. In the I-band the absolute magnitude depends on the period and on the metallicity of the RR Lyrae star, while the

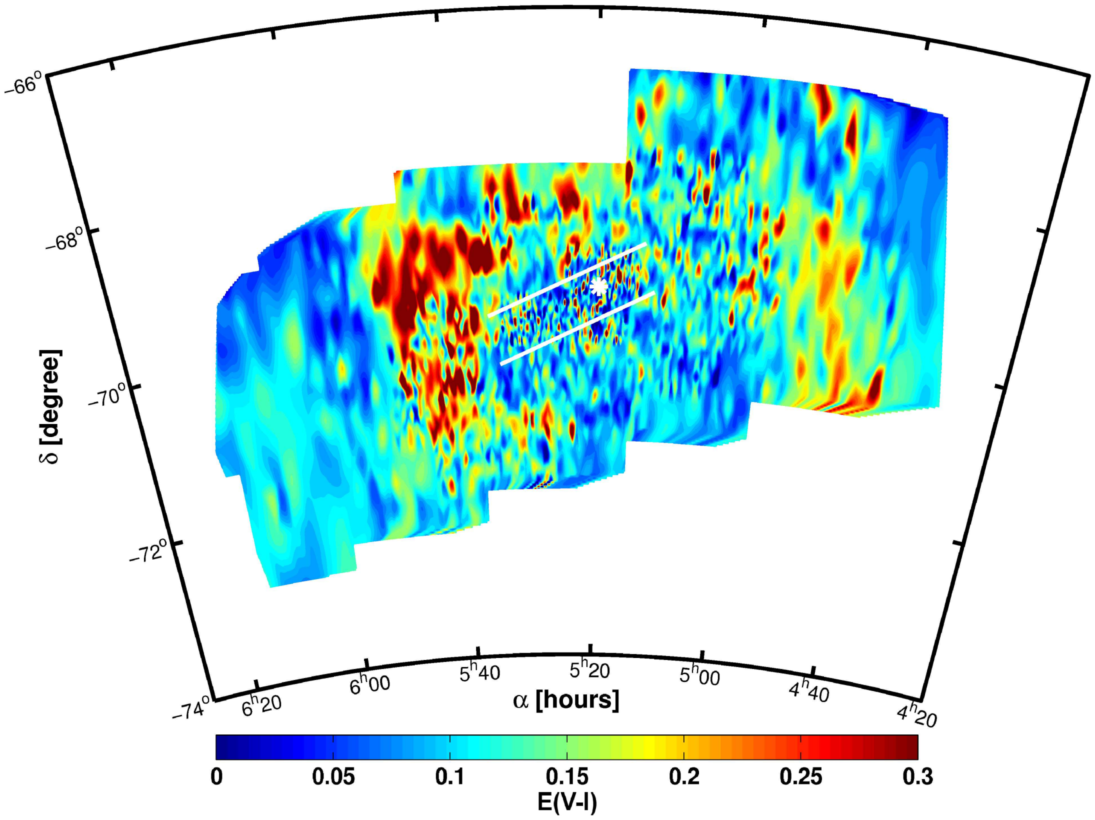

Figure 2.10: A reddening map of the LMC based on RR Lyrae averaged across the same fields as used for the RC method. A slightly higher mean reddening is visible than for the RC reddening, but overall the map shows a similar distribution of the reddening as in Figure 2.3, even though the methods are completely independent.

V-band magnitude only depends on metallicity. For the metallicity derived via Fourier decomposition Smolec (2005) states an uncertainty of $\sigma = 0.18$ dex, while the uncertainty of the periods, measured by the OGLE collaboration, is negligible. The uncertainty of the reddening is therefore determined to be $\sigma = 0.06$ mag. Many relations for calculating the absolute magnitudes of RR Lyrae stars have been published (see Sandage & Tammann 2006, for a review).

PS09 found that imposing certain colour and magnitude constraints ensures a reliable selection of RR Lyrae stars of type ab that are likely members of the LMC. We adopt similar constraints: periods between 0.45 days $< P <$ 0.80 days, amplitudes between 0.30 mag $< \Delta I <$ 0.85 mag, observed magnitudes of $V >$ 18 mag, observed colours between $(V - I) >$ 0.40 mag and metallicities between $-2.0 < [Fe/H] < 0.0$. The 17693 RR Lyrae ab found in the LMC are reduced to 13490 stars. In the SMC the number of stars is reduced from 1864 to 1529 RR Lyrae ab.

2.3.2 Results for the LMC

For each of the 13490 remaining LMC RR Lyrae a reddening value is calculated. The resulting values are plotted in Figure 2.9. To reduce the fluctuations due to the varying reddening values of the individual RR Lyrae stars we obtain a new reddening map of the LMC by averaging over the individual RR Lyrae reddening values in the same subfields chosen for the RC reddening. The mean reddening of all RR Lyrae stars located in each field is adopted in the reddening map shown in Figure 2.10. 120 fields are returned with no star allocation since the RR Lyrae are much more sparsely distributed than the RC stars. For each of these empty fields the mean reddening of the neighbouring fields is assigned as reddening.

The reddening map of the LMC obtained from RR Lyrae stars reveals a lot of structure. The highest reddening values are obtained in the leading edge, containing the spur and 30 Doradus. The highest value of a single RR Lyrae star is $E(V-I) = 1.42$ mag, while seven stars have a reddening of $E(V-I) > 1.0$ mag. The highest averaged field reddening value is $E(V-I) = 0.66$ mag. Another region with high RR Lyrae reddening values is found in the southwestern part of the OGLE III field ($RA = 4^h45^m$ and $DEC = -70°20'$). In the bar region the reddening is quite low and overall we find a mean reddening of 0.13 mag for the individual stars and the fields. The median reddening is slightly lower, namely $E(V-I) = 0.11$ mag. We find a standard deviation of 0.06 mag, a value of the same order of magnitude as the error for the RC method. While Figure 2.10 contains only a few spots of high reddening fluctuations between neighbouring areas, these are much more striking in Figure 2.9, which is to be expected since we are considering individual stars here. These fluctuations may be indicative of differential reddening along the line of sight.

Overall we find 635 stars (which corresponds to 5% of the whole sample) with a negative reddening down to $E(V-I) = -0.20$ mag. These lead to 33 fields (1% of all fields) with negative values. The field with the lowest mean RR Lyrae reddening $E(V-I)$ has -0.11 mag. The mean for the individual stars as well as for the fields with these negative values is $E(V-I) = -0.03$ mag. We inspect the lightcurve of every star with negative reddening. As one would expect, the shape of the light curves differs from star to star, but is well within the expected variations. The mean period of the RR Lyrae with negative reddening is higher by 10% than that of the bulk of the RR Lyrae stars. With a mean of $[Fe/H]_{E(V-I)<0} = -1.40$ the metallicity of these stars is lower than the overall mean of $[Fe/H]_{mean} = -1.23$. But there is no clear trend in the sense that most low metallicity stars or most high period stars have too low a reddening. The details of the MDF will be discussed in Chapter 3. The origin of the negative reddening remains unclear. If we set all negative values to zero, the resulting mean reddening of the LMC increases by just 1.5%.

2.3.3 Results for the SMC

Using the same procedure, we calculate reddening values for the SMC 1529 RR Lyrae ab stars. The resulting reddening is shown in Figure 2.11.

Even though much more substructure is visible in Figure 2.11 than in Figure 2.4 the overall patterns are similar. The bar and the wing have the highest reddening values. The differences on small scales are, as for the LMC, interpreted as differential reddening. The highest reddening value in the SMC with $E(V-I) = 0.36$ mag is located in the southwestern bar region. Overall we find that the mean reddening has a value of $E(V-I) = 0.07$ mag, with a standard deviation of 0.06 mag.

Negative reddening is found for 114 stars or 7% of the sample. The lowest reddening for an individual star is $E(V-I) = -0.15$ mag, while the mean of all stars with negative reddening is $E(V-I) = -0.03$ mag. If all negative reddening values are set to 0 the mean reddening increases by 3.5%. The mean metallicity of the stars with negative reddening is lower than for the whole sample of stars, i.e. we see the same trend as in the LMC. While the entire sample has a mean metallicity of $[Fe/H]_{mean} = -1.41$, for the negative reddening stars a metallicity of $[Fe/H]_{E(V-I)<0} = -1.63$ is obtained. The details of the metallicity distribution will be discussed in a separate paper. The period of the RR Lyrae stars with negative reddening is increased by 5% compared to the mean of all stars. Nevertheless, a clear trend that most of the metal-poor stars have a lower reddening is not apparent.

The intrinsic uncertainties of the parameters used for the reddening estimates are the same in the SMC as in the LMC. The uncertainty of the SMC RR Lyrae reddening is calculated to be $\sigma = 0.06$ mag. This is comparable with the uncertainty of the RC method.

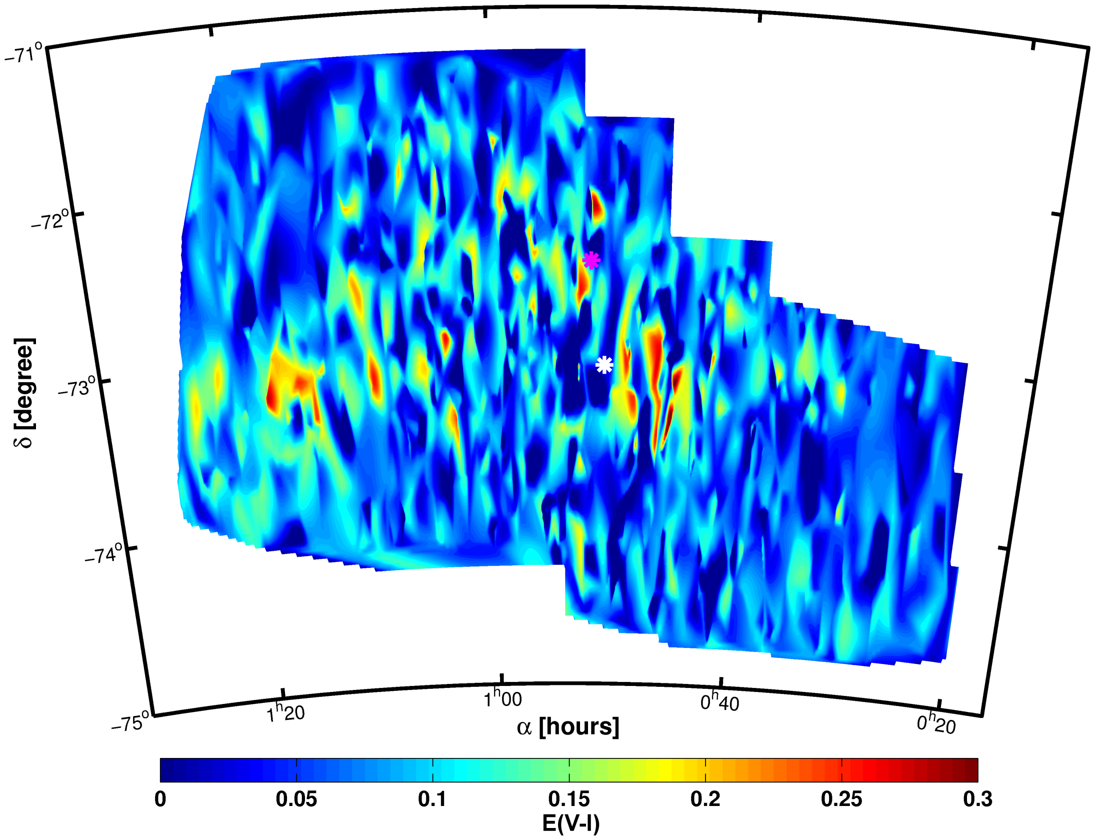

Figure 2.11: A reddening map for the SMC based on reddening estimates for individual RR Lyrae stars. Due to differential reddening effects the map shows a much patchier behaviour than Figure 2.4.

Use of the RR Lyrae reddening data

Using the RR Lyrae stars of the MCs we determine reddening values for lines of sight to individual stars. These values are strictly only valid for these particular RR Lyrae stars. We are not able to constrain the stars' distance independently of the reddening measurement. Therefore we are not able to distinguish between objects located at varying depth that might be affected by different amounts of differential reddening.

The RR Lyrae reddening maps are not necessarily useful for the reddening correction of other types of stars close by in projection. Therefore we do not provide the reddening values via the virtual observatory. Nonetheless, these data provide a detailed account of the reddening experienced by the old population of the MCs and are interesting to compare to reddening maps presented in Z02 and Z04 as well as to our RC reddening maps. We can obtain insights into the differential reddening which is of interest for a broad variety of subjects such as, e.g., gravitational lensing. Moreover these data are useful for comparison with the structural and geometrical properties of the MCs.

2.4 Discussion

2.4.1 The zeropoint of the RC colour

The crucial point in our RC reddening determinations are the unreddened theoretical colours, which depend on the metallicity and the age of the stellar population (see Section 2.4.2). In S05 and in our work the value for the RC colour was adopted from the work of Girardi & Salaris (2001). Both studies assume a metallicity of $z = 0.004$, which corresponds to a RC colour between 0.90 mag and 0.95 mag for stars with an age of $2 - 12$ Gyr. Other works, such as Cole et al. (2005) with spectroscopic measurements of red giants, find similar metallicities as assumed in these studies. Based on the photometric measurements of RC stars by Olsen & Salyk (2002) we adopt the value $(\mathrm{V}-\mathrm{I})_0 = 0.92$.

The reddening values obtained by Udalski et al. (1999a,b) with the RC method are much higher ($\mathrm{E(V-I)}_{\mathrm{mean}} = 0.20$ mag) than the reddening in S05 and in this study. S05 suggest that this discrepancy may be resolved by adopting a much lower metallicity of $z = 0.001$ for the LMC RC population, which would result in a bluer colour for the RC. Since neither the concrete method, nor the adopted metallicity is mentioned in Udalski et al. (1999b) we can only speculate about the cause(s) of the differences.

The overall metallicity of the SMC is lower than that of the LMC. Matteucci et al. (2002) showed that the RC in the SMC is shifted to bluer colours as compared to the LMC. Girardi & Salaris (2001) provide a RC colour of $0.90 < (V-I)_0 < 0.95$ mag for $z = 0.004$, while their models lead to a colour between $(\mathrm{V}-\mathrm{I})_0 = 0.78$ mag and $(\mathrm{V}-\mathrm{I})_0 = 0.84$ mag for $z = 0.001$. We assume that the metallicity of the SMC RC lies a bit below the metallicity value of the LMC and choose a RC colour of $(\mathrm{V}-\mathrm{I})_0 = 0.89$ mag. The metallicities of the intermediate age populations show a considerable spread at any given age (Glatt et al. 2008a). The mean metallicities found by Cole (1998) and Glatt et al. (2008a) agree with our assumption of a metallicity z between 0.002 and 0.003.

2.4.2 Possible caveats of the methods used

For the RC method different effects lead to a broadening of the clump, such as metallicity and age spreads, binaries, and differential reddening.

A lower metallicity would lead to a bluer colour of the RC and therefore enhance the overall reddening of all fields. The existing measurements of the metallicity of RC stars make this effect unlikely. An age spread among RC stars is present in all fields, but the effect on the colour is quite small as long as the metallicity does not change dramatically.

For the RR Lyrae stars we have derived the metallicity of each star individually in a separate paper (Chapter 3). We take these different metallicities into account while calculating the absolute colours of each RR Lyrae star. The uncertainties of the metallicity are about 0.2 dex, which corresponds to a colour difference of $\Delta(\mathrm{V}-\mathrm{I})_0 = 0.001$ mag.

The RR Lyrae stars are up to a few Gyr older than the RC stars, hotter by about 2000K (Puzeras et al. 2010; Smith 2004), and bluer by about $(\mathrm{V}-\mathrm{I}) = 0.3$ mag. The absolute magnitude of RR Lyrae and RC stars are similar. As discussed in Section 2.4.3 these differences are not expected to have a significant effect on the reddening obtained for these stars. Assuming that the spatial distribution of RC and RR Lyrae stars is similar, differences are mainly expected due to differential reddening, which gets averaged out in the RC method, while fully affecting the individual RR Lyrae measurements.

2.4.3 Comparison of our two approaches

LMC

In order to compare the RR Lyrae reddening with the RC reddening, the same field selection as in Section 2.2 is used in the LMC to find average values of RR Lyrae reddening.

As shown by Grebel & Roberts (1995), reddening varies as a function of temperature (or colour). However, in the colour range of RC stars and RR Lyrae hardly any variations are to be expected (see, e.g., Fig.3 in the above reference). Hence, theoretically both the RC and the RR Lyrae approach should yield fairly similar results if the reddening suffered by both types of stars is comparable.

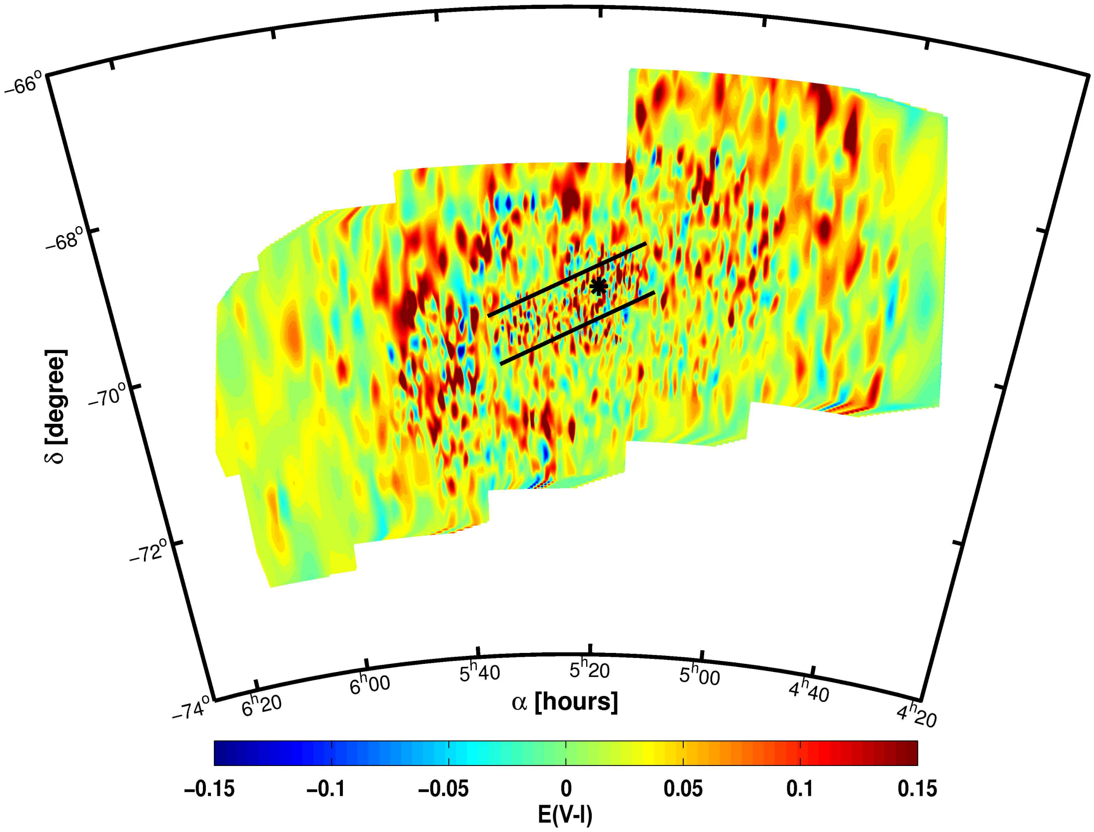

Figure 2.12: Difference map of the LMC. The RC reddening is subtracted from the RR Lyrae values: $E(V-I)_{RR} - E(V-I)_{RC}$. A small trend of higher reddening estimated from RR Lyrae stars is apparent. We find a mean difference of 0.03 mag, smaller than the mean error of both methods. Depending on the location the difference ranges from −0.19 mag to +0.52 mag.

For the LMC the overall agreement between the RC and the RR Lyrae map is striking, although the northwestern regions (RA $\sim 5^h00^m$ and DEC $\sim -68°00'$) have on average a higher reddening in the RR Lyrae map (Figure 2.12). In general we find a mean difference between the mean RC and the mean RR Lyrae reddening of $E(V-I) = +0.03$ mag when subtracting the RC map from the mean reddening map of the RR Lyrae. This is a difference of less than 1σ. We find a few regions with reddening values up to 0.52 mag higher in the RR Lyrae determination as compared to the RC map at the same location. Some fields have higher reddening values from the RC method than from the RR Lyrae estimates. The field with the highest difference is found with $E(V-I)_{RC} - E(V-I)_{RR} = 0.19$ mag. But in general only very few fields deviate strongly from each other. In only about 8% of the fields the variation exceeds a difference of more than 0.12 mag or 2σ. We attribute these differences primarily to differential reddening and small number statistics affecting the RR Lyrae values.

At the spatial position of 30 Doradus the reddening is highly dependent on the location of a given star with respect to the star-forming region. Westerlund (1997) and van der Marel (2006) mention that 30 Doradus seems to be located on the far side of the LMC as seen from us. If that were true the dust and gas of 30 Doradus would have an effect on only a minority of the much older RC stars. Therefore the (mean) reddening estimate of this region would be biased towards lower values and a long tail of higher reddening values would be measured (see Figure 2.7). For the RR Lyrae stars we compute a reddening value for every star. This results in a substantial differential reddening, due to the differing distances of these stars, and in a spread of the estimated reddening values in each subfield. Averaging these values for

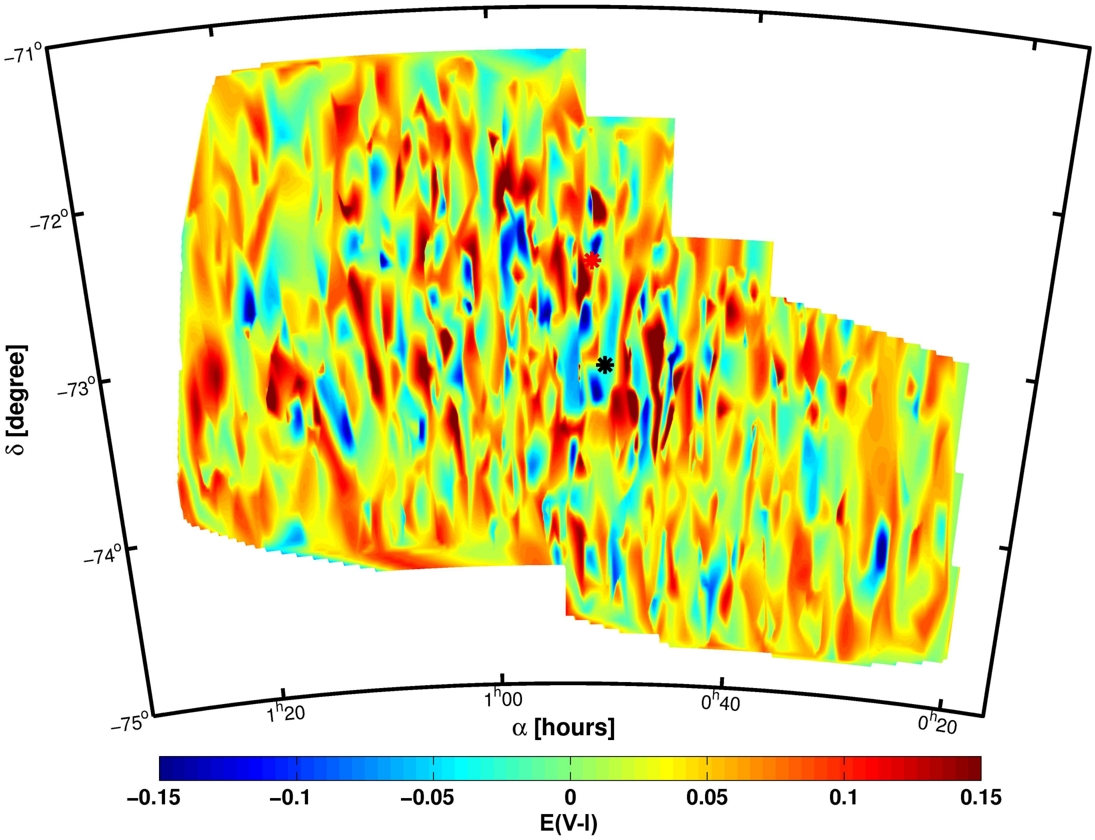

Figure 2.13: Same as Figure 2.12 for the SMC. The RR Lyrae map is much more patchy than the RC map. We conclude that this is a sampling effect owing to the small number of RR Lyrae. For regions with very low reddening the discrepancy between the two methods is basically zero.

a given subfield does not reduce the contribution of highly reddened stars behind 30 Doradus, as much as it might be the case for the RC method. We obtain higher average values for the same subfield by using the RR Lyrae stars than for the RC stars, which leads to the assumption of 30 Doradus being at the far side of the LMC.

The RR Lyrae stars are located at different distances throughout the LMC. In addition the dust content in the body of the LMC leads to differential reddening. In Figure 2.9 the effects of differential reddening are obvious. Fields very close to each other may have very different reddening values. For 958 stars, or 7%, of all RR Lyrae stars the reddening values of the individual stars differ by more than 0.18 mag or 3σ, from the corresponding mean value of the RC reddening. The effect of differential reddening therefore affects only a minor number of stars.

The adopted mean colour of the RC is crucial for the reddening computation. The very good overall agreement of RC and RR Lyrae maps in areas with very low reddening leads us to the conclusion that the theoretical colours are well chosen. For regions with $E(V-I)_{RR} < 0.1$ mag a mean difference of only 0.004 mag is found calculating $E(V-I)_{RR} - E(V-I)_{RC}$.

SMC

The SMC is populated much more sparsely in RR Lyrae stars, thus many fields defined earlier when using the RC method contain less than three RR Lyrae stars. Therefore we decided to compare the individual values of the RR Lyrae stars with the RC reddening (see Figure 2.13).

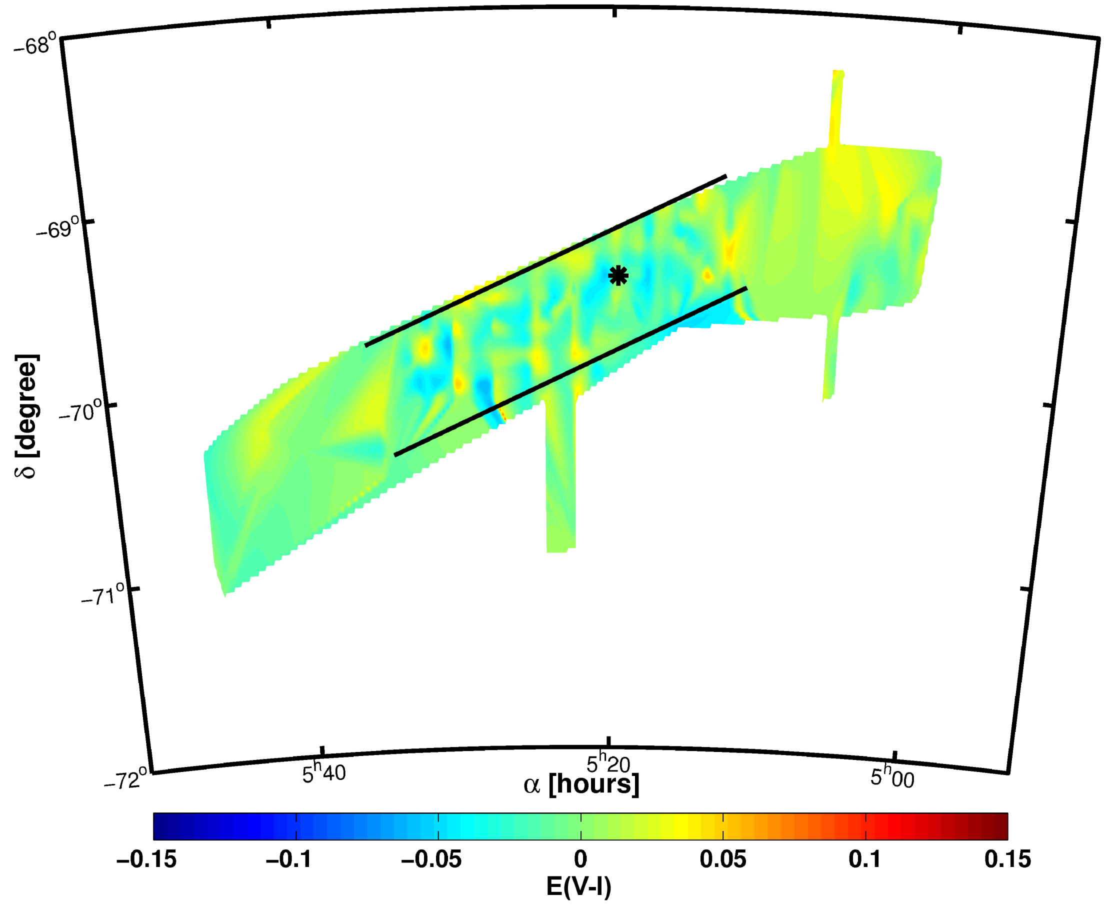

Figure 2.14: Difference map showing the reddening differences between S05 and the RC values in our study $(E(V-I)_{S05} - E(V-I)_{RC/HGD10}$. The region shown is the area covered by OGLE II in the LMC. Positive values show higher reddening inferred by S05. Negative values correspond to higher values in our dataset. Overall the differences are very small.

On average the RR Lyrae stars have a reddening that is higher by $E(V-I) = +0.03$ than the corresponding RC field. The differences between the two approaches vary between −0.19 mag and +0.28 mag. 348 stars (23%) have lower reddening with the RR Lyrae method than the corresponding RC reddening value. Only 48 stars, or 3%, of the RR Lyrae deviate by more than 2σ from the mean reddening of the field obtained by the RC method.

Even though the mean differences are small Figure 2.13 reveals that the RR Lyrae reddening map is much more patchy than the very smooth RC map. While we inspect and average over fields of a certain size with the RC method, the RR Lyrae measure just the line of sight reddening of individual objects. We find only 13 stars, which is less than 1% of the sample, where the reddening value of the RR Lyrae deviates by more than 3σ, or 0.18 mag, from the average value of the corresponding RC field. Hence we conclude that the poor sampling of the field is the major contribution for this patchy behaviour of the RR Lyrae reddening map.

The mean colour of the RC method for the SMC was adopted from Udalski et al. (1998) and was compared with the model predictions by Girardi & Salaris (2001) for a metallicity of $z = 0.0025$. Investigating the stars with $E(V-I)_{RR} < 0.03$ mag we find a very small difference of 0.006 mag between the RR Lyrae reddening values and the RC method. Thus, within the uncertainties, the RC and RR Lyrae reddenings agree very well for regions with low reddening.

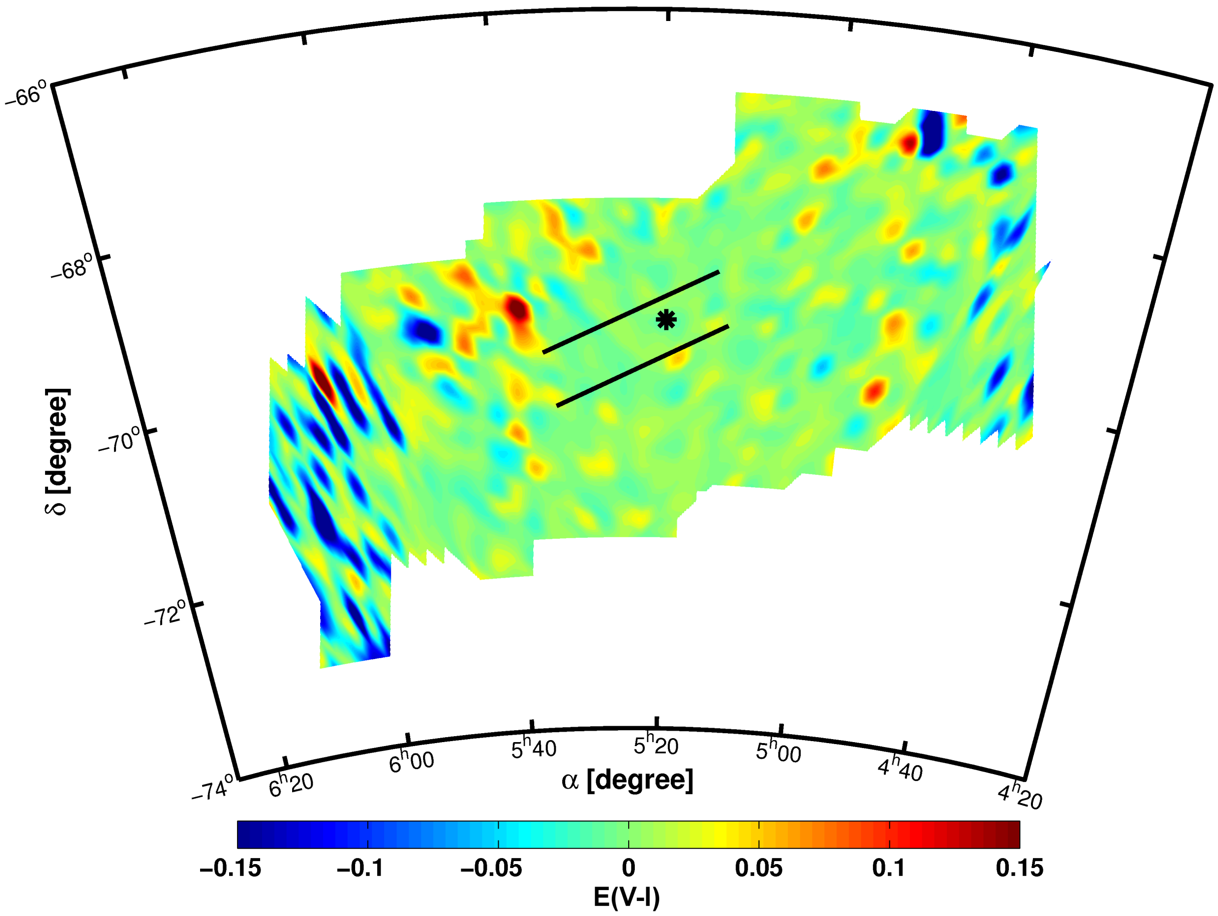

Figure 2.15: Difference map showing the reddening comparison between PS09 and our study of the RR Lyrae stars. The plot shows $E(V-I)_{PS09} - E(V-I)_{RR/HGD10}$. Blue colours indicate higher reddening values in our calculations. We find a very good agreement between the two different methods with a mean difference of 0.007 mag. In 30 Doradus the values by PS09 are higher than in our estimates.

2.4.4 Comparison with other studies

Previous studies of the reddening of the MCs concentrated mostly on the LMC. Below we compare our results for the LMC with the reddening maps inferred from OGLE II data by S05 (S09 is not publicly available), with PS09, who used RR Lyraes from the OGLE III survey, with the cool stars reddening map of Z04, and with CO and infrared maps from D08. For the comparison with the SMC we will concentrate on the reddening maps of Z02 and the CO and infrared measurements by D09.

Dobashi et al. (2008, 2009)

D08 and D09 have used infrared data from 2MASS to derive reddening maps of both MCs. The absolute reddening values are not published, but the images of the maps can be visually compared to the results of our study. The qualitative consistency between the overall appearance of the maps derived from infrared data and our $E(V-I)$ maps is very good. All regions with high reddening values in the infrared are well reproduced by the maps of our work (Figure 5 of D08 and D09, respectively).

As expected the very active star-forming region in the wing of the SMC, with many H II regions, is the area with the highest reddening, having reddening values up to $E(V-I)_{RC} = 0.16$ mag in our map. This region is very prominent in the infrared maps of Wilke et al. (2003, their Fig.1) as well. In the SMC

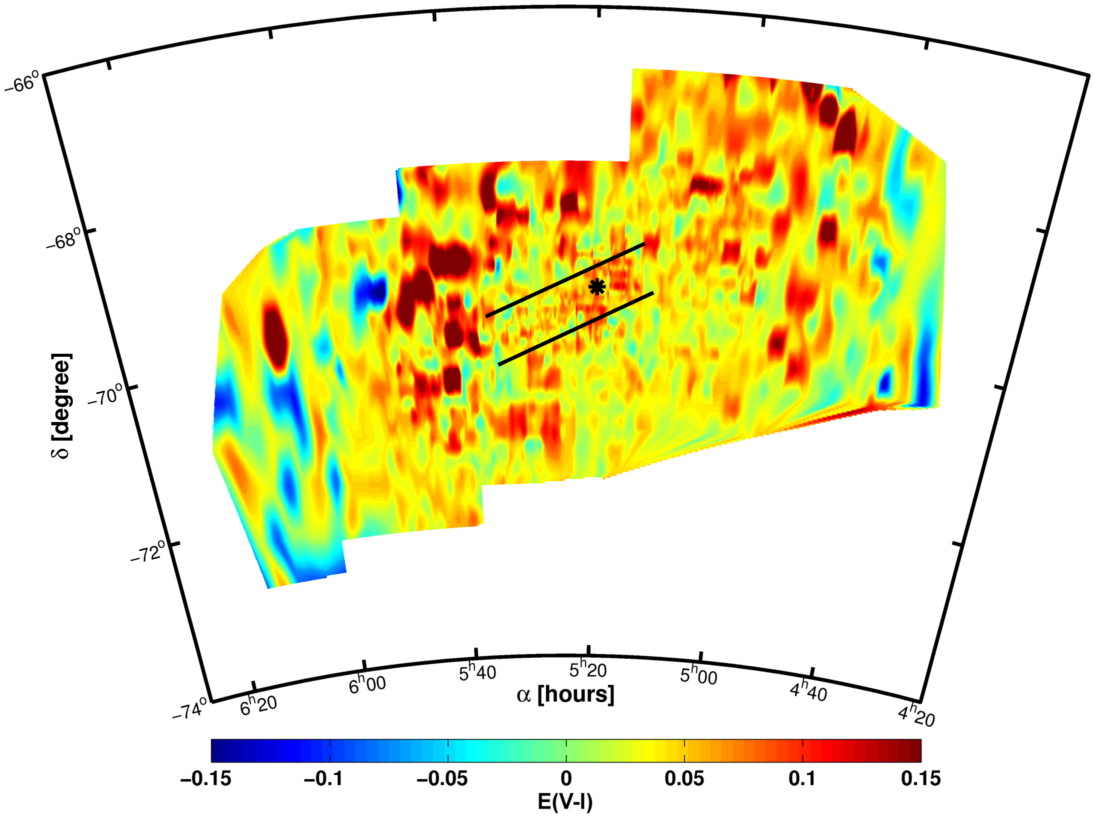

Figure 2.16: Difference map of the RR Lyrae-based reddening values of PS09, $E(V-I)_{PS09}$, minus our reddening values derived from the RC, $E(V-I)_{RC/HGD10}$. Overall the mean reddening of the map by PS09 is enhanced by 0.05 mag.

bar the region in the southwest corner has the highest reddening values (up to $E(V-I)_{RC} = 0.12$ mag in our work) in each of the inspected maps.

In the LMC the 30 Doradus region is the most prominent heavily reddened feature in each map. The location of the regions with high reddening is very similar. Additionally, the very low reddening of the LMC bar region found in our analysis is reproduced very well by the infrared maps of D08. Only one area of the LMC is not reproduced in D08. In the southwest corner of the observed OGLE III field a region with higher reddening is visible in the maps from our study, but not in the infrared data. Searching for extended gaseous features in this part of the sky we can only identify a higher concentration of HI clouds (see Kim et al. 1998b). However, there is very good agreement of our data with the reddening maps from the 2MASS catalogue.

Subramaniam (2005)

The differences in the photometry between OGLE II and OGLE III are marginal (Udalski et al. (2008a) quote ~ 0.001 mag). Hence we do not expect that the use of OGLE II or OGLE III data within the same area will introduce differences.

The comparison between S05, their Figure 1 and Figure 17, from OGLE II data, and our study shows very good agreement (see Figure 2.14). The mean difference of the RC reddening values is $E(V-I) = 0.017$ mag and therefore much smaller than the uncertainties. The fluctuations in the central parts are most likely caused by different subfield sizes. S05's spatial resolution is a bit higher, hence the differences could be generated by variations on very small scales. For the northwestern area of the S05 reddening

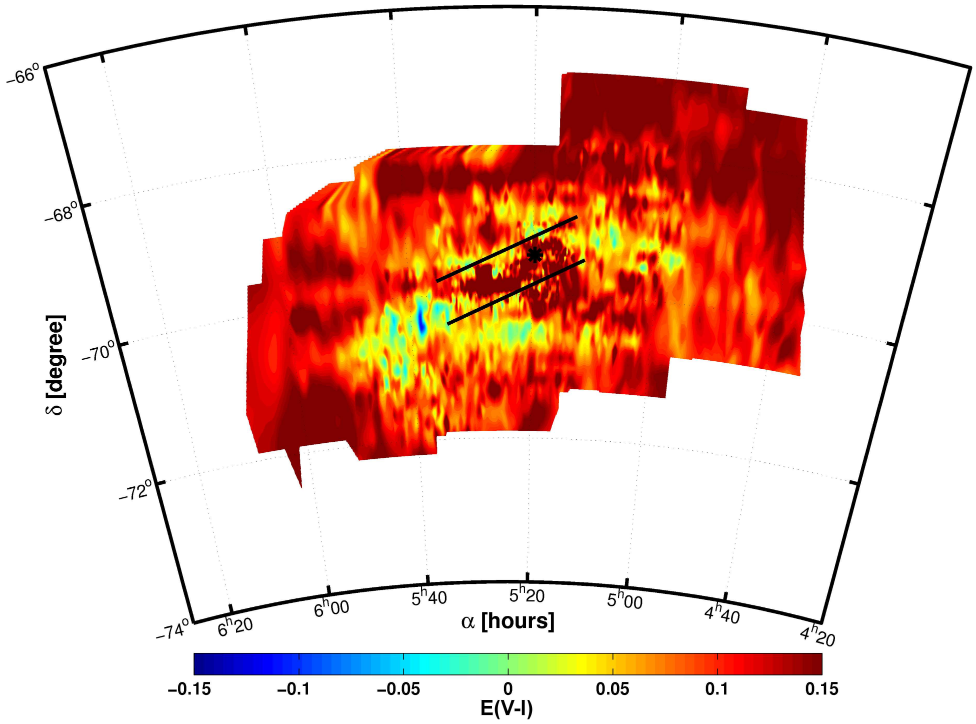

Figure 2.17: Difference map of the reddening values from the MCPS (Z04) for cool stars are compared with our reddening values from the RC method, $E(V-I)_{Z04} - E(V-I)_{RC/HGD10}$. We averaged the Z04 reddening in the fields defined by the RC method. Positive values indicate higher reddening in the work of Z04. The median difference of the two maps is 0.11 mag.

map our RC reddening values are lower. While S05 is limited by the OGLE II field our selection box includes many stars previously not observed. This difference in field selection might be the reason for the trend of slightly higher reddening in this region and in S05 in general. Overall the differences are very small and our results are in very good agreement with the data of S05.

Pejcha & Stanek (2009)

Based on RR Lyrae stars from the OGLE III survey PS09 use the period-colour relation of the unreddened cluster M3 to infer the $(V-I)_0$ of the LMC RR Lyraes. M3 has a metallicity of $[Fe/H] = -1.39$ dex (Cohen & Meléndez 2005), similar to the mean metallicity of the LMC RR Lyrae (Borissova et al. 2009). The difference between the theoretical and the measured colour yields the reddening. PS09 subdivided the OGLE area and calculated a mean reddening for every field with at least two RR Lyrae stars. With this method PS09 construct a map for nearly the whole LMC OGLE field of view.

While we used the same stars as PS09, there are two main differences in actually calculating the reddening values. First we accounted for the intrinsic metallicity of the RR Lyrae in our colour estimation. For different metallicity bins the mean colour varies significantly. The metallicity bin with the densest population and values between $-1.5 < [Fe/H] \leq -1.0$ has a mean colour of $(V-I) = 0.48$ mag. All other metallicity bins have a redder colour (see Table 2.3).

The other major difference is the formula used for calculating the colour of each RR Lyrae star. With a mean period $P = 0.57$ days and mean metallicity of -1.23 dex for all RR Lyrae stars we obtain a mean colour of 0.49 mag. The relation $(V-I)_0 = 0.69 + 0.89\,P$ (Equation 1 in PS09) leads to a mean colour of 1.20 mag when using the same mean period. Compared with Figure 2.1 this would place the RR Lyrae

Table 2.3: Mean colour of the RR Lyraes in certain metallicity bins.

metallicity bin	colour
$-2.0 < [Fe/H] \leq -1.5$	0.52
$-1.5 < [Fe/H] \leq -1.0$	0.48
$-1.0 < [Fe/H] \leq -0.5$	0.51
$-0.5 < [Fe/H] \leq -0.0$	0.54

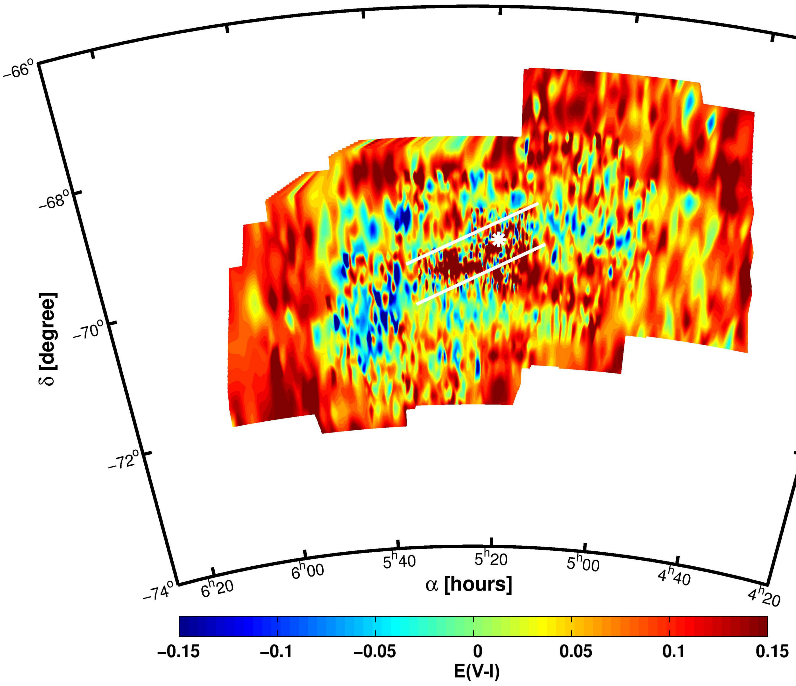

Figure 2.18: Difference map of the reddening determined by Z04, $E(V-I)_{Z04}$, for cool stars, minus our RR Lyrae based reddening, $E(V-I)_{RR/HGD10}$. The resulting map shows a generally higher reddening of Z04 by 0.07 mag. The reason for the high reddening residual in the centre of the LMC remains unclear. It has not be found in any other study.

stars redwards of the RC.

PS09 transformed their reddening values to extinctions A_I, which they made publicly available. We reverse the transformation and compare the reddening values $E(V-I)$ of PS09 with our mean reddening values of the RR Lyrae that are observed in each field via $E(V-I)_{PS09} - E(V-I)_{RR/HGD10}$.

On average we find that our reddening values agree very well with the reddening map presented by PS09 (see Figure 2.16). The mean difference is just −0.004 mag, with deviations ranging from −0.26 to 0.22 mag. For 11% of all PS09 fields a deviation of more than 0.06 mag or 1σ is found. The eastern regions of the LMC (RA > 6^h) are only sparsely populated and due to the selection criteria of PS09 these regions are not very well covered. Therefore the comparison in these regions is not reliable.

In addition to comparing the reddening values resulting from the different implementations of the RR Lyrae methods of PS09 and our work, we compare the values of PS09 to our reddening values from the RC method. We use the values of $E(V-I)$ computed above from the work of PS09 and subtract our reddening estimates of the RC method for the corresponding field. The field sizes of the two approaches differ significantly. We therefore recalculate the values of PS09 to fit into the spatial grid set by our RC method. The differences are evaluated using this grid and are shown in Figure 2.16. This leads to a mean

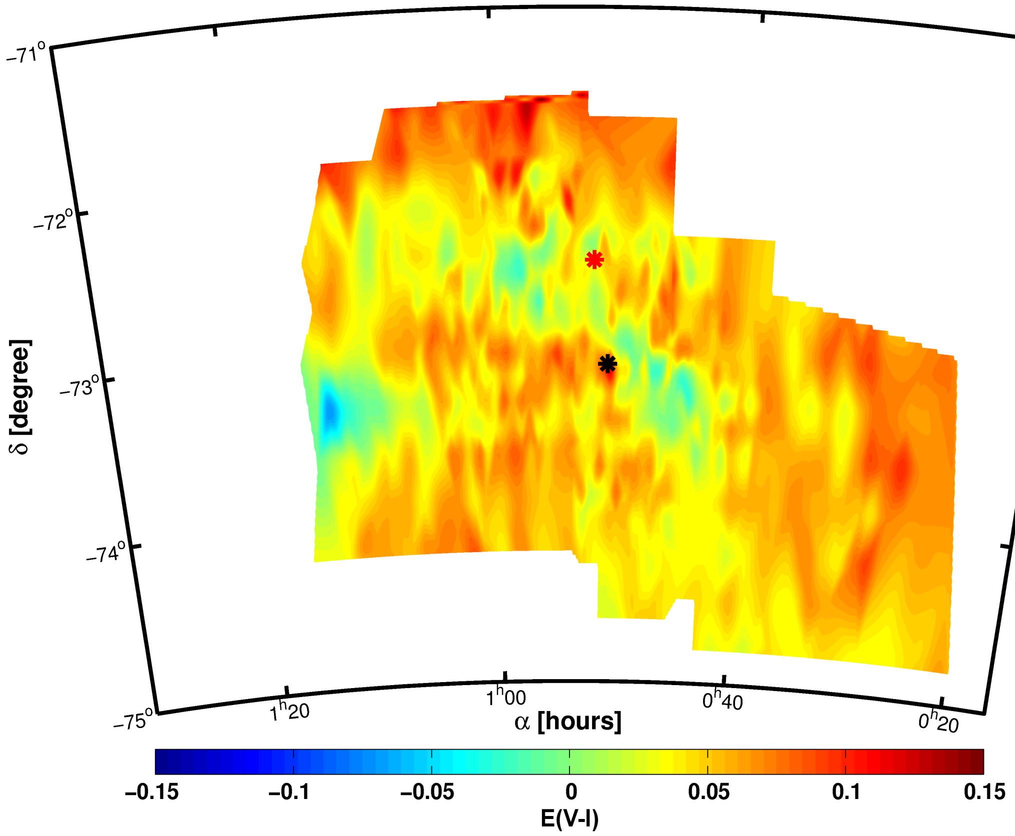

Figure 2.19: Difference map of our reddening values subtracted from Z02's reddening maps derived from the cool stars in the SMC. Despite the small offset to higher values in Z02s data, which is still within our estimated errors, the agreement is very good. The mean difference is 0.04 mag.

difference in reddening of $\overline{\mathrm{E(V-I)_{PS09} - E(V-I)_{RC/HGD10}}} = 0.05$ mag. The differences for individual fields range from -0.17 to 0.32 mag, but only 3% of all fields have deviations of more than 0.12 mag or 2σ.

Especially the region of 30 Doradus reveals much higher reddening values in the maps of PS09. Comparing the two RR Lyrae methods the same result is found, see Figure 2.16.

The northwestern region is higher in reddening as well in PS09. This result is also visible in the comparison of our RR Lyrae reddening estimates and the RC method (see Figure 2.12).

Most regions with higher reddening values from the PS09 map show indications of considerable differential reddening (compare with Figure 2 in PS09). As before we suggest that the most likely explanation is the differential reddening with its resultant asymmetric distribution of reddening values. Taking the mean of such a distribution yields higher values than the use of the peak of the distribution, as done for the RC stars. In addition, the sparser sampling of RR Lyrae stars as compared to the RC stars increases the scatter (see Section 2.4.3).

Zaritsky et al. (2002, 2004)

Z02(SMC) and Z04(LMC) used hot ($12000K < \mathrm{T_E} < 45000K$) and cool ($5500K < \mathrm{T_E} < 6500K$) stars to produce reddening maps of both MCs. These maps are based on the multi-colour data of the MCPS (Zaritsky et al. 1997) and cover 64 square degrees in the LMC and 18 square degrees in the SMC [1]. For

---

[1] The fits files containing the reddening data of the MCPS can be found at: `http://ngala.as.arizona.edu/dennis/`

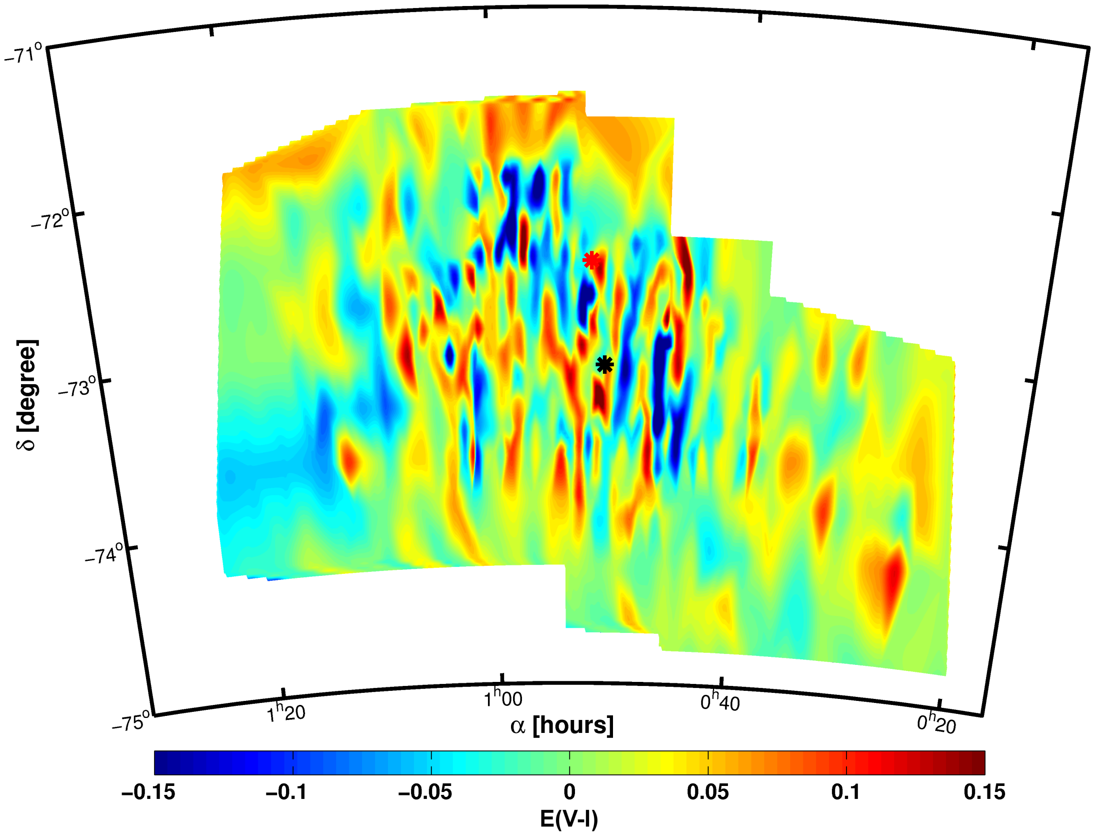

Figure 2.20: Difference map of the reddening determined by Z02, $E(V-I)_{Z02}$, for cool stars, minus our RR Lyrae based reddening, $E(V-I)_{RR/HGD10}$. The resulting map shows very good agreement between the two different methods although the fluctuations are now larger than in Figure 2.19. The mean difference is basically zero.

each hot and each cool star in the field a reddening value is estimated, but we only use the data of the cool stars, which are much closer to the characteristics of the RC, with T ∼ 5000 K (Bragaglia et al. 2001) and RR Lyrae stars, with T ∼ 6500 K (Barcza 2010) at minimum light, used in our work. These reddening values are compared with all data sets evaluated by us.

For better comparability of the differences we compute the averages of Z04's reddening values in the 3174 LMC fields used for the RC method and subtract $E(V-I)_{RC/HGD10}$ from the resulting $E(V-I)_{Z04/mean}$. The comparison maps for the LMC are shown in Figure 2.17 and Figure 2.18. The reddening maps for the LMC reveal differences between our two approaches and the Z04 estimate that exceed the errors found for the RC and RR Lyrae reddening values. While the central parts of the LMC are in general agreement, the reddening values for the less populated parts are considerably higher in the Z04 calculations. The origin of these differences remains unclear. Two major differences have to be taken into consideration: the different kinds of stars used and the different methods. Z02 and Z04 used stellar atmosphere models (from Lejeune et al. 1997) to calculate the reddening for each star, while we use models of the location of RC stars in a CMD to assume absolute magnitudes.

The mean difference between our RC map and Z04's values is 0.10 mag. For only 2% of all fields the mean reddening of the Z04 stars located therein is lower than the corresponding RC reddening. The reddening differences range from −0.11 to 0.46 mag. About 37% of all fields differ by more than 0.12 mag.

`mcsurvey.html`

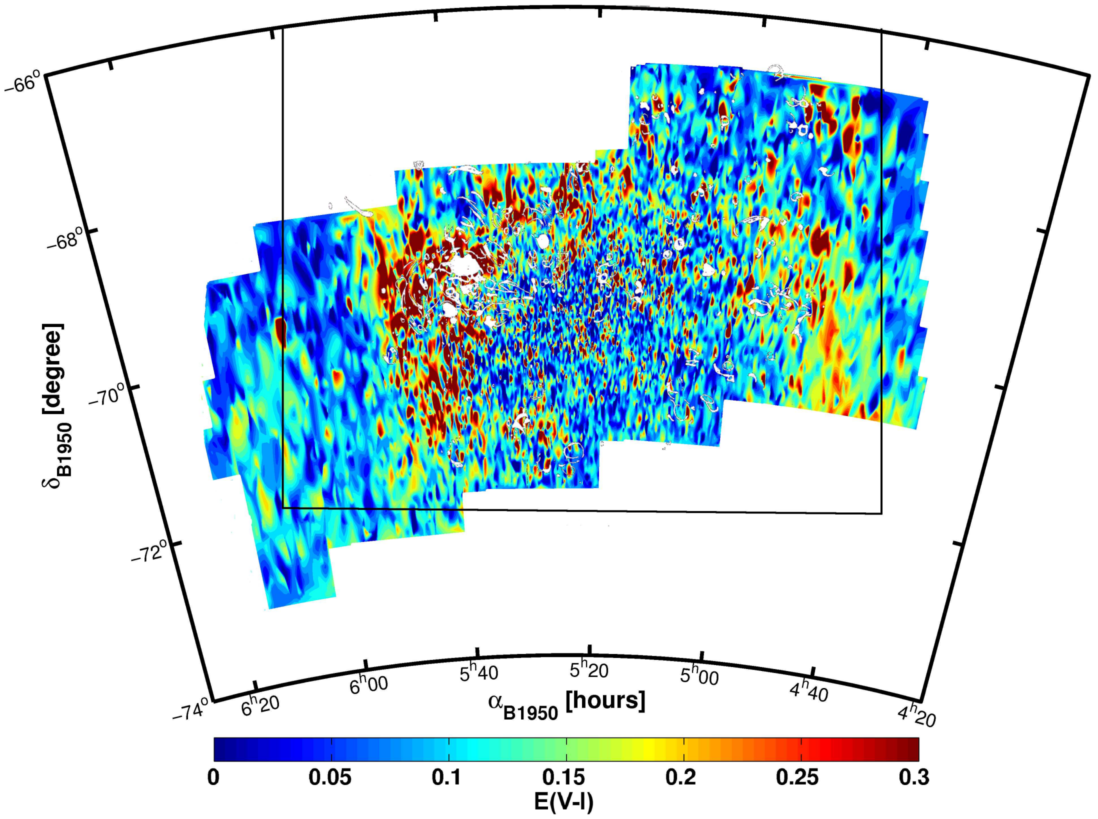

Figure 2.21: Superposition of the reddening map from Figure 2.9 and the map of H II regions by Davies et al. (1976, their Figure 1). The reddening enhancement is not conclusive by visual inspection, but the mean reddening at the centres of the H II regions is increased by 0.03 mag.

In order to compare our RR Lyrae reddening values with Z04's reddening estimates for the LMC we use the equation $E(V-I)_{Z04} - E(V-I)_{RR/HGD10}$. As for the RC reddening we average the RR Lyrae and the Z04 reddening in the grid set up for the RC method. This allows us to compare not single star values but mean values with each other.

The mean difference is found to be 0.07 mag (Figure 2.18), while the differences reach extremes of up to 0.50 mag and down to −0.40 mag. 17% of all fields have negative values, while 21% have discrepancies larger than 2σ. As for the comparison with the RC method, these two maps are not in very good agreement. Especially the offset for the central region is striking. The origin of the rather high reddening residuals of Z04 in the centre of the LMC (Figure 2.17 and 2.18) remains unclear. It has no counterpart in other reddening maps in the literature.

In contrast the agreement in the reddening values of the SMC derived via the RC method and the Z02 values is very good. We compute $E(V-I)_{Z02} - E(V-I)_{RC/HGD10}$ and find that the median difference is only 0.04 mag, while a general slight trend to higher values is obvious (Figure 2.19). But this offset is still well within the errors stated for the SMC reddening in our work. For the SMC about 2% of the stars have lower reddening in Z02 than the corresponding value from the RC method and only 2 fields have differences larger than 0.12 mag. The extremes range from −0.07 mag to 0.13 mag.

Comparing the reddening maps from Z02 and the RR Lyrae we find even better agreement (Figure 2.20) if we average the RR Lyrae values in the fields defined by the RC method. The difference $E(V-I)_{Z02} - E(V-I)_{RR/HGD10}$ is in agreement with zero, while the individual fields vary between −0.28 and 0.18 mag. The number of RR Lyrae stars per RC field is very low and the small number statistics

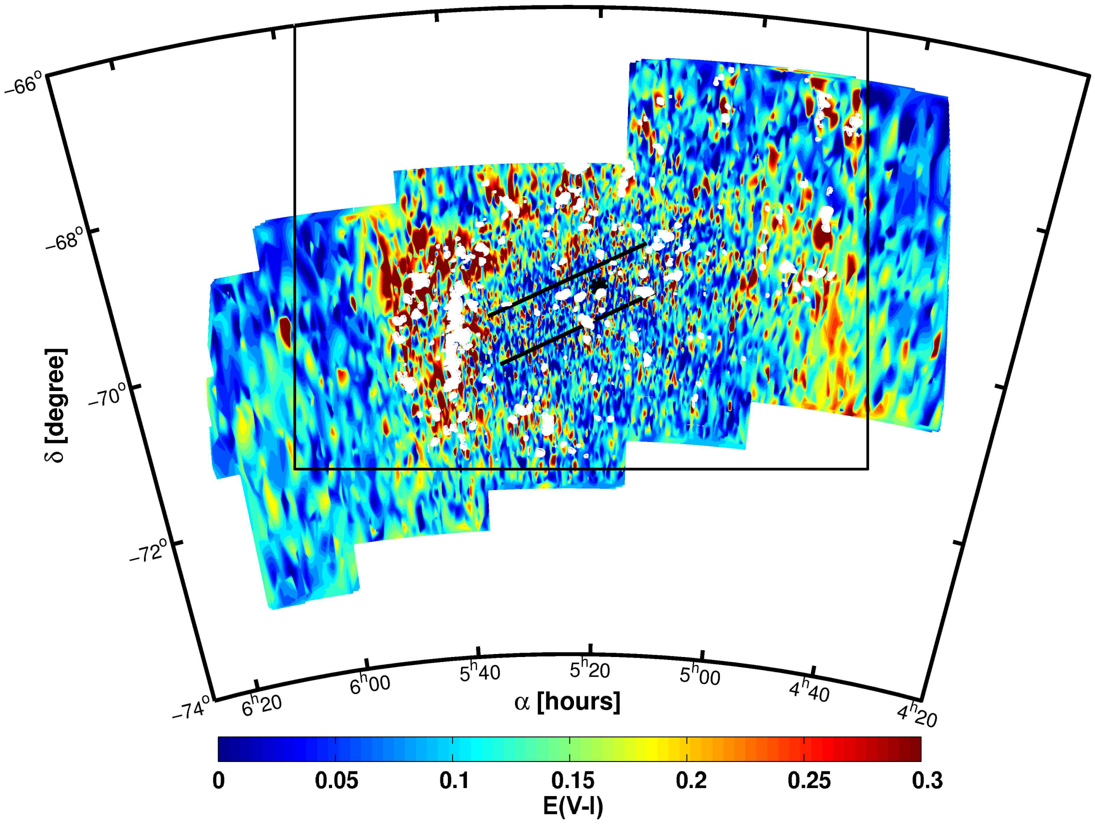

Figure 2.22: The reddening map from Figure 2.9 is superimposed with molecular clouds, traced by CO, from the catalogue by Fukui et al. (2008, white contours). Overall we find an enhanced reddening at the spatial positions of the molecular clouds. The black lines represent the observed field of NANTES.

lead to variations. Therefore we do not interpret the small scale variations as real features. Anyhow we find that there is an overall good agreement between the new reddening maps and the maps provided by Z02. Thus the reason for the large reddening differences for the LMC remains unsolved.

2.4.5 Other comparisons

In this section we will compare our reddening maps, mainly qualitatively, with the distribution of H II regions in the LMC (Davies et al. 1976; Book et al. 2008, 2009) and SMC (Davies et al. 1976; Bica & Schmitt 1995), with LMC CO maps, tracing molecular hydrogen clouds, by Fukui et al. (2008) and the Spitzer dust maps by Meixner et al. (2006) for the LMC and Bolatto et al. (2007) for the SMC.

We overlay the maps of Davies et al. (1976) of the LMC and SMC with our reddening maps (Figure 2.21). Visual inspection does not always show a noticeable increase of reddening at the positions of the H II regions. We tentatively attribute this to effects of dust destruction by hot massive stars in the HII regions as well as to stellar winds that push gaseous and dusty material out of the forming cavity within the HII regions. Furthermore we compare the central positions of the H II regions, taken from Davies et al. (1976); Bica & Schmitt (1995); Book et al. (2008, 2009), with the reddening values at that spatial location and find the reddening to be increased by 0.03 mag for the LMC and SMC, respectively.

In Figure 2.22 the map of molecular hydrogen clouds as observed by NANTEN (Fukui et al. 2008), and traced by CO, is superimposed with the reddening from the RR Lyrae stars. We find very good agreement of regions with enhanced reddening and the location of the clouds. This visual impression is verified by the computation of the mean reddening at the spatial positions of the molecular clouds. We find that the reddening is enhanced to a median value of $E(V-I)_{\mathrm{median}} = 0.19$ mag.

Finally we inspect the images of the SAGE (Surveying the Agents of Galaxy Evolution) survey of the LMC (Meixner et al. 2006) and find very good agreement of their 8μm map with the LMC reddening map as obtained by us. The 8μm emission originates from small dust grains as traced by polycyclic aromatic hydrocarbons (PAHs) located in the outskirts of star-forming regions (Meixner et al. 2006). Only the region of enhanced reddening in the south-west is not reproduced. However, we find good agreement of this region in the 160μm map of Spitzer. The absorbtion feature at larger wavelength are caused by greater particles. The 160 μm maps trace emission of relatively large and cool ($\sim$ 20 K) dust grains at larger distances from star-forming regions (Meixner et al. 2006). The SAGE-SMC (Bolatto et al. 2007) maps show very good agreement with the reddening map of the SMC as obtained by us.

2.5 Summary

In this paper new optical reddening maps for the MCs are presented using two different methods based on OGLE III photometry. The first one uses the theoretical position of the RC in $(V-I)_0$ colour in the CMD for a given mean metallicity. The observed shift of the measured RC position is used to determine the reddening. For this purpose we subdivide the original OGLE III fields into smaller fields and determine the mean colour of the RC in each of them. The size of the fields varies depending on the number of stars in each field. For the LMC we obtain 3174 subfields with a mean density of 1257 stars, while for the SMC the reddening is calculated in 693 subfields, with an average of 1318 stars per field.

The maps show in general a low reddening. In the LMC we find a mean $E(V-I) = 0.09 \pm 0.07$ mag and for the SMC $E(V-I) = 0.04 \pm 0.06$ mag. Nevertheless some regions show a much higher reddening. The star-forming region 30 Doradus in the LMC shows values up to $E(V-I) = 0.43$ mag. The high differential reddening in this region broadens the distribution of the RC stars and there is an extended tail of even higher reddening values in this region. Another region with high reddening is found in the southwest of the examined OGLE III field and coincides with an H I region. In contrast to the highly extincted star-forming regions the reddening in the bar of the LMC is quite low.

For the SMC the RC method reveals three pronounced areas of higher reddening. The highest reddening is reached, with $E(V-I) = 0.16$ mag, in an H II region in the wing. The other two regions are located in the bar. But overall the reddening is quite low.

For the second method the observed colour $(V-I)$ of RR Lyrae stars in the MCs is compared with the colour predictions of the calculated absolute magnitudes. These depend on the period and metallicity. The metallicity is evaluated via the Fourier decomposition of the lightcurve of each star. We obtain an independent reddening for each RR Lyrae star. For the LMC a median reddening of $E(V-I) = 0.11 \pm 0.06$ mag is obtained. In the star-forming region 30 Doradus the reddening reaches values up to $E(V-I) = 0.66$ mag. The RR Lyrae reveal a mean reddening of the SMC of $E(V-I) = 0.07 \pm 0.06$ mag.

The comparison with reddening maps derived from other studies show mostly good agreement. Moreover, a qualitative comparison with Spitzer maps shows areas of high reddening to coincide with regions of high dust emissivity from PAHs or larger dust grains at 8 and 160 μm, respectively.

These new reddening maps show a consistent picture of the reddening distribution of both MCs. we make our position-dependent reddening values derived with the RC method available via the GAVO interface at `http://dc.zah.uni-heidelberg.de/mcx`.

Kes: "These people are natural born explorers."
Neelix: "These people are natural born idiots!"
Star Trek: Voyager (The Cloud)

3

Metallicity distribution functions of the old populations of the Magellanic Clouds from RR Lyrae stars

We present the first metallicity distribution functions of the old field populations in the Magellanic Clouds. Our metallicities are based on the Fourier decomposition of Type ab RR Lyrae light curves from the Optical Gravitational Lensing Experiment. On the metallicity scale of Zinn & West; we find a mean metallicity of [Fe/H] = -1.50 ± 0.24 dex based on 16776 RR Lyrae stars in the Large Magellanic Cloud. For the Small Magellanic Cloud we obtain -1.70 ± 0.27 dex based on 1831 RR Lyrae stars. These uncertainties represent the intrinsic spread in the population rather than the standard deviation of the mean.

Our results are in good agreement with the few existing spectroscopic metallicity determinations for LMC RR Lyrae stars from the literature. For both the LMC and the SMC the metallicity spread exceeds 1 dex in [Fe/H]. The distribution of metallicities in both Clouds is very uniform, and no significant metallicity gradient is detectable. We also do not find any pronounced populations of extremely metal-poor RR Lyrae candidates with metallicities well below -2 dex, although we need to caution that the photometric method used may overestimate the metallicities of metal-deficient stars. Moreover, because of stellar evolutionary effects one does not expect to observe many RR Lyrae stars among very metal-poor horizontal branch stars.Â We suggest that the Magellanic Clouds experienced fairly rapid and efficient early enrichment involving pre-enriched gas as well as possibly gas infall, while metal loss through outflows does not seem to have played a significant role. Moreover we suggest that the differences in the metallicities of the old population of LMC and SMC make an origin from a single, common progenitor unlikely, unless the separation happened very early on.

This chapter is based on the paper Haschke, Grebel, Duffau, & Jin (2012)

3.1 Introduction

The origin and nature of the MCs pose an interesting puzzle. They have long been known as the closest irregular satellites of the MW, although galaxy surveys reveal that star-forming satellites in close proximity to massive galaxies are rare (e.g., James & Ivory 2011), while very accurate *Hubble Space Telescope*-based determinations of the proper motions of the MCs (Kallivayalil et al. 2006b; Piatek et al. 2008) have evoked a new discussion of their orbits (e.g., Besla et al. 2007, 2010). With recent new measurements of lower proper motions by Costa et al. (2011) and Vieira et al. (2010) the discussion has been further intensified. In particular, these studies have raised questions of whether the MCs might be on their first passage around the MW (e.g., Lux et al. 2010 and references cited above; but see also, e.g., Diaz & Bekki 2011). Similarly, it remains unclear whether the MCs were formed together, whether the SMC might have been captured by the LMC later on, or whether interactions or mergers might be responsible for the chemistry and peculiar structure of the SMC (e.g., Mathewson et al. 1988; Kallivayalil et al. 2006a; Costa et al. 2009; Tsujimoto & Bekki 2009).

One of the possible avenues of exploring the early history of the MCs relies on the study of their old populations. Generally, both GCs as well as field stars are suitable tracers of old populations. The LMC does indeed contain a number of old GCs that are similarly old as the oldest GCs in other Galactic satellites and in the MW (e.g., Brocato et al. 1996; Olsen et al. 1998; Grebel & Gallagher 2004). In terms of their chemical composition, the LMC's GCs span a similar range of metallicities and show similar [α/Fe] ratios as stars in the Galactic halo (e.g., Johnson et al. 2006; Mucciarelli et al. 2010). In contrast, the SMC only contains one old GC, NGC 121, which is a few Gyr younger than the oldest Galactic and LMC GCs (Glatt et al. 2008b). Thus one would ideally wish to turn to more numerous tracers of old populations such as those potentially present among field stars. However, genuinely old field stars are difficult to identify in galaxies that experienced long-lasting star formation such as the MCs (e.g., Holtzman et al. 1999; Gallart et al. 2008; Sabbi et al. 2009), since stellar populations of many different ages are then superimposed, rendering otherwise popular stellar tracers such as red giants rather ambiguous indicators (see, e.g., Figure 10 in Koch et al. 2006). Using star clusters with spectroscopic metallicities and ages from main-sequence fitting, Glatt et al. (2008a) showed that the SMC exhibits a considerable spread in metallicity at any given age. The study of evolutionary histories is further exacerbated if the galaxy in question has a non-negligible depth extent as appears to be the case for the SMC. Under such circumstances, using easily identifiable, special types of stars as tracers is a useful approach (see, e.g., Grebel 1997, Figure 3). One of these evolutionary tracers for evaluating the parameters of the old field population are RR Lyrae variables. With ages of at least 9 Gyr (e.g. Sarajedini et al. 2006), they allow us to explore the early stages of the evolutionary history of a galaxy.

When well-defined light curves are available, RR Lyrae stars can easily be identified. Apart from their distance and spatial distribution, their metallicity is a parameter of particularly high interest. Either spectroscopic measurements or Fourier decomposition of their light curves can be used to deduce the metallicity [Fe/H] (Kovács & Zsoldos 1995; Jurcsik & Kovács 1996).

Old populations including RR Lyrae stars tend to be widely distributed and often form the most extended stellar populations in galaxies. This provides us with the possibility to not only measure the mean metallicity of genuinely old stars but also to obtain the metallicity spread, to derive detailed MDFs, and to identify possible metallicity gradients. Overall, such studies can provide a fairly detailed picture of the chemical evolution that a galaxy experienced at early times.

Butler et al. (1982) first used the ΔS method (Preston 1959) to investigate the metallicity of six RR Lyrae stars in the LMC and ten RR Lyrae stars in the SMC. They found a significant difference between the two samples, with a mean metallicity of $[\mathrm{Fe/H}] = -1.4 \pm 0.1$ dex for the LMC and -1.8 ± 0.2 dex for the SMC. In more recent studies, spectroscopic metallicities of old stars in the LMC were determined for sets of 74 to 98 RR Lyrae stars (Gratton et al. 2004; Borissova et al. 2004, 2006, see

Table 3.1), while for the SMC no further spectroscopic data are available. These spectroscopic studies, which are concentrated close to the bar of the LMC, revealed mean metallicities of about [Fe/H] = -1.50 dex.

With microlensing surveys such as OGLE (Udalski et al. 1992, 1997, 2008a), carefully chosen, extended regions with high stellar densities have been regularly monitored. In the MCs, OGLE focussed on the dense central regions. These surveys are well suited for finding variable stars, such as RR Lyrae stars. Thanks to the large number of repeat observations, variability properties of these stars can be determined with high precision. The parameters of the observed light curves of RR Lyrae stars of type ab can be used to determine the metallicity as shown first by Kovács & Zsoldos (1995). Jurcsik & Kovács (1996) presented a formalism to derive metallicities as a function of the period and the Fourier phase ϕ_{31}. For cases where the Fourier parameters cannot be determined, for instance Brown et al. (2004) and Sarajedini et al. (2006) presented equations to infer the metallicity using only the period. These approaches have larger uncertainties than the equations presented by Jurcsik & Kovács (1996) and are not used in our study.

In recent years, the public data of the OGLE survey have been used to determine the MDF and the metallicity gradient of the MCs with RR Lyrae stars. The OGLE II data were used by Smolec (2005) to investigate the metallicity distribution of 5451 LMC RR Lyrae stars and the differences in [Fe/H] for Blazhko and non-Blazhko stars. For the non-Blazhko RR Lyrae stars a mean metallicity of [Fe/H] = -1.218 ± 0.004 dex was determined, while the Blazhko stars had a mean value of [Fe/H] = -1.28 ± 0.01 dex. DS10 used the OGLE II data of the SMC to determine metallicities for 335 RR Lyrae stars of type ab and found a mean metallicity of [Fe/H] = -1.56 ± 0.25 dex. In FAW10 a gradient of 0.01 ± 0.002 dex kpc^{-1} was inferred for the RR Lyrae stars of the LMC, observed by OGLE III.

We use the entire sample of RR Lyrae stars provided by the third data release of the OGLE collaboration to calculate individual metallicities for each star of the MCs. We discuss the origin of our data in Section 1.3. In Section 3.2 we present the method for calculating metallicities used in this paper. The results for the LMC are given in Section 3.3 and for the SMC in Section 3.4. We thus obtain an MDF of the old population and investigate the existence/absence of a metallicity gradient for both MCs. We test whether the photometric metallicities lead to similar results as spectroscopic values in Section 3.5 and compare different methods to estimate the metallicity from photometric data in Section 3.6. Section 3.7 discusses the results obtained.

3.2 Method of metallicity determinations

Determining metallicities of a sample of this size is currently only feasible via photometric estimates. We therefore use the techniques of metallicity estimates based on Fourier-decomposed light curve parameters. Simon & Lee (1981) introduced this method for variable stars, using the first few orders of a Fourier decomposition,

$$V = A_0 + \sum_{k=1}^{N} A_k \sin(k\omega t + \phi_k) \tag{3.1}$$

where V is the observed magnitude, $A_{0/k}$ is the amplitude, ϕ_k the phase, ω the angular frequency, and t the specific time at which a data point was measured. N is the order to which the Fourier series is developed.

The Fourier parameters of the different orders of the decomposition contain information about important physical properties of the variables. While the amplitude A_k is a measure of the skewness, the phase ϕ_k corresponds to the acuteness of the light curve (Stellingwerf & Dickens 1987). Simon & Clement (1993) showed how the Fourier parameters $\phi_{31} = \phi_3 - 3\phi_1$ are related to temperature and luminosity, while Kovács & Zsoldos (1995) presented the close connection between the period, the Fourier parame-

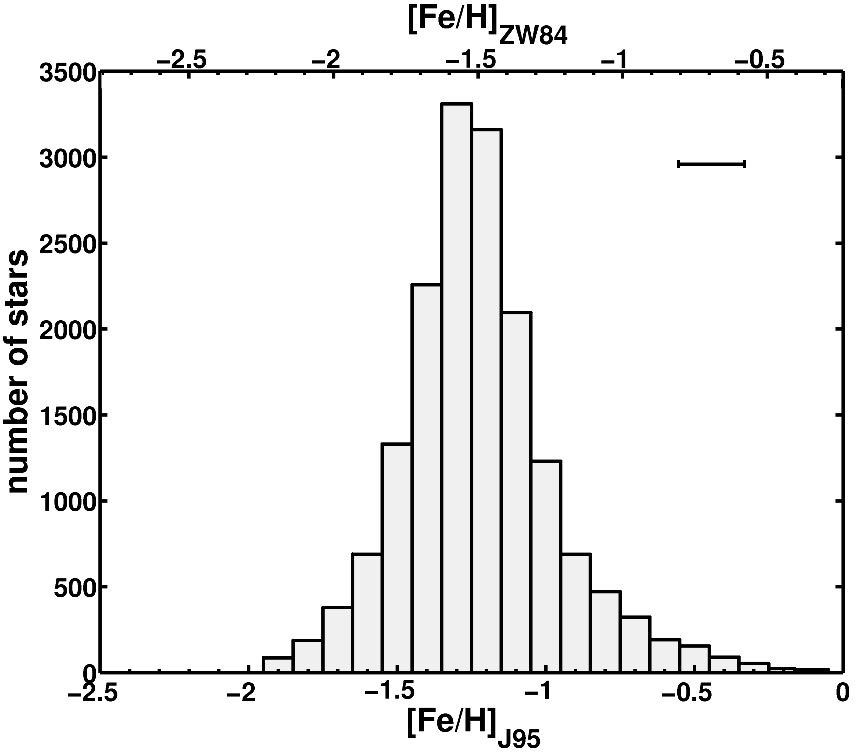

Figure 3.1: Metallicity distribution of LMC RR Lyrae stars, computed based on the Fourier decomposition of their light curves. We find a mean metallicity of $[\mathrm{Fe/H}]_{\mathrm{mean}} = -1.22$ dex on the scale of J95. The bottom axis shows the scale of J95, while the top axis shows the scale by ZW84, for which we find $[\mathrm{Fe/H}]_{\mathrm{mean}} = -1.49$ dex, using the transformation of Papadakis et al. (2000). The distribution has a standard deviation of 0.26 dex. We also find a few candidates for very metal-poor stars. The error bar shows the typical uncertainty of the metallicities for individual stars.

ter ϕ_{31} and the metallicity of RR Lyrae stars. The relation for a sinusoidal Fourier decomposition of a V band light curve is given by Equation 3 of Jurcsik & Kovács (1996).

Fourier parameters differ depending on the filter in which the light curve is observed. As the OGLE photometry is mostly done in the I band, the V band equation by Jurcsik & Kovács (1996) cannot be used. Smolec (2005) recalibrated the relation to be suitable for I band photometry. Combining light curve parameters of 28 RR Lyrae stars with their spectroscopic metallicities ranging from -1.71 dex $<$ $[\mathrm{Fe/H}]_{\mathrm{J95}} < +0.08$ dex, on the metallicity scale of J95, Smolec (2005) found the linear equation

$$\begin{aligned}[\mathrm{Fe/H}]_{\mathrm{J95}} &= (-3.142 \pm 0.646) - \\ &\quad (4.902 \pm 0.375)\,P + (0.824 \pm 0.104)\,\phi_{31}, \end{aligned} \tag{3.2}$$

with ϕ_{31} being the Fourier phase and P being the period of the RR Lyrae star. We adopt a slightly larger metallicity range of -2.0 dex $<$ [Fe/H] $< +0.2$ dex as a presumably reliable domain. This larger range is the metallicity range given by the calibration in Smolec (2005) plus the mean uncertainty of the method (±0.18 dex).

The J95 metallicity scale, which is the basis for the relation by Smolec (2005), leads to higher metallicities compared with other scales. Gratton et al. (2004) find that the J95 scale is more metal-rich by 0.28 dex than the scale of Zinn & West (1984, later on ZW84), in agreement with Sandage (2004) and Clementini et al. (2005). Using six GCs with metallicities between -2.25 dex $<$ [Fe/H] < -1.0 dex,

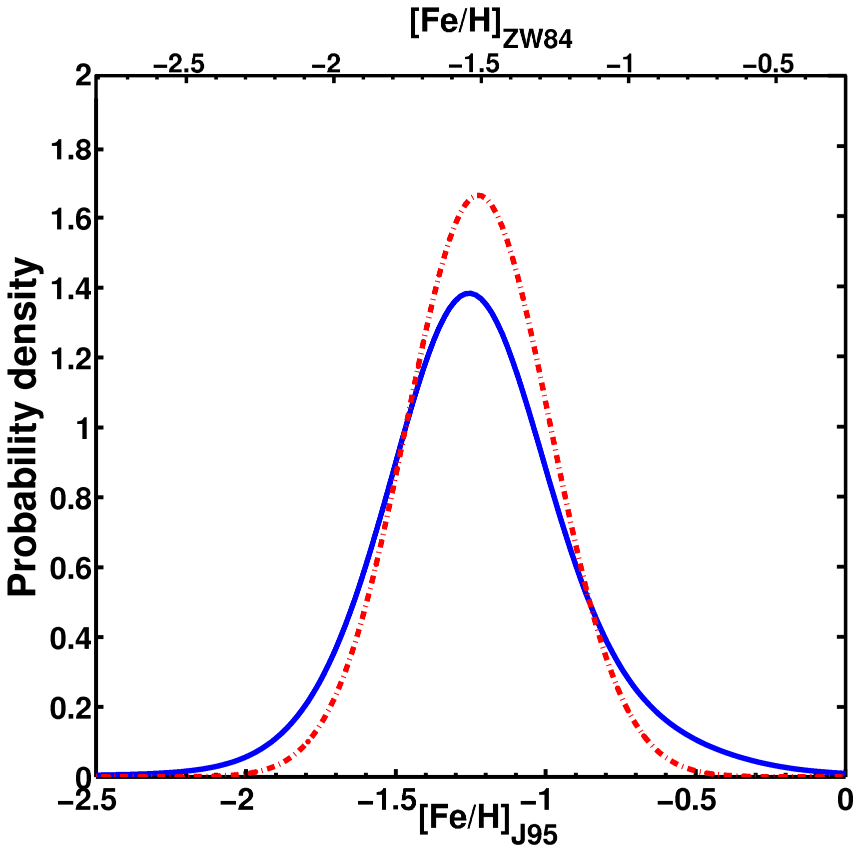

Figure 3.2: Probability distribution function for the metallicity of LMC RR Lyrae stars. The solid blue curve shows the sum of individual stellar metallicities convolved with Gaussian uncertainties, while the red dash-dotted curve is the likelihood distribution. The computation of the metallicities is based on the Fourier decomposition of their light curves. We find a mean metallicity of the likelihood distribution of $[\mathrm{Fe/H}]_{\mathrm{mean}} = -1.23$ dex on the scale of J95 (bottom axis). The top axis shows the ZW84 scale, with a mean value of $[\mathrm{Fe/H}]_{\mathrm{mean}} = -1.50$ dex, using the transformation of Papadakis et al. (2000). The MDF has an intrinsic spread of 0.24 dex.

Papadakis et al. (2000) derived the transformation relation

$$[\mathrm{Fe/H}]_{\mathrm{ZW84}} = 1.028\,[\mathrm{Fe/H}]_{\mathrm{J95}} - 0.242 \tag{3.3}$$

between the two metallicity scales. Several other metallicity scales are also commonly used. A widely-used scale is that of Carretta & Gratton (1997). With a new and larger sample, Carretta et al. (2009) recalibrated the metallicity scale of Carretta & Gratton (1997) and provide a quadratic relation between their new metallicity scale and the metallicity scale of ZW84. Another popular metallicity scale was introduced by Harris (1996), which, according to Gratton et al. (2004), is indistinguishable from ZW84.

3.3 Metallicities of the LMC

For all RR Lyrae stars of type ab in the LMC for which ϕ_{31} values are available from the OGLE III catalogue, we compute metallicities using Equation 3.2. This results in a dataset of 16949 stellar metallicities (Figure 3.1).

Table 3.1:

study	mean [Fe/H]	σ	number of stars
Gratton et al. (2004)	−1.48	0.03	98
Borissova et al. (2004)	−1.46	0.09	74
Borissova et al. (2006)	−1.53	0.02	78

3.3.1 Mean metallicities and metallicity distribution function

Using the J95 scale, we find a mean metallicity of $[\mathrm{Fe/H}] = -1.22$ dex with a standard deviation of 0.26 dex. This translates to a mean metallicity of $[\mathrm{Fe/H}] = -1.50$ dex on the ZW84 metallicity scale. The uncertainties of the Fourier parameters are not mentioned by the OGLE collaboration. Taking the uncertainty of the observed magnitude as the $1\,\sigma$ standard deviation of its assumed Gaussian error distribution, we randomly vary the observed magnitudes to perform Monte Carlo simulations of the light curve for each individual star and redetermine the Fourier parameters. We find very good agreement between the parameter values obtained by OGLE and via our Monte Carlo approach. The resulting range of parameters allows us to calculate the uncertainty for ϕ_{31} and thus of the corresponding metallicity of each star. For the mean uncertainty of the metallicity we find $\sigma_{\mathrm{intrinsic}} = 0.10$ dex. This uncertainty is quadratically added to the systematic uncertainty of $\sigma_{\mathrm{sys}} = 0.18$ dex mentioned by Smolec (2005) and results in a total uncertainty of $\sigma_{[Fe/H]} = 0.21$ dex.

We convolve the individual metallicity values obtained with the derived constant (Gaussian) uncertainty of 0.21 dex and sum up the resulting Gaussian distributions to obtain the “observed” MDF. The solid blue line in Figure 3.2 shows the MDF normalized to 1 (i.e., a probability distribution function).

Motivated by the near-Gaussian profile of the observed MDF, we also use a maximum-likelihood approach to constrain the underlying MDF of the LMC RR Lyrae population. Using such an approach allows us to determine the *intrinsic* width of the MDF (assuming a Gaussian profile) while simultaneously accounting for the contribution of the measurement uncertainties to the width of the observed distribution. The likelihood of our observed data set originating from an underlying Gaussian MDF with its mean, μ, and standard deviation, σ, is given by the function

$$\mathcal{L}(\mu,\sigma) = \quad \prod_{i=1}^{N} \frac{1}{\sqrt{2\pi\left(\sigma^2+{\sigma_i}^2\right)}} \exp\left(-\frac{1}{2}\frac{(x_i-\mu)^2}{\sigma^2+\sigma_i^2}\right) \tag{3.4}$$

where N is the total number of stars, x_i is the metallicity of star i and σ_i is the associated measurement uncertainty. We seek to find the parameters μ and σ that maximize this likelihood function.

The dash-dotted line in Figure 3.2 represents the best fit of μ and σ and reveals the underlying true MDF with a mean metallicity of $[\mathrm{Fe/H}] = -1.23$ dex and an intrinsic width of the distribution of 0.24.

The highest metallicity found in our sample is $[\mathrm{Fe/H}]_{max} = 2.0$ dex, while the lowest value is $[\mathrm{Fe/H}]_{min} = -3.81$ dex. As explained in Section 3.2, we only consider the reliable domain of the calibration and thus exclude 107 stars (0.6% of the complete sample) at the low-metallicity end and 66 stars (0.4% of the complete sample) at the high-metallicity end from the dataset when applying this selection. This leaves us with a sample of 16776 RR Lyrae stars. However, the mean and the standard deviation of the metallicity of the reduced sample remain unchanged in comparison with the full sample.

Results on different metallicity scales cannot easily be compared. We transform all metallicities to the scale of ZW84 using Equation 3.3. This transformation leads to a mean metallicity of $[\mathrm{Fe/H}]_{\mathrm{mean/ZW84}} = -1.50$ dex on the ZW84 scale, which is in excellent agreement with mean values of spectroscopic measurements of RR Lyrae metallicities in the LMC (Gratton et al. 2004; Borissova et al. 2004, 2006, who used the ZW84 metallicity scale as well).

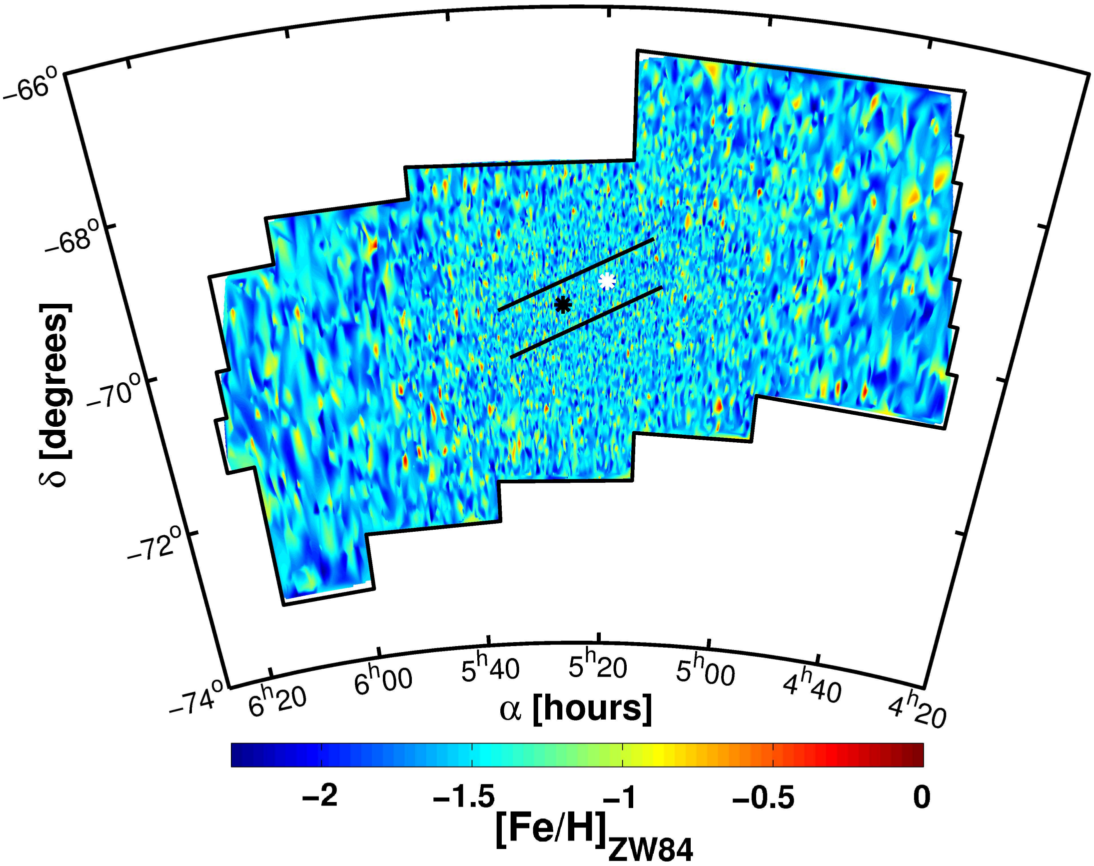

Figure 3.3: Distribution of metallicity in the LMC. Metal-poor regions are coded in blue, metal-rich regions are red. Overall the contour plot is smooth and no gradient or distinct feature is visible. For the contour plot, only stars with $-2.3 < [\mathrm{Fe/H}]_{\mathrm{ZW84}} < 0.0$ are taken into account. The black lines in the middle represent the bar. While the white asterisk marks the optical center of the LMC found by de Vaucouleurs & Freeman (1972), the black asterisk shows the center of the RR Lyrae stars as found by Chapter 4.

3.3.2 Spatial variations in metallicity

Figure 3.3 shows the spatial distribution of the metallicities. Only stars with a metallicity from the reliable domain of the Smolec (2005) calibration are used in this figure. Individual stars are used for the contour plot, to which a grid with constant boxwidth of $1.5' \times 1.5'$ was then applied. Figure 3.3 shows the median metallicity values of these boxes.

In general, a smooth distribution with small-scale variations, but without any obvious gradients or distinct features, is visible. Towards the center of the LMC, the density of RR Lyrae stars increases. Differences in metallicity are therefore observed on smaller scales in the central parts than in the outskirts. This leads to the higher resolution in the center of the figure. The stars that are excluded due to their metallicity being above or below the adopted validity range are distributed randomly across the whole field of OGLE III.

Figure 3.4 examines the mean metallicity as a function of the distance from the center of the RR Lyrae stars of the LMC at $\alpha = 5^h26^m$ and $\delta = -69°75'$ as found by Chapter 4. We investigate the metallicity and distance distributions in bins of 0.1 dex and rings of varying radius. The radii are chosen such that all annuli have the same area. The density of stars in each box is determined. The contour plot is smoothed with a Gaussian filter using 3×3 boxes and a width of one box. Additionally we calculate the median

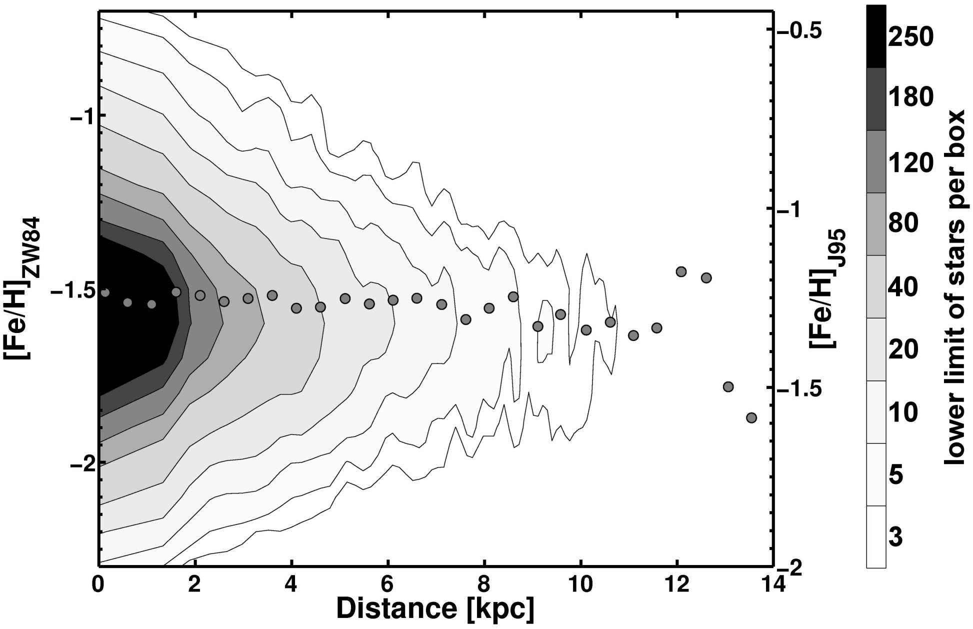

Figure 3.4: The contours show the total number of RR Lyrae stars of a given metallicity as a function of the projected distance relative to the center of the LMC as found from RR Lyrae stars. The mean metallicity does not change, within the errors, with increasing distance from the center. The grey dots represent the median metallicity in bins of 0.5 kpc.

metallicity of each distance bin of 0.5 kpc width, this “running median”is represented by the grey dots in Figure 3.4.

To determine the gradient of the metallicity, the median metallicity is computed in bins of 0.1 kpc and fitted using a first-order polynomial. The resulting gradient for the whole distribution of -0.03 ± 0.07 dex kpc^{-1} is consistent with zero. If we take only the innermost 8 kpc from the center of the RR Lyrae stars into account, a gradient of -0.010 ± 0.014 dex kpc^{-1} is found. The median metallicity seems to be constant in the inner parts of the LMC and dropping slightly towards the outskirts.

To test for non-radial gradients, we divide the OGLE III field into 15 similarly-sized fields. As shown in Figure 3.5, the mean metallicity of these fields drops in accordance with the very small metallicity gradient obtained above. The outer fields always show slightly lower metallicities than the innermost fields. The median values are nearly identical to the mean values.

FAW10 determined the metallicity gradient of the old population using OGLE III RR Lyrae stars. These authors calculated photometric metallicities with two sets of equations, both with the period as the only free parameter. The uncertainty of this method is therefore higher ($\sigma = 0.46$ dex) than with the method of Jurcsik & Kovács (1996) ($\sigma = 0.16$ dex). We recalculate our metallicities using the equations utilized by FAW10 and compare them with our estimates (see Table 3.2). Equation 2 of FAW10 and our estimates transformed to the ZW84 metallicity scale lead to similar results when averaging over all metallicities. For subsets of the sample, however, we find considerable differences. We divide the sample into subsets where all stars are more metal rich than our average or more metal poor. The more metal-rich stars have in general higher metallicities in our Fourier-based estimates. The metallicities below the mean are in general lower in our calculations than the values computed with Equation 2 by FAW10. When only considering stars at the extremes of our metallicity estimates this trend becomes even stronger (Table 3.2). However, the spatial distribution of the RR Lyrae stars in each metallicity bin is very similar to the overall distribution.

FAW10 conclude that there is a very small gradient of -0.0104 ± 0.0021 dex kpc^{-1} for the RR Lyrae

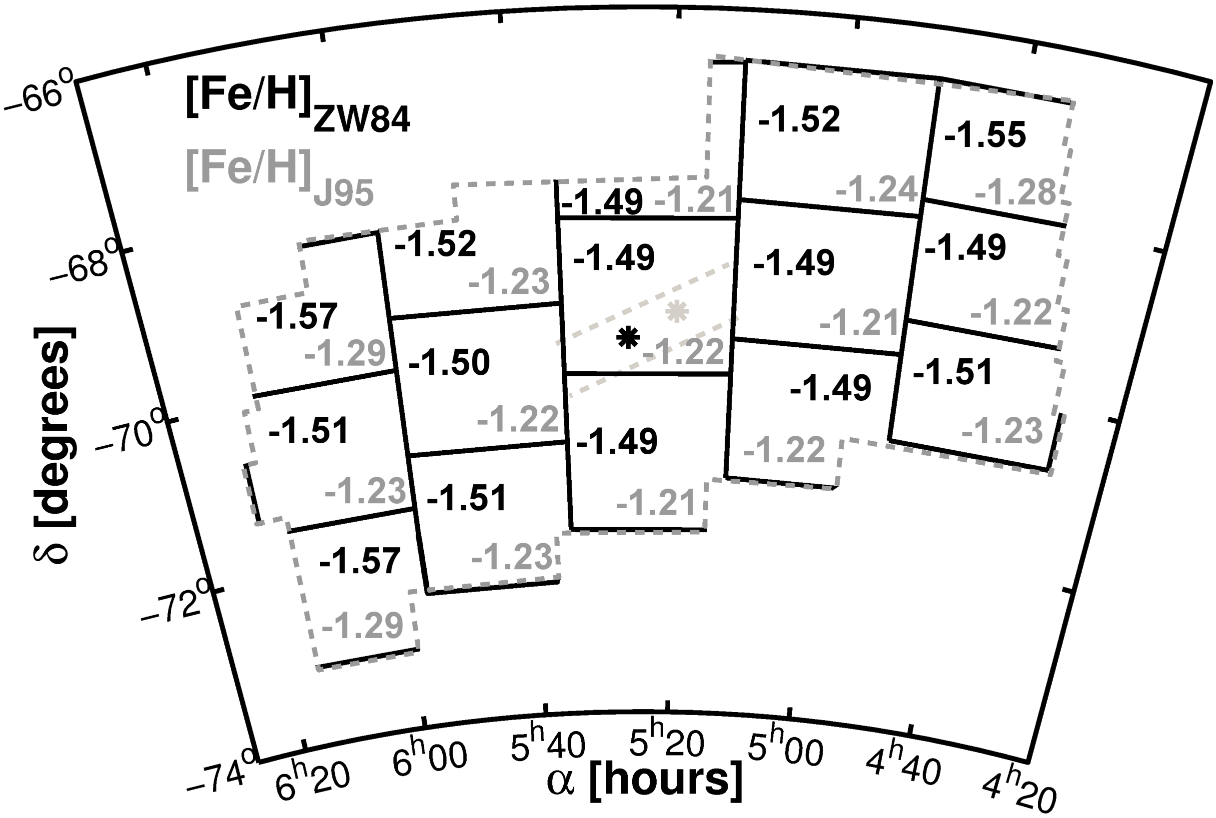

Figure 3.5: The variance of metallicity between the inner- and outermost fields is tested by dividing the LMC field into 15 similarly sized fields. The mean metallicity values on the ZW84-scale are shown in black, grey values represent the scale of J95. We see a small decline of the metallicities in the outermost regions sampled by OGLE III. The boundaries of the bar are illustrated with the dashed grey lines, while the black asterisk marks the center as found by RR Lyrae stars and the grey asterisk the optical center of the LMC.

Table 3.2: Differences between metallicity estimates by FAW10 and by us for different ranges of metallicity. The first column gives the metallicity scale we adopt, the second column the equation used by FAW10 in order to derive the metallicity, the third column the metallicity range used for the comparison is shown, and the fourth column shows the difference found by calculating Δ_{HF} = $[\mathrm{Fe/H}]_{\mathrm{HGDJ11}} - [\mathrm{Fe/H}]_{\mathrm{FAW10}}$.

$[\mathrm{Fe/H}]_{\mathrm{HGDJ11}}$ scale	$[\mathrm{Fe/H}]_{\mathrm{FAW10}}$ equation	$[\mathrm{Fe/H}]_{\mathrm{J95}}$ range	Δ_{HF}
J95	$[\mathrm{Fe/H}] = -5.62 \log P - 2.81$	$-2.00 < [\mathrm{Fe/H}] < +0.20$	0.17
J95	$[\mathrm{Fe/H}] = -7.82 \log P - 3.43$	$-2.00 < [\mathrm{Fe/H}] < +0.20$	0.25
ZW84	$[\mathrm{Fe/H}] = -5.62 \log P - 2.81$	$-2.00 < [\mathrm{Fe/H}] < +0.20$	−0.11
ZW84	$[\mathrm{Fe/H}] = -7.82 \log P - 3.43$	$-2.00 < [\mathrm{Fe/H}] < +0.20$	−0.03
ZW84	$[\mathrm{Fe/H}] = -7.82 \log P - 3.43$	$-1.23 < [\mathrm{Fe/H}] < +0.20$	0.23
ZW84	$[\mathrm{Fe/H}] = -7.82 \log P - 3.43$	$-2.00 < [\mathrm{Fe/H}] < -1.23$	−0.18
ZW84	$[\mathrm{Fe/H}] = -7.82 \log P - 3.43$	$-0.50 < [\mathrm{Fe/H}] < +0.00$	0.52
ZW84	$[\mathrm{Fe/H}] = -7.82 \log P - 3.43$	$-1.00 < [\mathrm{Fe/H}] < -0.50$	0.41
ZW84	$[\mathrm{Fe/H}] = -7.82 \log P - 3.43$	$-1.50 < [\mathrm{Fe/H}] < -1.00$	−0.05
ZW84	$[\mathrm{Fe/H}] = -7.82 \log P - 3.43$	$-2.00 < [\mathrm{Fe/H}] < -1.50$	−0.17

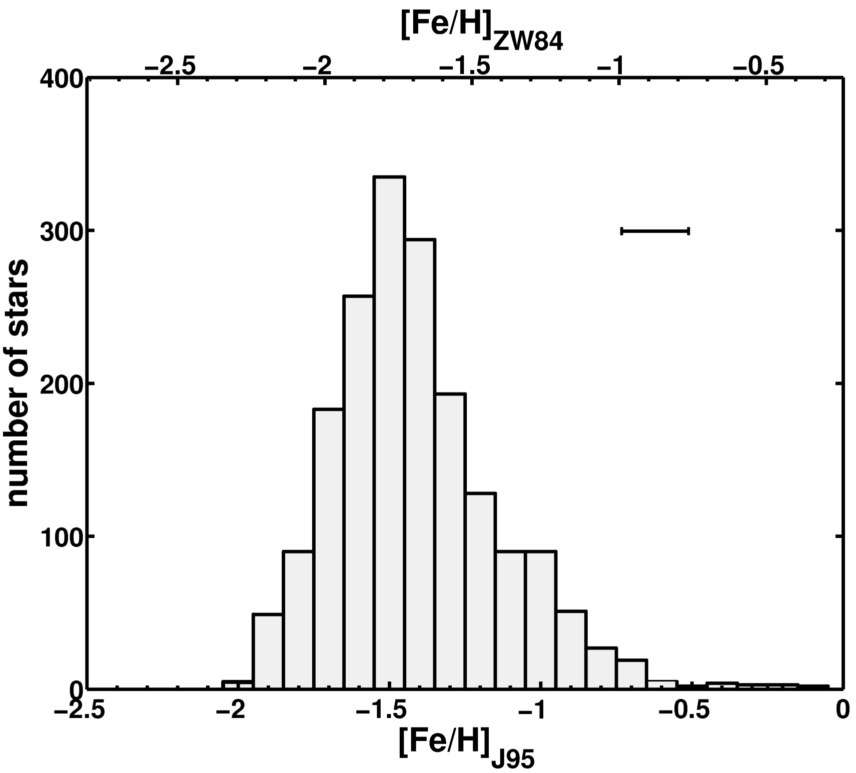

Figure 3.6: The metallicity distribution for the old population of the SMC. For 1864 RR Lyrae stars [Fe/H] is determined and a mean metallicity of $[Fe/H]_{mean} = -1.42$ dex on the scale of J95 is obtained (bottom axis), while on the scale of ZW84 we find $[Fe/H]_{mean} = -1.70$ dex (top axis). The standard deviation of the distribution is 0.33 dex. The error bar represents the typical uncertainty of the metallicities for individual stars.

stars of the innermost 6 kpc of the LMC. This result is in very good agreement with the gradient found in our study. Our error estimate is a bit more conservative, as we take the intrinsic uncertainties of the metallicity into account. Within the errors, we are not able to distinguish between no gradient and a very small gradient.

The result of essentially no metallicity gradient confirms the findings of Grocholski et al. (2006); Cole et al. (2009) and Sharma et al. (2010), who used either star clusters with ages between 1 and 10 Gyr or red giants to determine the metallicity gradient of the LMC. A small gradient of -0.047 ± 0.003 dex kpc^{-1} was obtained by Cioni (2009) using AGB stars, which span an age range of 3 – 10 Gyr. Based on spectroscopy of red giants, Carrera et al. (2011) find that the metallicity of these stars in the inner 6 kpc of the LMC is roughly constant, but then decreases with increasing radii. This result is supported by our findings with the (on-average) older RR Lyrae stars.

3.4 Metallicities of the SMC

In the SMC, Fourier parameters were determined for 1864 RR Lyrae stars of type ab by the OGLE III collaboration (Soszyński et al. 2010a). The resulting metallicity distribution is shown in Figure 3.6.

Following the same maximum-likelihood approach as described for the LMC RR Lyrae, we find the underlying MDF of SMC RR Lyrae to have a mean value of $[Fe/H] = -1.42$ dex on the scale of J95 with a standard deviation of 0.27 dex as shown in Figure 3.7. As explained in Section 3.2, we choose the metallicity regime between $-2.0 < [Fe/H] < +0.2$ on the scale of J95 as the reliable domain of the

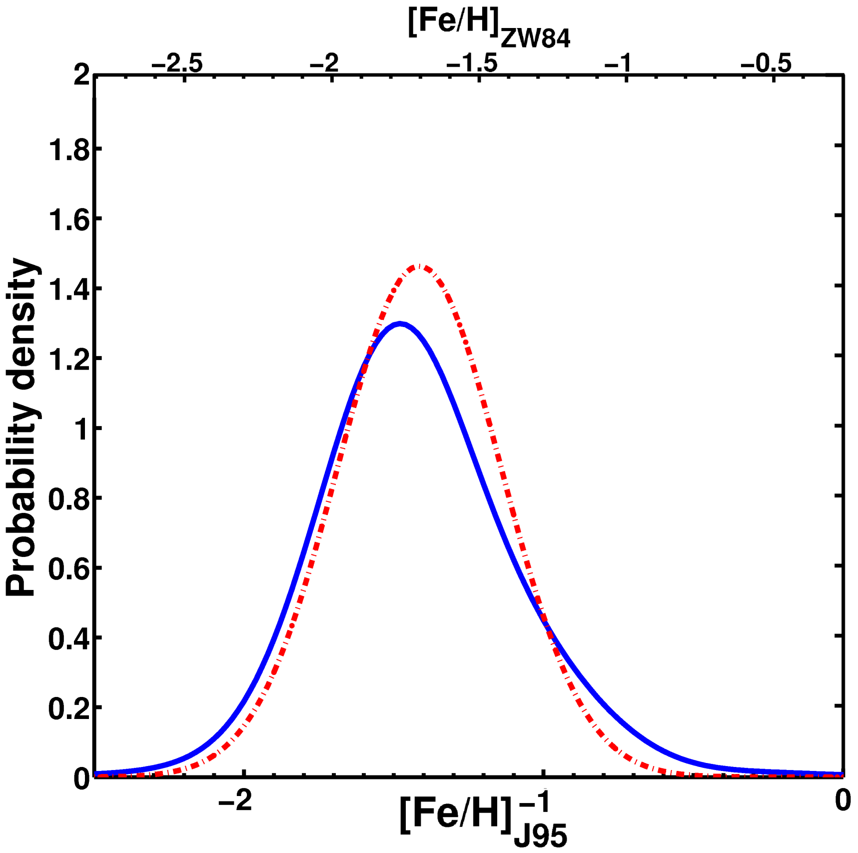

Figure 3.7: Metallicity probability distribution functions for the SMC. The solid blue curve represents the measured metallicities convolved with Gaussian uncertainties. A likelihood distribution is determined from the solid curve and given by the red dash-dotted line. We use 1831 RR Lyrae stars and find a mean metallicity of $[Fe/H]_{\rm mean} = -1.42$ dex on the scale by J95 (bottom axis). $[Fe/H]_{\rm mean} = -1.70$ dex is obtained for the scale of ZW84 (top axis). The intrinsic spread of the distribution is 0.27 dex.

calibration by Smolec (2005). All values outside of this calibration range are rejected. 27 stars with metallicities below $[Fe/H] = -2.0$ dex are found, while the lowest value is measured to be $[Fe/H]_{min} = -3.3$ dex. Only 6 RR Lyrae with metallicities above $[Fe/H] = +0.2$ dex are present and a maximum of $[Fe/H]_{max} = 1.7$ dex is found. Eliminating these stars, which are randomly distributed in space, leaves us with a sample of 1831 RR Lyrae stars with presumably reliable metallicities.

The resulting mean metallicity of the old population of the SMC is $[Fe/H]_{\rm mean} = -1.42$ dex on the scale of J95 and $[Fe/H]_{\rm mean} = -1.70$ dex on the ZW84 metallicity scale. So far no spectroscopic measurements of RR Lyrae field stars have been published. We therefore compare our result with the metallicity of NGC 121, the only GC of the SMC in the age range bracketed by our RR Lyrae stars. Glatt et al. (2008b) found an age of 10.5 Gyr for NGC 121 using main-sequence fitting with Dartmouth (Dotter et al. 2007) isochrones. Da Costa & Hatzidimitriou (1998) used the Ca II triplet to determine the mean metallicity of NGC 121 and found $[Fe/H] = -1.46 \pm 0.10$ on the scale of ZW84, in very good agreement with the results we obtain for the old population of the SMC.

Recently Kapakos et al. (2011) used a sample of 100 RR Lyrae stars from the OGLE III catalogue to determine photometric metallicities using the relation by Jurcsik & Kovács (1996). They decomposed the *V* band light curves to determine the Fourier parameters of each star. On the metallicity scale of J95 they found a mean metallicity of $[Fe/H]_{\rm mean} = -1.51 \pm 0.41$ dex. This is again in very good agreement with the metallicities found with our sample.

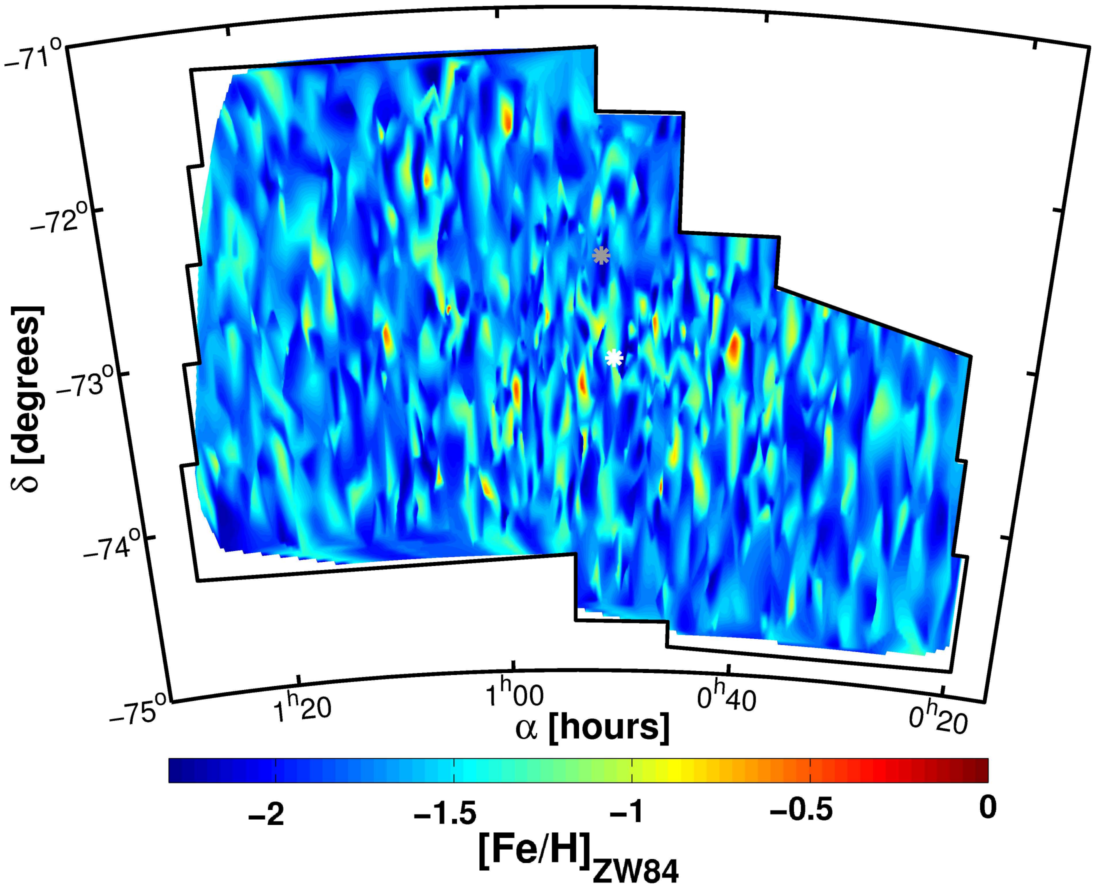

Figure 3.8: Distribution of metallicity in the SMC. Metal-poor regions are coded in blue, metal-rich regions are red. Overall the contour plot is smooth and no gradient or distinct feature is visible. For the contour plot only stars with $-2.0 < [\mathrm{Fe/H}] < +0.2$ are taken into account. The white asterisk represents the center found by G09, the grey asterisk the center of Piatek et al. (2008).

We use our metallicity estimates on the scale of J95 for the individual RR Lyrae stars to plot a contour map of the metallicity distribution of the old population (Figure 3.8). The overall distribution of the metallicity is quite smooth and no distinct features are visible. The black lines indicate the borders of the OGLE III field. In the white regions within this polygon no RR Lyrae stars were detected and therefore no contours are drawn.

The metallicity gradient is measured with respect to the center of the SMC determined by K-, M- and faint carbon stars ($\alpha = 0^h51^m$ and $\delta = -73°7'$, G09) This center is indicated in Figure 3.8 with a white asterisk. The spatial density distribution of RR Lyrae stars is bimodal (Chapter 5) and the determination of a single center is therefore rather difficult. We have chosen to adopt the values by G09, because they represent the mean center of the RR Lyrae distribution quite well. The stellar density is evaluated in boxes of 0.1 dex with a changing radius to keep the total area of each annulus constant. The resulting contours are smoothed with a Gaussian kernel and shown in Figure 3.9.

In order to investigate the presence of a gradient we fit a first-order polynomial to the running median of the SMC. We find a gradient of 0.00 ± 0.06 dex kpc^{-1}. We subdivide the OGLE III field of the SMC into 9 fields of similar area and determine the mean metallicity in each (Figure 3.10). We note that the mean is very similar to the median value. The metallicity stays basically constant, as expected from the essentially zero gradient.

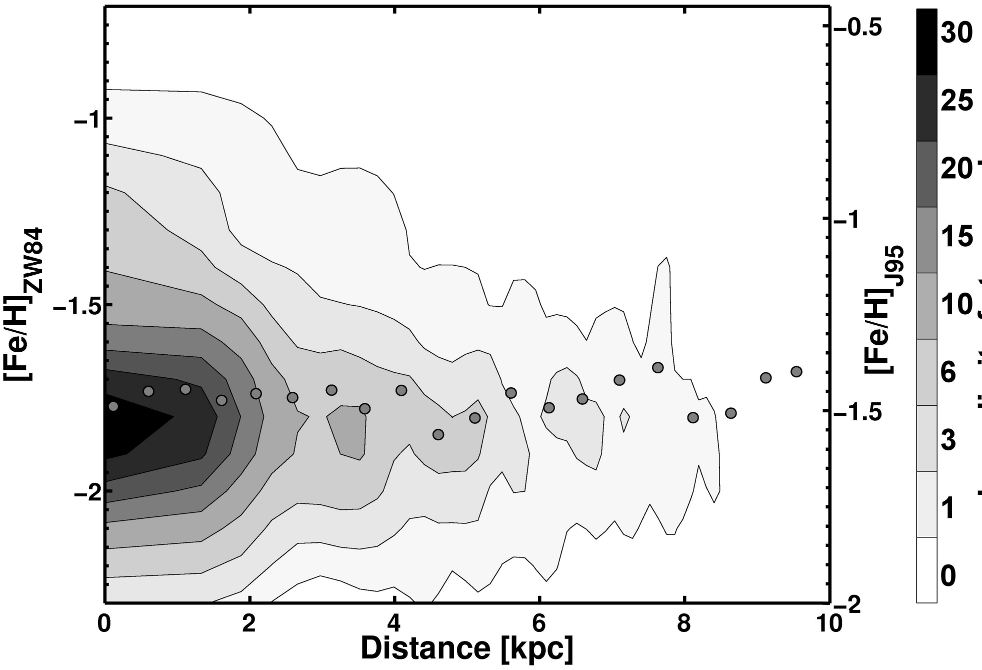

Figure 3.9: The total number of stars in boxes of metallicity versus the projected distance from the center as determined by G09 (white star in Figure 3.8). The grey dots represent the median metallicity of small distance bins of 0.5 kpc. Within the uncertainties no radial gradient of the metallicity is found.

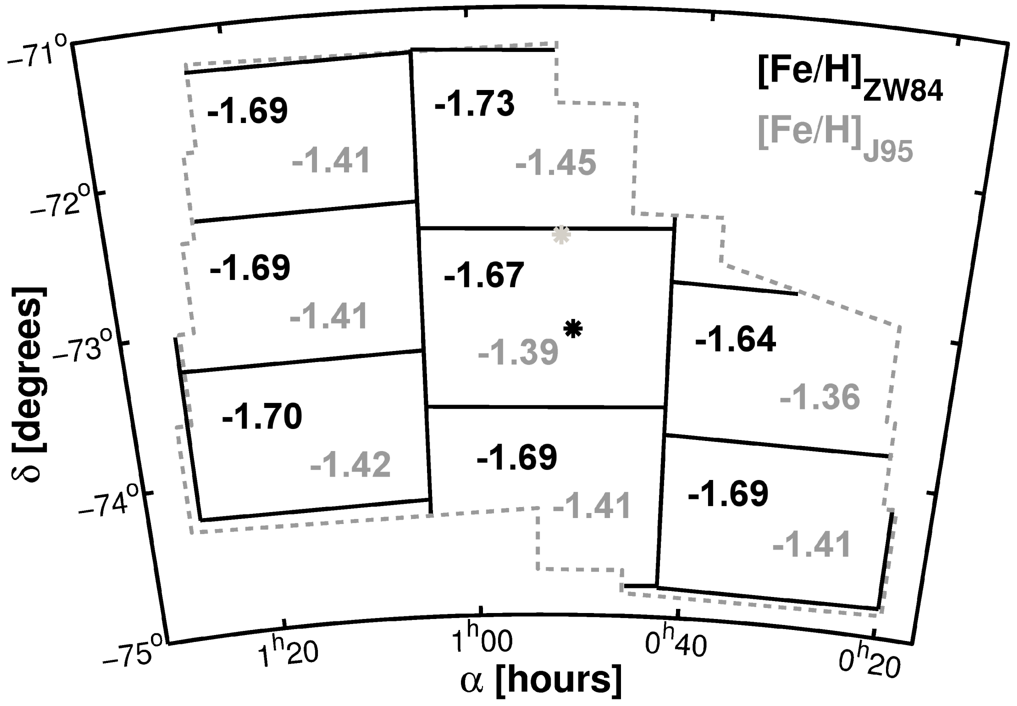

Figure 3.10: The SMC field is divided into nine similarly sized fields and the mean metallicity for each field is obtained. The mean values on the J95 and ZW84 scales are shown in grey and black, respectively. The values of the different fields are very similar to each other. The black and grey asterisk indicates the center of the SMC as found by G09 and Piatek et al. (2008), respectively.

Piatek et al. (2008) used HST proper motion data to determine the kinematical center of the SMC. They found $\alpha = 0^h52^m8^s$ and $\delta = -72°30'$, which is shown by the grey star in Figure 3.8. We do not find pronounced radial trends in the metallicity when using this center of the SMC either.

Metallicity gradients of the SMC have been studied using star clusters and red giants. Da Costa & Hatzidimitriou (1998) used spectroscopic measurements of giants and star clusters to search for a possible metallicity gradient and did not find any evidence. Glatt et al. (2008a) studied six intermediate age clusters and found a spread of 0.6 dex between the most metal-poor and most metal-rich clusters. The spectroscopic metallicity estimates lead to the conclusion that no smooth, monotonic age metallicity relation is present, but that instead there is a spread in metallicity at any given age (Kayser et al. 2007; Glatt et al. 2008a). Using spectroscopic data of red giants Parisi et al. (2009) did not find a gradient, while Carrera et al. (2008a) suggest that one exists using a different sample of spectroscopic observations of red giant field stars. Carrera et al. (2008a) argue that this gradient is the result of different ages of the red giants at different locations of the SMC. They conclude that further star formation has taken place in the inner parts and led to the metallicity gradient among these intermediate-age stars with ages between 3 and 10 Gyr. However this would not have affected our old RR Lyrae stars.

3.5 Comparison of spectroscopic and photometric metallicities

For some RR Lyrae stars located in the bar of the LMC, spectroscopic metallicities were determined in earlier studies. 149 LMC RR Lyrae with spectroscopic metallicities from Gratton et al. (2004) and Borissova et al. (2004, 2006) also have OGLE light curves and are thus part of our sample. Figure 3.11 shows the photometric metallicities we determine with the Fourier decomposition method versus the difference of photometric minus spectroscopic metallicities from the literature.

The spectroscopic measurements of Borissova et al. (2004) are based on the method of Layden (1994), who used the comparison of the equivalent width of Ca II K line with hydrogen lines. The resulting metallicity is on the scale of ZW84. Borissova et al. (2006) and Gratton et al. (2004) used the method of line indices (Preston 1959) as outlined in Gratton et al. (2004). This method is linked to the metallicity scale of Harris (1996), which has a very small offset of +0.02 ± 0.01 dex compared to ZW84 (Gratton et al. 2004). Due to the nearly negligible offset we do not adjust the metallicity values when applying the comparison to the photometric metallicities.

In Figure 3.11 we see that there appears to be a systematic trend in the deviation between spectroscopic and photometric measurements such that for low metallicities (lower than ~ -1.8 dex on the ZW84 scale) the spectroscopic metallicities are typically higher, while for photometric metallicities higher than ~ -1.3 dex the spectroscopic values are on average increasingly lower. These trends are fitted with linear polynomials (Figure 3.11 and Table 3.3). The median deviation, when subtracting the spectroscopic metallicity from the photometric metallicity, is +0.05 dex, while we find a standard deviation of 0.35 dex. However, the spectroscopic values in the three studies cited above show very different characteristics, as presented in Table 3.3. For the 58 RR Lyrae from the sample by Gratton et al. (2004) and the 28 stars in common with Borissova et al. (2004) we find a median deviation of 0.01 dex and −0.05 dex with a standard deviation of 0.25 dex and 0.49 dex, respectively, whereas we find a median difference of 0.15 dex and a standard deviation of 0.35 dex for the 66 RR Lyrae taken from Borissova et al. (2006). They quote an uncertainty range of 0.20 dex for their spectroscopic metallicities.

In Kunder & Chaboyer (2008) the same spectroscopic metallicities as used here are compared with the photometric data of the V band lightcurves of the LMC RR Lyrae stars from the MACHO survey. They do not find any evidence for a systematic discrepancy between the spectroscopic values and the photometric metallicities calculated with the relation by Jurcsik & Kovács (1996, our Equation 3.5). This leads to the conclusion that the systematic difference in our study is introduced by using the relation by Smolec (2005). However, most of the stars are located in the photometric metallicity regime where

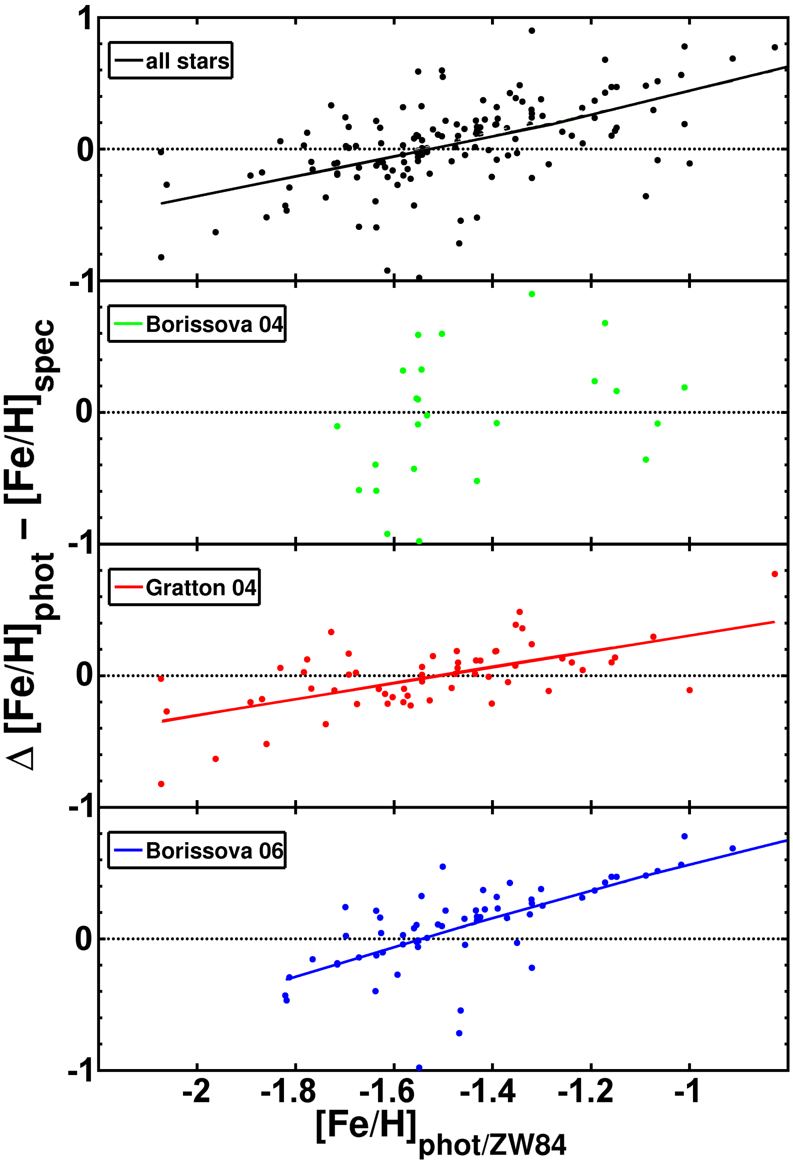

Figure 3.11: Comparison of our photometric metallicities with spectroscopic metallicities from the literature for LMC RR Lyrae stars. All metallicities are on the ZW84 scale. Calculating Δ[Fe/H] = $[\mathrm{Fe/H}]_{phot} - [\mathrm{Fe/H}]_{spec}$ we find a median difference of 0.05 dex for stars with photometric metallicities and their counterparts in the samples of Gratton et al. (2004) and Borissova et al. (2004, 2006). The trends in each sample, except for Borissova et al. (2004), are fitted with a linear polynomial.

Table 3.3: Differences between the photometric and spectroscopic metallicities for a sample of 149 RR Lyrae stars. We calculate the mean, median and standard deviation for the whole set of stars and for every study. To test for systematics we fit the distribution with a linear least-square fit.

	all stars	Gratton et al. (2004)	Borissova et al. (2004)	Borissova et al. (2006)
mean	0.037	−0.008	−0.041	0.108
median	0.051	0.011	−0.052	0.145
std	0.346	0.254	0.492	0.347
fit	0.8160[Fe/H]	0.6181[Fe/H]	—	1.0272[Fe/H]
	+1.2427	+0.9388	—	+1.5884

Table 3.4: Parameters to transform the Fourier coefficient ϕ_{31} from the I band to the V band.

$\phi_{31}^{V} = \alpha + \beta\phi_{31}^{I}$	α	β
DF99	−0.039	0.788
DS10	0.436	0.568

the differences to the spectroscopic measurements are quite small.

We also searched the spectroscopically studied, presumably old, star clusters of Colucci et al. (2011); Grocholski et al. (2006) and Mucciarelli et al. (2010) for RR Lyrae stars detected by OGLE. We do not find any coincidences of RR Lyrae stars in our sample within the clusters' diameter.

3.6 Metallicities from transformed ϕ_{31} values

Jurcsik & Kovács (1996) used V band light curves to determine a relation between ϕ_{31} and metallicity. Dorfi & Feuchtinger (1999, from now on DF99) and DS10 established two independent linear relations of the form $\phi_{k1}^{V} = \alpha + \beta\phi_{k1}^{I}$ to transform the I band Fourier parameters to V band values. The values for α and β shown in Table 3.4 are taken from Table 3 of DS10.

DS10 used the observed light curves of the RR Lyrae stars of two GCs, with metallicities of −2.16 dex (M68, Lee et al. 2005) and −1.39 dex (M3, Cohen & Meléndez 2005), to calculate Fourier parameters. With these data they obtained values for α and β that are significantly different from DF99, who used Fourier-decomposed theoretical light curve models of RR Lyrae stars to determine the relation. These models were matched with observational data from three GCs with metallicities of -2.16 ± 0.02 dex (M68, Lee et al. 2005), -1.52 ± 0.12 dex (IC4499, Hankey & Cole 2011) and -1.18 ± 0.02 dex (NGC1851, Carretta et al. 2010).

We transform the Fourier parameters provided by OGLE using the relations listed in Table 3.4. The recalculated values of ϕ_{31}^{V} are inserted into the formula determined by Jurcsik & Kovács (1996):

$$[\mathrm{Fe/H}] = -5.038 - 5.394P + 1.345\phi_{31}^{V} \tag{3.5}$$

to redetermine the MDF of the MCs. All metallicities presented in this section are on the J95 scale. Owing to the very small number of calibration clusters and the narrow metallicity range of DF99 and DS10, we use this relation with a note of caution outside the metallicity regime defined by the GCs.

3.6.1 LMC

The relation by DF99 leads to a very different metallicity distribution (upper panel in Figure 3.12) than obtained in Figure 3.1. The resulting metallicity distribution is much broader with a standard deviation of 0.38 dex, while the mean metallicity of $[\mathrm{Fe/H}]_{\mathrm{mean/DF99}} = -1.20 \pm 0.38$ dex is very similar to the value obtained with the Smolec (2005) relation.

Using coefficients from DS10 to calculate metallicities of all RR Lyrae stars results in a metallicity distribution (lower panel in Figure 3.12) similar in shape to that shown in Figure 3.1. The mean metallicity is comparable within the errors. With $[\mathrm{Fe/H}]_{\mathrm{mean/DS10}} = -1.33 \pm 0.29$ dex, we find a metallicity that is about 0.1 dex lower than from the Smolec (2005) method. For this distribution a standard deviation of 0.29 dex is obtained assuming a Gaussian distribution.

3.6.2 SMC

Using the DF99 relation, the mean metallicity, on the J95 scale, is $[\mathrm{Fe/H}]_{\mathrm{mean/DF99}} = -1.43$ dex with a standard deviation of 0.40 dex. As with the LMC, the shape of the SMC metallicity distribution is much

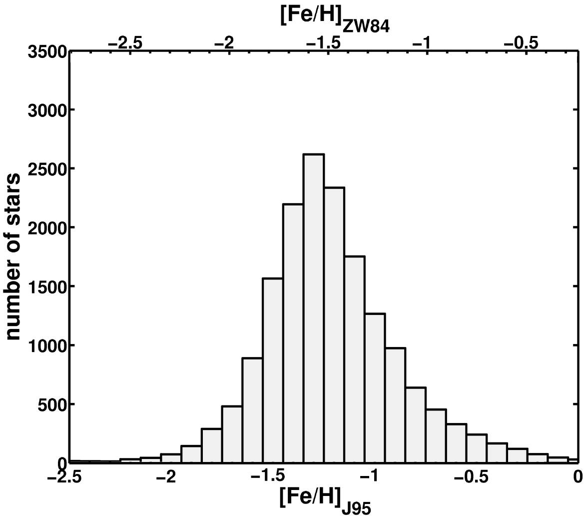

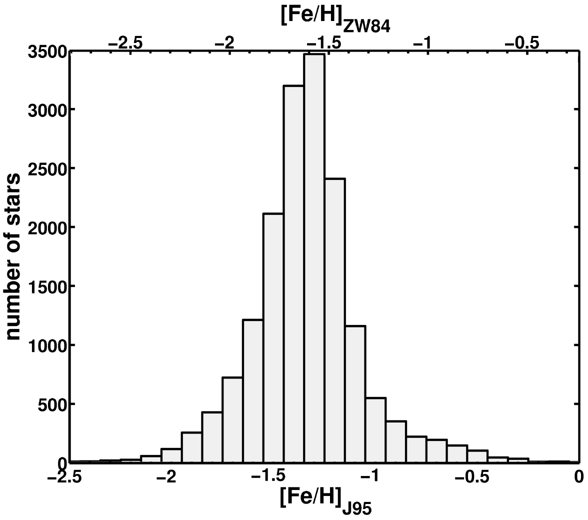

Figure 3.12: The upper panel shows the histogram of the LMC metallicity distribution obtained using the conversion of ϕ^I_{31} to ϕ^V_{31} by DF99, while the lower panel is obtained with the relation of DS10.

flatter and wider than with the relation by Smolec (2005), while the mean metallicity is very similar (upper panel of Figure 3.13).

The relation of DS10 reveals a similar shape of the metallicity distribution compared with that based on the relation by Smolec (2005). However, the metallicity is about 0.1 dex lower with $[Fe/H]_{mean/DS10} = -1.53$ dex, while the standard deviation is 0.32 dex. These results are shown in the lower panel of Figure 3.13 and are analogous to the outcome for the LMC.

Overall, 72% of the SMC metallicities determined with the relation by DS10 and 21% of the metallicities from the relation by DF99 lie outside of the metallicity range defined by the calibrating clusters used to derive the relations. The relation by Smolec (2005) has not been calibrated for such low metallicities as the ones we find for some of our RR Lyrae stars, but includes a wider metallicity range. Especially in the metallicity interval of $-1.71\,\text{dex} < [Fe/H]_{J95} < -1.30\,\text{dex}$, where most of the RR Lyrae stars are located in our sample, Smolec (2005) has a good coverage with 13 stars, thus justifying our use of Smolec (2005) relation as opposed to the other relations described here.

3.7 Conclusions

We derive photometric metallicities for 16949 RR Lyrae stars in the observed OGLE III field of the LMC using the Fourier decomposition of the light curves (Jurcsik & Kovács 1996). On the J95 metallicity scale we find a mean metallicity of $[Fe/H]_{mean} = -1.23$ dex. This corresponds to a metallicity of $[Fe/H]_{mean} = -1.50$ dex on the ZW84 scale, which is in excellent agreement with the spectroscopic measurements of LMC RR Lyrae stars in the literature (Borissova et al. 2004, 2006; Gratton et al. 2004). Our results are also in excellent agreement with those of Smolec (2005). The mean metallicity of his dataset, which is divided into Blazhko and non-Blazhko RR Lyrae stars, is $[Fe/H]_{mean} = -1.23$ dex. The difference in the mean metallicities between the two types ($\Delta[Fe/H] = 0.06$ dex) is much smaller than the uncertainties associated with our method. We conclude that we would not detect a significant difference between the two types of RR Lyrae stars and therefore treat the stars independently of their type. Although star-to-star fluctuations in metallicity are observed on small scales, we find no evidence for a spatial metallicity gradient in the LMC.

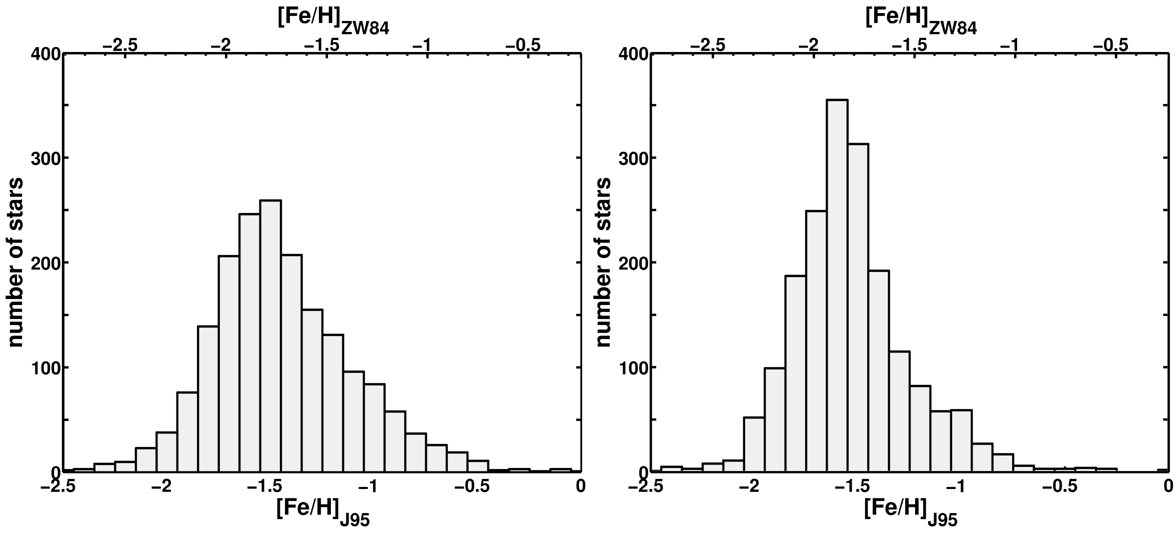

Figure 3.13: DF99 conversion of the Fourier parameter ϕ^I_{31} to ϕ^V_{31} is used in the upper panel to determine the metallicity of the SMC RR Lyrae stars. In the lower panel the relation by DS10 is applied to determine the metallicity distribution.

For the SMC we find a mean metallicity of $[\mathrm{Fe/H}]_{\mathrm{mean}} = -1.42$ dex on the J95 scale based on 1831 RR Lyrae stars of type ab. This translates to a value of $[\mathrm{Fe/H}]_{\mathrm{mean}} = -1.70$ dex on the scale of ZW84, and is in very good agreement with the spectroscopic determinations by Butler et al. (1982) and the photometric metallicities by Kapakos et al. (2011). No metallicity gradient is observed in the old population of the SMC.

In the LMC, several old GCs with ages greater than 10 Gyr are known. The metallicities of these clusters span at least one dex in [Fe/H] (e.g, Johnson et al. 2006; Mucciarelli et al. 2010). This is smaller than the range of metallicities observed for Galactic halo GCs, but well within the range of what we found for the RR Lyrae field stars, although most of the old LMC GCs with spectroscopic metallicity determinations are more metal-poor than the peak of our MDF of the RR Lyrae stars. In the SMC only one GC, NGC 121, is known (Glatt et al. 2008b), and has a metallicity of −1.46 ± 0.1 dex on the ZW84 scale (Da Costa & Hatzidimitriou 1998), well within the range of metallicities of SMC field RR Lyrae stars. The peak of our SMC RR Lyrae MDF is slightly more metal-poor than the metallicity of NGC 121. The SMC in fact shows a wide range of metallicities at any given age (e.g., Kayser et al. 2007; Glatt et al. 2008a).

Large metallicity spreads have also been found in most Local Group dSphs, usually exceeding one dex even when focusing on their old RGB populations (e.g., Grebel et al. 2003). For the old population of the LMC we find an intrinsic metallicity spread of $\sigma = 0.24$ dex (in terms of one standard deviation of the distribution), and $\sigma = 0.27$ dex for the SMC. The full range of metallicities of the RR Lyrae stars exceeds 1 dex in [Fe/H] and is difficult to constrain owing to the limits of the validity range of our calibration. As pointed out already, in neither of the two Clouds do we find a statistically significant trend in metallicity with position despite the spread.

While we cannot assign specific ages to our individual RR Lyrae stars, we suggest that this spread was caused by inhomogeneous, localized enrichment, which may happen on relatively short time scales as discussed by Marcolini et al. (2008). Detailed spectroscopic element abundance ratios measured for red giants in old LMC GCs indicate star formation from gas enriched by supernovae of Type II with prominent contributions from the r-process (Mucciarelli et al. 2010). The α enhancement is comparable to Galactic halo stars (and thus inconsistent with the $[\alpha/\mathrm{Fe}]$ ratios found in the old populations of many of the Galactic dSph and ultra-faint dSph stars; e.g., Koch et al. (2008a) and Adén et al. (2011). Johnson et al. (2006) find differences between LMC GC element abundance ratios both in comparison to dSphs and to Galactic GCs, emphasizing that the LMC experienced a different SFH than the Galactic old populations. No such detailed, age-dateable information is available for the SMC thus far.

If we qualitatively compare our RR Lyrae MDFs to MDFs derived spectroscopically for Galactic dSphs (see, e.g., Figure 13 in Koch et al. 2006; Figure 7 in Koch et al. 2007a; Figure 12 in Koch et al. 2007b, and Figure 1 in Kirby et al. 2011) we find that the MDFs of the Clouds do not show the steep drop-off at the metal-rich end found in some dSphs. In the chemical evolution models for dSphs of Lanfranchi & Matteucci (2004), such a steep decline is caused by gas outflows, which then do not seem to have played a defining role in the evolution of the old population of the MCs. This may not be surprising given the presumably much deeper potential wells of the Clouds. The shape of the MDFs of the MCs' old populations nevertheless resembles the shape of the MDFs of several Galactic dSphs that, according to Kirby et al. (2011), agree well with the gas-infall models of Lynden-Bell (1975) and Pagel (1997), suggesting gas accretion from the intergalactic medium at early times. Note that since many of the Galactic dSphs contain predominantly old populations, we are comparing stars formed during similar epochs here.

Although the MDFs of the RR Lyrae stars in the MCs reveal a considerable metallicity spread, we do not see evidence for a large population of stars with [Fe/H] < -2 dex. We caution that the calibration of the Fourier decomposition method does not extend to low metallicities and that it has been suggested that this method overestimates metallicities at low [Fe/H] values (Dékány & Kovács 2009, but see also Arellano Ferro et al. 2011). Additionally the number of RR Lyrae stars with low metallicities could be influenced by the shift of the instability strip to lower temperatures with lower metallicities. This could result in fewer horizontal branch stars experiencing the RR Lyrae phase (Yoon & Lee 2002). However, very metal poor GCs (e.g. NGC 2419 and NGC 7078) also contain a considerable fraction of RR Lyrae stars (Catelan 2009). On the other hand, there are a number of metal-poor GCs both in the MW and in the LMC that are dominated by blue horizontal branch morphologies and that essentially do not contain any RR Lyrae stars (Catelan 2009). Hence it is conceivable that the apparent lack of metal-poor RR Lyrae stars is also caused by this evolutionary effect. Nonetheless, the apparent absence of a substantial, very metal-poor old population suggests that the early enrichment in the MCs proceeded rapidly and efficiently. The MCs show a similar lack of metal-deficient stars as the Galactic dSphs and the Galactic halo (also known as the "G dwarf problem"), suggesting that the majority of the old stars formed from pre-enriched gas. Spectroscopic studies of our RR Lyrae metal-poor candidates would be desirable to confirm their metallicities.

The differences in the mean metallicities of the old populations in the LMC and SMC makes a common origin of these two galaxies from a single protogalactic fragment unlikely, unless such a putative progenitor would have been separated into two objects very early on. Recently, Yang & Hammer (2010) proposed that the LMC might have been ejected from M31 in a major merger event. The comparatively high metallicity of old GCs in M31 (Caldwell et al. 2011) as compared to the properties of the MDF of the old LMC population seems to argue against this scenario.

Dr. McCoy: "Please, Spock, do me a favor ... 'n' don't say it's 'fascinating'..."
Spock: "No... but it is... interesting..."

Star Trek (The Ultimate Computer)

4

Three dimensional maps of the Magellanic Clouds using RR Lyrae stars and Cepheids
I. The Large Magellanic Cloud

The new data for Cepheids and RR Lyrae stars of the Optical Gravitational Lensing Experiment (OGLE III) survey allow us to study the three-dimensional distribution of stars corresponding to young (a few tens to a few hundreds of millions of years) and old (typically older than ~ 9 Gyr) populations of the Large Magellanic Cloud traced by these variable stars. We estimate the distance to 16949 RR Lyrae stars by using their photometrically estimated metallicities. Furthermore the periods of 1849 Cepheids are used to determine their distances. Three-dimensional maps are obtained by using individual reddening estimates derived from the intrinsic color of these stars. The resulting median distances of the RR Lyrae stars and Cepheids appear to resolve the long and short distance scale problem for our sample. With median distances of 53.1 ± 3.2 kpc for the RR Lyrae stars and 53.9 ± 1.8 kpc for the Cepheids, these two distance indicators are in very good agreement with each other in contrast to a number of earlier studies. Individual reddening estimates allow us to resolve the distance discrepancies often observed while comparing Cepheids and RR Lyrae stars. For both stellar populations we find the inclination angle of the LMC to be 32 ± 4° and the mean position angle to be 115 ± 15°. The position angle increases with galactocentric radius, indicative of mild twisting. Within the innermost 7 degrees of the LMC covered by OGLE III the change in position angle amounts to more than 10 degrees. The depth of the RR Lyrae stars of 5.0 ± 0.2 kpc is higher than the depth of the much younger Cepheids (4.0 ± 0.2 kpc). In both populations the western parts of the LMC show significantly higher depth than the eastern parts. However, we interpret this as indicative of an old, thick-disk-like component and a young, thin-disk-like component in the LMC. In agreement with earlier studies we do not find evidence for an extended spherical stellar halo. The bar stands out as an overdensity both in RR Lyrae stars and in Cepheids. In RR Lyrae stars the bar can be traced as an overdensity with a line-of-sight depth of almost 5 kpc in front of the main body of the disk.

This chapter is based on Haschke, Grebel, & Duffau (submitted)

4.1 Introduction

The LMC is one of the closest and the largest satellites of the Galaxy with a heliocentric distance of $(m - M) = 18.50$ (~ 50 kpc) (Alves 2004; van der Marel 2006). Therefore, the LMC is used as benchmark for, e.g., cosmological distance measurements (e.g., Freedman et al. 2001) or the evolution of the Local Group (e.g., Besla et al. 2007; Bekki 2009b).

A large variety of methods and objects have been used to investigate the structure and evolution of the MCs. For instance, star clusters can be used to determine individual distances and the chemical footprint at distinct times in the galaxy's past (e.g., Kerber et al. 2007; Glatt et al. 2008b; Sharma et al. 2010). In Grocholski et al. (2007) the mean distance to a set of populous clusters in the LMC was measured to be $(m - M) = 18.40 \pm 0.12$.

To gain a more comprehensive picture of the evolution of a galaxy different classes of stars can be utilized to describe different evolutionary stages. The oldest stellar populations can be traced with RR Lyrae stars. These have a well defined metallicity-luminosity relation and therefore are valuable standard candles as long as the metallicity is known. For the LMC, RR Lyrae stars have been used in a variety of investigations. For example, Clementini et al. (2003) analyzed photometric and spectroscopic data for more than a hundred RR Lyrae stars in two fields close to the bar and found a mean distance modulus of $(m - M) = 18.45 \pm 0.07$. These values for the distance were confirmed by the photometric and spectroscopic results published in a series of papers by Borissova et al. (2004, 2006, 2009). With deep infrared observations Szewczyk et al. (2008) found a mean photometric distance of $(m - M) = 18.58 \pm 0.11$ for 65 RR Lyrae stars located in the LMC bar, 0.13 mag more distant than Clementini et al. (2003) although these distance moduli agree within the uncertainties.

Distance measurements of populations with an age of a few Gyr can be conducted by, e.g., using RC stars. Koerwer (2009) found a mean distance modulus of $(m - M) = 18.54 \pm 0.06$ based on measurements across the body of the LMC.

Cepheids are excellent distance tracers for the young stellar population, within an estimated age range of approximately 30 − 300 Myr (Grebel & Brandner 1998). Groenewegen & Oudmaijer (2000) found $(m - M) = 18.60 \pm 0.11$ using Hipparcos data of LMC Cepheids. With the same dataset but a different period-luminosity relation Luri et al. (1998) derived $(m - M) = 18.35 \pm 0.13$. Using a least square fitting method, Ngeow & Kanbur (2008) found a mean distance modulus of $(m - M) = 18.48 \pm 0.03$ for 630 Cepheids taken from the second phase of the OGLE survey (Udalski et al. 1992, 1999b).

The OGLE experiment looks for microlensing events in the Galactic center and the MCs. Therefore a considerable portion of the dense regions in these galaxies was monitored for years (Udalski et al. 1992, 1997, 2008a). The new OGLE III data release combine six years of observations with the largest field coverage in the MCs (~ 40 degrees) of the OGLE experiment obtained thus far.

The distance determinations for the LMC suffer from intrinsic differences between different standard candles. For instance, the calibrations tend to assign a larger distance to Cepheid measurements than to RR Lyrae stars. This is known as the "long and short distance scale problem" (e.g., Carretta et al. 2000b).

The orientation and three-dimensional shape of the LMC have been studied repeatedly. For red giants van der Marel (2001) found a position angle $\Theta = 122.5^\circ \pm 8.3^\circ$ in good agreement with Subramaniam & Subramanian (2009a), who analyzed RR Lyrae stars from the OGLE III dataset (Soszyński et al. 2009). Using the same data PS09 published a position angle consistent with the value published by Subramaniam (2004) of $\Theta = 114^\circ \pm 22^\circ$ for RC stars. In contrast to these determinations Nikolaev et al. (2004) found $\Theta = 154^\circ \pm 3^\circ$ with Cepheids from the MACHO survey. This is in agreement with the work of Koerwer (2009) using the RC of the LMC.

The distance measurements of the LMC suggest that the eastern parts are closer to the Sun than the western side. The deduced inclination angle varies between $i = 23.5^\circ \pm 0.4^\circ$ (Koerwer 2009) and $i = 34^\circ \pm 6^\circ$ (van der Marel & Cioni 2001). The studies by Lah et al. (2005), Nikolaev et al. (2004), and

Subramaniam & Subramanian (2009a) infer inclination angles within this range.

RC stars observed in OGLE III indicate a line of sight depth of 4 kpc for the LMC bar and 3.4 kpc for the disk (S09), in good agreement with Clementini et al. (2003) evaluating RR Lyrae stars.

Zhao & Evans (2000) found first evidence for a bar located in front of the LMC. These results were confirmed by Nikolaev et al. (2004) using Cepheids in the LMC. They showed that the bar is at least 0.5 kpc in front of the disk. Model fitting based on the data of the MCPS by Zaritsky (2004) obtained a similar result as Nikolaev et al. (2004). In contrast to these results Subramaniam & Subramanian (2009b) did not find evidence for a bar in front of the LMC investigating RC stars from the OGLE III data. Bekki (2009a) proposed the collision of a dark halo with the LMC as the origin for a bar located in front of the main body of the LMC.

We use the entire sample of OGLE RR Lyrae stars and Cepheids, covering a field much larger than in previous studies of these objects, to obtain three-dimensional maps of the old and young population of the LMC. This can ultimately also help us to understand the evolution of the LMC better. The distances are derived while taking into account star-by-star extinction corrections.

Distance estimations and reddening corrections are discussed in Section 4.2. We then first analyze the spatial distribution of our stars projected in two dimensions in Section 4.3, before using the metallicities of the individual RR Lyrae stars, determined in Chapter 3 to calculate the reddening-corrected distances in Section 4.4. In Section 4.5 structural characteristics such as the inclination, the position angle and the scale height of the LMC are presented. We summarize and discuss our results in Section 4.6.

4.2 Distance measurements

We use RR Lyrae stars and Cepheids to determine the distances of the old and the young population of the LMC, respectively. For the old population RR Lyrae stars, with their ages of at least 9 Gyr (e.g. Sarajedini et al. 2006) permit a glance into the early stages of the evolutionary history of a galaxy. A more recent period in the evolution of a galaxy can be traced by the fairly bright and variable Cepheids, which cover an age range of approximately 30 to 300 Myr (Grebel & Brandner 1998; Luck et al. 2003).

4.2.1 RR Lyrae

The absolute luminosity M_V of the RR Lyrae stars depends only on their metallicity. In Chapter 3 we present individual photometric metallicity estimates for 16949 RR Lyrae stars. These values, on the metallicity scale of ZW84, are applied together with the widely used relation by Clementini et al. (2003) to calculate absolute magnitudes for each single star

$$M_V = 0.84 + (0.217 \pm 0.047)\,[\mathrm{Fe/H}] \tag{4.1}$$

We tested various equations for the absolute magnitude of RR Lyrae stars, quadratic in their metallicity term, by Catelan et al. (2004) and by Sandage & Tammann (2006). The quadratic equations always lead to slightly higher absolute magnitudes than the relation by Clementini et al. (2003). For the relation by Catelan et al. (2004, their equation 8) a median difference of +0.08 mag is found, while the median difference for Sandage (2006, their equation 7) is below +0.01 mag. These differences are small and we decide to use the relation by Clementini et al. (2003).

The absolute magnitude together with the mean observed magnitudes and a reddening correction (see Section 4.2.3) leads to the true distance modulus of each star. This permits us to investigate the three-dimensional distribution of the old stellar population in the LMC.

4.2.2 Cepheids

Cepheids follow a well-known period-luminosity relation. We adopt the relations derived by Sandage et al. (2004). For LMC Cepheids these authors found that there are two different sets of relations depending on the length of the period. For periods *shorter* than 10 days they found

$$\mathrm{M}_V = -(2.963 \pm 0.056) \log \mathrm{P} - (1.335 \pm 0.036) \tag{4.2}$$

$$\mathrm{M}_I = -(3.099 \pm 0.038) \log \mathrm{P} - (1.846 \pm 0.024) \tag{4.3}$$

and for periods *longer* than 10 days

$$\mathrm{M}_V = -(2.567 \pm 0.102) \log \mathrm{P} - (1.634 \pm 0.135) \tag{4.4}$$

$$\mathrm{M}_I = -(2.822 \pm 0.084) \log \mathrm{P} - (2.084 \pm 0.111) \tag{4.5}$$

where P is the period of the Cepheid in days.

We apply the appropriate relations to all available Cepheids in the OGLE III archive and calculate the apparent distance modulus using the mean magnitudes provided by OGLE. In the next step, we correct these apparent distance moduli for extinction effects.

4.2.3 Reddening correction

In Chapter 2 we used two different methods to obtain reddening maps of the MCs. Both methods were applied to correct the distances, calculated above, for extinction effects.

Area-averaged reddening correction: The red clump method

RC stars of the LMC are utilized in Chapter 2 to calculate the reddening on scales of a few arcminutes. Depending on the metallicity, the RC is situated at a well-defined color in the color-magnitude diagram (Girardi & Salaris 2001). When the metallicity is known, the difference between the measured mean color of the RC and the theoretically predicted color provides the mean reddening toward this part on the sky (Wozniak & Stanek 1996).

In Chapter 2 we subdivide the OGLE III area into a grid of smaller fields each of which contains at least a few hundred RC stars of the OGLE III photometric atlas (Udalski et al. 2008a). The size of these squares is adjusted to the different RC star densities across the field covered by OGLE III and varies from 4.5×4.5 arcmin to 36×36 arcmin. For each square the mean color is computed and compared to the theoretically unreddened color. We adopt the value found by Olsen & Salyk (2002) for the unreddened color of the RC of the LMC. For each position of the 16949 RR Lyrae stars and 1849 Cepheids the appropriate reddening of its field is applied. Using the relations by SFD98 between total and selective extinction in different bands

$$\mathrm{A_V} = 3.24(E(V-I)/1.4) \tag{4.6}$$

$$\mathrm{A_I} = 1.96(E(V-I)/1.4) \tag{4.7}$$

we correct the distance modulus, determined above for every star, with the mean extinction at the location of the very star on the sky.

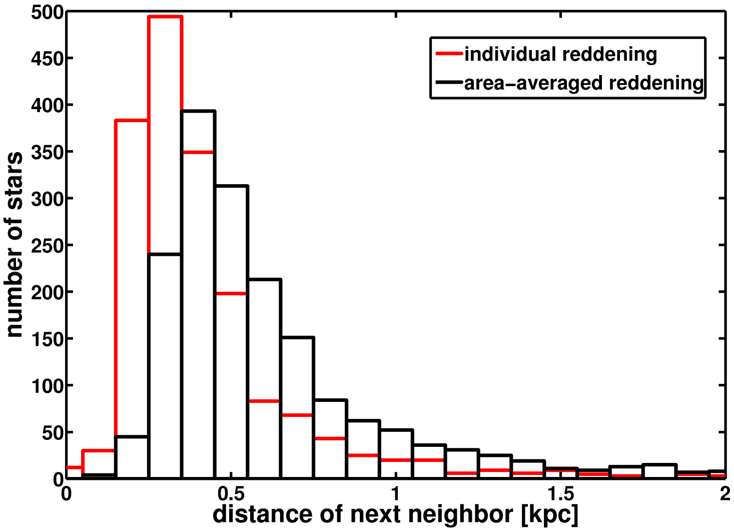

Figure 4.1: The distances to the next neighbors of each Cepheid are computed. We draw a histogram with the distance to the fifth nearest neighbor and find that the individually dereddend Cepheids have smaller mean distances. We conclude that the individual reddening is preferable.

Individual reddening corrections: Intrinsic colors of variable stars

RR Lyrae

Individual reddening estimates are calculated in Chapter 2, for each of the 12675 RR Lyrae stars with a mean magnitude in V and I band in the LMC OGLE III database. Differences between the color of the observed mean magnitudes and the theoretically determined absolute magnitudes are computed taking our photometric metallicities into account.

For the absolute magnitudes Chapter 2 uses the relations developed by Catelan et al. (2004). They are similar to Equation 4.1 by Clementini et al. (2003) but provide consistent relations for different bands. In Chapter 2, we derive the predicted absolute magnitude in the V and I bands and define an ’absolute color’ $(V-I)$. The observed apparent color $(v-i)$ of the RR Lyrae stars is calculated by subtracting the measured i band from v band mean magnitudes, provided by OGLE III. The difference $E(V-I) = (v-i) - (V-I)$ of these two colors provides the reddening.

We use the Equations 4.6 and 4.7 to calculate extinctions for 12675 RR Lyrae star and correct their apparent distance moduli accordingly.

Cepheids

The basic approach of individual reddening estimates is used also to calculate Cepheid reddenings. Equations 4.2, 4.3, 4.4, and 4.5 are used to calculate the “absolute color” $(V-I)$ for each Cepheid based on its period. With the mean magnitudes from the OGLE III catalog, the observed apparent color $(v-i)$ is computed. We then derive the reddening from the difference of the apparent and absolute colors and use it in order to calculate the absolute distance moduli of the 1849 Cepheids.

Test of individual reddening vs. area-averaged reddening

In star forming regions many stars are produced in a short amount of time and eventually a couple of them are in the Cepheid-phase at the same time. We expect that these Cepheids are still in close proximity to their place of birth. Therefore we expect the mean distance of the Cepheids to the next neighbors

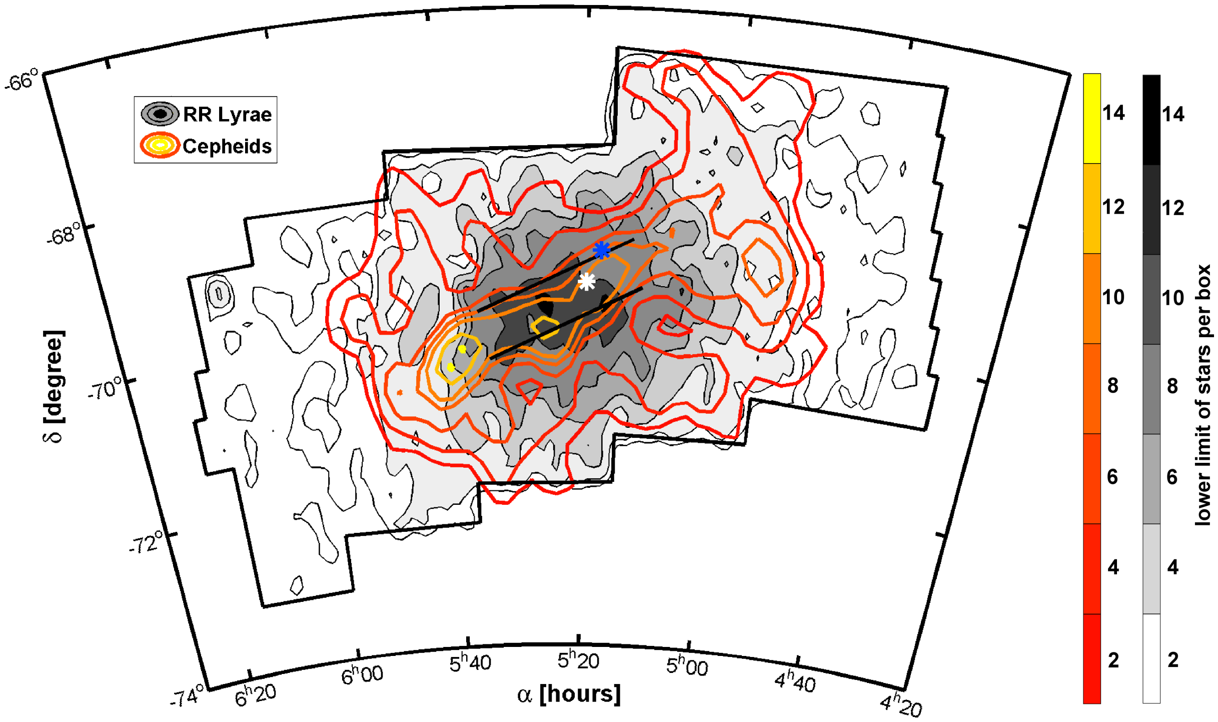

Figure 4.2: Densities of RR Lyrae stars (filled grey contours) and Cepheids (colored contours) are shown as a function of right ascension, α (J2000), and declination, δ (J2000). The highest densities of RR Lyrae stars are found in the bar region. Further away from the bar the RR Lyrae distribution becomes much more circular. The high density regions of the Cepheid distribution are prolate and trace the bar. The thick black polygon delineates the boundaries of the OGLE III region. The optical center of the LMC found by de Vaucouleurs & Freeman (1972) is marked with a white asterisk. The kinematical center from H I observations of Kim et al. (1998a) is marked by a blue asterisk. The box sizes of the evaluated fields are listed in Table 4.1.

to be small. On the sky we can directly observe this close proximity of stars and we expect a superior reddening method to reflect this by a smaller mean distance on the z-axis as well.

For each Cepheid we calculate the distances to all other Cepheids present in the sample. Then we determine the distance to the fifth and tenth closest neighbor of each Cepheid. We find that the individually dereddened Cepheids have smaller mean distances to their next neighbors than the Cepheids with an area-averaged dereddening. For the fifth nearest neighbor a median distances of 0.35 kpc and 0.52 kpc, respectively, for the two reddening approaches is found. The tenth nearest neighbor has a median distance of 0.50 kpc and 0.75 kpc, respectively.

The individual reddening clearly leads to smaller mean distances between the Cepheids and we therefore trust this method to be better than the area-averaged reddening estimates.

4.3 Star densities in the OGLE III field

The OGLE III data cover nearly 40 square degrees of the LMC. Figure 4.2 shows the distribution of the RR Lyrae stars and the Cepheids located in this field. The number of RR Lyrae stars is counted in fields of 0.25° × 0.125° in right ascension and declination, respectively. This leads to the center of the RR Lyrae distribution at $\alpha = 5^h26^m$ and $\delta = -69°75'$. Due to the much lower density of the Cepheids their distribution is evaluated in larger fields of 0.5° × 0.25° in right ascension and declination, respectively

Table 4.1: Binsizes of the fields evaluated to obtain the densities of RR Lyrae and Cepheid stars in the LMC. The grid of the boxes defined here is used in Figure 4.2,4.3, and 4.4 to show the distribution of young and old stars in the LMC.

	RR Lyrae	Cepheids
α bin [degree]	0.25	0.5
δ bin [degree]	0.125	0.25
distance bin [kpc]	0.25	0.5

(Table 4.1). We then smooth the resulting density distributions using a Gaussian kernel. To illustrate the location of the bar region we adopt its approximate location from Zhao & Evans (2000) (see the black diagonal lines in Figure 4.2.

For the RR Lyrae stars the highest density of stars is found along the bar. The highest density of RR Lyrae stars does not coincide with the kinematical or optical center of the LMC. With increasing distance from the bin of highest density and with decreasing density of stars the distribution becomes more ellipsoidal. Unfortunately the OGLE III data do not cover the low density outskirts of the LMC in the southern and northern directions.

For the Cepheids we find a different picture than for the old RR Lyrae population. The distribution of stars is elongated and the highest density of stars is again found along the bar region. The Cepheids show different locations of enhanced density. They are formed at various locations with varying intensities reflecting regions of enhanced star formation activity during the past 30 to 300 Myr (e.g., Grebel & Brandner 1998). Neither the RR Lyrae nor the Cepheid density maximum coincide with the optical center of the LMC found by de Vaucouleurs & Freeman (1972) or with the kinematical center found by Kim et al. (1998a) (see Figure 4.2).

Using data from the 2MASS (Skrutskie et al. 2006) and Deep Near-Infrared Southern Sky Survey (DENIS) (Epchtein et al. 1997) the distribution of RGB and AGB stars in the LMC was investigated by van der Marel (2001). Cioni et al. (2006) found average ages of 5-6 Gyr for the AGB stars, Salaris & Cassisi (2005) obtained average ages of about 4 Gyr for the RGB stars of the LMC. In Figure 2 of van der Marel (2001) the density distribution of these intermediate-age stars is shown. The bar region is clearly visible and has the highest stellar density. Toward the outskirts of the LMC the density distribution becomes first rounded, and then elongated in the north-south direction, approximately perpendicular to the bar. These outer parts of the density map are not covered by the OGLE III area and can therefore not be compared with the density distribution of Cepheids and RR Lyrae stars that we obtain in our present paper.

The distribution of RR Lyrae stars closely resembles that of the intermediate-age (AGB/RGB) star density distribution in the central region of the LMC while the Cepheid distribution shows more substructure. With decreasing age of the stellar population the high density regions become increasingly elongated along the LMC bar, extending further in eastern and western direction than the main body of the bar traced by the RR Lyrae stars.

4.4 Three dimensional maps

The distances of RR Lyrae and Cepheids are calculated with the equations described in Section 4.2. We obtain four sets of maps, two for each the young and the old stars when applying either average RC or individual reddening corrections.

Table 4.2: Recent distance estimates of the LMC using RR Lyrae stars or Cepheids. For results using other distance indicators such as eclipsing binaries, RC stars, SN light echos, star clusters, etc., see Alves (2004). In the last line the mean distance to the LMC found by Alves (2004) using many different indicators is stated.

type of indicator	$(m-M)_{mean}$	σ	reference
Cepheids	18.35	0.13	Luri et al. (1998)
Cepheids	18.60	0.11	Groenewegen & Oudmaijer (2000)
Cepheids	18.48	0.04	Ngeow & Kanbur (2008)
Cepheids	18.85	0.08	this work - area averaged reddening
Cepheids	18.65	0.07	this work - individual reddening
RR Lyrae	18.45	0.07	Clementini et al. (2003)
RR Lyrae	18.48	0.08	Borissova et al. (2004)
RR Lyrae	18.54	0.09	Marconi & Clementini (2005)
RR Lyrae	18.44	0.11	Catelan & Cortés (2008)
RR Lyrae	18.58	0.11	Szewczyk et al. (2008)
RR Lyrae	18.53	0.13	Borissova et al. (2009)
RR Lyrae	18.60	0.17	this work - area averaged reddening
RR Lyrae	18.62	0.13	this work - individual reddening
multiple indicator mean	18.50	0.04	Alves (2004)

4.4.1 Maps corrected with RC reddening

In this subsection we apply the reddening estimates derived with the RC method to correct the distances of the RR Lyrae stars and Cepheids obtained in Section 4.2.

In the upper panel of Figure 4.3 we plot the density distribution of RR Lyrae stars (grey contours) and Cepheids (colored contours) in right ascension versus distance. In the lower panel of Figure 4.3 these density distributions are plotted as a function of declination vs. distance. This implies a view from above the LMC in the upper panel and from the side in the lower panel. The field sizes within which the density of stars is evaluated are shown in Table 4.1. The contour plots are smoothed with a Gaussian kernel, which uses 3×3 bins and a width of 1 bin to reduce the variance on very small scales. For the uncertainties of the density contours we assume Poisson noise. The noise is usually smaller than the binsizes.

The spatial distribution of the RR Lyrae and Cepheids form distinct groups whose centroids do not coincide. Without correcting for the inclination, computing the median distance of the RR Lyrae stars leads to $D_{\mathrm{RRL/median}} = 52.7 \pm 3.9$ kpc ($(m-M)_0 = 18.60 \pm 0.17$). For the Cepheids we find a distance of $D_{\mathrm{Cep/median}} = 58.8 \pm 2.2$ kpc ($(m-M)_0 = 18.85 \pm 0.08$). By deprojecting the spherical coordinates into a cartesian coordinate system (Weinberg & Nikolaev 2001) the median distances change slightly to $D_{\mathrm{RRL/median}} = 54.4 \pm 3.9$ kpc and $D_{\mathrm{Cep/median}} = 58.6 \pm 2.2$ kpc. These values are very similar and we use the mean distances as measured without correcting for the inclination angle. The uncertainties are computed using error propagation adopting a mean magnitude error of 0.07 mag, as stated by the OGLE collaboration, the mean extinction uncertainty of 0.08 mag from Chapter 2 and a metallicity uncertainty for the RR Lyrae stars of 0.23 dex (Chapter 3). The uncertainty of the period is so small that it can be neglected. Taking the errors into account the resulting median distances of the old and young population agree within 2σ.

Our RR Lyrae distance is in agreement with the literature values, while the Cepheid distance differs by more than 3σ from the mean values of the literature (see Table 4.2).

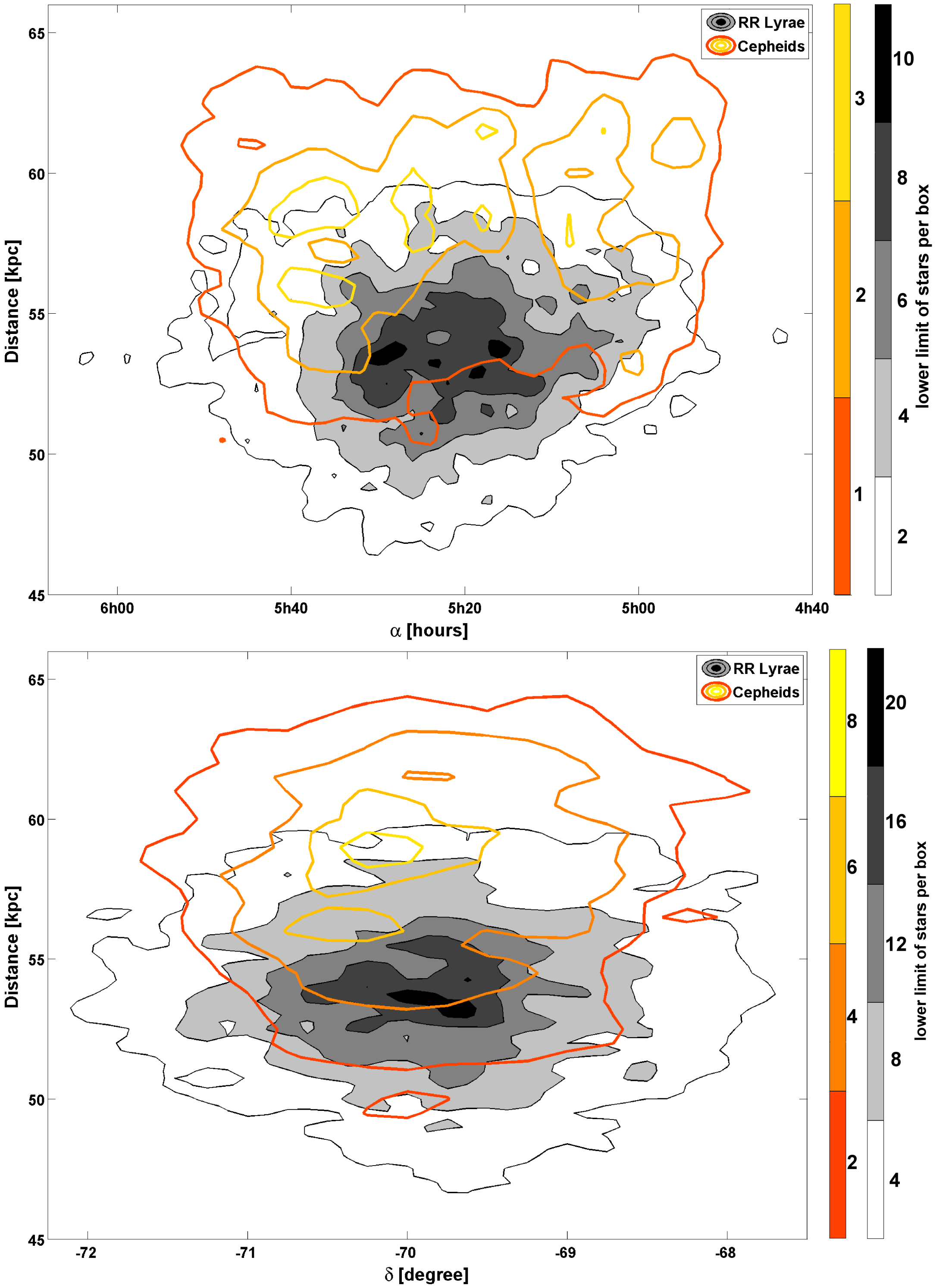

Figure 4.3: Stellar densities of RR Lyrae (filled grey contours) and Cepheids (colored contours) are shown as a function of distance and right ascension, in the upper panel, and as a function of distance and declination in the lower panel. All distances are extinction-corrected using the mean RC reddening values. The main concentration of the RR Lyrae is much closer and more centrally concentrated than that of the Cepheids. The box sizes of the evaluated fields are listed in Table 4.1.

4.4.2 Maps corrected with individual reddening

In the previous section we used reddening values based on the color of the RC (see Chapter 2 for details). Instead we can also compute the reddening for each of our Cepheid or RR Lyrae stars individually as described in Section 4.2.3, a more accurate method that does not average over an area and that does not use other stellar populations (RC stars) as tracers of the reddening of much younger or much older populations. For a more detailed discussion of population- or temperature-dependent reddening see Grebel & Roberts (1995) and Zaritsky (1999).

The resulting maps (Figure 4.4) show a reduced depth of the LMC as compared to Figure 4.3. The calculated positions of the Cepheids are in better agreement with the overall distribution of the RR Lyrae. The computed distances, without correcting for the intrinsic shape of the LMC, of the Cepheids decrease, while the RR Lyrae distances remain similar to the RC reddening approach. We find a median distance for all RR Lyrae stars of $D_{\mathrm{RR\,Lyrae/median}} = 53.1 \pm 3.2$ kpc ($(m-M)_0 = 18.62 \pm 0.13$) and for the Cepheids of $D_{\mathrm{Cep/median}} = 53.9 \pm 1.8$ kpc ($(m-M)_0 = 18.65 \pm 0.07$). The deprojection of the coordinates leads to very similar distances of $D_{\mathrm{RR\,Lyrae/median}} = 53.4 \pm 3.2$ kpc and $D_{\mathrm{Cep/median}} = 54.0 \pm 1.8$ kpc. Later on we refer to the not deprojected distances only. A mean magnitude error of 0.07 mag is stated by OGLE, a mean extinction error of 0.06 mag is found in Chapter 2 and an uncertainty for the metallicity of 0.23 dex is estimated by Chapter 3. The resulting distance errors are calculated using error propagation. The error of the period is so small that it can be neglected.

Our distances calculated with the metallicity on the scale by J95 are compared with the results using the metallicity-scale of ZW84. The median distance of the RR Lyrae stars is just 0.02 mag higher with the ZW84 metallicities. The choice of the the metallicity scales thus has a negligible effect on the distance determination of RR Lyrae stars.

The change in the median RR Lyrae distance is small and agrees well within the uncertainties with the previously calculated value from Section 4.4.1. For the Cepheids the change in distance calculated with the individual extinction corrections and with the area-averaged reddening values of the RC method is greater than the uncertainties of both determinations together. Cepheids undergo considerable mass loss, which may lead to an accumulation of circumstellar dust around these stars (Barmby et al. 2011). This might result in additional differential reddening not accounted for by the RC maps. Moreover Cepheids are located in or close to recent star-forming regions with potentially higher dust and gas content. This may lead to fluctuations and variations on scales, that are not resolved by the RC method (see Chapter 2).

Although the mean distances of the young and old population agree now within their uncertainties, the Cepheids are distributed differently than the RR Lyrae stars. While the RR Lyrae are densest in the center of the LMC, the highest concentrations of the Cepheids closely follow the entire extent of the bar. The upper panel of Figure 4.4 shows two concentrations of Cepheids towards the eastern and western end of the bar, while in the lower panel a southward shift of the Cepheids is visible. This kind of behavior is typical for irregular galaxies: Younger populations trace the often widely scattered distribution of recent star-forming regions, while older populations show a much more regular spherical distribution (see also Grebel 2001; Tikhonov 2005; Hidalgo et al. 2009; Glatt et al. 2010).

Our mean distance of the RR Lyrae stars is, within 1 σ, in good agreement with the values found in the literature for LMC RR Lyrae stars as shown in Table 4.2 as well as with the mean distance of many different tracers given in the review by Alves (2004). For the Cepheid results from the literature the uncertainties of the distances are typically smaller than for the RR Lyrae distances. Within 1 σ, our new Cepheid distance modulus does not agree with most of the literature values or the mean value by Alves (2004). However, our mean Cepheid distance agrees with the Cepheid distances by Groenewegen & Oudmaijer (2000) using Hipparcos data.

No indication for a differing “long” and “short” distance scale is found in our work when using the individual reddening corrections. This is in contrast to the discrepant distances resulting when using the RC reddening correction for Cepheids and RR Lyrae stars. Clearly our new extinction measurements

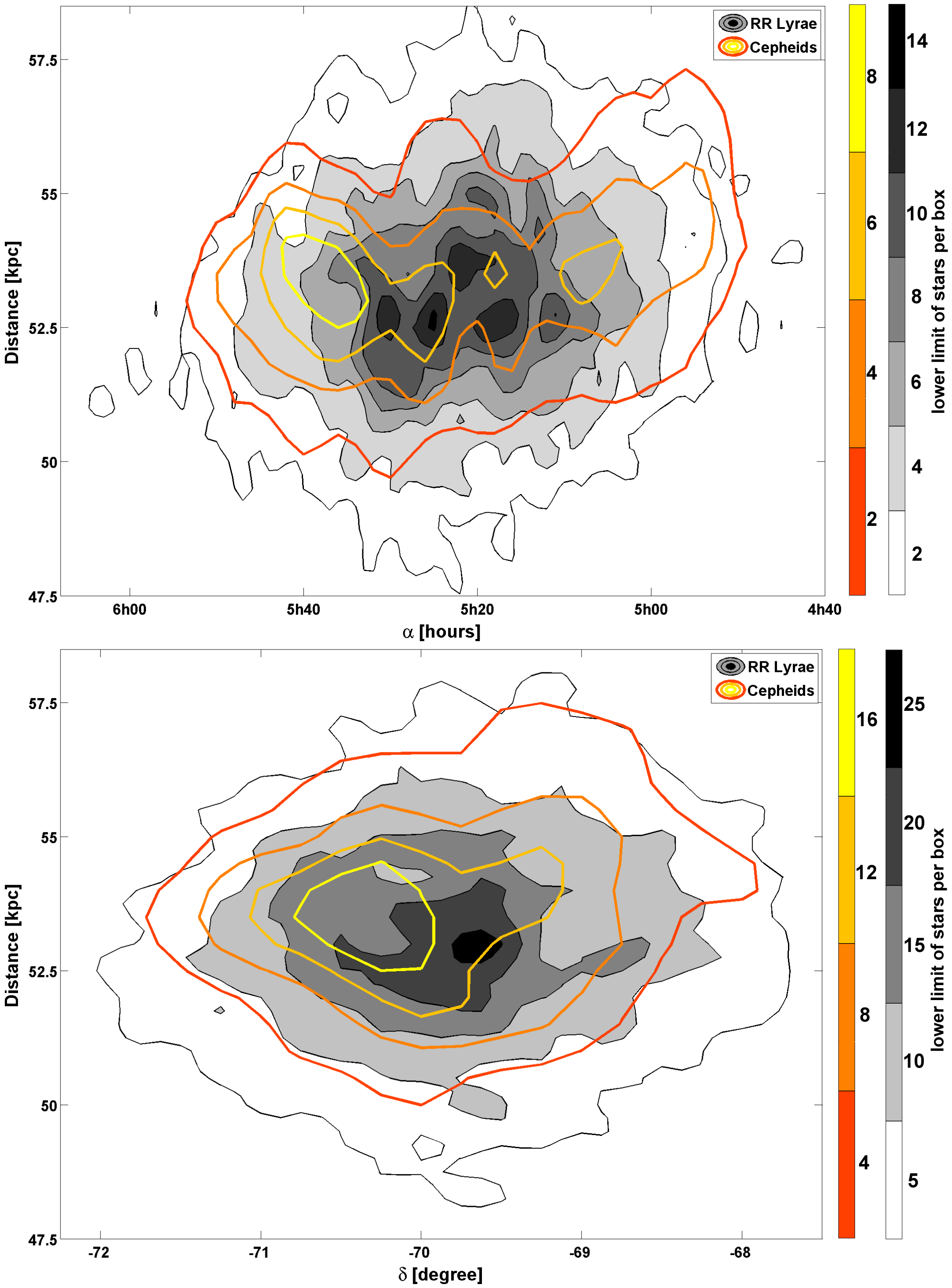

Figure 4.4: Stellar densities of RR Lyrae stars (filled grey contours) and Cepheids (colored contours) are shown as a function of distance and right ascension in the upper panel and distance and declination in the lower one. All distances are extinction-corrected using the individual, intrinsic color reddening values. The Cepheids agree very well with the RR Lyrae distances within the errors. The Cepheids are not as centrally concentrated as the RR Lyrae and trace the elongated distribution of the bar. The box sizes of the evaluated fields are listed in Table 4.1.

play a major role for the resulting distances.

4.5 Three dimensional structure

4.5.1 LMC in slices

Our data permit us also to obtain more information about the location and orientation of the young and old population of the LMC. In this subsection we slice the LMC by using only stars of distinct distance bins to reveal more information about the internal properties.

RR Lyrae stars

In Figure 4.5 we show the projected distribution of 12675 RR Lyrae stars in four different distance bins. The upper two panels show the closest parts of the LMC with RR Lyrae stars in a distance range between 45 to 47.5 kpc (left panel) and 47.5 to 50 kpc (right panel). These bins are of the same order as the typical distance uncertainties of individual RR Lyrae stars at this distance of about 3 kpc. Figure 4.5 demonstrates that the stars are highly concentrated in the central region of the LMC. The upper left panel indicates that the closest stars are mostly located in the bar. Moreover more stars are located in the eastern part of the LMC in this closest distance bin. The total number of stars in the two distance bins considered above is 1114 (9% of the sample). The density east of the center of the LMC is 50% larger than in the western part in this distance range.

In the lower left panel of Figure 4.5 the distance range between 50 to 55 kpc is displayed. We increased the bin size because the individual uncertainties grow with the distance. Overall this distance slice contains the highest number of stars with 8151 RR Lyrae stars (67% of the sample). The central region of the LMC is particularly densely populated. The bar does not stand out as a distinct feature in this distance slice, while star counts reveal that the number distribution in the western and eastern parts is approximately equal. The most distant set of RR Lyrae stars is shown in the lower right panel with distances between 55 and 60 kpc and contains 2916 stars (24% of the sample). The central region is less densely populated than in the closer bins, and as before the bar is no longer visible. For the western parts of the LMC we find 60% more stars than in the eastern parts at this distance, clear evidence for a tilt of the LMC.

In order to further quantify the location of the bar with respect to the disk, we compare the cumulative distribution of stars along the line of sight to the bar with the adjacent regions. In Figure 4.5 we draw the approximate northern and southern boundaries of the bar of the LMC. The dimensions and orientation are taken from Zhao & Evans (2000) and Mancini et al. (2004) and were optimized by visual inspection. These boundaries define a parallelogram that contains most of the bar of the LMC. We plot a normalized cumulative distribution of the line-of sight distances of the RR Lyrae stars within these bar boundaries in Figure 5. We compare this distribution with the normalized cumulative distribution of RR Lyrae stars in two fields of the same size shifted by 0.6° above and below the bar (see Figure 4.6). In order to avoid being influenced by the inclination of the disk of the LMC or by warps we add up the data of the two fields outside of the bar region. We find the stars in the bar region to stand out as an overdensity largely in front of the main body of the disk. The overdensity can be traced across line-of-sight distances ranging from about 45 kpc to about 53 kpc. The bar region thus appears to extend across some 8 kpc in diameter along the line of sight, overlapping at its far end with the main body of the disk. We check for the significance of the difference of the two cumulative distributions by applying a Kolmogorov-Smirnov test (K-S test). With more than 99% confidence we can rule out that the two distributions come from the same continuous distribution.

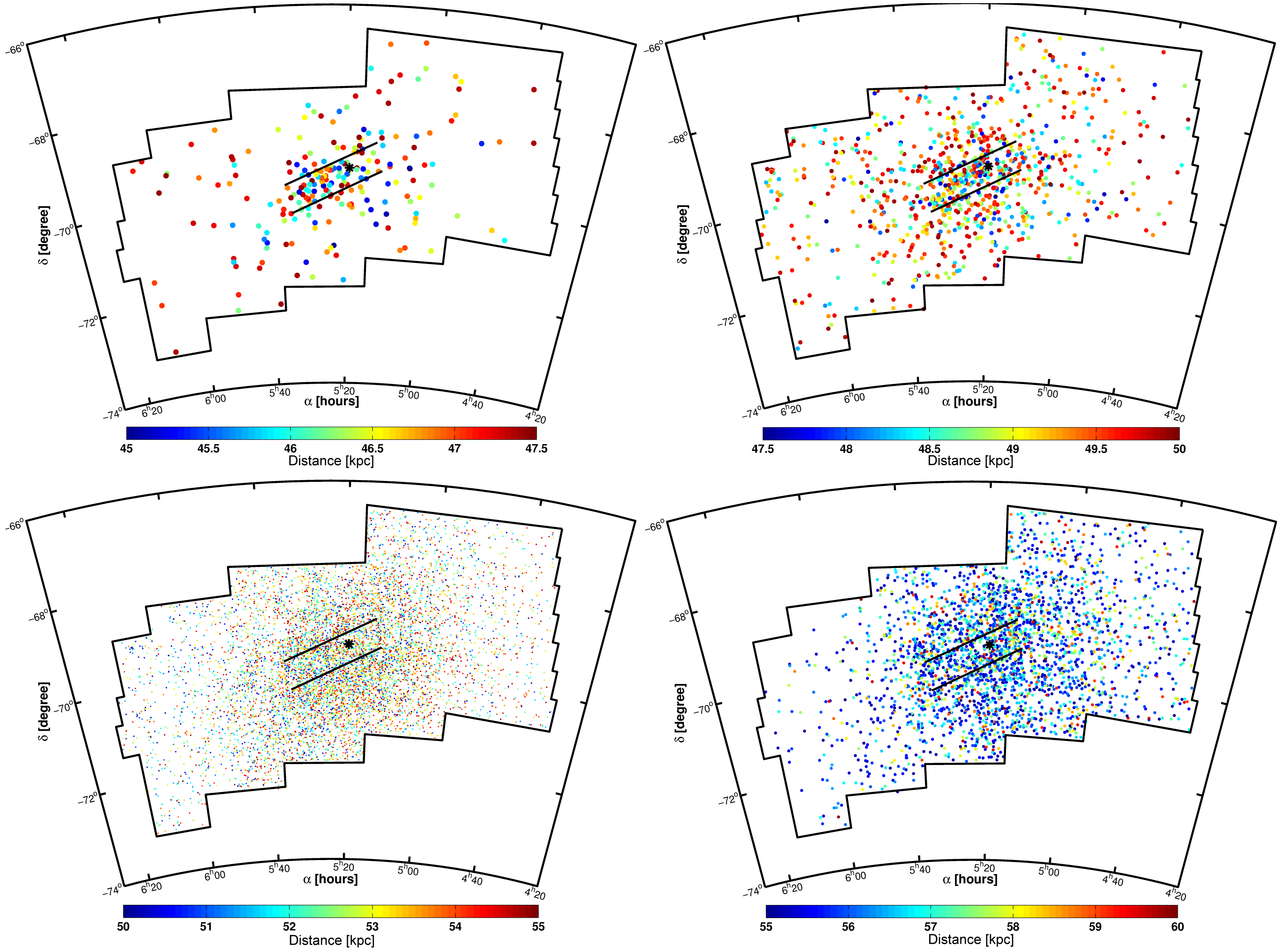

Figure 4.5: The spatial position of the RR Lyrae stars is plotted for four different distance ranges. Each star is color-coded with its distance (blue - close and red - far) as quantified in the color bar at the bottom of each panel. Each panel shows a different distance regime of the LMC, covering line -of-sight distances of 45 to 60 kpc altogether. In the closest regions the bar is very well visible, while it disappears as a distinct overdensity in the farther regions. The eastern region of the LMC is closer than the western one. The individual distance uncertainties are of the order of 8% of the calculated distance. The black polygon shows the boundaries of the OGLE III field and the black diagonal lines show the approximate location of the bar. The black star represents the optical center of the LMC found by de Vaucouleurs & Freeman (1972). The upper left panel contains 221 stars, the upper right panel 893 stars, while the lower left panel shows 8151 stars and the lower right one 2916 stars.

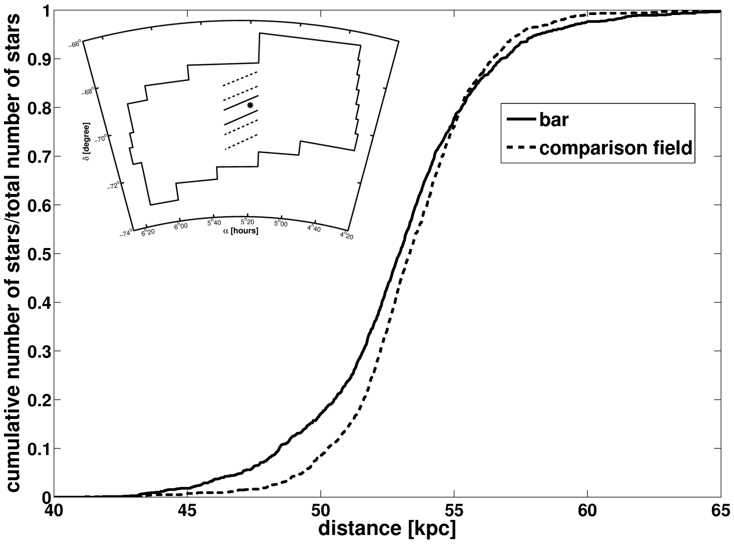

Figure 4.6: The normalized cumulative distribution of the line-of-sight distances of RR Lyrae stars of the bar region (solid line) is compared with the distribution of the sum of two similar fields located above and below the bar (dashed line). The inset on the upper left shows the location of our three fields superimposed on the OGLE footprint of the LMC. The cumulative distribution of the stars in the region of the bar shows a higher stellar density at closer distances than what is seen in the comparison fields.

Cepheids

In Figure 4.7 the distance distribution of the Cepheids is subdivided into three slices of 5 kpc depth each, covering distances in the range from 45 to 60 kpc. Overall the density of the Cepheids found by OGLE is smaller by a factor of ten compared to the RR Lyrae stars.

The closest part of the LMC is represented by a distance slice between 45 and 50 kpc (Figure 4.7, upper left panel). While nearly 10% of all RR Lyrae stars are located in this distance range, only 1% of all Cepheids are found in this slice. Out of these nearly 20% of the Cepheids are located in the bar region, whose position is marked with the black diagonal lines in Figure 4.7. In the intermediate distance range between 50 and 55 kpc (Figure 4.7, upper right panel) the bar and its extension to the east and to the west is a well visible feature, while the eastern parts of the observed field ($\alpha > 6^h00^m$) are nearly without any Cepheids. The areas west and south of the bar are well populated and the superimposed distribution of the H I shells shows good agreement for many Cepheids. The shells LMC 2 and LMC 9 coincide with higher densities of Cepheids.

In the farthest part of the LMC at distances of 55 to 60 kpc (Figure 4.7, lower panel) the density of Cepheids in the bar has considerably diminished and the panel is dominated by a concentration of stars west of the center. The shells LMC 6 and LMC 8 are in good agreement with the Cepheid location – a possible indication of long-lasting star formation given that the dynamical ages of these two supershells are only $\sim$ 11 Myr (Kim et al. 1998a) and thus younger than those of the Cepheids. The eastern part of the Cepheid map is devoid of stars beyond $\alpha > 5^h50^m$.

While the eastern part of the LMC is closer to us, the western part is located further away. We conclude that the shape of the disk for the old and young stars in the LMC has a similar pattern.

4.5.2 Inclination angle

The structural properties of smaller sections of the LMC are investigated by subdividing the OGLE III field of the LMC in a grid of $0.3^\circ \times 0.3^\circ$ boxes in right ascension and declination. We calculate the

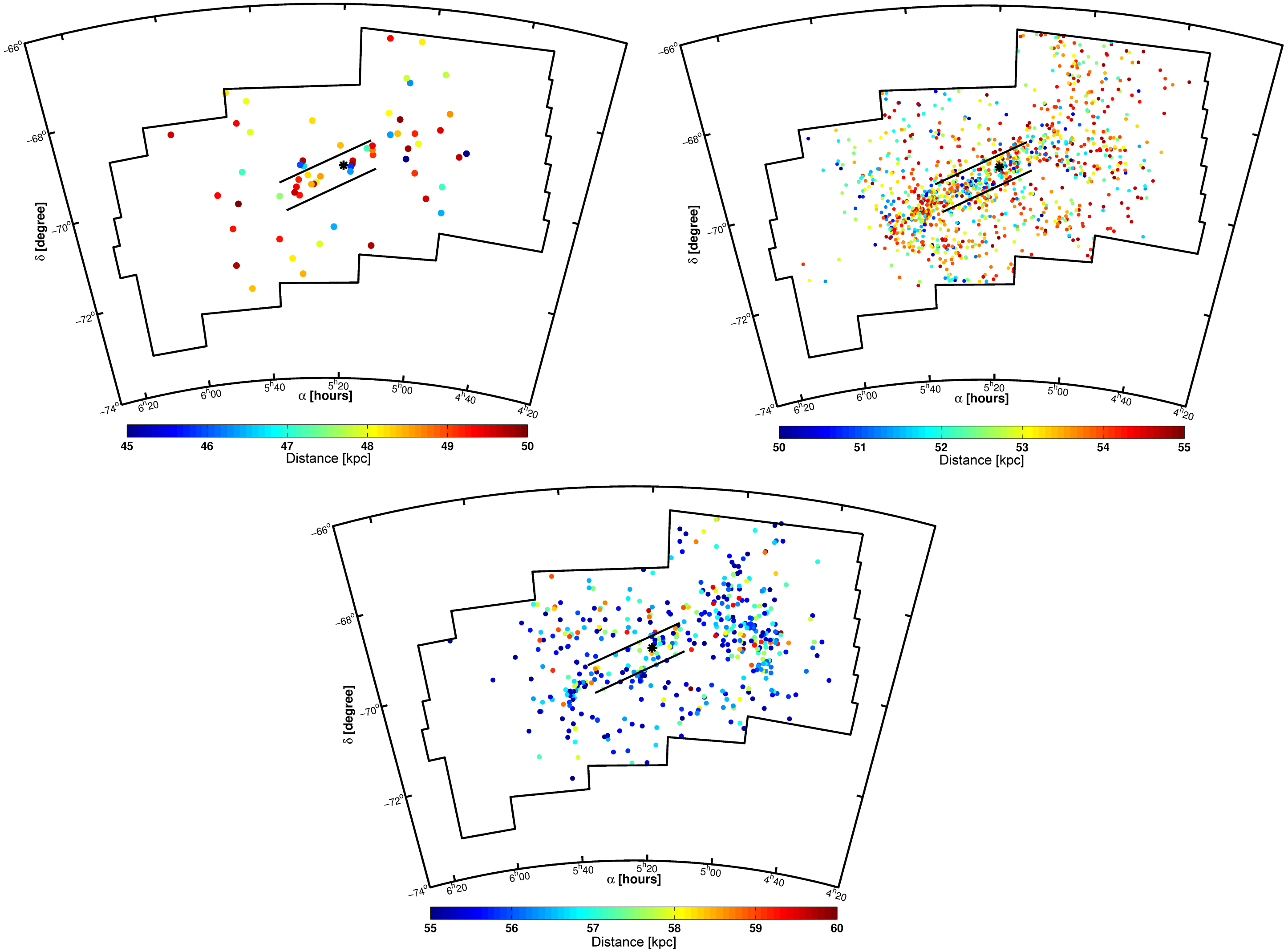

Figure 4.7: Position of Cepheids in the LMC color-coded by their distance in different distance slices. Each panel shows a 5 kpc distance slice, with the upper left panel comprising 62 stars, the upper right panel including 1207 stars and the lower left panel containing 470 stars. Overall, these three panels cover a distance range from 45 to 60 kpc. The bar is better visible at closer distances, but is partially visible in all distance bins.

Table 4.3: A compilation of inclination (i) and position angle (θ) values from the recent literature.

type of Stars	θ [degree]	σ [degree]	i [degree]	σ [degree]	author
Cepheids	151	3	31	1	Nikolaev et al. (2004)
RC	114	22	—	—	Subramaniam (2004)
RC	154	1	23.5	0.4	Koerwer (2009)
red giants	122	8	—	—	van der Marel & Cioni (2001)
red giants	—	—	34	6	van der Marel (2001)
red giants	—	—	29	—	Lah et al. (2005)
RR Lyrae	124	12	31	4	Subramaniam & Subramanian (2009a)
RR Lyrae	112	—	—	—	PS09

median distance to all stars in these boxes. The inclination angle is computed with a linear fit over all these median distances.

For the RR Lyrae stars the western part is 2.5 ± 0.5 kpc farther away than the eastern area of the LMC. A similar trend is found for the Cepheids, where the median distance of the western part is 2.7 ± 0.5 kpc larger than for the eastern part. These values correspond to an inclination of $32° \pm 4°$ in very good agreement with the literature values by, e.g., van der Marel (2001), who used red giants (Table 4.3). PS09 infer, using RR Lyrae stars, that the eastern part is closer than the western, but do not quantify the inclination angle.

Along the short north-south axis covered by OGLE both the RR Lyrae and Cepheid distributions show very similar behavior. For the Cepheids no inclination can be observed, while there may be a weak trend for the RR Lyrae stars. Using a linear fit of the RR Lyrae distribution we find the southern part of the OGLE III region to be 0.9 ± 0.2 kpc closer than the northern part.

4.5.3 Position angle

For the evaluation of the position angle of the LMC we count the number of all RR Lyrae stars and separately all Cepheids, in boxes of $0.3° \times 0.3°$ in right ascension and declination. We determine the boxes with the highest population in annuli of 0.3° and fit these boxes with a first-order polynomial.

The position angle varies somewhat depending on the location where it is measured. We find $\Theta_{\rm RRL} = 102° \pm 21°$ and $\Theta_{\rm Cep} = 113° \pm 28°$ if we take into account only the most populated areas in the innermost 3° from the visual center of the LMC, as found also by de Vaucouleurs & Freeman (1972). For the fields in a ring within a distance of $3° < \text{center} < 7°$ we find $\Theta_{\rm RRL} = 122° \pm 32°$ and $\Theta_{\rm Cep} = 116° \pm 25°$. Thus for both tracer populations the position angle is found to increase at larger radii, indicative of mild twisting. The mean position angle over the entire field of the LMC is found to be $\Theta_{\rm RRL} = 114° \pm 13°$ and $\Theta_{\rm Cep} = 116° \pm 18°$. The number of Cepheids is much smaller, hence the statistics are worse and the uncertainty larger than for the RR Lyrae stars.

Our results are in good agreement with the values found for the LMC RR Lyrae stars, e.g. PS09 obtained $\Theta_{\rm RRL} = 112.4°$, as well as for various types of stars, as red giants or RC stars, in other investigations (Table 4.3). The difference of the position angle as a function of the position of the LMC was also pointed out by van der Marel & Cioni (2001) using red giants.

4.5.4 Depth and scale height

Before we determine the depth and scale height of the LMC we deproject the spatial positions of the stars by the inclination and position angle, determined above, and with respect to the center of the RR Lyrae

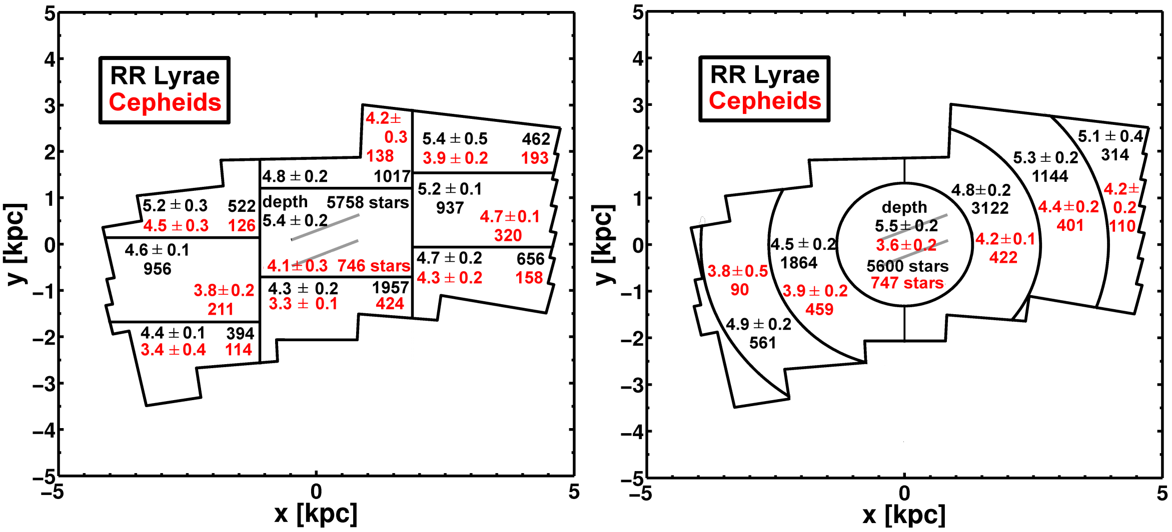

Figure 4.8: Depth is measured for two different sets of fields. In the upper panel the OGLE III field is divided into nine similarly sized squared fields, while in the lower panel the depth is measured for four rings. The rings are furthermore divided into subfields with stars with positive, respectively negative, x-values only. The black data denotes the depth of the RR Lyrae stars and the red data the depth of the Cepheids of the particular field.

star distribution at $\alpha = 5^h26^m$ and $\delta = -69°75'$. Using the approach of Weinberg & Nikolaev (2001) we determine the x,y,z coordinate of every star and use two different sets of fields to measure the depth and scale height of the LMC.

The density distribution of the RR Lyrae stars changes over the OGLE III field (see Figure 4.2) and we want to approximate the isodensity contours. To do so the OGLE III field is divided into nine squared fields of similar size, as well as into four rings (Figure 4.8), with respect to the origin of the new coordinate system. For each field we calculate a cumulative distribution function of all stars present, as shown in Figure 4.6. The depth is calculated by measuring the minimal and maximal distances of the central 68% of the distribution. This is accomplished by computing the distance where 16%, minima of the depth, and accordingly 84%, maxima of the depth, of the whole sample of stars, have shorter distances than the particular star. Using this approach we become independent of possible asymmetric geometry of the LMC, as observed in the bar region. To estimate the uncertainty of the calculations of the depth, we dither the central 68% of our cumulative distribution by 5% in both directions. The mean of the depth differences is assumed to be the uncertainty of each field.

The number of RR Lyrae stars per field as well as the depth of the old population of the LMC varies within the OGLE field, as shown in Figure 4.8. For the squared fields we find values from 4.4 kpc to 5.4 kpc (black data in upper panel of Figure 4.8), with a mean value of 4.9±0.2 kpc. The circular fields are divided further by considering stars with either positive or negative values of x only. With this approach depth between 4.5 to 5.5 kpc are determined (black data in lower panel of Figure 4.8), with a mean value of 5.0 ± 0.2 kpc. (A mean effective thickness of 9.4 ± 1.3 kpc is found for the area-averaged reddening.) In the central parts, including the bar, the depth is enhanced. Comparing the western parts with the eastern we find a significantly higher depth for the RR Lyrae stars in the western fields of OGLE III.

Even though the density of the Cepheids is much lower, we evaluate the depth in the same manner and for the same fields as for the RR Lyrae stars. The red data in the upper panel of Figure 4.8 shows the measured depth of the circular fields with values from 3.3 to 4.7 kpc and a mean value of 4.0 ± 0.2 kpc. For the circular fields, denoted in the red data in the lower panel of Figure 4.8, depth between 3.6 to

Table 4.4: Distances and structural parameters for the LMC derived in this paper.

	RR Lyrae		Cepheids	
	value	σ	value	σ
distance [kpc] - area averaged reddening	52.7	3.9	58.8	2.2
distance [kpc] - individual reddening	53.1	3.2	53.9	1.8
inclination [degree]	32	4	32	4
position angle [degree]	114	13	116	18
position angle [degree] - innermost 3°	102	21	113	28
position angle [degree] - 3° – 7°	122	32	116	25
depth [kpc]	4.9	0.2	4.0	0.2
scale height [kpc]	2.3	0.2	1.9	0.2

4.4 kpc are estimated. The mean value for the circular fields is 4.0 ± 0.2 kpc, as well. (Using the area-averaged reddening a mean depth of 10.4 ± 1.0 kpc is found.) A similar trend of higher depth values in the western parts as in the eastern parts of the LMC is found for the Cepheids. But overall the depth values for the Cepheids are significantly smaller than the estimates obtained for the RR Lyrae stars.

The higher difference between the area-averaged and individual reddening corrected depth for the Cepheids implies that Cepheids are more strongly affected by differential reddening than RR Lyrae stars. This could be due to their being associated with regions of more recent star formation or due to effects of circumstellar dust around these extended supergiants Barmby et al. (2011).

The scale height of a disk is defined as the distance, where the density of stars has decreased by a factor of $1/e$. Using the same approach as for calculation of the depth two times the scale height would correspond to a central width of 63.2% in the cumulative distribution of each field. Therefore we can calculate the scale height by multiplying the depth with a factor of

$$\frac{\text{scale height}}{\text{depth}} = \frac{1 - 2(\frac{1}{2e})}{2 \times 0.68} = 0.4648. \tag{4.8}$$

Using this formulae we estimate mean scale heights of 2.3 ± 0.2 kpc for the RR Lyrae stars and 1.9 ± 0.2 kpc for the Cepheids.

In S09 the depth of the RC stars is determined for the OGLE II fields, which cover only the most central parts of the LMC. They reveal a mean depth of 4.0 ± 1.4 kpc for the bar region, with no indication of the eastern parts having a lower depth than the western parts. These results agree well with our results, because the difference in the eastern and western parts is not covered by the OGLE II fields. In Subramaniam & Subramanian (2009a) the scale height of the RR Lyrae stars for the OGLE III field is investigated, but due to large uncertainties no value is determined. In van der Marel et al. (2002) the kinematics of carbon stars are investigated and they found that the LMC has the characteristics of a thick disk rather than a thin disk and is flared. These results are in good agreement with the simulations by Weinberg (2000) and Alves & Nelson (2000), and also explain why the Cepheid depth is higher than expected from assuming a pure thin-disk model for the young population.

4.6 Conclusions

We calculate distances to individual RR Lyrae stars observed by the OGLE III survey using the metallicity estimates based on the Fourier decomposition of their light curves (Chapter 3). Additionally we use the Cepheids present in the OGLE III data to determine distances to the young population of the LMC.

Extinction corrections are applied using two different techniques presented in Chapter 2. In the first one we calculate the mean reddening of a field with a certain size that contains a certain number of RC stars. In the second approach we calculate individual reddening values for each RR Lyrae star and Cepheid by comparing the absolute magnitudes of the stars with the observed magnitudes. With this second technique we are able to correct the actual reddening at the position of the star. We create a self-consistent three-dimensional map of the LMC for young Population I and old Population II stars using both kind of reddening corrections.

The distance results obtained with the individual extinction corrections appear to resolve the problem of the long and short distance scale of the LMC. We obtain a median distance of $D_{RRL/median} = 53.1 \pm 3.2$ kpc for the RR Lyrae stars and a median distance of $D_{\mathrm{Cep/median}} = 53.9 \pm 1.8$ kpc for the Cepheids, i.e., the distances agree very well within the uncertainties. If we use the average reddening values from the RC stars instead, the median locus of the RR Lyrae stars is 6 kpc closer than that of the Cepheids (see Table 4.4).

Our investigation thus suggests a possible solution of the long and short distance scale problem for RR Lyrae and Cepheid distances in the LMC. The discrepancy of distance moduli from RR Lyrae stars and Cepheids has been known for many decades (e.g., Tammann 1977). The distances of Population II stars are on average shorter than the distances resulting from Population I stars (Clementini et al. 2003), while the discrepancy is often larger than the errors of the individual estimates. With our result of $\Delta(m - M) = 0.03$ mag for the individually reddening-corrected distances this difference is much reduced as compared to earlier studies and smaller than the uncertainties of the distance estimates.

The long and short distance scale problem may be related to the extinction correction. In Chapter 2 we have shown that the reddening estimates of different authors using diverse techniques can be significantly different. This may in part be caused by using averaged reddening estimates which are affected by differential reddening on small scales. As shown recently in Barmby et al. (2011) Cepheids may have considerable mass loss, which leads to a light-absorbing gas reservoir in the vicinity of the star. This effect may dim the star light and, if unrecognized, lead to a larger distance. The individual de-reddening does therefore lead to more reliable result. The problem of the long and short distance scale for RR Lyrae stars and Cepheids may have been caused by intrinsic reddening effects of the Cepheids.

The distribution of stars in the LMC can be described as an inclined disk (e.g., van der Marel & Cioni 2001). The gas, traced by H I, is rotating in a disk as well (e.g., Olsen & Massey 2007), while the dynamical centers of the stellar and the gaseous distribution are separated by 1.2° (van der Marel & Cioni 2001). Borissova et al. (2004, 2006) measured the velocity dispersion of RR Lyrae stars along and below the LMC bar. Their rather high velocity dispersion of $\sim 50\,\mathrm{km\,s^{-1}}$ suggests the presence of a kinematically hot halo, yet to be confirmed by measurements of RR Lyrae farther away from the LMC center. Red giants show a much smaller velocity dispersion of $24.7\,\mathrm{km\,s^{-1}}$ and are confined to the disk (Cole et al. 2005).

Using the individually reddening-corrected distances we obtain an inclination angle of $i_{\mathrm{RRL,Cep}} = 32° \pm 4°$ for RR Lyrae and Cepheids, where the eastern parts are closer to us than the western parts. For the position angle of the RR Lyrae stars we find evidence for a dependence on galactocentric distance. Overall we get $\Theta_{\mathrm{RRL}} = 114° \pm 13°$ for the RR Lyrae stars and $\Theta_{\mathrm{Cep}} = 116° \pm 18°$ for the Cepheids, respectively. For the innermost 3 kpc from the optical center we obtain $\Theta_{\mathrm{RRL}} = 102°$ and for the outer regions in a distance from 3 kpc to 7 kpc from the optical center $\Theta_{\mathrm{RRL}} = 122°$. Overall our results of the structural parameters of the LMC are in very good agreement with the literature (Table 4.3 and Table 4.4). Our results thus confirm earlier findings of an inclined LMC disk. Moreover, the change of position angle – seen both in tracers of the old and of the young population – suggest a twisted or warped disk, which may be the result of interactions. Indications for a warped disk were also found in other studies, e.g., by van der Marel (2001) from RGB stars. We note that the OGLE data, while covering the main body of the LMC, do not cover its full extend. Hence, based on our data alone, we can not investigate the behavior in the LMC's outskirts.

The depth of the LMC RR Lyrae stars varies over the OGLE field between 4.3 kpc and 5.5 kpc, with a mean depth of 4.9 ± 0.2 kpc. The depth of the RR Lyrae stars is larger in all fields than the depth of the Cepheids, which vary between 3.3 kpc and 4.7 kpc, and has a mean of 4.0 ± 0.2 kpc. The scale height of each field can be calculated by multiplying the depth with a factor of 0.4648, which results in mean scale heights of 2.3 ± 0.2 kpc for the old population and 1.9 ± 0.2 kpc for the young Cepheids. The old population (RR Lyrae stars) extends further out than the Cepheids and may form the thick disk of the LMC while for the Cepheids a "thin disk" character is present. This broadening of the apparent thick disk of old stars might be a result of interaction between the SMC and the LMC (e.g., Cole et al. 2005). The fraction of stars located outside of the disk is rather small with only 3% of all RR Lyrae stars. Therefore we do not see evidence for an extended spherical stellar halo of stars belonging to the old population.

The RR Lyrae stars show an extended smooth distribution in the LMC, while the clumpy distribution of the Cepheids still traces their irregularly distributed formation sites. Bonatto & Bica (2010) showed that clusters with ages greater than 600 Myr, several times larger than the crossing time of the LMC (~ 175 Myr for the LMC, Bastian et al. 2009) are well mixed in the LMC and their origin can not be traced any longer (see also Glatt et al. 2010). When using intermediate-age and older stars such as AGB and RG stars, the LMC shows a smooth disk and a pronounced bar (van der Marel & Cioni 2001). A similar picture can be seen for the RR Lyrae stars in our data.

The locus and extent of the bar region of the LMC is significantly different from that of the main disk. The density of stars located more than 1σ in front of the median distance of the RR Lyrae stars is quite low, compared with the main locus of the disk of the LMC, but in the bar region the density of stars is about 50% higher than in the other regions covered by OGLE III. We find that for the RR Lyrae stars the bar protrudes out of the disk by ~ 5 kpc. This is of the same order as the depth of the LMC RR Lyrae stars. For the Cepheids we do not find the bar to be such an outstanding feature. But overall the stars in the bar region have a trend for lower distances.

A number of different explanations for the unusual structure of the bar have been discussed in the literature. For instance, the off-center location compared to the optical and kinematical center (van der Marel 2001) and the extent outwards of the disk (Nikolaev et al. 2004) led to the suggestions that the LMC might have collided with a small galaxy (Zhao & Evans 2000) or with a dark halo with a few percent of the mass of the LMC (Bekki 2009a). Zaritsky et al. (2004) suggested that the bar might be a bulge, which does not seem to be consistent with our findings. Interestingly Subramaniam & Subramanian (2009b) did not find evidence for a bar located in front of the LMC using the RC data of OGLE III. Based on our current study, we conclude that the bar of the LMC is a well defined structure largely in front of the LMC disk. Dependent on the stellar tracers the bar feature has different characteristics but is well visible in the different populations.

"Computer, compute to the last digit the value of pi"
Spock - Star Trek (Wolf in the Fold)

5

Three dimensional maps of the Magellanic Clouds using RR Lyrae stars and Cepheids II. The Small Magellanic Cloud

The data on variable stars from the Optical Gravitational Lensing Experiment (OGLE III) survey are used to determine the three-dimensional structure of the Small Magellanic Cloud. Therefore individual distances to RR Lyrae stars and Cepheids are used to investigate the proportions of the old and young population. Photometrically estimated metallicities are used to determine the distances to 1494 RR Lyrae stars, which have typical ages greater than 9 Gyr. For 2522 Cepheids, with ages of a few tens to a few hundred Myr, the distances are calculated using their period-luminosity relation. Individual reddening estimates from the intrinsic color of each star are used to ensure high precision three dimensional maps. The distances of RR Lyrae stars and Cepheids are in very good agreement with each other. The median distance of the RR Lyrae stars is computed to 64.6 ± 3.4 kpc. For the Cepheids a median distance of 63.1 ± 3.0 kpc is obtained. Both populations show an extended scale height, with 3.7 ± 0.4 kpc for the RR Lyrae stars and 4.5 ± 0.3 kpc for the Cepheids. This confirms the large depth of the SMC suggested by a number of earlier studies. The young population is very differently orientated than the old stars. While we find an inclination angle of 7° ± 15° and a position angle of 81° ± 21° for the RR Lyrae stars, for the Cepheids an inclination of 74° ± 9° and a position angle of 71° ± 15° is obtained. Major interactions between the SMC and other galaxies have introduced significant changes in the shape and appearance of the SMC.

This chapter is based on Haschke, Grebel, & Duffau (in prep.a)

5.1 Introduction

The SMC is the only dwarf irregular satellite of the MW. It is interacting with its larger companion, the LMC, and with the MW. A number of studies have suggested that the apparently disturbed shape and large depth extent of the SMC were caused by there interactions, although the details and the three-dimensional shape of the SMC remain under debate (Bekki & Chiba 2009).

The distance to the SMC is usually quoted with 60 kpc or $(m - M) = 18.90$ mag (e.g., Westerlund 1997). But even the usage of a specific distance calibrator may still show deviations between different observations. Using, for instance, eclipsing binaries to determine the mean distance of the SMC North et al. (2010) obtained $(m - M) = 19.11 \pm 0.03$ mag, while Hilditch et al. (2005) found a mean value of $(m - M) = 18.91 \pm 0.03$ mag in very good agreement with the mean distance quoted above.

The only option to obtain comparable and trustworthy mean distances and structural parameters in general of different stellar tracers are large surveys. For these the systematic uncertainties are lower, because they have been observed, reduced and analyzed following a coherent procedure. However, the need of tracers of different and distinct ages is indispensable to resolve the different evolutionary states the galaxy has passed through during its history. For the SMC (small) sets of very different stellar tracers, representing young, intermediate age and old populations, have been investigated for many decades to find a common mean distance. The differences between the tracers, but also within the results obtained using a distinct tracer are greater than the 1σ-uncertainties claimed. This is on one side a strong indication for a significant depth extend of the SMC, but shows on the other side that it is absolutely necessary to analyze large datasets instead of choosing a small subsample of stars within the SMC.

Using Cepheids to trace the young population Laney & Stobie (1986) found a mean distance modulus of $(m - M) = 19.05 \pm 0.06$ mag, while Stothers (1988) obtained $(m - M) = 18.80 \pm 0.06$ mag. More recent estimations of the mean distance using Cepheids led to values of $(m - M) = 19.11 \pm 0.11$ mag (Groenewegen & Oudmaijer 2000), $(m - M) = 18.93 \pm 0.024$ mag (Keller & Wood 2006) or the distance of Ciechanowska et al. (2010) of $(m - M) = 18.85 \pm 0.07$ mag.

The intermediate age regime is characterized by different distance tracers as AGB and RGB stars as well as clusters. Using the tip of the RGB Cioni et al. (2000) found a mean distance to the SMC of $(m - M) = 18.99 \pm 0.03$ mag. Red Clump stars are used by Popowski (2000) to measure the distance to $(m - M) = 18.77 \pm 0.08$ mag. In Glatt et al. (2008a) the distances to six SMC clusters are determined and values between $(m - M) = 18.50$ mag to $(m - M) = 19.12$ mag are found. This corresponds to a distance difference of 17 kpc for the closest and farthest cluster.

For the distance estimations from RR Lyrae stars, representing the old population of the SMC, plenty of observations have been conducted. For a review of older measurements, which found distances between $(m - M) = 18.78 \pm 0.15$ mag and $(m - M) = 19.20$ mag, we refer to the book by Westerlund (1997). Since then Udalski (2000) revealed a a very short distance of $(m - M) = 18.76 \pm 0.07$ mag using OGLE II data. In the framework of the Araucaria project Szewczyk et al. (2009) found a distance of $(m - M) = 18.97 \pm 0.03$ mag, while Deb & Singh (2010) reanalyzed OGLE II data to find a mean distance of $(m - M) = 18.84 \pm 0.01$ mag. Recently Kapakos et al. (2011) analyzed 100 RR Lyrae stars of the central parts of the OGLE III fields and found mean distance estimates of $(m - M) = 18.90 \pm 0.18$ mag for stars of type *ab* and $(m - M) = 18.97 \pm 0.14$ mag for stars of type *c*.

These differences in the mean distance are most certainly be introduced by a large depth of the SMC as found by e.g., Mathewson et al. (1988). They showed, using Cepheids, that the SMC has a considerable depth of ~ 20 kpc. Newer estimates used intermediate age tracers and led to lower values of the line of side depth. In Crowl et al. (2001) a depth between 6 kpc and 12 kpc, in dependence of reddening, is estimated using cluster distances. In S09 the distribution of RC stars is estimated and a depth of less than 5 kpc is found for the SMC, in good agreement with the results of Subramanian & Subramaniam (2012). They also investigated the depth of the old population by using RR Lyrae stars and found a mean depth of 4.07 ± 1.68 kpc. This is in very good agreement with the 4.13 ± 0.27 kpc found for the line of sight depth of RR Lyrae stars by Kapakos et al. (2011). All these results are in agreement with the finding of Zaritsky et al. (2000) that the structural parameters change for the different populations of the SMC.

Lah et al. (2005) conducted a study utilizing different stellar tracers to show that RGB and AGB stars might be further away from us than the main body of the SMC (see their Fig. 4). In Subramanian & Subramaniam (2012) the inclination angle of the RC stars and the RR Lyrae stars is determined to $i \simeq 0.5^\circ$. Furthermore they found a position angle of $PA = 58.3^\circ$ for the RR Lyrae stars and of $PA = 55.5^\circ$ for the RC stars, respectively. For the other determinations of the structural parameters of the SMC only young stars have been used. With 63 Cepheids Caldwell & Coulson (1986) found an inclination angle of $i = 70^\circ \pm 3^\circ$ and a position angle $PA = 58^\circ \pm 10^\circ$. With a different sample of 23 Cepheids Laney & Stobie (1986) obtained $i = 45^\circ \pm 7^\circ$ and a position angle $PA = 55^\circ \pm 17^\circ$ in good agreement with Caldwell & Coulson (1986). A much larger sample of Cepheids was investigated by Groenewegen & Oudmaijer (2000), who found an inclination angle of $i = 68^\circ \pm 2^\circ$ and a position angle of the line of nodes of $\Theta = 238^\circ \pm 7^\circ$.

The center of the SMC is also not very well constrained. The optical center (see e.g., Westerlund 1997) and the center of the K- and M-stars (G09, found by) are basically identical with $\alpha = 0^{\mathrm{h}}51^{\mathrm{m}}$ and $\delta = -73.1^\circ$. From HST measurements Piatek et al. (2008) found the kinematical center of the SMC to be $\alpha = 0^{\mathrm{h}}52^{\mathrm{m}}8^{\mathrm{s}}$ and $\delta = -72.5^\circ$, while Stanimirović et al. (2004) found $\alpha = 0^{\mathrm{h}}47^{\mathrm{m}}33^{\mathrm{s}}$ and $\delta = -72^\circ5'26''$ for the highest H I column density. Throughout this paper we will mostly refer to the optical center and the result by G09.

Distances to all RR Lyrae stars and Cepheids present in the OGLE sample are calculated. In Section 5.2 we use the metallicity estimates of Chapter 3 and the periods obtained by OGLE. Moreover we apply the reddening maps of Chapter 2 to correct for individual reddening effects. The two dimensional spatial distribution of the stars is investigated in Section 5.3 and the three dimensional maps are presented in Section 5.4. This three dimensional map is analyzed and the structural parameters of the young and old population are determined in Section 5.5. The results are discussed and summarized in Section 5.6.

5.2 Distance measurements

In this Section we discuss our distances to RR Lyrae stars as tracers of the old population (≥ 9 Gyr, e.g., Sarajedini et al. 2006) and to Cepheids for the young population (∼ 30 − 300 Myr, Grebel & Brandner 1998; Luck et al. 2003) of the SMC. Distance estimates are calculated individually star by star.

5.2.1 RR Lyrae

In Chapter 3 the photometric metallicity of 1864 RR Lyrae stars from the OGLE III sample of the SMC were calculated. The absolute luminosity of RR Lyrae stars depends on metallicity only and we use these estimates on the metallicity scale of ZW84, to calculate the absolute V band magnitude M_V of the RR Lyrae stars by using the relation introduced in Clementini et al. (2003)

$$M_V = 0.84 + (0.217 \pm 0.047)\,[Fe/H] \tag{5.1}$$

We also tried out quadratic equations by Catelan et al. (2004); Sandage & Tammann (2006) and Bono et al. (2007). The mean absolute magnitudes of the RR Lyrae stars are quite different from each other and we find median differences of $\Delta M_V = 0.03$ mag for Sandage & Tammann (2006, their equation 7), $\Delta M_V = 0.10$ mag for Catelan et al. (2004, their equation 8) and $\Delta M_V = 0.13$ mag for Bono et al. (2007, their equation 10). All of these absolute magnitudes are larger than those calculated with the relation by Clementini et al. (2003). This reflects the comparatively large uncertainty of the magnitude zeropoint of the RR Lyrae stars. We take these systematics for our error analysis into account and decide to follow Benedict et al. (2011), who found that the relation by Clementini et al. (2003) fits their HST observations of RR Lyrae stars best. We, therefore, use the metallicity-luminosity relation from Clementini et al. (2003) which is furthermore the only one calibrated by using RR Lyrae stars from the MCs.

The absolute magnitude of each RR Lyrae star together with the observed mean magnitude from the OGLE collaboration yields a distance modulus once a reddening correction is applied. In Section 5.2.3 we apply two different approaches to correct for the reddening and to obtain the three dimensional structure of the SMC.

5.2.2 Cepheids

The correlation between absolute magnitude and period is well known for Cepheids. Using Cepheids from the SMC Sandage et al. (2009) obtained one relation for B, V and I band, which only depends on the period P of the Cepheid investigated.

$$M_V = -(2.588 \pm 0.045) \log P - (1.400 \pm 0.035) \tag{5.2}$$

$$M_I = -(2.862 \pm 0.035) \log P - (1.847 \pm 0.027) \tag{5.3}$$

There might be a break in the relation for the SMC at $P = 10$ days as found for the LMC (Sandage et al. 2004), but Sandage et al. (2009) claims that this break is not significant.

The distance moduli are calculated using the mean observed magnitude of each star, provided by the OGLE collaboration, and the absolute magnitude from these relations. The correction for the reddening effects is described in the next section.

5.2.3 Reddening correction

Chapter 4 used two different approaches to correct for the reddening of the LMC, which were adopted from Chapter 2. We use the same method here, which will be shortly outlined. Further details are described in Chapter 4 and Chapter 2.

Area-averaged reddening corrections: The red clump method

RC stars are located at a certain color and luminosity range of the CMD. That position depends on the distance, the metallicity, and the reddening of these stars. Girardi & Salaris (2001) predicted the theoretical color of the RC for distinct metallicities using models. Assuming a metallicity of $z = 0.025$ (Cole 1998; Glatt et al. 2008a) for the SMC RC population the difference of the observed to the theoretically predicted color provides the reddening (Wozniak & Stanek 1996).

In Chapter 2, we estimated reddening values $E(V - I)$ for 681 subfields in the OGLE III field of the SMC. These were converted using the relation by SFD98

$$A_V = 3.24(E(V - I)/1.4) \tag{5.4}$$

$$A_I = 1.96(E(V - I)/1.4) \tag{5.5}$$

to correct the apparent magnitudes of the stars with the mean extinction in the corresponding field.

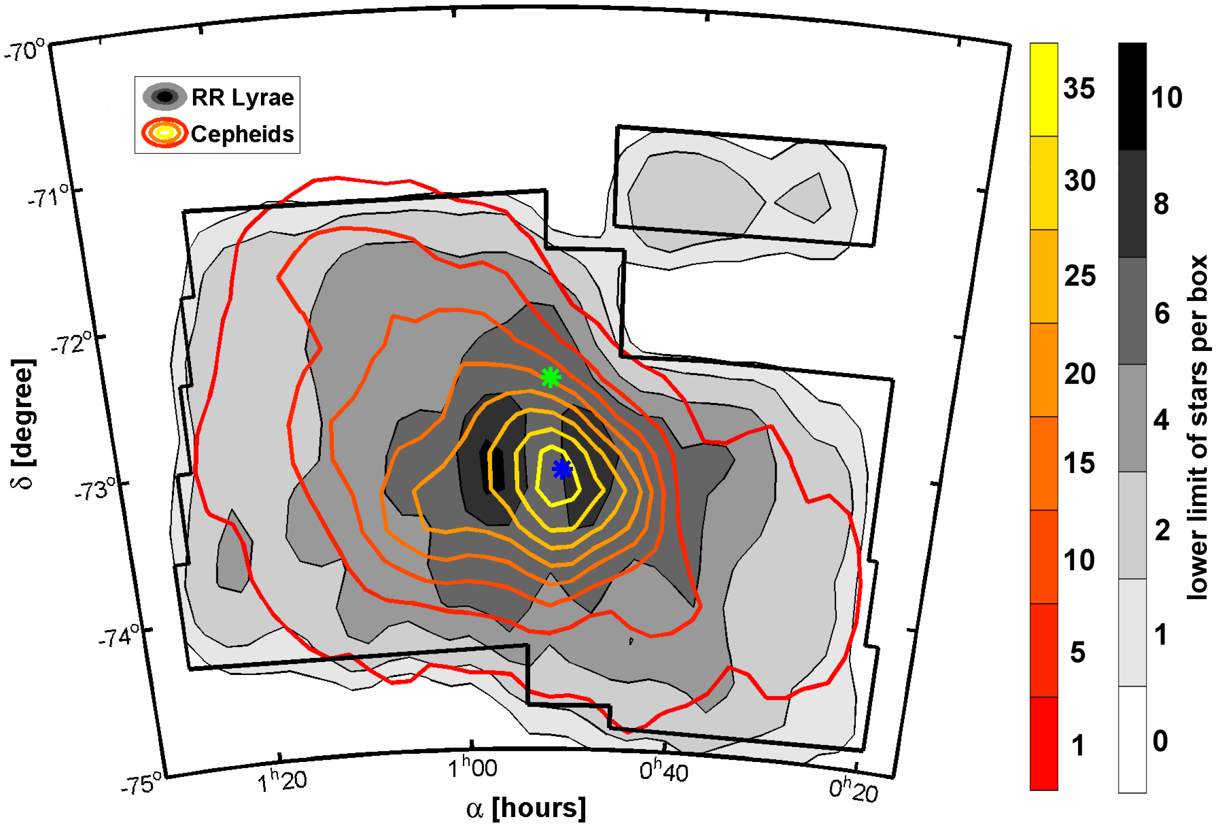

Figure 5.1: Densities of RR Lyrae stars (filled grey contours) and Cepheids (colored contours) are shown as a function of right ascension, α (J2000), and declination, δ (J2000). While the RR Lyrae stars show a bimodal distribution, the density of Cepheids decreases with distance from the center found by G09 and is marked with a blue asterisk. The green asterisk represents the center found by Piatek et al. (2008) using *HST* proper motions. The boxsizes of the evaluated fields are shown in Table 5.1.

Individual reddening correction: Intrinsic colors of variable stars

The difference between the observed color of an RR Lyrae star or Cepheid and the theoretical prediction from the calculated absolute magnitudes is assumed to be the reddening.

For the RR Lyrae and the Cepheids this task has been accomplished with the same techniques as described in Chapter 2. Finally we calculated the reddening with the relation $E(V-I) = (v-i) - (V-I)$, where $(v-i)$ stands for the observed magnitudes and $(V-I)$ are the intrinsic absolute magnitudes of each star.

With Equation 5.4 and Equation 5.5 the observed magnitudes are extinction corrected and the reddening free distances are calculated.

5.3 Star densities in the OGLE III field

The central parts of the SMC, including the bar and the wing of the SMC, are part of the field of OGLE III. Overall 14 square degrees are covered and Figure 5.1 shows the distribution of RR Lyrae stars and Cepheids in the observed field. The stars are counted in boxes of $0.5° \times 0.25°$ in α and δ, respectively, (Table 5.1) and the resulting distributions are smoothed using a Gaussian kernel.

For the RR Lyrae stars the distribution is very smooth and increases steadily from the outskirts to-

Table 5.1: Binsizes of the fields evaluated to obtain the densities of stars in the SMC. The density of the boxes defined here are used in Figure 5.1,5.2 and 5.3 to show the distribution of young and old stars in the SMC.

	RR Lyrae	Cepheids
α bin [degree]	0.5	0.5
δ bin [degree]	0.25	0.25
distance bin [kpc]	0.5	0.5

wards the center, found by G09 from K- and M-stars. However the highest density of RR Lyrae stars is not at the center, but the peak of the distribution is nearly bimodal, as shown in Figure 5.1. In the northwestern part of the SMC it seems that a considerable amount of RR Lyrae stars may be outside of the OGLE III field. These stars are located at the same spatial coordinates as 47 Tuc. For distance estimates with RC correction these stars are excluded, while they are taken into account for the individual reddening corrected distance estimates. Overall we expect that a considerable amount of stars is located outside of the OGLE III region, since this survey only covers the dense inner regions of the SMC.

The distribution of the Cepheids is very different from the old population traced by the RR Lyrae. Very close to the center of G09 the density of Cepheids is highest. Then it drops with increasing distance from the center. First the isodensity lines are nearly circular, but with increasing distance from the center the isodensity contours become more elongated towards the west and northeastern directions. This might be an effect of the OGLE III field, but interestingly no stars are found in the most northern fields, as well as at the position of 47 Tuc. The recent star formation has therefore not taken place in these outer regions of the SMC.

5.4 Three dimensional maps

For each RR Lyrae star and Cepheid in our sample distances are calculated using the relations described in Section 5.2. Either the averaged reddening from the RC stars or the individual reddening method is applied. This results in two independent sets of distance maps for each population.

5.4.1 Maps corrected with area averaged reddening

In this subsection the area averaged reddening values obtained from the RC stars are used. All RR Lyrae and Cepheids located in one subfield defined by the RC reddening method are extinction corrected using the same RC reddening value (for details see Chapter 2).

Figure 5.2 plots the spatial position of the RR Lyrae stars (grey contours) and Cepheids (colored contours) in α and δ, respectively, versus distance. This corresponds to a change of the viewing direction of the observer to a position above the SMC in the upper panel, and to the side in the lower panel. The density contours should allow for a better visibility. Table 5.1 lists the box sizes, within which the density of stars is evaluated. To smooth the contour plot a Gaussian kernel with a width of 3×3 bins is used. The variances on very small scales are diminished by this procedure.

The location of the central concentrations of the two populations coincide. The RR Lyrae stars have a median distance of $D_{\mathrm{RRL/median}} = 66.7 \pm 4.3$ kpc ($(m-M) = 19.13 \pm 0.13$ mag). The median distance of the Cepheids is a bit farther away with a distance of $D_{\mathrm{Cep/median}} = 68.1 \pm 4.1$ kpc ($(m-M) = 19.17 \pm 0.12$ mag). For the uncertainties we take the mean magnitude error of 0.07 mag, stated by the OGLE collaboration, the error of the metallicity of 0.23 dex, as determined by Chapter 3 and the mean extinction error of 0.08 mag, found by Chapter 2, and compute the value by using error propagation. The error of the period as stated by OGLE is too small to be a contributing factor. With these uncertainties the mean distances of the old and young population of the SMC are in very good agreement.

5.4.2 Maps corrected with individual reddening

A more precise reddening correction can be applied by using individual reddening estimates for each Cepheid or RR Lyrae star, instead of using an area averaged reddening value for a large number of RC stars. We use the reddening estimates developed in Chapter 2 to correct for the individual intrinsic color differences. The color from the absolute magnitudes in the V and I band are compared with the color from the observed v and i apparent magnitudes. The difference is assumed to be the intrinsic reddening of this star, as described in Section 5.2.3. Details on the differences of population- and temperature-dependent reddening are discussed in Grebel & Roberts (1995) and Zaritsky (1999).

Figure 5.3 reveals shorter distances of the SMC than when using the RC reddening values in Figure 5.2. The median distance of the RR Lyrae stars is found to be $D_{\mathrm{RRL/median}} = 64.6 \pm 3.4$ kpc ($(m - M) = 19.05 \pm 0.11$ mag), a bit closer than using the RC reddening method. For the Cepheids we find a closer distance as well using the intrinsic reddening values. It leads to $D_{\mathrm{Cep/median}} = 63.1 \pm 3.0$ kpc ($(m - M) = 19.00 \pm 0.10$ mag).

The uncertainties of the distances are calculated by using error propagation of the intrinsic magnitude error of 0.07 mag, stated by the OGLE collaboration, the uncertainty of the metallicity estimate of 0.23 dex, as found by Chapter 3, plus the uncertainty of the reddening, which we estimated to be 0.06 mag in Chapter 2. The period is measured with such high accuracy by OGLE III that it does not influence the uncertainty determination.

In Chapter 2, we point out that in regions with substantial amounts of dust and gas the reddening can fluctuate significantly with depth and position. Such local differential reddening cannot be resolved by the RC reddening method. As pointed out by Barmby et al. (2011), Cepheids suffer from considerable mass loss, leading to circumstellar dust around the star. This leads to additional differential reddening, which is not accounted for by the RC maps. Therefore a more accurate distance estimate can be reached by using the intrinsic reddening method.

The mean distances of the RR Lyrae and Cepheid population are in good agreement within their uncertainties. As found with the RC reddening the SMC has a considerable depth, even though it is reduced, as expected, by using the intrinsic reddening. The internal structure of the SMC changes as well. In the upper panel of Figure 5.3 we obtain a lower density for the RR Lyrae stars in the center of the SMC. Moving away from the center of the RR Lyrae distribution, a ring-like structure of higher density encircles the center. Further outwards the density drops steadily. We check if this pattern is an artifact introduced by the smoothening with the Gaussian kernel, but the unsmoothed figure contains the same pattern as shown in this representation. By plotting single stars instead of contours we find the same effect and preclude that it is made by the used contour algorithm. For the Cepheids we find a much more centrally concentrated distribution when using the individual stellar reddening. One center of highest density, which coincides with the low density center of the RR Lyrae (see Figure 5.3) and the center of G09, is obtained. First the density drops very regularly in every direction while moving away from the center, then the contour lines become elongated. Towards the northeast of the OGLE field the density contours have the closest distance to the MW and the highest irregularity. This is in the direction of the Magellanic Bridge and we conclude that this may be a detection of a connection between the Bridge and the SMC.

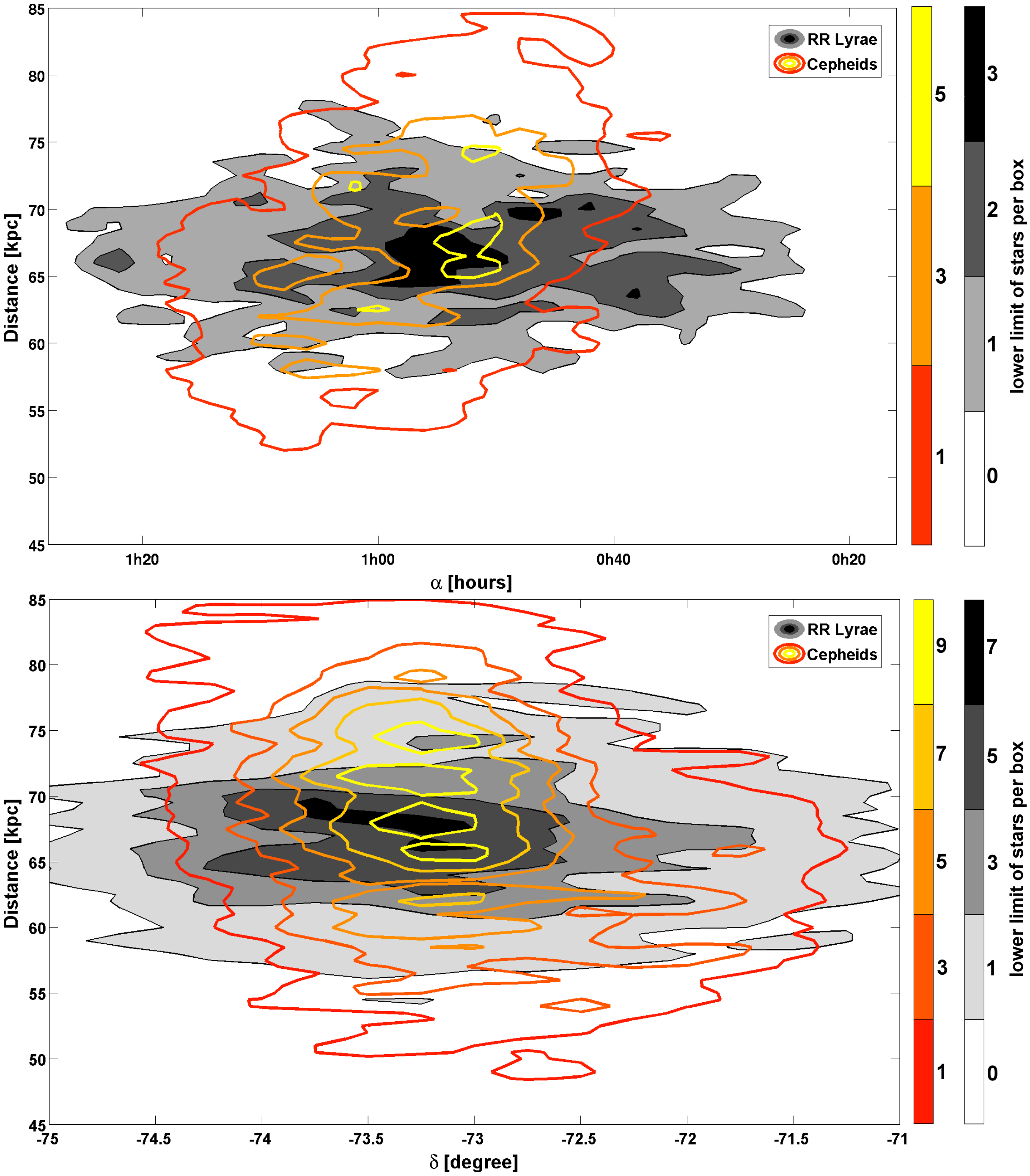

Figure 5.2: Stellar densities of RR Lyrae (filled grey contours) and Cepheids (colored contours) are shown as a function of distance and α, in the upper panel, and as a function of distance and δ in the lower panel. Area averaged reddening values are used to correct all distance estimates. The main concentration of both populations is located nearly at the same position. But the inclination angle of the young and old population is very different from each other. In Table 5.1 the sizes of the evaluated boxes are listed.

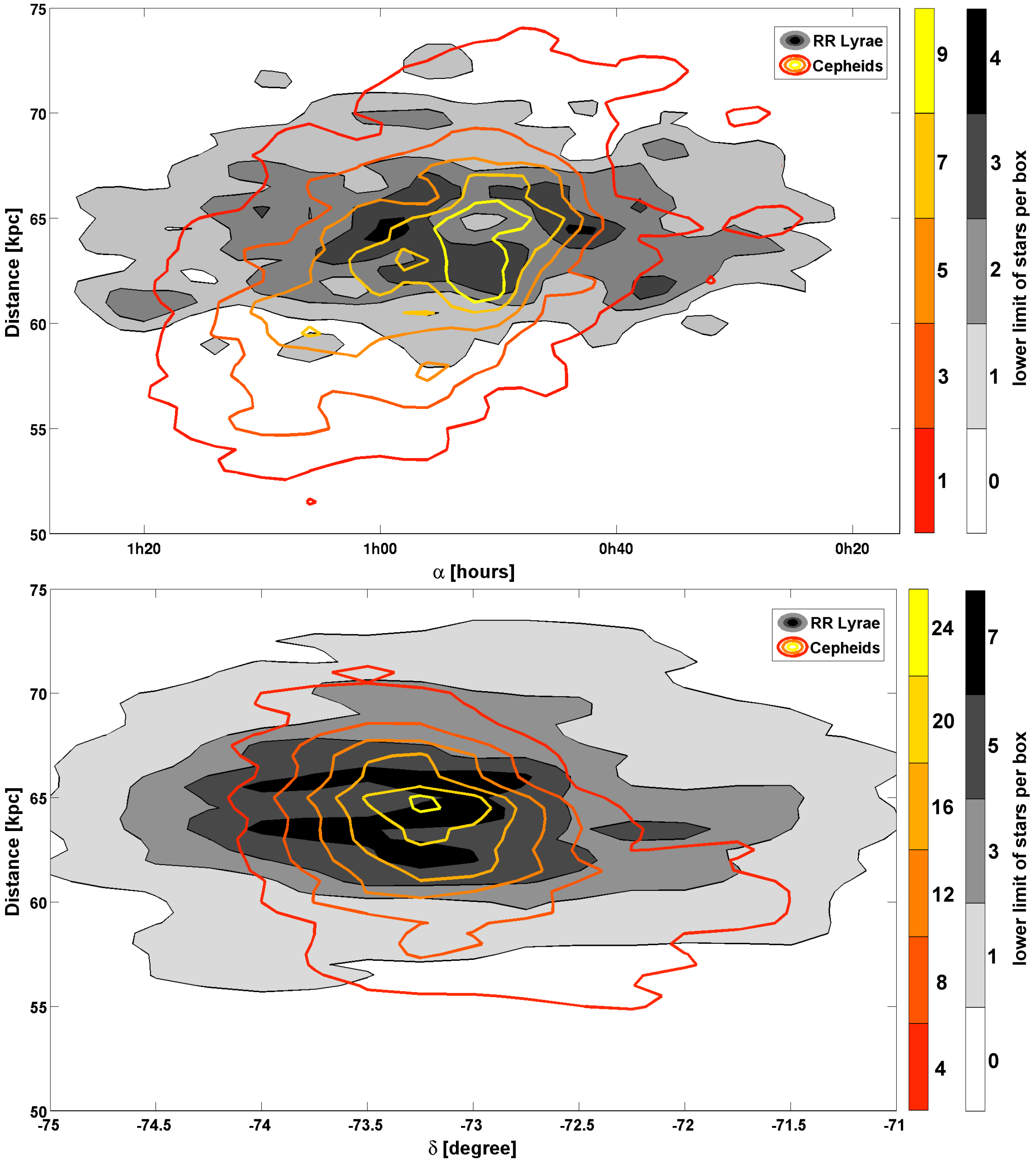

Figure 5.3: For RR Lyrae (filled grey contours) and Cepheids (colored contours) stellar densities are shown as a function of distance and α in the upper panel and as a function of distance and δ in the lower one. All distances are extinction corrected using the intrinsic color reddening values. The RR Lyrae stars and the Cepheids have a very different orientation in the SMC. While the RR Lyrae are not inclined, the Cepheids do show a large inclination angle. Furthermore, the RR Lyrae show a low density pattern in the center of the SMC, which is not visible for the Cepheids. The sizes of the boxes used to evaluate the density are listed in Table 5.1.

Table 5.2: Compilation of distance estimates for the SMC from different tracers using recent literature values and this work.

type of indicator	mean distance $(m - M)$	σ	reference
Cepheids	19.11	0.11	Bono et al. (2001)
Cepheids	18.85	0.14	Ciechanowska et al. (2010)
Cepheids	19.11	0.11	Groenewegen (2000)
Cepheids	18.93	0.024	Keller & Wood (2006)
Cepheids	19.17	0.12	this work - area averaged reddening
Cepheids	19.00	0.10	this work - individual reddening
CMD fitting	18.88	0.08	Dolphin et al. (2001)
Eclipsing Binaries	18.89	0.14	Harries et al. (2003)
Eclipsing Binaries	18.91	0.13	Hilditch et al. (2005)
Eclipsing Binaries	19.11	0.03	North et al. (2010)
Red Clump	18.77	0.08	Popowski (2000)
RGB tip	18.99	0.11	Cioni et al. (2000)
RR Lyrae	18.86	0.01	Deb & Singh (2010)
RR Lyrae *cab*	18.90	0.18	Kapakos et al. (2011)
RR Lyrae *c*	18.97	0.14	Kapakos et al. (2011)
RR Lyrae	18.97	0.15	Szewczyk et al. (2009)
RR Lyrae	19.13	0.13	this work - area averaged reddening
RR Lyrae	19.05	0.11	this work - individual reddening

5.5 Three dimensional structure

5.5.1 SMC in slices

The three dimensional data for the two populations allows us to gain a better insight into the internal structural properties of the SMC. We slice the SMC into three bins of 10 kpc depth each. All stars are color coded based on their distance and plotted with their spatial coordinates. The individual distance uncertainties of each star are about 8%, therefore well below the binsize.

RR Lyrae stars

The projected distribution of the old population of stars is shown in Figure 5.4 for three different distance bins. In the upper left panel of Figure 5.4, which represents RR Lyrae stars that are closer than 55 kpc, we find only very few stars of the old generation. Only 1.5% of all RR Lyrae stars are present in this distance bin. These stars are randomly distributed and no pattern or structure is visible.

The intermediate distance bin from 55 kpc to 65 kpc (upper right panel) is dominated by stars with distances between 60 kpc and 65 kpc, while 52.6% of the whole sample are in this distance range. We find that no overall structural pattern is visible and the stars are distributed over the whole body of the SMC measured by OGLE III. But investigating the smaller structures we find that stars of very similar distance are often concentrated at a certain spatial position and accumulate in cluster-like structures. The region in the very center is nearly empty of any old stars, while the regions surrounding the center are well populated (compare as well with Figure 5.3). Because we use the intrinsic colors to determine the reddening, we believe this not be caused by a reddening effect. Furthermore we find other regions with low densities of stars. However, the densities are not very high and we might be influenced by small number statistics. We can draw the conclusion that the distribution of old stars is not as smooth as expected for a well mixed old population, even though no pronounced large scale pattern is present.

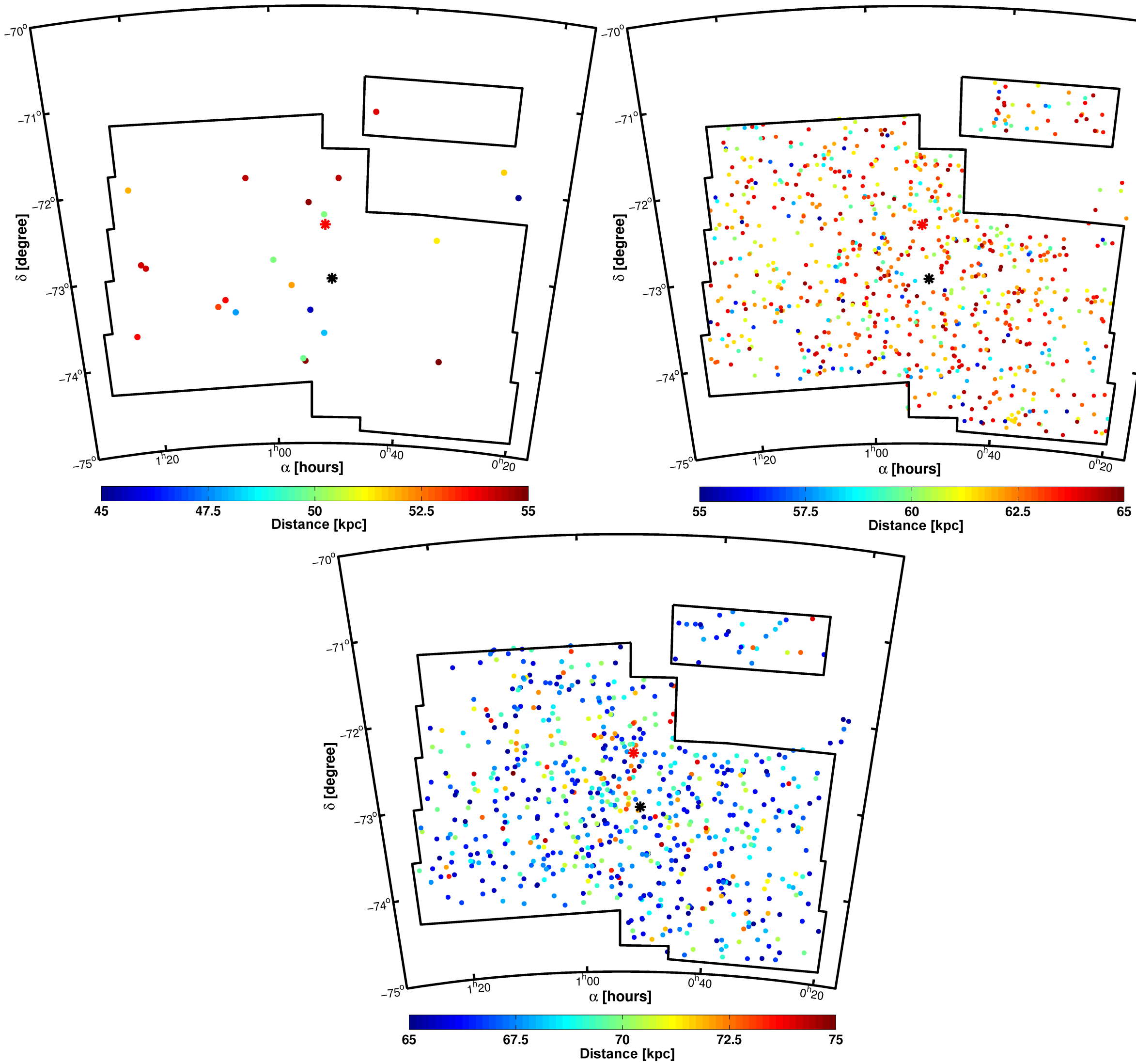

Figure 5.4: Color-coded distance map for individual RR Lyrae stars in three SMC distance bins. The distances are sliced into three distance bins of 10 kpc each, covering 45 to 75 kpc. The closest bin (upper left panel) has hardly any stars and no patterns are visible. For the other two bins we can not see much structure. The stars seems to be very evenly distributed. The black asterisk represents the center found by G09. The upper left panel contains 22 stars, the upper right one 786 RR Lyrae and the lower one 686 stars.

The farthest bin of 65 kpc to 75 kpc contains 45.9% of the RR Lyrae stars and is dominated by stars at distances between 65 kpc and 70 kpc. Overall no structural patterns are visible. But, as for the closer distance bin, we find the same substructure of regions with reduced density and clumpy structures of increased density. The locations of these patterns do not agree with the patterns of the upper right panel, however, the region around the center of G09 is less densely populated as other regions in its vicinity. The density distribution of this panel is similar to the intermediate distance bin.

A slight increase in density is visible for the wing in the RR Lyrae map. This is in good agreement with the results found by McCumber et al. (2005), who found that bursts of star formation have taken place in this region of the SMC throughout the last 12 Gyr. The mean distance of the wing is slightly shorter than for the whole SMC. We find that it is located 3 kpc in front of the mean distance of the bar.

Cepheids

Figure 5.5 shows distance bins, covering the distance range from 45 kpc to 75 kpc, of 10 kpc depth each. The distribution of the Cepheids in these three slices shows a very different picture as for the old population. The distance bin of 45 kpc to 55 kpc contains 122 stars or 5% of the entire sample of the Cepheids. Most of these stars are concentrated in the eastern parts of this closest distance bin.

The central distance bin of the SMC with a distance range from 55 kpc to 65 kpc (upper right panel) contains the majority, nearly 63%, of Cepheids. The panel is dominated by a distance gradient stretching from the northeast to the southwest. The northeastern parts are closest to us. Moving to the southwest the distances increase. The highest density of the Cepheids coincides with the center found by Gonidakis et al. (2009) very well. The most southernwestern, as well as the most northwestern parts, of the OGLE III region do not contain any Cepheids.

The farthest bin, with stars at a distance of 65 kpc to 75 kpc, contains a concentration of stars in the projected central region of the OGLE III field. The eastern parts are nearly devoid of stars in this distance bin and towards the southwest the most distant Cepheids of the SMC are present. Most of the stars concentrated in the central parts of this panel have a similar distance, which is between 65 kpc and 70 kpc. In the northwest of this concentration the density of Cepheids drops drastically and in the most northwestern fields no stars of the young population are present. Recent star formation only took place at locations close to the bar of the SMC and the orientation of the young population is towards the LMC.

The lower right panel in Figure 5.5 (taken from Lorimer et al. 2007) shows the H I contours (observed by Stanimirović et al. 1999) overlayed with visible light in greyscale. The Cepheids trace the location of the bar very well. The highest density of visible light agrees with the highest density of Cepheids visible in the upper right and lower left panel. As expected we also find good agreement between the Cepheids and the H I map, as observed for the LMC (Chapter 4). The number density of Cepheids decreases from the bar to the wing and the wing itself is not visible as a significant distinct feature. This might be caused by the outflow of gas into the Magellanic Bridge, which prevents extensive recent star formation in this region. As mentioned in the previous Section, the northeastern region of the OGLE III field contains the Cepheids with the closest distance. We observe that the density decreases, but that a considerable number of stars are present. This may be a connection between the SMC and the Magellanic Bridge, even though, the gas part of the Bridge seems to emanate from the wing of the SMC. More data on a larger field is needed to confirm this. This will certainly be accomplished by the OGLE IV fields.

5.5.2 Position angle

The number of RR Lyrae stars and Cepheids in boxes of 0.3° × 0.3° in α and δ, respectively, is counted. Moving inside out, the position of the fields with the highest number density are fitted with a first order polynomial, using the center by G09 as origin.

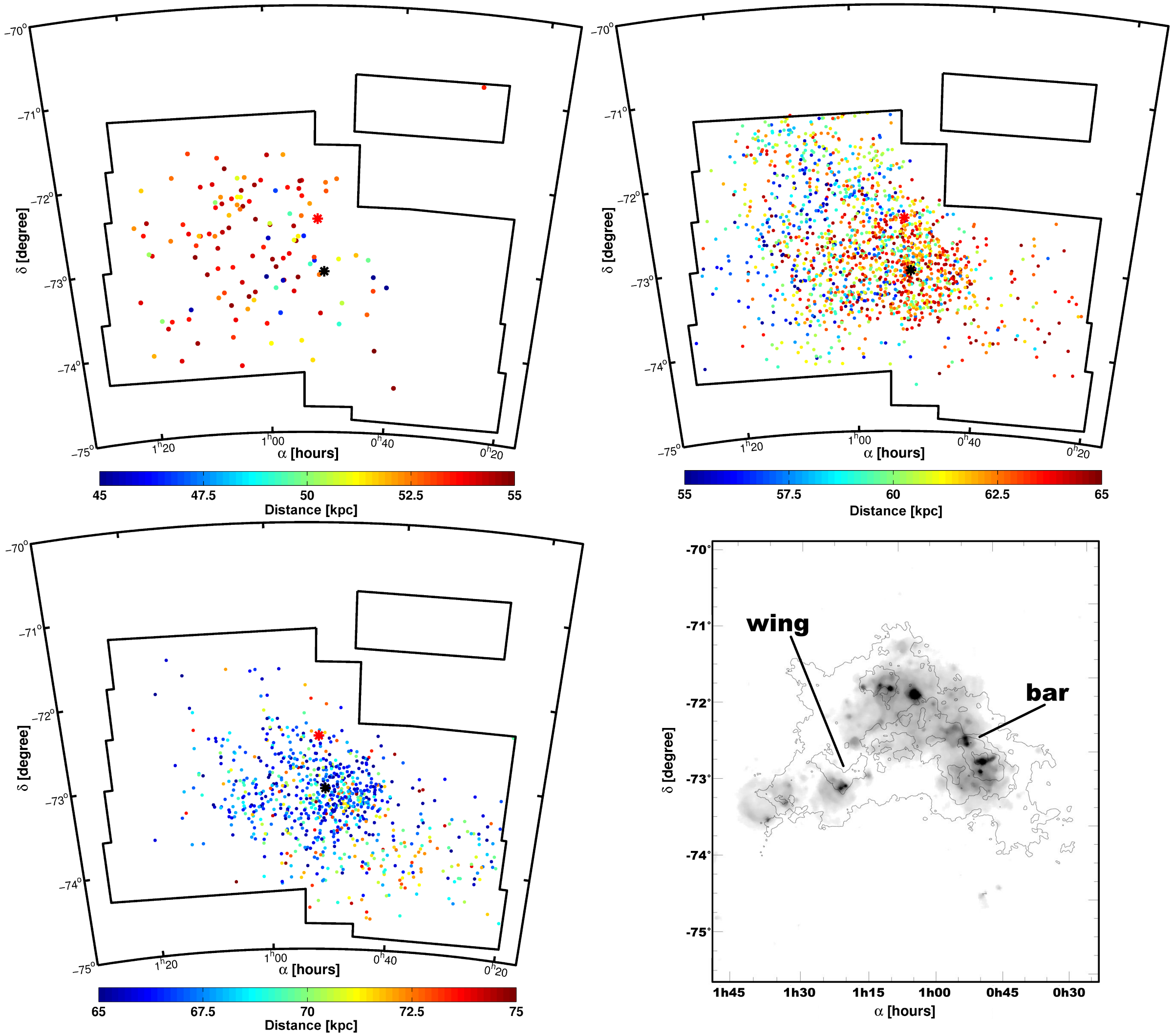

Figure 5.5: Colour coded distance map of the Cepheids in the SMC. The stars are shown in three bins of 10 kpc depth each. The upper left panel, representing the closest bin, shows that all stars are concentrated in the eastern regions of the SMC. The other panels show that for the location of the highest density moves west for more distant bins. The outer regions of the SMC are devoid of young population stars. The lower right panel is taken from Lorimer et al. (2007) and shows the visible light in in greyscale and the H I in contours. The main concentrations are in good agreement with the bar and wing of the SMC. The black asterisk indicates the center of the SMC as found by G09, while the red asterisk represents the center found by Piatek et al. (2008). The panels are populated with 122, 1585 and 815 stars, respectively, when moving from the closest to the farthest bin.

Table 5.3: Literature values of inclination (i) and position angle (θ)

type of Stars	θ [degree]	σ [degree]	i [degree]	σ [degree]	author
Cepheids	58	10	70	3	Caldwell & Coulson (1986)
Cepheids	55	17	45	7	Laney & Stobie (1986)
Cepheids	238	7	68	2	Groenewegen & Oudmaijer (2000)
Red clump	55.5	—	0.58	—	Subramanian & Subramaniam (2012)
RR Lyrae	58.3	—	0.50	—	Subramanian & Subramaniam (2012)

The position angle of the young and old population of the SMC is quite similar. While we obtain $\Theta = 71° \pm 15°$ for the Cepheids, an position angle of $\Theta = 81° \pm 21°$ is found for the old population represented by the RR Lyrae stars.

The RR Lyrae stars are distributed very homogeneously, the position angle does not change if we consider only stars located inside the innermost 3° around the center of G09. For the Cepheids we find a shift of the position angle to $\Theta = 87° \pm 12°$ if taking only the innermost 3° of the SMC into account.

The values of the Cepheids agree, within the uncertainties, with the literature values for Cepheids of 58° ± 10° found by Caldwell & Coulson (1986) and 55° ± 17° by Laney & Stobie (1986). Groenewegen & Oudmaijer (2000) found a value of $238° \pm 7°$, which is in good agreement with our result as well, given a periodicity of π of the position angle. All the different position angles are summarized in Table 5.3. The values for the RR Lyrae stars found by Subramanian & Subramaniam (2012) are a bit lower than the values obtained in our study, however they do not quote uncertainties for their values. Therefore it is hard to compare these two estimates.

5.5.3 Inclination angle

The inclination angle of the SMC is investigated by subdividing the observed fields in boxes of $0.3° \times 0.3°$ in α and δ, respectively. For each field the mean distance is determined. These values are fitted by a linear function to estimate the inclination angle.

For the RR Lyrae stars we find a very small inclination angle of $i = 7° \pm 15°$. This is in agreement with no inclination of the old population of the SMC whatsoever, as found by Subramanian & Subramaniam (2012). Contrary to the RR Lyrae stars the distribution of the Cepheids is clearly inclined with respect to our line of sight. For the western parts we find mean distances that are about 15 kpc farther away from us than the eastern parts of the SMC. Overall this results into an inclination angle of $i = 74° \pm 9°$, in very good agreement with the literature values of 68° ± 2° from Groenewegen & Oudmaijer (e.g., 2000, Table 5.3).

5.5.4 Scale height

Several investigations have shown that the SMC has a considerable depth (e.g., Mathewson et al. 1988; Crowl et al. 2001; Subramanian & Subramaniam 2012). To determine the depth of the SMC, we use the orientation of the Cepheids and RR Lyrae stars as they are on the sky and do not rotate the stars to align the major axes of the different populations. This approach is taken to keep the data comparable to other investigations that did not carry out such rotations either.

To account for the possibly different depths of stars within the observed field of the SMC (compare Figure 5.5) we divide the OGLE III field into nine rectangular fields, as well as into four rings (Figure 5.6). The depth of the SMC is determined by calculating a cumulative distribution of all stars present in the evaluated field. The distance values where 16% and 84% of all stars, respectively, have shorter individual distances than the remaining stars of the distribution, are assumed to be the lower and upper limit of the depth. These limits define the innermost 68% of the population. The depth is determined in

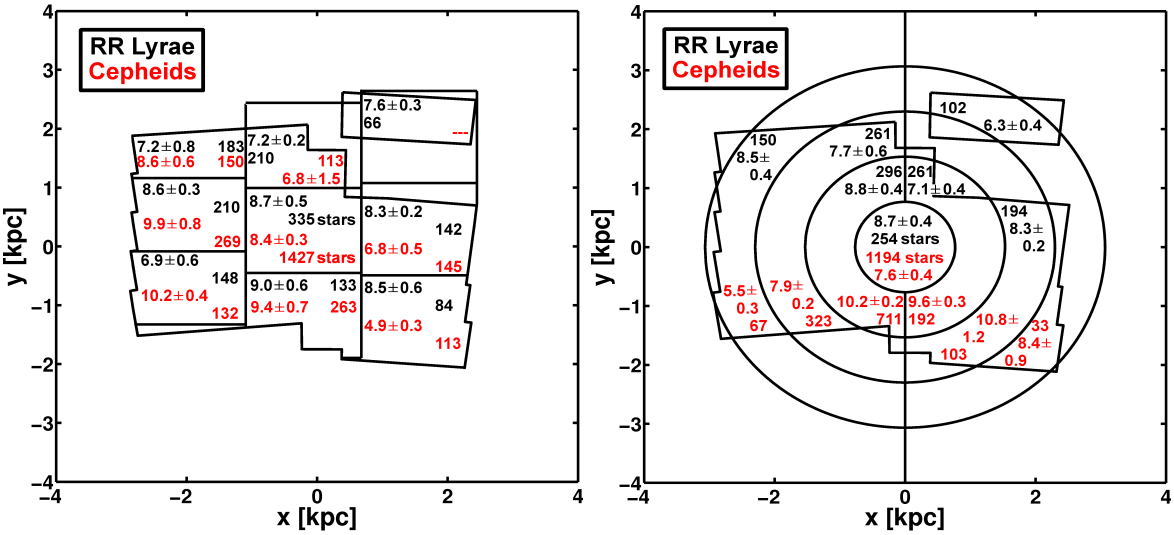

Figure 5.6: The distribution of scale height of the SMC for the RR Lyrae stars (upper panel) and Cepheids (lower panel) is calculated. In fields of 1° × 1° the scale height is determined. We find median scale heights of 5.1 ± 2.1 kpc for the RR Lyrae stars and 5.2 ± 2.3 kpc for the Cepheids. For the outer fields the density of stars is too low to compute a reliable value for the scale height. The black asterisk indicates the center of the SMC as found by G09.

each of these fields individually. To compute uncertainties for the depth we vary the minima and maxima of the depth by 5% each and take the mean difference as the error estimate.

The number of RR Lyrae stars varies from field to field and decreases steadily towards the outskirts of the OGLE III field. For the rectangular fields the depth is quite similar for all the fields chosen, as shown in the upper panel of Figure 5.6. The depth of the fields varies between 6.9 kpc and 9.0 kpc, with a mean depth of 8.0 ± 0.4 kpc. The lower panel of Figure 5.6 shows the circular fields, divided further by considering only stars with either positive or negative x-values for the non-central fields. The individual values of the fields vary between 6.3 kpc and 8.8 kpc, while a mean value 8.0 ± 0.3 kpc is found. Overall a trend of higher depth within the bar region (see Figure 5.5) as compared to the fields located to the northwest and southeast is revealed. However, the density of stars in these fields is not significantly reduced.

Most Cepheids are concentrated in the region close to the center of the SMC (Figure 5.1). However, the depth in the central fields is significantly lower for the rectangular and the circular fields than for some of the surrounding fields. This is surprising, because we would expect the highest number of stars to coincide with the largest depth. For the rectangular fields we find depth values between 4.9 kpc and 10.2 kpc, with a mean value of all fields of 8.1 ± 1.8 kpc. The separate field to the northwest contains only one Cepheid, and is thus excluded. The annuli have depth estimates ranging from 5.5 kpc to 10.8 kpc. The mean of the annular fields is 8.6 ± 1.8. Evaluating the whole OGLE III field without cutting it into pieces leads to a (mean) depth of 9.6 ± 0.3 kpc.

The depth can easily be transformed into a scale height. The scale height is the point where the density of stars has dropped by a factor of $1/e$. Therefore this quantity is half of the innermost 63%, instead of the 68% used for the depth. Therefore the equation

$$\frac{\text{scale height}}{\text{depth}} = \frac{1 - 2(\frac{1}{2e})}{2 \times 0.68} = 0.4648. \tag{5.6}$$

gives the transformation from the depth to the scale height. Using this transformation we obtain mean scale heights of 3.7 ± 0.4 kpc for the RR Lyrae stars. For the Cepheids the different field selections lead to different scale height estimates. They range from 3.7 ± 0.4 kpc for the rectangular fields to 4.5 ± 0.3 kpc evaluating the whole OGLE III field.

Several estimates of the depth have been provided in the literature leading to very different pictures of the SMC. Using Cepheids Mathewson et al. (1988) found a depth of 20 kpc, twice as much as found in our work. With RC stars S09 and Subramanian & Subramaniam (2012) concluded for the OGLE II and OGLE III field, respectively that the depth is below 5 kpc, significantly lower than our estimates. They used the width of the distribution of magnitudes of the RC stars to estimate the depth. This width originates from several different factors, such as reddening, metallicity differences, depth or intrinsic differences. Therefore it might be possible that some other parameters were overestimated and therefore too low a value was calculated for the depth. For the RR Lyrae stars present in OGLE III Kapakos et al. (2011) and Subramanian & Subramaniam (2012) used the same approach as taken by S09 for the RC stars. Both investigations found a 1σ width of the distribution of stars of $\sim$ 4 kpc. However, Subramanian & Subramaniam (2012) conclude that the depth could be as much as 14 kpc taking 3.5σ of the distribution into account. Our value is between these two and it seems that the choice of parameters for the width determination could probably be improved. Too few stars were investigated in Kapakos et al. (2011) to determine spatial differences for the line-of-sight depth. Using the complete OGLE III dataset of the RR Lyrae stars, Subramanian & Subramaniam (2012) investigated the depth of 70 very small fields and found that the northern and eastern parts may have a bit decreased depth. This is in good agreement with our results. Furthermore, the estimates of the depth relying on cluster distances agree very well with our calculations. Crowl et al. (2001) found a depth of 6 kpc to 12 kpc, while the six clusters studied by Glatt et al. (2008a) lead to a depth of $\sim$ 10 kpc, excluding NGC 419, which seems to be 6 kpc closer than the closest of the other six clusters.

5.6 Conclusions

We investigate the three dimensional structure of the young and old population of the SMC by calculating individual distances to 2522 Cepheids and 1494 RR Lyrae stars. The absolute magnitudes of the RR Lyrae stars are calculated from the photometric metallicity estimates in Chapter 3. These are based on the Fourier decomposed lightcurves of the RR Lyrae stars observed by the OGLE III survey. The period data to compute absolute magnitudes for the Cepheids are taken from the dataset of the OGLE III survey as well.

We use two different approaches to correct for the reddening that the investigated stars are experiencing. First the color differences of RC stars to their zeropoint are used to estimate an area-averaged reddening value. For the other technique individual reddening estimates of each star are calculated by comparing the color of the absolute magnitudes with the color from observed magnitudes for each star individually. Therefore we are able to correct the actual reddening at the very position of the star. The reddening maps of both techniques are shown in Chapter 2. These result in two sets of self-consistent three-dimensional maps of the SMC for the young Population I and the old Population II stars.

Using this approach we calculate a median distance of $(m-M)_{\mathrm{RRL/median}} = 19.05 \pm 0.11$ for the RR Lyrae stars and $(m-M)_{\mathrm{Cep/median}} = 19.00 \pm 0.10$ for the Cepheids. The results of the median distances are in very good agreement with each other.

Using the individual intrinsic reddening estimates for correction, the median distance estimates of the old and young population are in very good agreement with the distances obtained in the literature (Table 5.2 and Table 5.4). By applying reddening values obtained with the area averaged reddenings we find distances that are a bit higher than the literature values, but still in good agreement with many distance estimates (Table 5.2). We explain the larger distances values of the area-averaged extinction technique with unresolved differential reddening effects (e.g., Barmby et al. 2011). Additionally we do not find any evidence for a long and short distance scale problem. These results are in agreement with

Table 5.4: Results for the distances and structural parameters of the SMC.

	RR Lyrae		Cepheids	
	value	σ	value	σ
distance $(m-M)$ - area averaged reddening	19.13	0.13	19.17	0.12
distance $(m-M)$ - individual reddening	19.05	0.11	19.00	0.10
inclination [degree]	7	15	74	9
position angle [degree]	81	21	71	15
scale height [kpc]	3.7	0.4	4.5	0.3

our results for the LMC in Chapter 4, where these have been discussed in detail.

The SMC has experienced several close encounters with more massive galaxies in the recent past. Recent simulations of the SMC's orbit implies that the SMC just passed the periGalacticon (e.g., Besla et al. 2007). Moreover the LMC/SMC system may have had several very close encounters, the last one about 200 Myr ago (e.g., Yoshizawa & Noguchi 2003). These interactions led to disturbances especially of the gas of the SMC. Glatt et al. (2010) found that the cluster formation rate increased due to the interactions and reached a peak about 160 Myr ago. For Cepheids in the SMC Röck & Grebel (priv. comm.) found a very similar peak. We find that most of the Cepheids are located in the bar, where the interaction have triggered a lot of recent star formation. Comparing the density distribution of the Cepheids with the numerous young SMC clusters, investigated in Glatt et al. (2010), we find very good agreement. Interestingly only very few clusters are present in the wing, as we find for the Cepheids. This is in agreement with the results of McCumber et al. (2005) determining the evolution of the stellar populations of the wing. They concluded that some recent star formation ($\sim$ 100 Myr) has occurred, but that the wing was less active in the last several hundred Myr. Comparing the distribution of H I gas, mapped by Stanimirović et al. (1999), with the Cepheids we find good agreement for the bar region. Considerable gas is observed in the wing, while only little recent star formation has taken place there. Therefore, we interpret the differences between the structural properties of the RR Lyrae stars and the Cepheids to be an approximation for the original and the actual orientation of the gas distribution in the main body of the SMC.

The interactions have imprinted major differences between the old and young populations in the SMC. The position angle of the two populations are similar. For the Cepheids we obtain $\Theta_{\mathrm{Cep}} = 71^\circ \pm 15^\circ$, while $\Theta_{\mathrm{RRL}} = 81^\circ \pm 21^\circ$ is found for the RR Lyrae stars. Unlike the position angle the inclination angle has changed significantly between the old and young population. We find an inclination angle of $\mathrm{i}_{\mathrm{RRL}} = 7^\circ \pm 15^\circ$ for the RR Lyrae stars, which is in agreement with zero. For the Cepheids an inclination of $\mathrm{i}_{\mathrm{Cep}} = 74^\circ \pm 9^\circ$ is obtained. The inclination is orientated such that the northeast is much closer to us than the southwest and is therefore roughly pointing towards the LMC. The main part of the Magellanic Bridge emanates from the wing of the SMC. Only very few Cepheids are found in this region. However, there are weaker gaseous filaments to the north of the main part of the Bridge (Muller et al. 2003), which are in good agreement with the locations of the Cepheids in the OGLE III field. To conclude, if there is a connection additional observations of a larger field, as obtained by OGLE IV or VISTA, are needed. Overall, the comparison of the literature values of the Cepheids and the RR Lyrae stars to the results found in this study yield good agreement (Table 5.3 and Table 5.4).

But not only the orientation of the populations is different, but also the stellar density distribution. While the RR Lyrae stars have a similar density in all fields covered by OGLE III, the Cepheids are concentrated along the bar and towards the center of the SMC. This is in agreement with models that the gas in the outskirts of the SMC fuels the Magellanic Bridge and Magellanic stream (Muller et al. 2004). The wing of the SMC is not populated in the Cepheid map, while the density for the RR Lyrae stars is slightly enhanced. This is in agreement with McCumber et al. (2005), who found that the star formation in the wing shut off about 100 Myr ago and was less effective for another 100 Myr. Cepheids with ages of 30 − 300 Myr trace this age range very well. The RR Lyrae stars with ages larger than 9 Gyr should trace the bursts of star formation which have taken place up to about 12 Gyrs ago (McCumber et al. 2005). In the maps compiled from the individually dereddend distances the wing seems to be located about 3 kpc in front of the central concentration of stars located in the bar.

The RR Lyrae stars show a particularly interesting pattern at the center of the SMC (as found by Gonidakis et al. 2009). The density is reduced with respect to the fields surrounding the center, while the Cepheids have the highest density at the center. This effect is not introduced by data processing, but intrinsic to the distribution of stars on the sky. It is also not a sampling effect, the OGLE collaboration claim their sample to be nearly complete (Soszyński et al. 2010a). Therefore we believe this feature to be real. Even though the recent formation of stars might lead to a reduction in gas density, a diminishing of star density is not expected. Therefore we can not explain this feature.

The depth of the SMC has been under extensive discussion for the last decades. Mathewson et al. (1988) claimed the SMC to be very extended with a depth of 20 kpc, while S09 and Subramanian & Subramaniam (2012) and Kapakos et al. (2011) found less than 5 kpc. With our result of very differently orientated stellar populations with respect to age the claim for a unique depth is probably not very feasible. If we would measure the closest and farthest Cepheid the answer would certainly be very different than doing the same measurement for an RR Lyrae star. Therefore we decided to measure the depth of seven circular and nine rectangular fields, respectively. The median scale height that we obtain using this method are very similar for RR Lyrae stars and Cepheids. For the RR Lyrae stars we find a scale height of 3.7 ± 0.4 kpc (corresponding to a depth of 8.0 kpc), while the scale height for the Cepheids is measured, depending on the field selection, between 3.7 ± 0.3 kpc and 4.5 ± 0.3 kpc (or a depth of 9.6 kpc). Usually the scale height for the young population is expected to be smaller, than for old populations. Finding similar values is only feasible, assuming strong interactions of the SMC with another galaxy that have either pushed the gas to the outskirts, or that new gas has been falling in from this other galaxy. For the central parts of the SMC bar we find the scale height of the RR Lyrae stars and the Cepheids to be decreased. These results are in disagreement with a bulge-like feature at the center of the SMC, proposed by S09. These scale height values agree well with the results by Crowl et al. (2001), who used clusters for their investigation.

The actual shape of the SMC is still under debate. Crowl et al. (2001) proposed that the depth extent might be larger than the spatial extent on the sky. However, Nidever et al. (2011) proposed, using photometric and spectroscopic data of fields in the outskirts of the SMC, that we might underestimate the spatial extent of the SMC. Only large scale surveys of the whole SMC including the outskirts will solve this issue.

The very similar scale height for young and old populations implies that the gas content was significantly changed during the interactions of the SMC. We find as expected a wider distribution of old star, due to tidal heating. But we only see this effect in projection on the sky. For the scale height of the SMC we find very similar results. Therefore gas was removed from the northwest and southeast, as well as from the outskirts of the SMC, while the gas along the bar was stretched along the line of sight. Otherwise we would expect the scale height of the Cepheids to be lower than for the RR Lyrae stars.

"If there's nothing wrong with me...maybe there's something wrong with the universe!"
Beverly Crusher - Star Trek: The Next Generation (Remember Me)

6

Reddening maps, metallicity distribution function and three-dimensional maps of RR Lyrae stars towards the Galactic Bulge and in the Sagittarius Stream

We present reddening maps, metallicity distribution functions and three-dimensional maps of a region close to the Galactic bulge which covers a part of the Sagittarius stream located behind the bulge. Quite severe differential reddening is found with values up to $E(V-I) = 4.63$ mag. The sample of extinction corrected RR Lyrae stars is divided into two distance bins. The Galactic bulge region is investigated using RR Lyrae stars with heliocentric distances of 3 kpc to 15 kpc. For the Sgr stream a distance bin of 18 kpc to 32 kpc is chosen. Using two different reddening laws we find median distances of the bulge of 8.0 ± 1.7 kpc and 8.8 ± 1.6 kpc, respectively. No strong indications for a bar are found for the RR Lyrae stars in the bulge region studied here. For the Sgr stream median distances of 24.0 ± 3.6 kpc and 25.2 ± 3.9 kpc are obtained using the two reddening laws. The density distribution indicates that the stream itself is rather thin, while around the stream an extended population with low density of RR Lyrae stars is present. This is interpreted as the slow dispersion of the stream into the Galaxy. The MDF of the bulge region reveals a nearly Gaussian distribution of the metallicities, with a mean value of $[\mathrm{Fe/H}]_{\mathrm{ZW84}} = -1.25$ dex. The metallicity of the Sgr stream is lower ($[\mathrm{Fe/H}]_{\mathrm{ZW84}} = -1.50$ dex) and the shape of the MDF is slightly asymmetric. For metallicities $[\mathrm{Fe/H}]_{\mathrm{ZW84}} > -1.0$ dex the number of RR Lyrae stars is decreased compared to a Gaussian distribution. This mean metallicity estimate for the RR Lyrae stars is in good agreement with the RR Lyrae stars of the Large Magellanic Cloud. We find, furthermore, very good agreement of our results with the literature for the Galactic bulge as well as for the Sgr stream.

This chapter is based on Haschke & Grebel (in prep.)

6.1 Introduction

How has the MW been formed? Searle & Zinn (1978) proposed that the MW has accreted several satellite galaxies throughout its history and that this had a significant impact on the build-up of the Galaxy, especially on the halo. However, it has not been clearly resolved yet how many stars of the halo were born in situ, especially in GCs, and how many stars were accreted (e.g., Bell et al. 2008; Martell et al. 2011). The models predict that a merger with a galaxy of the Magellanic type is needed to build up the halo (e.g., Robertson et al. 2005), but only debris of mergers with smaller constituents have been found so far (e.g., Newberg et al. 2002; Belokurov et al. 2007; Grillmair 2009). This indicates that such a larger merger would have happened many Gyrs ago and its tracers have been dispersed over the Galaxy.

The first proof for an ongoing merger event was presented by Ibata et al. (1994) with the finding of the Sgr dwarf galaxy. This was the first detection of a stellar stream from a merger event in our Galaxy. Since then large survey programs have shown several streams and overdensities which might constitute the tidal debris of former or ongoing merger events (e.g., Yanny et al. 2003; Duffau et al. 2006; Martin & Jin 2010). The properties of Sgr have been extensively investigated using a vast set of stellar tracers (e.g., Majewski et al. 2003; Peñarrubia et al. 2011; Carlin et al. 2012) as well as numerical simulations (e.g., Law & Majewski 2010; Myers et al. 2010) to constrain the origin and orbit of Sgr, but also, for instance, to find evidence for the shape of the gravitational potential of the MW.

The progenitor of Sgr was a dSph with a mass of approximately $10^9\,M_\odot$ (Niederste-Ostholt et al. 2010). These authors also estimated that nowadays 70% of the original luminosity of the galaxy is located in the stellar stream. The stream stretches basically across the whole sky, while the core of Sgr is associated with the GC M54. The core fragment of Sgr is currently, in projection, not very far from the Galactic bulge and moving north towards the Galactic disk. Some of the fields of the OGLE III are located close to the bulge region of the Galaxy (Szymański et al. 2011). Therefore these fields are also close to the core region of Sgr and cover parts of the leading arm of Sgr (compare our Figure 6.1 with Figure 1 in Niederste-Ostholt et al. 2010).

Populations of purely old stars are very powerful tracers to estimate the early history of a galaxy. RR Lyrae stars are such tracers and due to their variability they are easily recognizable. Furthermore they are excellent distance tracers and their lightcurves can also be used to estimate photometric metallicities (Simon 1985; Kovács & Zsoldos 1995). The GC M54 has been intensively investigated for RR Lyrae stars and Sollima et al. (2010) found more than 100 of them. A mean distance of $(m - M) = 17.13 \pm 0.11$ mag (26.7 ± 1.4 kpc) was obtained by these authors. Using photometric metallicity estimates of mainly RR Lyrae stars, a mean metallicity of $[\mathrm{Fe/H}] = -1.65 \pm 0.16$ dex was found on the metallicity scale of Layden (1994), which is basically identical to the scale of ZW84. The RR Lyrae stars of the stellar stream of Sgr have been investigated in several different studies. Vivas et al. (2005) found for 16 spectroscopically investigated stars a mean metallicity of $[\mathrm{Fe/H}] = -1.76 \pm 0.22$ dex on the Layden (1994) metallicity scale. In stripe 82 of the Sloan Digital Sky Survey (SDSS) 270 $\deg^2$ along the celestial equator were repeatedly observed for about 80 times. This allows one to determine parameters of variable stars with high precision. Watkins et al. (2009) and Sesar et al. (2010) investigated these data and found many RR Lyrae stars, several of which belong to the trailing arm of the Sgr stream. Watkins et al. (2009) found a mean distance of 26.1 ± 5.6 kpc ($(m - M) \sim 17.1$ mag), while Sesar et al. (2010) obtained a mean distance of $(m - M) = 17.2$ mag (~ 27.5 kpc) to these RR Lyrae stars. The mean metallicities derived for the RR Lyrae stars possibly belonging to Sgr in SDSS stripe 82 are also rather different. While Watkins et al. (2009) derived their own metallicity-period-ϕ_{31} relation based on the Fourier decomposition method, inspired by Jurcsik & Kovács (1996), Sesar et al. (2010) adopted the method of Ivezić et al. (2008) using SDSS photometry. Watkins et al. (2009) found mean values of $[\mathrm{Fe/H}] = -1.43 \pm 0.30$ dex while Sesar et al. (2010) obtained $[\mathrm{Fe/H}] = -1.2$ dex. The two metallicity scales adopted in these studies may be different. The SDSS metallicity scale is about 0.07 dex more

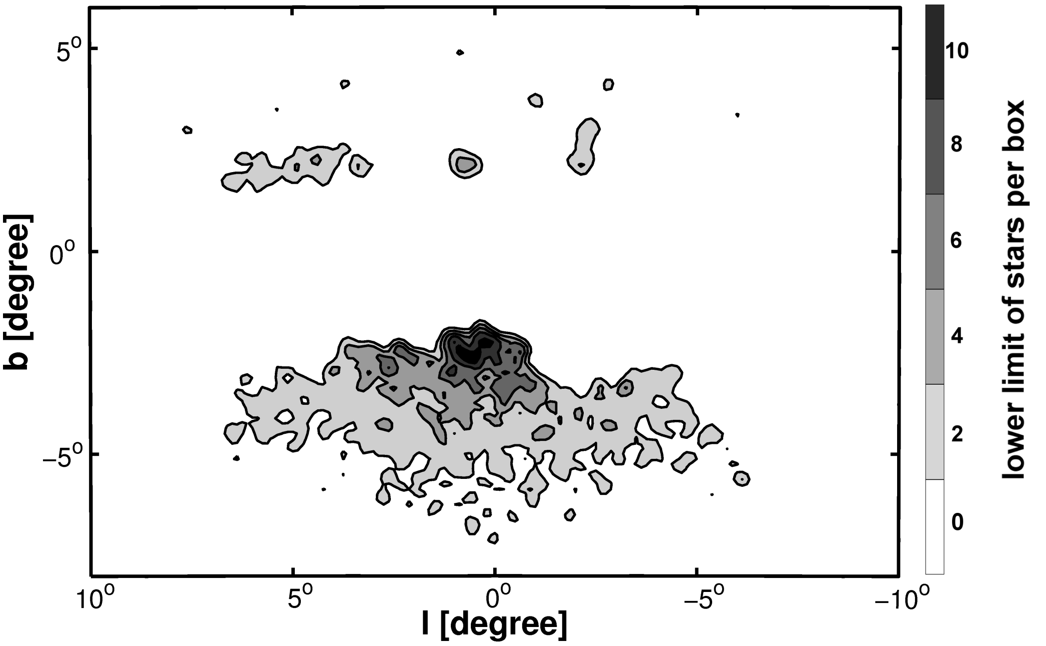

Figure 6.1: Density map of the RR Lyrae stars observed by OGLE III towards the Galactic bulge. The main field is located south of the Galactic equator. Comparing the observed field with Figure 1 in Niederste-Ostholt et al. (2010) we see that the Sgr stream is part of the observations.

metal rich than ZW84 (Sesar et al. 2010). For the metallicity scale used in Watkins et al. (2009) no calibration to other scales is provided. The MACHO survey (Alcock et al. 2000) and the OGLE survey are looking for microlensing events and monitor therefore high density regions, such as the Galactic bulge. The bulge fields chosen for the two survey are similar but overlap only in a minor fraction of fields. In the MACHO survey of the bulge more than 2600 RR Lyrae stars were detected and Kunder & Chaboyer (2008) used the Fourier decomposition method of Kovács & Zsoldos (1995) to determine metallicities on the scale of ZW84. For the Galactic bulge a mean metallicity of $[Fe/H] = -1.25$ dex was found, while the stars located at the distance of the Sgr stream behind the bulge have a mean metallicity of $[Fe/H] = -1.55$ dex. For the part of the trailing arm of the Sgr stream observed by MACHO Kunder & Chaboyer (2009) obtained a distance of 24.8 ± 0.8 kpc ($(m - M) = 16.97 \pm 0.07$ mag). The RR Lyrae stars of the OGLE III survey have been used to determine parameters of the Galactic bulge (Pietrukowicz et al. 2011, from now on PUS11). These authors found a mean metallicity of $[Fe/H] = -1.02$ dex, on the metallicity scale of J95, and a mean distance of 8.35 ± 0.43 kpc. The stars located at the distance of the Sgr stream have been excluded by PUS11.

This Chapter is organized as follows. First the reddening values of all RR Lyrae stars in the sample are determined in Section 6.2 and comprised in a reddening map. In Section 6.3 the actual photometric metallicities and dereddend distances of these stars are calculated using different extinction laws. The MDF of the bulge and the region behind the bulge are shown in Section 6.4. Three dimensional maps of different distance bins covering the Galactic bulge and the Sgr stream are presented in Section 6.5. The final Section 6.6 summarizes and concludes this chapter.

6.2 Reddening maps

Towards the Galactic bulge severe extinction is present and differential reddening leads to varying corrections for stars along the same line of sight. Therefore it is important to obtain reliable reddening maps with good spatial resolution. In PUS11 the RR Lyrae stars observed during the third phase of the OGLE survey were used to determine the ratio of total to selective extinction $R_I = A_I/E(V-I)$, which was found to be anomalous compared with the mean values evaluated by Clayton & Cardelli (1988) and used by SFD98 for their all-sky maps. A value of $R_I = 1.085 \pm 0.013$ was determined by PUS11 which is in good agreement with Udalski (2003a), but deviates significantly from the mean value of $R_I = 1.4$ of the full sky (SFD98). The selective extinction $E(V-I)$ for each RR Lyrae star in PUS11 was calculated by using the relation for the intrinsic color $(V-I)_0$ by Piersimoni et al. (2002). This relation was determined from stars of the GC NGC 3201 which has a metallicity of [Fe/H] = −1.42 dex. The mean metallicity of the bulge as found by PUS11 is [Fe/H] = −1.02.

In Chapter 2 the computation of reddening maps has been introduced, which takes the individual properties of each RR Lyrae star into account. We use the relations of Catelan et al. (2004) to calculate the absolute magnitudes of each RR Lyrae star in the V and I band individually. With these magnitudes the intrinsic color $(V-I)_0$ of each star is computed using its individual metallicity, period and Fourier parameter ϕ_{31}.Using this method we may be able to improve the reddening maps for the Galactic bulge. However, the difference between the mean color of our sample and the color of an RR Lyrae star at a metallicity of [Fe/H] = −1.42 dex is just 0.02 mag and we do not expect large differences.

The reddening values used in PUS11 are not shown in a map. In Figure 6.2 the reddening map obtained with our method is presented. It is obvious that the reddening is most severe close to the inner regions of the bulge of the MW. The disk itself, however, is not part of the observations of OGLE III.

Absolute magnitudes of the RR Lyrae stars are calculated using the metallicity scales by J95 and ZW84, respectively (see Section 6.3 or Chapter 3). Comparing the differences in $(V-I)$ color of these two scales we find that they are negligible. A median difference of $(V-I) = -0.01$ mag is obtained. The maximum reddening measured for a single RR Lyrae star is $E(V-I) = 4.63$, while 912 RR Lyrae stars or 8% of the whole sample experience reddening more severe than $E(V-I) > 2$.

6.3 Metallicity and distance determinations

The metallicity of each RR Lyrae star is estimated using the approach described in Chapter 3. We will only shortly summarize the most important steps here.

In Kovács & Zsoldos (1995) and Jurcsik & Kovács (1996) it was shown that the Fourier decomposition of an RR Lyrae star lightcurve can be used to determine the metallicity of this star. Smolec (2005) extended the relation between the period P, the Fourier phase parameter ϕ_{31} and the metallicity to be applicable to lightcurves taken in the I band as in the OGLE dataset.

$$[\mathrm{Fe/H}] = -3.142 - 4.902P + 0.824\phi_{31} \tag{6.1}$$

These parameters are provided by the analysis of the OGLE collaboration and are presented in Soszyński et al. (2011). PUS11 has used Equation 6.1 to determine the metallicity of the RR Lyrae stars of the bulge present in the OGLE III dataset. However, the stars located behind the bulge were ignored by these authors. The Sgr stream passes through this region of the sky and we will try to derive the metallicity distribution of the RR Lyrae stars belonging to the stream.

The relation by Smolec (2005) reveals metallicities on the scale of J95. This metallicity scale is about 0.3 dex more metal-rich than the widely used scale by ZW84 (Gratton et al. 2004). Using the relation of Papadakis et al. (2000) (see Chapter 3) we transform the metallicities from the scale of J95 to the ZW84 scale and do all distance calculations in both metallicity scales.

The absolute magnitude of the RR Lyrae stars in the V band is determined by applying the relation by Clementini et al. (2003)

$$M_V = 0.214[\mathrm{Fe/H}] + 0.84 \tag{6.2}$$

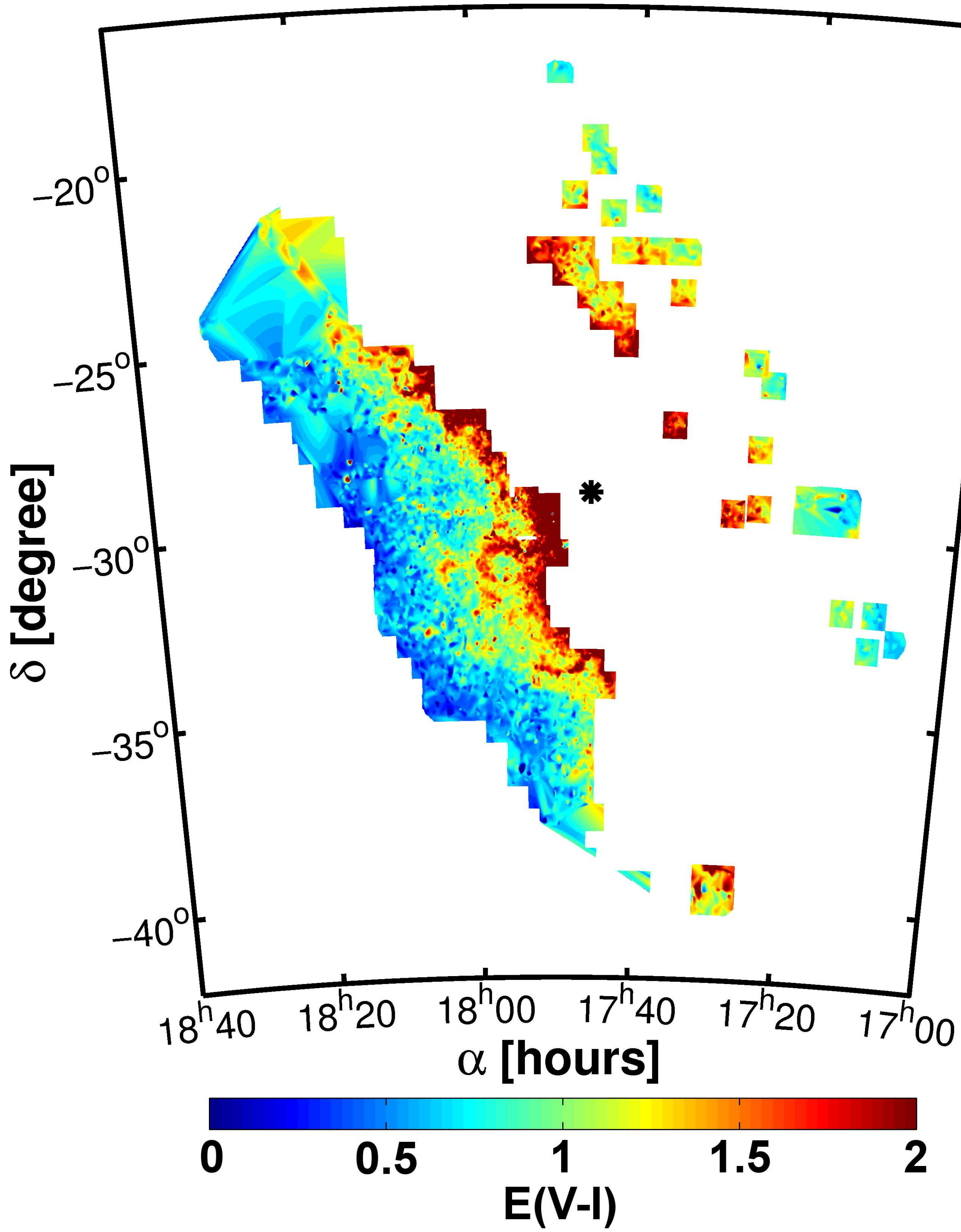

Figure 6.2: Reddening map of the OGLE III field towards the Galactic bulge. The reddening is computed comparing the observed colors of the RR Lyrae stars with the colors computed from their absolute magnitudes. The maximum reddening found for a single RR Lyrae star in the sample is $E(V-I) = 4.63$. Some regions of the OGLE III field have small gaps between each other, which are interpolated by the fitting routine (compare Figure 6.4). The black asterisk indicates the location of the Galactic center.

Benedict et al. (2011) concluded that this relation fits their new *HST* data best and that no significant difference to the quadratic relations, presented in Chapter 3, can be found. For the *I* band we use the equation by Catelan et al. (2004)

$$M_I = 0.471 - 1.132 log_{10} P + 0.205 log_{10} Z \tag{6.3}$$

Before we are able to determine which stars belong to the Sgr stream, we need to calculate the distances to each object individually. Because of the high extinction present towards the Galactic center this is not straightforward.

In Chapter 6.2 we have shown that the calculation of selective extinction is rather easy. However, the computation of a total extinction might introduce significant differences. As mentioned in Chapter 6.2, PUS11 found that the extinction law is anomalous towards the Galactic bulge. The distribution of RR Lyrae stars in their color-magnitude diagram was binned and fitted with a linear regression. These procedure led to a value of $R_I = 1.085 \pm 0.013$. This result is in good agreement with Sumi (2004), who found $R_V = 1.964 \pm 0.085$ using the observations of OGLE II towards the bulge. Several other investigations of the central region of the Galaxy found similar results. Udalski (2003a) used red giants of OGLE II to determine an anomalous extinction law in agreement with PUS11 towards the Galactic bulge. The analysis of near infrared data together with OGLE data towards the bulge by Nishiyama et al. (2008) led to a value of $R_V = 1.8$. With HST data of the central $6.6' \times 6.6'$ field of the Chandra bulge field, Revnivtsev et al. (2010) confirmed the anomalous extinction law of the other investigations. But not only local investigations of the Galactic center lead to these anomalous extinction laws. Using 2MASS data to study the large scale extinction law, Zasowski et al. (2009) showed that the Galactic bulge has a shallower extinction law.

The different extinction law might be a result of variations in the composition of the dust. Fritz et al. (2011) showed that the distribution of extinction is not consistent with a dust model consisting of pure carbonaceous and silicate grains only. Mapping the innermost parts of the Galactic center region Arendt et al. (2008) found that the amount of PAHs is higher than usual, while no extreme interstellar radiation field (ISRF) is present. The PAHs are larger than usual dust grains and have therefore a higher heat capacity, which leads to a different behavior of the extinction law. The bulge region is also very gas rich, the central molecular zone contains about 10% of the molecular gas of the Galaxy (e.g., Morris & Serabyn 1996). The molecular gas is influencing the extinction as well. Active star formation in the central regions leads to increased radiation fields and supersonic shocks. These might effect the PAHs and locally alter the extinction, as observed for instance by Fritz et al. (2011). Another effect which might play a role here is the coating of ice around dust grains. As pointed out by Draine (2003) dust will be covered by ice in very dense environments. This might be the case for the Galactic center region.

To determine the distance of each RR Lyrae star we use

$$D = 10^{\frac{(v-V-A_V)}{5}+1} = 10^{\frac{(v-V-(R_V\,E(V-I)))}{5}+1} \tag{6.4}$$

or the equivalent equation using *I* band measurements.

After calculating the individual distances to all stars, we investigate the median distance to the group of stars we believe to belong to the Galactic bulge. A subsample of RR Lyrae stars, from now on called bulge, is produced which contains only stars with distances between 3 kpc and 15 kpc. Using the *I* band relation of Equation 6.4 with the value of R_I from PUS11 a mean distance of 8.8 ± 1.6 kpc is found for 10339 stars. If not stated differently, the uncertainties of all distances presented here are the standard deviations of the group of stars present in each subsample. For the *V* band, applying Sumi (2004), 10194 RR Lyrae stars are present in the designated distance bin. The RR Lyrae stars have a median distance of 9.7 ± 1.7 kpc. In Figure 6.3 the distribution of stars is shown with the black dotted line for the *V* band value by Sumi (2004) and the blue line for the *I* band value of PUS11. Distances calculated with

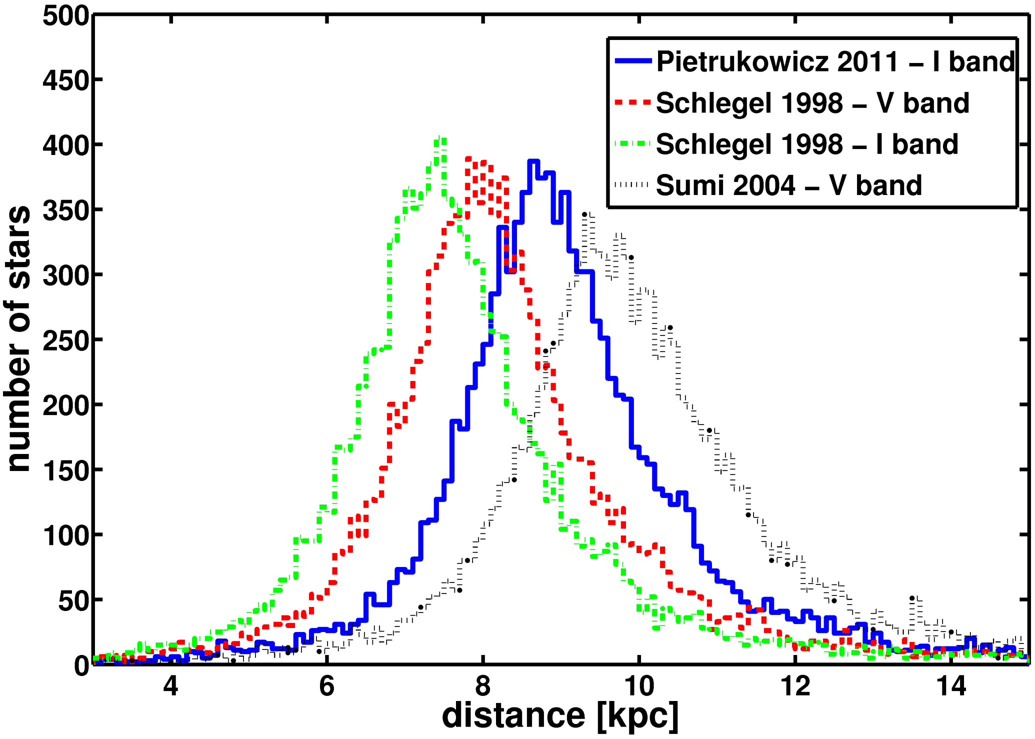

Figure 6.3: Distance estimates for the RR Lyrae stars using different values of R_x.

metallicities on the scale of ZW84 are on average 0.2 kpc and 0.1 kpc farther away, respectively, while the standard deviations stay unchanged.

The median distances estimated here are a bit larger than the median values usually assumed for the Galactic center. Therefore we decide to test the distance estimates with the values of $R_{V/I}$ from SFD98. They found $R_V = 2.31$ and $R_I = 1.4$. These values lead to median distances of 8.0 ± 1.7 kpc for the V band and 7.5 ± 1.7 kpc for the I band. The difference between the V and I band magnitudes originates from the calibrations of the absolute magnitudes. By applying the V band relation of Catelan et al. (2004) the median distance would decrease by 0.25 kpc. Using the metallicities of ZW84 the median distances are 0.1 kpc farther away. The distributions are also shown in Figure 6.3 with the red dashed line for the V band and the green dash-dotted line for the I band. The median distances are shorter by $\sim$ 1.5 kpc than the distances determined by using the values of PUS11 and Sumi (2004).

These results show how much the distance determinations depend on the extinction laws and with our sample it is impossible to determine which law is the most trustworthy one. We do expect that the RR Lyrae stars are homogenously distributed around the Galactic center and therefore the median distance estimates are compared with the recent literature on the distance of the Galactic center, i.e. Sag A*. The median values of SFD98 for the V band and PUS11 for the I band are the closest matches to the literature values of Ghez et al. (2008) and Gillessen et al. (2009) (see Section 6.5). Therefore the distances from these two extinction laws are used in our further evaluation of the data.

We test whether the Galactic bar has an influence on our dataset. Comparing our fields with the simulations by Cabrera-Lavers et al. (2007) it turns out that the inclined bar is confined to the innermost parts of the disk and should not have a significant influence on our data.

In Figure 6.4 and Figure 6.5 the distribution of distances of the RR Lyrae stars on the sky are shown for the V band and I band, respectively. It is obvious that the distances of the V band determination are in general a bit lower. Especially the part of highest reddening close to the Galactic center (compare Figure 6.2) is significantly bluer than the other regions. It seems that the total extinction is overestimated

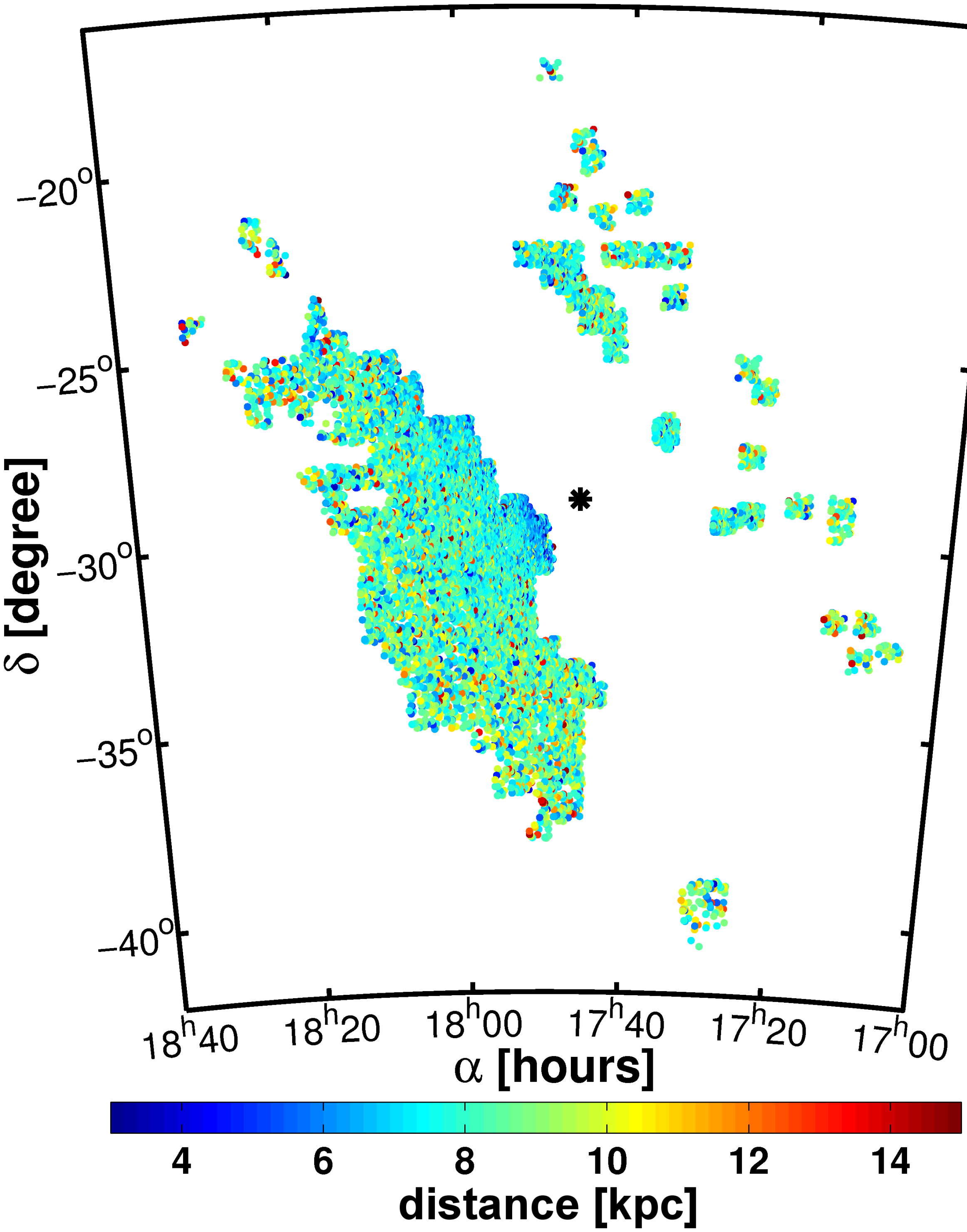

Figure 6.4: Color coded distances of RR Lyrae stars belonging to the Galactic bulge region. All stars between 3 kpc and 15 kpc are color coded with respect to their distance using the R_V value of SFD98.

in this part. This effect does not appear in Figure 6.5, which used the R_I value of PUS11.

For the regions located behind the Galactic bulge we expect to find tracers of the Sgr stream. In projection the stream passes very close to the Galactic center at a distance of roughly 20 kpc to 30 kpc from us. The RR Lyrae stars present in the stream were formed long before the interactions of the dSph with the MW started. Therefore these stars trace the conditions present before the accretion and interaction. However, it is difficult to disentangle RR Lyrae stars intrinsic to the MW from those, that were brought in by Sgr. Therefore the distances are compared and we look for overdensities in the sample. For stars with Galactic origin we expect a smooth distribution. In Figure 6.6 and Figure 6.7 the RR Lyrae stars of the distance bin 15 kpc to 35 kpc are shown for the V band and I band, respectively.

For the V band 537 stars have distances between 15 kpc and 35 kpc. With the I band estimates we obtain 622 stars inside this distance bin. Computing a median distance is rather meaningless for this sample. Investigating Figure 6.6 and Figure 6.7 we find that a box between $18^{h00} < \alpha < 18^{h20}$ and $-30° < \delta < -25°$ is dominated by a single color, indicating a distance around 25 kpc. These coordinates are in good agreement with the expected location of the Sgr stream. We will investigate the metallicity of this region in Section 6.4 and the three-dimensional structure in Section 6.5.

The number of stars found at distances greater than 35 kpc is very low. These stars do not clump into overdensities and are excluded from our investigation. Therefore, we do not show a Figure to illustrate their distribution on the sky.

6.4 Metallicity distribution function

In PUS11 the MDF of the Galactic bulge was investigated using magnitude cuts to select the stars. A mean metallicity of $[\mathrm{Fe/H}] = -1.02$ dex on the metallicity scale of J95 was found. We use a slightly different selection of stars likely belonging to the Galactic bulge. We use the dereddend distances, using the R_V value of SFD98, to infer whether a star belongs to the bulge. Therefore our sample of stars is slightly different to the choice of PUS11. In total 10354 stars have distances between 3 kpc and 15 kpc from us and are counted into the bulge sample. The mean metallicity of these stars to the scale of J95 is $[\mathrm{Fe/H}] = -0.97$ dex with a standard deviation of 0.30 dex. These values are transformed to the metallicity scale of ZW84 using the relation by Papadakis et al. (2000). This leads to a mean metallicity of $[\mathrm{Fe/H}] = -1.25 \pm 0.31$ dex. The MDF is shown with the black dotted line in Figure 6.8.

For metallicities greater than -1 dex, the black dotted line in Figure 6.8 is basically identical with the green dashed line, which represents the whole sample of RR Lyrae stars present in the OGLE III field of the bulge. For lower metallicities significant deviations are obvious. This indicates that the sample of RR Lyrae stars located behind the bulge have on average lower metallicities than those in the bulge. The stars in the distance bin of 15 kpc to 35 kpc from us are shown with the blue line in Figure 6.8. The mean metallicity of these 520 stars is found to be $[\mathrm{Fe/H}]_{\mathrm{J95}} = -1.17$ dex. This translates to $[\mathrm{Fe/H}]_{\mathrm{ZW84}} = -1.44$ dex. Comparing Figure 1 in Niederste-Ostholt et al. (2010) with the OGLE III fields of observation we conclude that the trailing arm of Sgr passes through the fields with $\alpha > 18^h$ and $\delta > -30°$. We further restrict the selection of stars to fields with these coordinates and distances between 15 kpc and 35 kpc. The metallicity changes by only -0.02 dex. Restricting the distances of the sample even further to 18 kpc to 32 kpc lowers the mean metallicity to $[\mathrm{Fe/H}]_{\mathrm{J95}} = -1.23$ dex or $[\mathrm{Fe/H}]_{\mathrm{ZW84}} = -1.50$ dex, respectively. The standard deviation of this sample is 0.28 dex and the distribution of the MDF is shown with the red dash-dotted line in Figure 6.8. In the Figure it is obvious, that the number of stars with high metallicity ($[\mathrm{Fe/H}] > -0.9$ dex) within the distance bin containing Sgr is clearly reduced compared to the full sample of stars with distances greater than 15 kpc. We interpret that as an indication that there are relatively few field RR Lyrae stars from the population of the MW, and that most of the RR Lyrae stars in this bin originate from Sgr. However, there might still be considerable contamination, which can not be disentangled here.

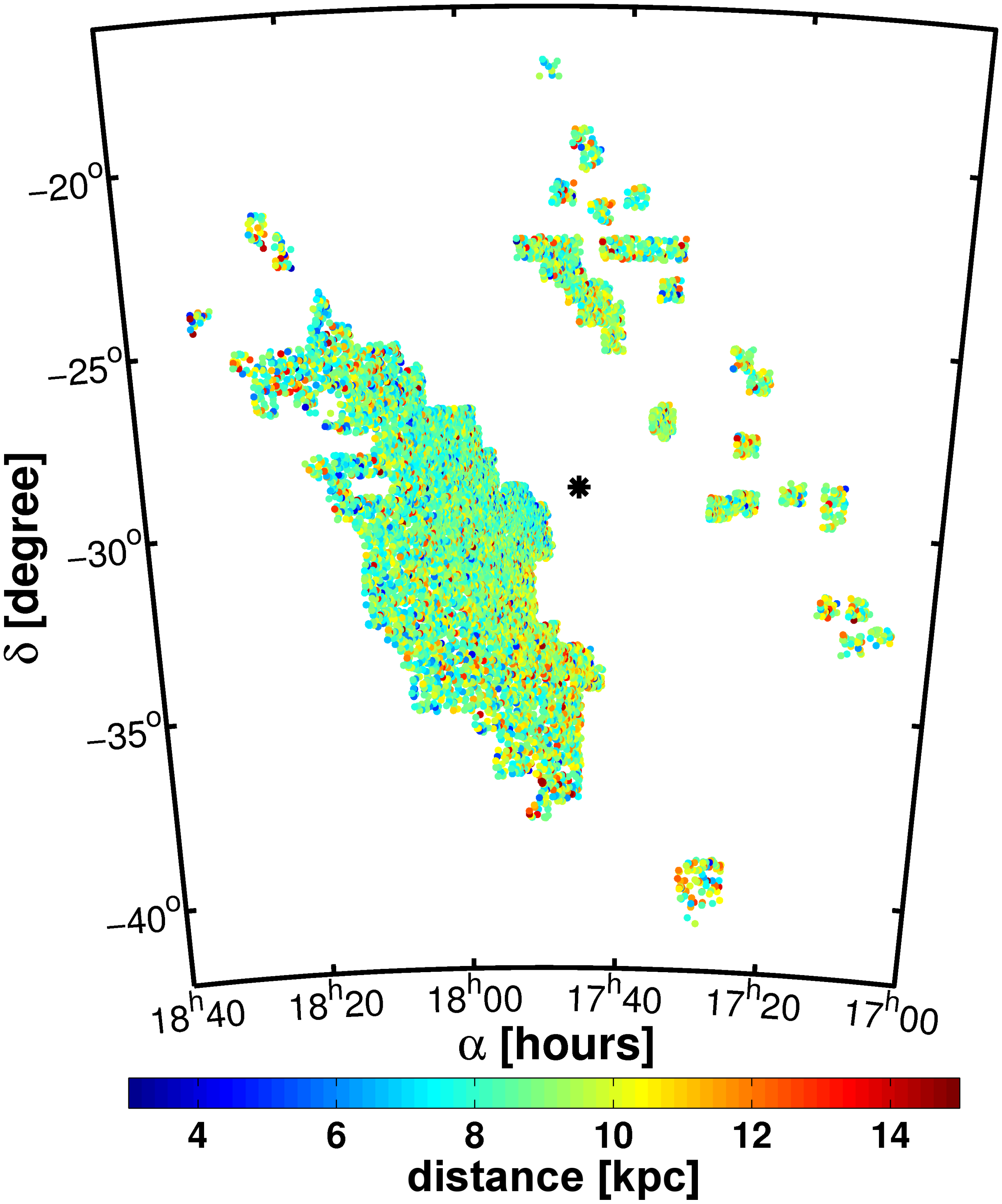

Figure 6.5: Distances to RR Lyrae stars belonging to the Galactic bulge region. The color-coding represents the distances using the R_I value of PUS11 of the single stars. Only stars with distances between 3 kpc and 15 kpc are shown.

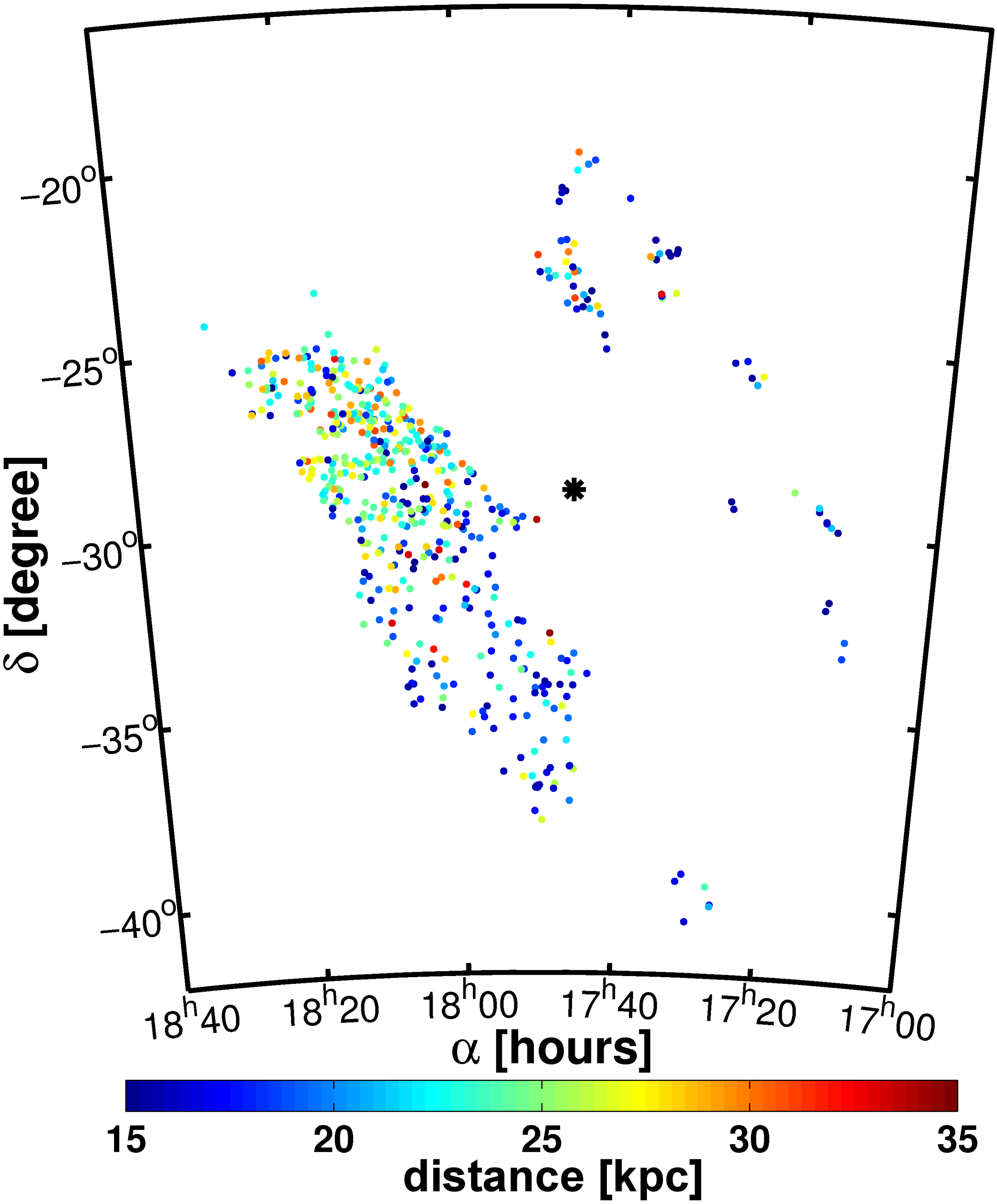

Figure 6.6: Distribution of RR Lyrae stars at the distance of the Sgr stream between 15 kpc and 35 kpc and located in the OGLE bulge fields. The color coding indicates the distances using the R_V value of SFD98.

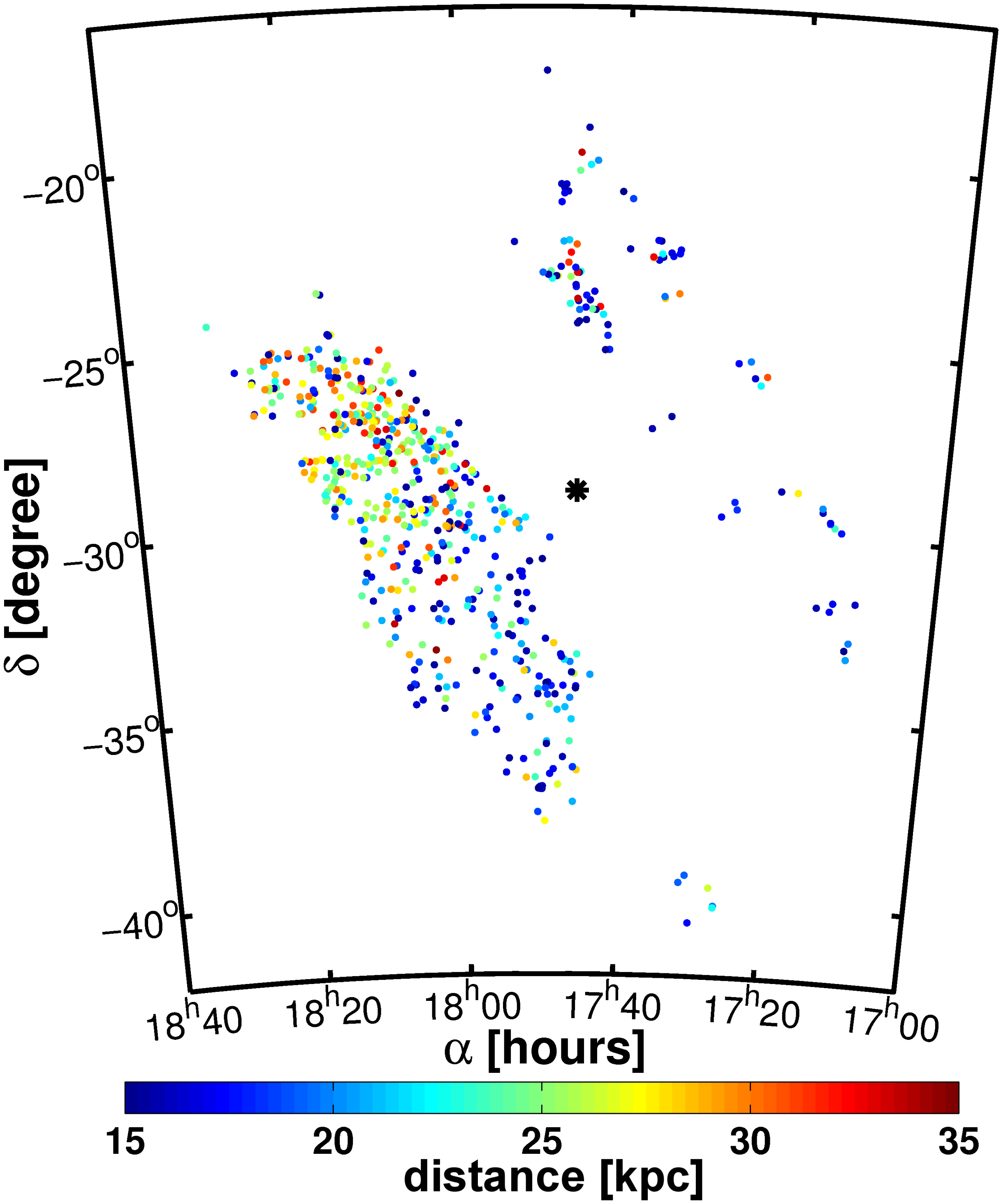

Figure 6.7: RR Lyrae stars with color coded distances between 15 kpc and 35 kpc. The distances are calculated using the R_I value of PUS11.

Table 6.1: Binsizes of the fields evaluated to obtain the density distribution of RR Lyrae in the Galactic bulge and in the Sgr stream.

	3 – 15 kpc	15 – 35 kpc
α bin [degree]	0.250	1.0
δ bin [degree]	0.125	0.5
distance bin [kpc]	0.250	1.0
l bin [degree]	0.125	0.5
b bin [degree]	0.125	0.5
X bin [kpc]	0.125	0.5
Y bin [kpc]	0.125	0.5
Z bin [kpc]	0.125	0.5

The Sgr stream has significant differences and a substantial spread in its metallicity, which are explained by an intrinsic metallicity gradient in the progenitor galaxy (Chou et al. 2007). Therefore it is not possible to compare the metallicity estimates of different fields within the stream in a straightforward manner. Additionally the different metallicity estimates rely on a diversity of scales, which may introduce additional uncertainties. In Morgan et al. (1998) the RR Lyrae stars located in the Galactic bulge fields of OGLE I were investigated. The Fourier decomposition method was used to determine metallicities and a mean value of $[\mathrm{Fe/H}]_{\mathrm{J95}} = -1.34 \pm 0.37$ dex was obtained, slightly lower than the our value. The MACHO fields investigated by Kunder & Chaboyer (2008) are slightly different from the OGLE III fields. However, the mean metallicity of the RR Lyrae stars found with the Fourier decomposition method of Jurcsik & Kovács (1996) has a value of $[\mathrm{Fe/H}]_{\mathrm{ZW84}} = -1.55 \pm 0.02$ dex and is basically identical to the value of our investigation. The RR Lyrae stars observed in stripe 82 of SDSS are quite far away from the Galactic bulge. Therefore the differences in the mean metallicity to the investigations by Watkins et al. (2009, $[\mathrm{Fe/H}] = -1.43 \pm 0.30$ dex) and Sesar et al. (2010, $[\mathrm{Fe/H}]_{\mathrm{ZW84}} = -1.27$ dex) are not very surprising. For the investigations obtained in similar regions of the sky very good agreement is found.

Additionally it is worth mentioning that the mean metallicity of the RR Lyrae stars in the portion of the Sgr stream studied here is the same as for the LMC RR Lyrae stars (Chapter 3). This result supports the idea that Sgr was a rather massive galaxy (Niederste-Ostholt et al. 2010) before its disruption. The shape of the MDF is a bit different, there are more stars with high metallicity in the LMC. That could, however, be an effect of the small number of stars detected for the Sgr stream.

6.5 Three dimensional structure

The three-dimensional structures of the Galactic bulge and the Sgr stream are analyzed as in Chapter 4 and Chapter 5. The individual distances of the RR Lyrae stars are used to determine density distributions of the different regions of the Galaxy. Table 6.1 summarizes the bin sizes of the evaluated fields. The distributions are smoothed using a Gaussian kernel of 3×3 bins with a width of 1 bin. This should reduce the variances on small scales.

6.5.1 The Galactic bulge region

To investigate the density contours of the Galactic bulge region we take all stars with distance determinations between 3 kpc and 15 kpc into consideration. The density contours shown in Figure 6.9 are in Galactocentric coordinates, while we assume a distance of 8 kpc to the Galactic center (Ghez et al.

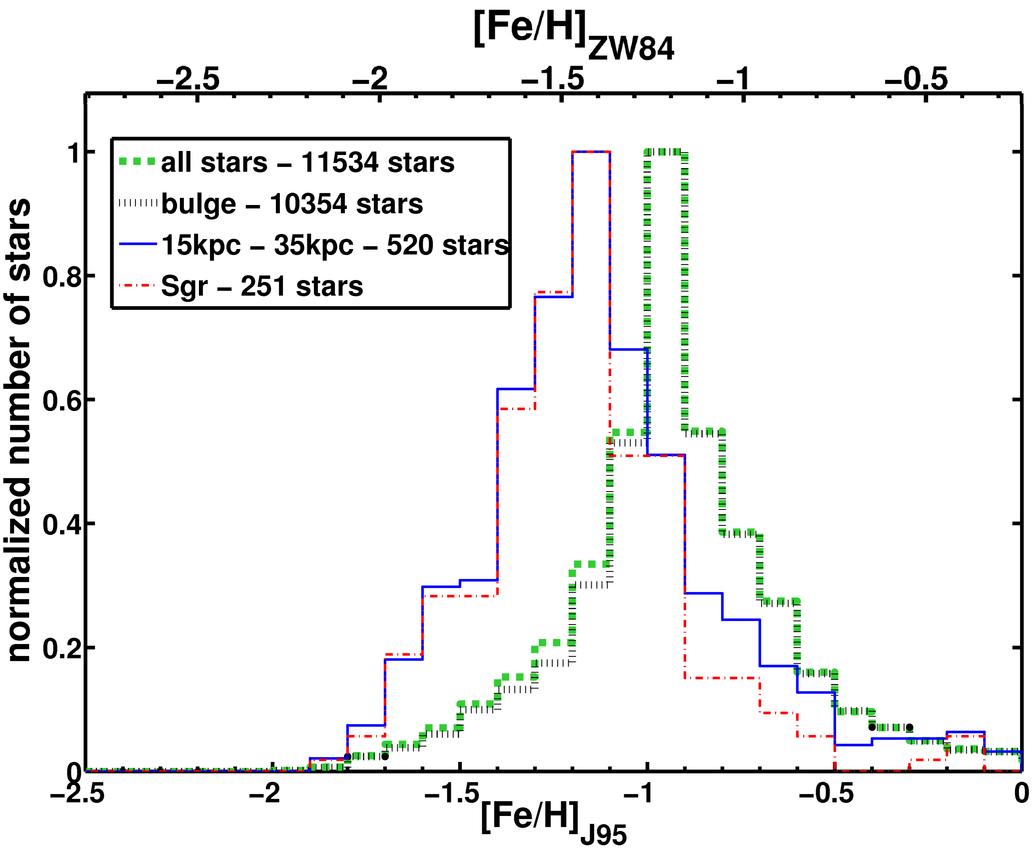

Figure 6.8: The MDF of four different data sets are shown. The samples are normalized by dividing the number of stars in each bin by the greatest number in a single bin. The green dashed line represents the whole sample of stars, while the black dotted line are the stars of the bulge region. The mean metallicity is $[Fe/H]_{ZW84} = -1.25$ dex. The blue line comprises all stars with distances between 15 kpc and 35 kpc. The mean metallicity of this sample is $[Fe/H]_{ZW84} = -1.44$ dex. Restricting the sample of stars to objects with $\alpha > 18^h$ and $\delta > -30°$ and distances of 18 kpc to 32 kpc a mean metallicity of $[Fe/H]_{ZW84} = -1.50$ dex is found, represented by the red dash-dotted line. The legend shows how many stars are present in each sample.

2008). From Figure 6.9 as well as from Figure 6.1 it is obvious that we do not show the center of the bulge region, but concentrate on a region south of the center.

The density distribution has been investigated as well in PUS11. They split the sample in several bins in Galactic latitude and investigated the distribution in every bin individually. For the slice $-4° < b < -3°$ they found an indication for a bar with an inclination angle of 27°. For the other slices no clear bar was revealed. We use, however, the whole sample of stars to investigate the distribution towards the Galactic bulge. The left panels show the distribution obtained with the R_V value of SFD98, while the right panels use the R_I value of PUS11. As already shown in Figure 6.3, the distances with the extinction law by SFD98 reveal lower values than PUS11. The density distributions are also slightly different. The shapes of the contours in the panels showing the Z-direction are biased by the orientation of the field on the sky. The inclination angle is an artefact of the field selection, not a real effect. For the upper panels, showing X versus Y, no selection effect is biasing the density distribution. Taking the complete sample of RR Lyrae stars we do not find a strong indication for a bar. There is, however, a difference of about 0.7 kpc in the median distances computed with both reddening estimates between the distributions of RR Lyrae stars located at $Y > 0.5$ and the RR Lyrae stars at $Y < -0.5$. PUS11 found indications for a bar with an inclination angle of 27°. This agrees well with our distance difference.

The highest concentration of the RR Lyrae stars is found in the central region of the distribution and close to the median distance determined in Section 6.3. Interestingly the rather flat and broad maximum of the distance distribution shown in Figure 6.3 is not very clearly reproduced by the density contours in the $X - Y$ panels. The contours have a peak in the distributions, while the flat maximum in Figure 6.3 extends for nearly 1 kpc. We suspect that the smoothing in the fitting routine of the density distribution as well as the binning reduce the extent of the peak. Therefore it seems less extended than in Figure 6.3.

Our distance estimates of the Galactic bulge are in very good agreement with the 8.0 ± 0.6 kpc from Ghez et al. (2008) and $8.33 \pm 0.17_{stat} \pm 0.31_{sys}$ kpc by Gillessen et al. (2009). These two groups independently determined the distance to the central black hole by observing the movement of the closest stars to the Galactic center. These values are mostly used as references for the determination of the distance to the Galactic center. Another study that is in good agreement with these values is Groenewegen et al. (2008). They estimated a distance to the center of $7.94 \pm 0.37 \pm 0.26$ kpc from Cepheids and RR Lyrae stars. For this study extinction had only a minor influence, because the observations were taken in the infrared K band. Infrared observations of long period variable stars were used by Matsunaga et al. (2009) to determine a mean distance of $8.24 \pm 0.08 \pm 0.42$ kpc, while Matsunaga et al. (2011) found a distance of 7.9 ± 0.2 kpc to the Galactic center with infrared observations of Cepheids. The evaluation of the OGLE III data by PUS11 led to a mean distance estimate of 8.35 ± 0.43 kpc, still in good agreement with our estimates.

6.5.2 The Sagittarius stream

The Sgr stream passes through the OGLE III area at $\alpha > 18^h$ and $\delta > -30°$ or in Galactic coordinates at $l > 0°$. In Galactic coordinates basically all stars with $l > 0°$ are located in the line of sight of the stream. In the representation with celestial coordinates each bin in α or δ versus the distance is contaminated by stars from regions that are not part of the stream. Therefore we present only the figures with Galactic coordinates in Figure 6.10. The panels on the left use the R_V value of SFD98, while for the right panels R_I of PUS11 is adopted.

In the left panels of Figure 6.10 the highest concentration of stars is found in the median distance of $D = 24.0 \pm 3.6$ kpc, using the extinction law by SFD98. Applying the R_I value of PUS11, we find a greater median distance of $D = 25.2 \pm 3.9$ kpc. For the calculation of the uncertainties the standard deviations of the distribution are determined. These values are relatively high, because the density of stars is much lower than in the Galactic bulge. The intrinsic uncertainties of the distance estimate of each RR Lyrae star depend on its observed magnitude and are about 7% of its actual distance. The upper panels of Figure 6.10 show that a very distinct concentration of stars is found at $l = 4°$. The concentration seems to be elongated along the line of sight, especially in the upper left panel. In the lower panel it is shown that the median distance of the highest concentration becomes smaller while approaching the Galactic plane.

Investigating the lower panel these elongations in the upper panels seem to be an artifact of the plotting procedure. In each panel for either l or b we add up all values of the other coordinate, respectively. Therefore we obtain an elongation if the distance changes with the other coordinate. Another caveat of the plotting is the unequal number of fields, which are added up. Comparing with Figure 6.1 we find that the number of fields with $b < -6°$ and $b > -3°$ are significantly reduced compared to the number of fields in $-6° < b < -3°$. For the longitudinal coordinate the number of fields does not vary much and has therefore not a big influence. This explains why for the lower panels a decrease in density to the outskirts of the OGLE III field is observed.

Taking this three-dimensional information into account, we conclude that the central parts of the Sgr stream are not very extended in depth and width. It rather seems to be a very distinct feature with a rapid decrease in density to the outskirts of the stream. The very low density of RR Lyrae stars for

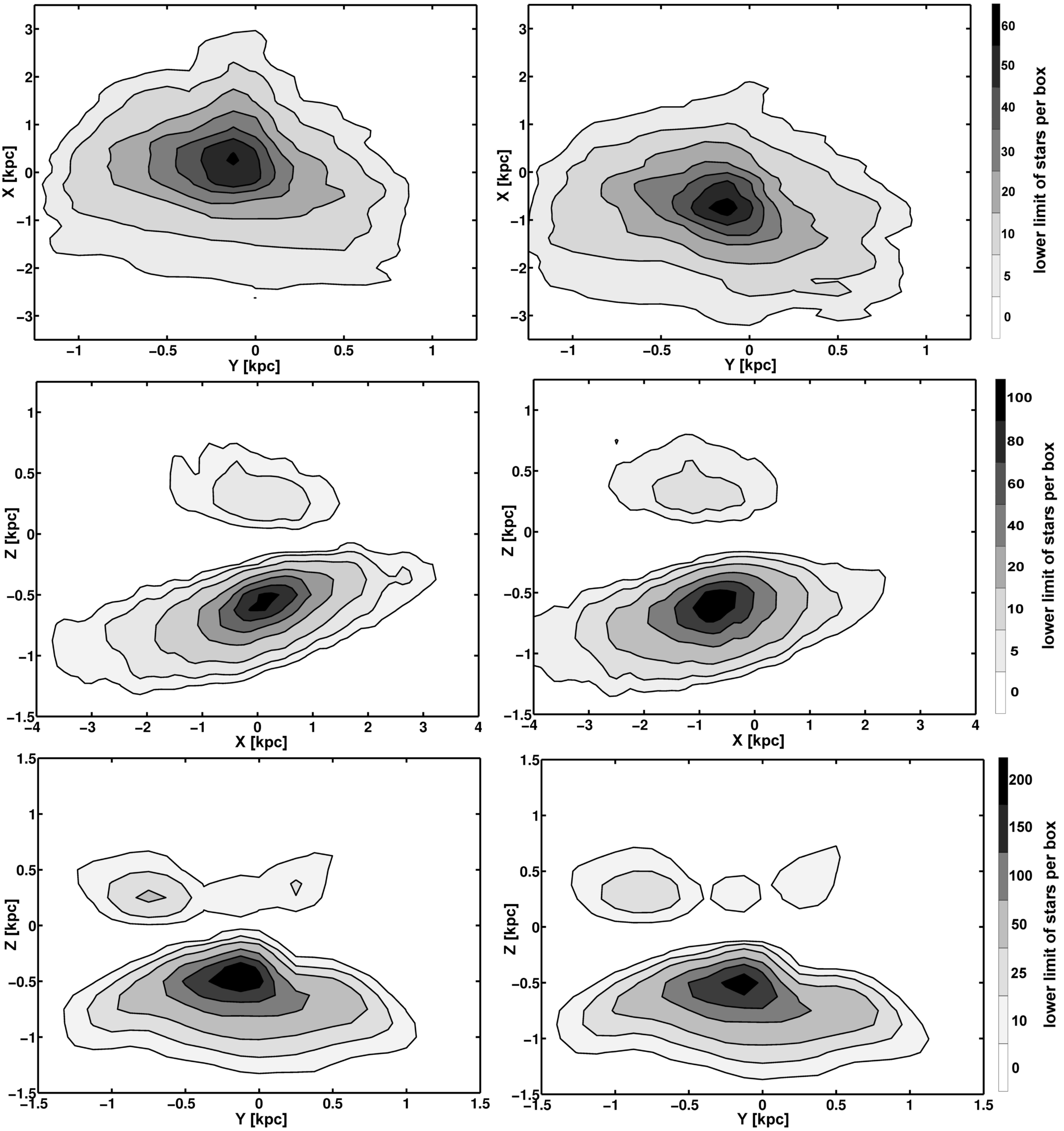

Figure 6.9: Density contours of the RR Lyrae stars towards the Galactic bulge. The contours are shown in Galactocentric coordinates, with a distance of 8 kpc from the sun to the Galactic center. The panels on the left show the distribution using the distances evaluated using the R_V value of SFD98. For the right panels the R_I value of PUS11 has been used. Positive values of X indicate the direction towards the sun.

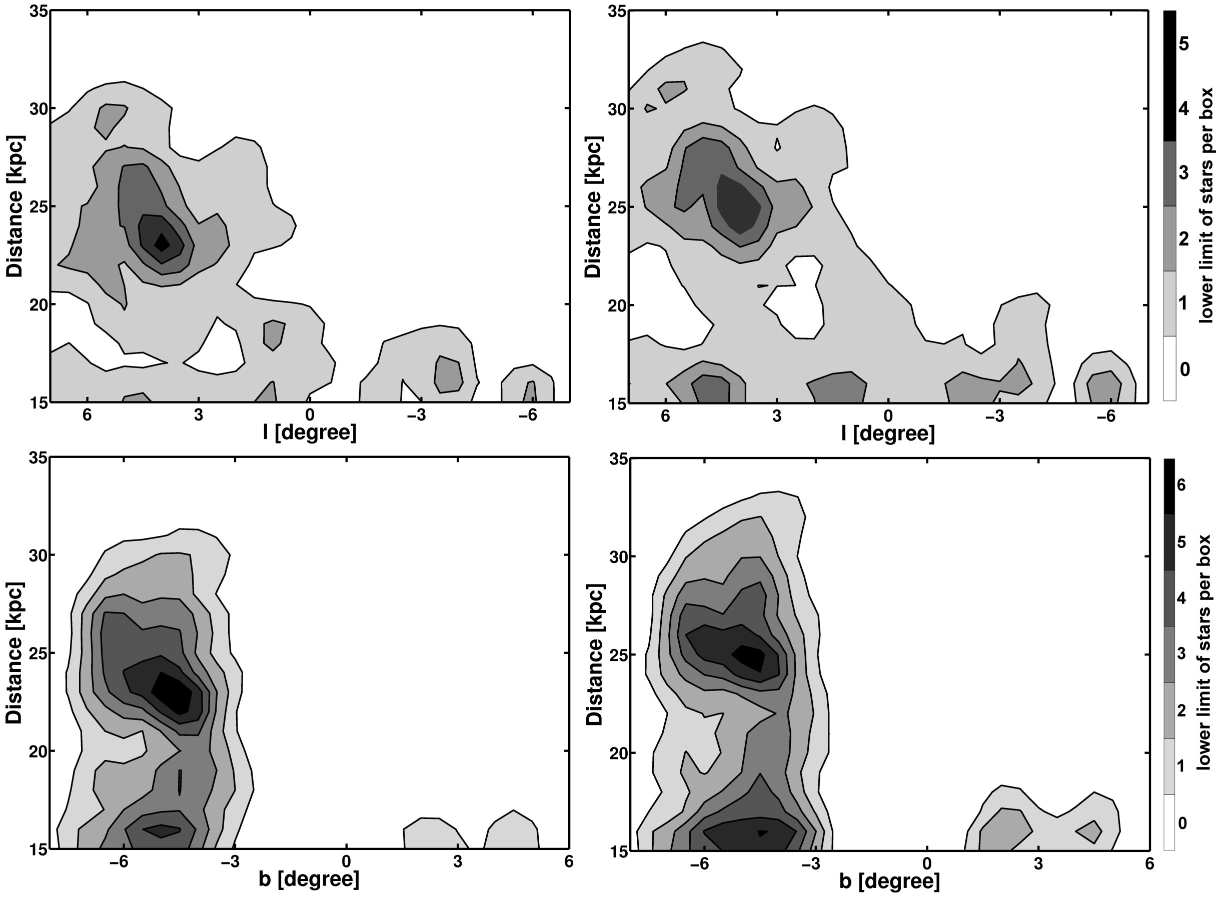

Figure 6.10: Density contours of parts of the Sgr stream and the surrounding area. The left panels use the value of R_V from SFD98. For the right panels the R_I of PUS11 is used to determine the distances. The density contours reveal a clear peak for the location at which we expect to find the Sgr stream. The distances vary a bit due to the different reddening estimates.

$l < 0°$ in the upper panels suggests that most of the stars with distances larger than 20 kpc are related to the Sgr stream and are slowly dispersed throughout the Galaxy. This is in good agreement with the MDF evaluated in Section 6.4. In the distance bin used to evaluate the MDF of the Sgr stream a different metallicity distribution with a lower mean value for [Fe/H] is found (Section 6.4).

Assuming a distance of 8 kpc for the Galactic center, Kunder & Chaboyer (2009) found a distance of 24.8 ± 0.8 kpc for the MACHO RR Lyrae stars of the Sgr stream. These stars are located a bit further south than the OGLE fields. This distance is significantly shorter than the RR Lyrae distance estimates to M54 of 26.7 ± 1.4 kpc (Sollima et al. 2010) and Kunder & Chaboyer (2009) concluded that the stream might be inclined. This hypothesis would match our findings very well. Covering a field that includes the MACHO, as well as parts of the OGLE III field Alard (1996) investigated RR Lyrae stars and obtained a mean distance of 24 ± 2 kpc for the Sgr stream. These results are in very good agreement with the values found by Kunder & Chaboyer (2009) and by our investigation. The quite different distances found for Stripe 82 of the SDSS in Watkins et al. (2009) and Sesar et al. (2010) support the idea of an inclined stream as indicated in the investigation by Majewski et al. (2003, Figure 8 to 11). This would also explain the width in the distributions of Figure 6.11, where we show the number density of RR Lyrae stars versus distance. The distribution is clearly non-Gaussian. The slope towards us is much steeper than away from the Galactic center. This is certainly not an effect of reddening, because we expect all stars to experience

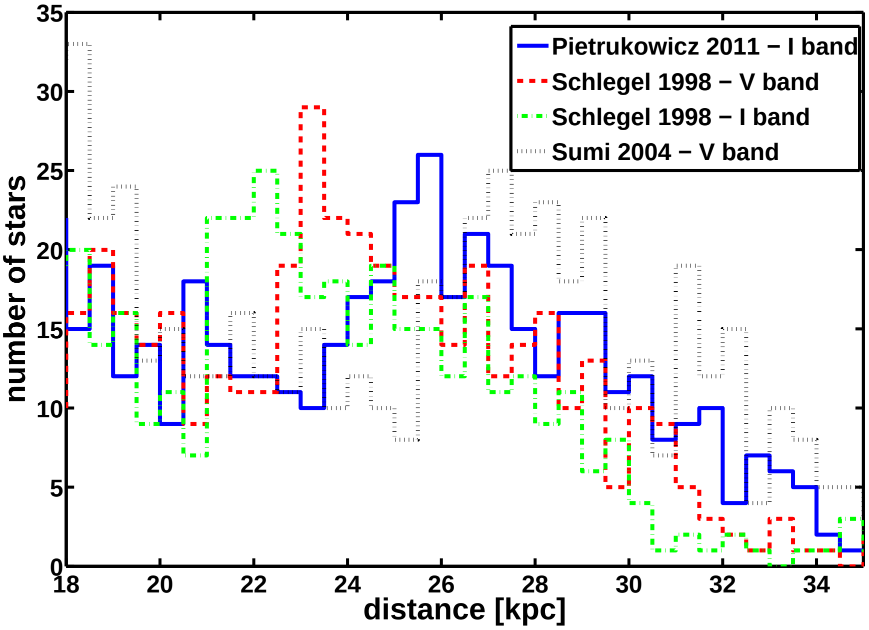

Figure 6.11: Sgr stream distance estimates for the RR Lyrae stars. For the curves the different values of R_x are used. A clear peak is visible for all distributions although it is obviously located at different distances.

most of their reddening while the light is travelling through the Galactic bulge region.

The shape of the stream revealed by us is in good agreement with Majewski et al. (2003, 2004). They concluded that the stream has a width below 2 kpc, but that there are stars scattered out to much larger distances. With RC stars Correnti et al. (2010) found a width of the stream that is compatible with the results of Majewski et al. (2003). The result of a rather thin stream is, however, in contradiction to the investigation by Cole et al. (2008). They simulated the distribution of stars using more than 100,000 F turnoff stars from the SDSS and found for about 16,000 stars of the Sgr stream a full width half maximum (FWHM) of 6.74 ± 0.06 kpc.

6.6 Summary

In this Chapter we present optical reddening maps, a MDF of the old population and three-dimensional maps for the Galactic Bulge region and the Sgr stream covered by OGLE III. The majority of the field extends approximately from $-6° < l < 6°$ and $-7° < b < -2°$, with a few small fields above the Galactic equator at $b \sim 3°$ (Figure 6.1). In total 11534 RR Lyrae stars are present in the field. These are subdivided into two subgroups. The first group contains 10354 stars and covers the dereddend distance from 3 kpc to 15 kpc. The second group of RR Lyrae stars has distances from 18 kpc to 32 kpc and includes 251 stars which are in the distance domain of the Sgr stream.

Photometric metallicities of the RR Lyrae stars are calculated using the parameters of the Fourier decomposition of their lightcurves and their periods (Kovács & Jurcsik 1996). These metallicities are on the scale of J95 and are transformed to the scale of ZW84 by the relation of Papadakis et al. (2000). Clementini et al. (2003) and Catelan et al. (2004) found relations for the V and I band, respectively, between the metallicity and the absolute magnitude of RR Lyrae stars. These are used to compute the colors of and the distances to the stars.

The parts closest to the Galactic center experience quite severe reddening. It is therefore necessary to have a good idea about the differential reddening, which is indispensable in order to obtain a reliable reddening map for correct distances. The reddening is calculated individually for each RR Lyrae star by comparing the observed color with its color calculated from the absolute magnitudes in the I and V band. This allows us to have a distinct reddening value for each star, taking differential reddening into account. The highest value that we obtain is $E(V-I) = 4.63$ mag.

To determine the MDFs of the RR Lyrae stars we use the smaller subgroups defined before. The main sample are the RR Lyrae stars with distances between 3 kpc and 15 kpc. The resulting metallicity of the old population of the bulge is rather high. These stars have a mean metallicity of $[\mathrm{Fe/H}]_{\mathrm{ZW84}} = -1.25$ dex, in very good agreement with Kunder & Chaboyer (2008) and PUS11. The MDF has a Gaussian shape, even though the bin with the highest number of stars is rather strongly peaked.

For the Sgr stream it is known that the metallicity changes throughout the stream (Chou et al. 2007). We investigate the RR Lyrae stars in the farther distance bin of 18 kpc to 32 kpc to find a MDF of the stream. The MDF is slightly asymmetric, it falls off more steeply for higher metallicity values. Only very few RR Lyrae stars with $[\mathrm{Fe/H}]_{\mathrm{ZW84}} > -1.0$ dex are present at this distance range. The mean metallicity of $[\mathrm{Fe/H}]_{\mathrm{ZW84}} = -1.50$ dex is significantly lower than the metallicity of the bulge. The result is good agreement with other metallicity estimates for the old population of Sgr made in fields close by, e.g., by Morgan et al. (1998) and Kunder & Chaboyer (2008).

We start our investigaton with four different reddening laws to transform from $E(V-I)$ to $A_{V/I}$. These result in quite different median distances for the Galactic bulge. We keep the values obtained by using the reddening transformation parameter $R_{V/I}$ of SFD98 and PUS11 and rejet the other two distance estimates. With these values median distances to the Galactic bulge of $D_{\mathrm{SFD98}} = 8.0 \pm 1.7$ kpc and $D_{\mathrm{PUS11}} = 8.8 \pm 1.6$ kpc are obtained, in good agreement with the recent literature (e.g., Ghez et al. 2008; Groenewegen et al. 2008; Gillessen et al. 2009). The three-dimensional structure of the bulge region does not reveal a strong indication for a bar traced by in the RR Lyrae stars. Distance differences of about 0.7 kpc are, however, found when comparing the median distances of stars located at $Y > 0.5$ kpc and $Y < 0.5$ kpc.

The Sgr stream has a median distance of $D_{\mathrm{SFD98}} = 24.0 \pm 3.6$ kpc and $D_{\mathrm{PUS11}} = 25.2 \pm 3.9$ kpc, respectively. The density of stars in regions without the stream is very low and we conclude that most of the stars located in our second distance bin are part of the Sgr stream. A rather low width of the stream is found, in good agreement with Majewski et al. (2003, 2004). In our dataset the stream seems, furthermore, to be inclined. This would explain the slightly higher distance estimates of Kunder & Chaboyer (2009) for the MACHO fields, which are located a bit south of the OGLE field.

"Resistance is futile."
Data - Star Trek 8 (First Contact)

7

Chemical abundances of metal-poor RR Lyrae stars in the Magellanic Clouds

We present for the first time a direct spectroscopic investigation of chemical element abundances of RR Lyrae stars in the Large and Small Magellanic Cloud. Using the Magellan Echellette spectrograph at the 6.5 m Magellan telescopes, we obtain medium resolution ($R \sim 2000 - 6000$) spectra of six RR Lyrae stars in the LMC and three RR Lyrae stars in the SMC. These stars were chosen because their previously determined photometric metallicities were among the lowest metallicities found for stars belonging to the old populations in the Magellanic Clouds. We find the spectroscopic metallicities of these stars to be as low as $[\mathrm{Fe/H}]_{\mathrm{spec}} = -2.7$ dex, the lowest metallicity yet measured for any star in the Magellanic Clouds. We confirm that for metal-poor stars, the photometric metallicities from the Fourier decomposition of the lightcurves are systematically too high compared to their spectroscopic counterparts. However, for even more metal-poor stars below $[\mathrm{Fe/H}]_{\mathrm{phot}} < -2.8$ dex this trend is reversed and the spectroscopic metallicities are systematically higher than the photometric estimates. We are able to determine abundance ratios for ten chemical elements (Fe, Na, Mg, Al, Ca, Sc, Ti, Cr, Sr and Ba), which extend the abundance measurements of chemical elements for RR Lyrae stars in the Clouds beyond [Fe/H] for the first time. For the overall $[\alpha/\mathrm{Fe}]$ ratio, we obtain an overabundance of 0.36 dex, which is in very good agreement with results from metal-poor stars in the Milky Way halo as well as from the metal-poor tail in dwarf spheroidal galaxies. Comparing the abundances with those of the stars in the Milky Way halo we find that the abundance ratios of stars of both populations are consistent with another. Therefore, we conclude, that from a chemical point of view, early contributions from Magellanic-type galaxies to the formation of the Galactic halo are plausible.

This chapter is based on Haschke, Grebel, Frebel, Duffau, Hansen, & Koch (in prep.b)

7.1 Introduction

Hierarchical galaxy formation models predict that larger galaxies are formed by the accretion of smaller systems. Recent simulations (e.g., Robertson et al. 2005; Tumlinson 2010) suggest that the accretion of galaxies with masses comparable to those of the MCs provided the major contribution of stellar mass to the present-day MW halo. These accretion events would have happend early (more than $8-9$ Gyr ago), contributing primarily stars enriched by Type II supernovae (e.g., Font et al. 2006).

The low luminosity dSphs contain primarily old populations, which have similar ages as the oldest stars in the MW halo (Grebel & Gallagher 2004). A number of recent studies succeeded in detecting extremely metal-deficient red giants in Galactic dSphs (e.g., Frebel et al. 2010a,b; Tafelmeyer et al. 2010; Cohen & Huang 2009, 2010; Norris et al. 2010c,a), concluding that these galaxies may plausibly have contributed to the early build-up of the Galactic halo. For the ultra-faint dSph galaxies the similarities to the MW halo are even more pronounced than for the classical dSphs. Therefore it is of particular importance to address the question of the evolution of metallicity in dependence of galaxy mass and type to learn more about the similarities and differences between dSphs and dwarf irregular galaxies, such as the MCs, especially in their earliest evolutionary phases. According to the aforementioned cosmological models, the most significant contribution to the build-up of the MW halo should have come from the early progenitors of MC-like galaxies.

In galaxies that experienced star formation throughout cosmic history, the identification of purely old populations is difficult. For instance, the abundant red giants can cover ages of more than ten Gyr. Thus one can either turn to GCs as easily identifiable and reliably age-dateable populations or to uniquely identifiable, old tracer stars among field populations. For field stars the exclusively old Population II can only be traced with certain objects, such as RR Lyrae stars. Metallicity estimates of these stars therefore allow an insight into the early evolutionary phase of a galaxy.

For the LMC, low-resolution spectroscopic observations of RR Lyrae were performed by Gratton et al. (2004) and Borissova et al. (2004, 2006). These studies investigated predominantly stars located in the bar and the central regions of the LMC and found very similar mean metallicities of $[\mathrm{Fe/H}] \sim -1.5$ dex. The spectroscopic metallicities of RR Lyrae stars, determined through comparison of the Ca II K line with the hydrogen lines H_δ, H_γ and H_β, were found to be between $[\mathrm{Fe/H}] = -2.33$ dex and $[\mathrm{Fe/H}] = -0.57$ dex. These studies could produce overall metallicity estimates only. The abundances of individual elements in RR Lyrae stars of the MCs were never investigated.

The OGLE survey (Udalski et al. 2008a,b) monitored the MCs for several years and provided very accurate lightcurves of a large sample of RR Lyrae stars (Soszyński et al. 2009, 2010a). In Chapter 3, the Fourier-decomposition method by Kovács & Zsoldos (1995) is used to determine individual photometric metallicity estimates for these old Population II stars, and MDFs for both MCs are derived. In the LMC, Chapter 3 obtain Fourier decomposition metallicities for 16776 RR Lyrae stars of type *ab*, and in the SMC metallicities for 1831 of these stars could be measured. On the ZW84 scale the peak of the LMC MDF is at $[\mathrm{Fe/H}] = -1.50$ dex with a full width at half maximum of 0.24 dex. The SMC is found to be more metal-poor with its MDF peaking at $[\mathrm{Fe/H}] = -1.70$ dex (FWHM = 0.27 dex).

These results are in agreement with Carrera et al. (2008b) and Carrera et al. (2011), who used Ca II triplet spectroscopy investigating red giants in the LMC to determine the age-metallicity relation, as well as with metallicities from Ca II triplet spectroscopy for SMC red giants determined by Carrera et al. (2008a). These studies estimate the mean metallitiicy of the “old” LMC population as traced by field red giants to be $[\mathrm{Fe/H}] \sim -1.2$ dex and that of the SMC to be $[\mathrm{Fe/H}] \sim -1.4$ dex. The age determination for individual field red giants, however, is rather difficult, and is exacerbated by uncertainties in the distance and the reddening of these stars. In contrast, star clusters usually have a well defined age with a common metallicity for all stars. Kayser et al. (2007) and Glatt et al. (2008a) found a metallicity spread for SMC star clusters of intermediate age, in agreement with the spectroscopic results by Da Costa &

Hatzidimitriou (1998), and concluded that no smooth, monotonic age-metallicity relation is present.

Hence, the only source of direct abundance measurements for purely old stars of the MCs are investigations of GCs. In the LMC seven old GC were spectroscopically investigated by Johnson et al. (2006) and Mucciarelli et al. (2009, 2010) using red giants. They found that the different LMC GCs studied have mean iron abundances between $-2.20\,\mathrm{dex} < [\mathrm{Fe/H}] < -1.23\,\mathrm{dex}$. These findings support that a considerable metallicity spread is present in the old population. While the GCs of Mucciarelli et al. (2010) are all α-enhanced by $\sim 0.4\,\mathrm{dex}$, the GCs investigated in Johnson et al. (2006) are only slightly α-enhanced. However, the abundances of the α and other elements agree well with the abundances determined for stars within the MW halo. The SMC only contains one GC and this object is $2-3\,\mathrm{Gyr}$ younger than the oldest GCs in the LMC and in the MW (Glatt et al. 2008b).

But even for Galactic field RR Lyrae stars hardly any data are available concerning the $[\alpha/\mathrm{Fe}]$ ratio. Clementini et al. (1995, from now on C95) reported an overabundance of $[\alpha/\mathrm{Fe}] = 0.4\,\mathrm{dex}$ and $[\mathrm{Mn/Fe}] = 0.6\,\mathrm{dex}$ for 10 Galactic field RR Lyrae stars, which is in agreement with Fernley & Barnes (1996), who found an overabundance of $[\mathrm{Ca/Fe}] = 0.4\,\mathrm{dex}$ for nine field stars. In the MW GC M3 Sandstrom et al. (2001) measured a similar overabundance using 29 RR Lyrae stars. Two very metal-poor RR Lyrae stars were investigated with high resolution spectroscopy in Hansen et al. (2011). They obtained elemental abundances for 16 different elements, and found the $[\alpha/\mathrm{Fe}]$ ratio to be very similar to the other investigations. For et al. (2011) investigated the properties of eleven nearby field RR Lyrae stars and obtained very precise abundances for several elements. For the α-elements, a mean overabundance of $[\alpha/\mathrm{Fe}] = 0.5\,\mathrm{dex}$ was found in their study.

This lack of information about α-elements for LMC RR Lyrae stars and the lack of spectroscopic investigations of SMC RR Lyrae stars is caused in part by the great difficulties of taking spectra of comparatively faint objects at these distances. Their variability changes their stellar parameters significantly during a given pulsation period and therefore the integration times have to be kept short. At distances beyond $\sim 50\,\mathrm{kpc}$, only the > 6-m class telescopes and state-of-the-art instruments are able to obtain spectra of sufficient quality to permit us to determine the chemical composition of these stars. Therefore, for the time being, photometric estimates are the only way to determine metallicities for large samples of RR Lyrae stars. Photometric metallicity calibrations at the low metallicity end, however, are still somewhat uncertain (e.g., Arellano Ferro et al. 2011; Dékány & Kovács 2009), owing to the lack of suitable calibration stars. To arrive at more secure metallicity estimates of metal-poor candidates, spectroscopy is inevitable.

Of particular interest are the very metal-poor populations of the MCs to learn more about the earliest stages of their evolution and to compare the early enrichment history of the MCs with the properties of the Galactic halo and other galaxies orbiting the MW. In this study, we therefore chose to conduct spectroscopic follow-up observations of six LMC RR Lyrae stars and three SMC RR Lyrae stars that were previously identified as very metal-poor candidates in our photometric analysis. Their photometric metallicities, deduced from the method introduced by Kovács & Zsoldos (1995) are all below $[\mathrm{Fe/H}] < -2.3\,\mathrm{dex}$ on the scale of ZW84. For more details on the metallicities of RR Lyrae stars within the MCs see Chapter 3.

In Section 7.2, the target selection and the observational procedure to obtain spectra for these stars is described. Furthermore, the reduction procedure of the data is explained. We measure the radial velocities of the RR Lyrae stars in Section 7.3 and correct the spectra accordingly to obtain equivalent width measurements in Section 7.4. The stellar parameters are deduced and discussed in Section 7.5. Equivalent width (EW) measurements as well as synthesized spectra are used in Section 7.6 to calculate abundances for eleven different elements. In Section 7.7 the results are discussed and summarized.

Table 7.1: Properties of RR Lyrae stars observed with Magellan/MagE. The star ID of the LMC objects is taken from the identifier in the OGLE III dataset, for the SMC objects the OGLE II identifier are used.

star	V [mag]	RA (J2000) [hh:mm:ss]	Dec (J2000) [°:′:″]	UT date	No. int	$t_{\rm exp}$ [s]	slit [″]	$[{\rm Fe/H}]_{\rm phot}$ [dex]	period [days]
RR15903	18.78	05:27:18.77	−69:32:22.5	01/18	4	4800	0.7	−2.20	0.7453
RR8645[1]	19.23	05:14:42.54	−68:59:26.9	01/18	3	5400	0.7	−2.63	0.5293
RR1422	19.11	04:51:54.23	−66:58:46.1	01/18	2	5100	0.7	−3.38	0.6148
RR177	18.84	04:35:33.16	−68:12:25.8	01/19	3	2700	2.0	−2.10	0.8246
RR11371	19.27	05:19:27.68	−71:20:45.0	01/19	2	3600	2.0	−2.80	0.5590
RR22827	19.16	05:46:40.62	−69:44:26.1	01/19	1	3000	2.0	−2.80	0.5720
RR122432	19.63	00:47:39.98	−73:08:43.0	08/05	3	4100	0.7	−3.41	0.5904
RR50180	20.17	00:43:07.78	−72:49:22.1	08/06	2	3000	0.7	−2.95	0.5858
RR143874	20.21	00:47:42.57	−72:43:15.5	08/06	3	5600	0.7	−2.03	0.5520

7.2 Observations and Reductions

7.2.1 Target selection

The OGLE III survey[1] (Udalski et al. 2008b) monitored the MCs from 2001 to 2009. Soszyński et al. (2009, 2010a) extracted very precise light curves for several thousand RR Lyrae stars in both Clouds and Fourier-decomposed these light curves, following the method by Kovács & Zsoldos (1995), to determine their Fourier parameters. Smolec (2005) introduced a relation using the Fourier parameter ϕ_{31} and the period of the RR Lyrae stars to determine a metallicity on the metallicity scale of J95. In Chapter 3, this relation is used to evaluate photometric metallicities for 16676 LMC RR Lyrae stars and 1831 SMC RR Lyrae stars. Papadakis et al. (2000) found a transformation relation between the metallicity scales by J95 and ZW84, showing that the scale by J95 is about 0.3 dex higher than the metallicity scale by ZW84.

For the LMC, our candidate list contains 35 RR Lyrae stars of type *ab* with photometric metallicities below $[{\rm Fe/H}] = -2.0$ dex on the J95 scale, which scales to $[{\rm Fe/H}] = -2.3$ dex on the scale of ZW84. When we compiled the candidate list for the SMC spectroscopic observations the data on the RR Lyrae stars from OGLE III were not available. We therefore had to rely on OGLE II data (Udalski et al. 1997; Soszyński et al. 2003), which results in 14 RR Lyrae type *ab* stars with metallicities $[{\rm Fe/H}]_{\rm ZW84} < -2.3$ dex.

7.2.2 Observation

The observations were conducted using the Magellan Echellette (MagE) spectrograph (Marshall et al. 2008) on the 6.5 m Magellan Clay telescope at Las Campanas, Chile, on 2010 January, 17th and 18th and August, 4th and 5th. During the first run only LMC objects were observed, while the second run concentrated on the SMC. The target list is shown in Table 7.1 and Figure 7.1.

The MagE spectrograph has several slits with a length of 10″and widths from 5″to 0.5″. The observed spectrum is divided into 15 orders which allow us to cover a wavelength range of 3000Å to 10500Å with one exposure. The wide wavelength range limits the resolution, which is $R \sim 6000$ for an 0.7″slit. We will calculate the actual resolving power for different slits later. The f/1.4 Schmidt vacuum camera is equipped with an E2V back illuminated CCD, which has 2048×1024 pixels. Each pixel covers 0.33″on the sky and a dispersion from 0.3Å pixel^{-1} in the blue to 0.6Å pixel^{-1} in the red part is achieved.

---

[1] `http://ogle.astrouw.edu.pl/`

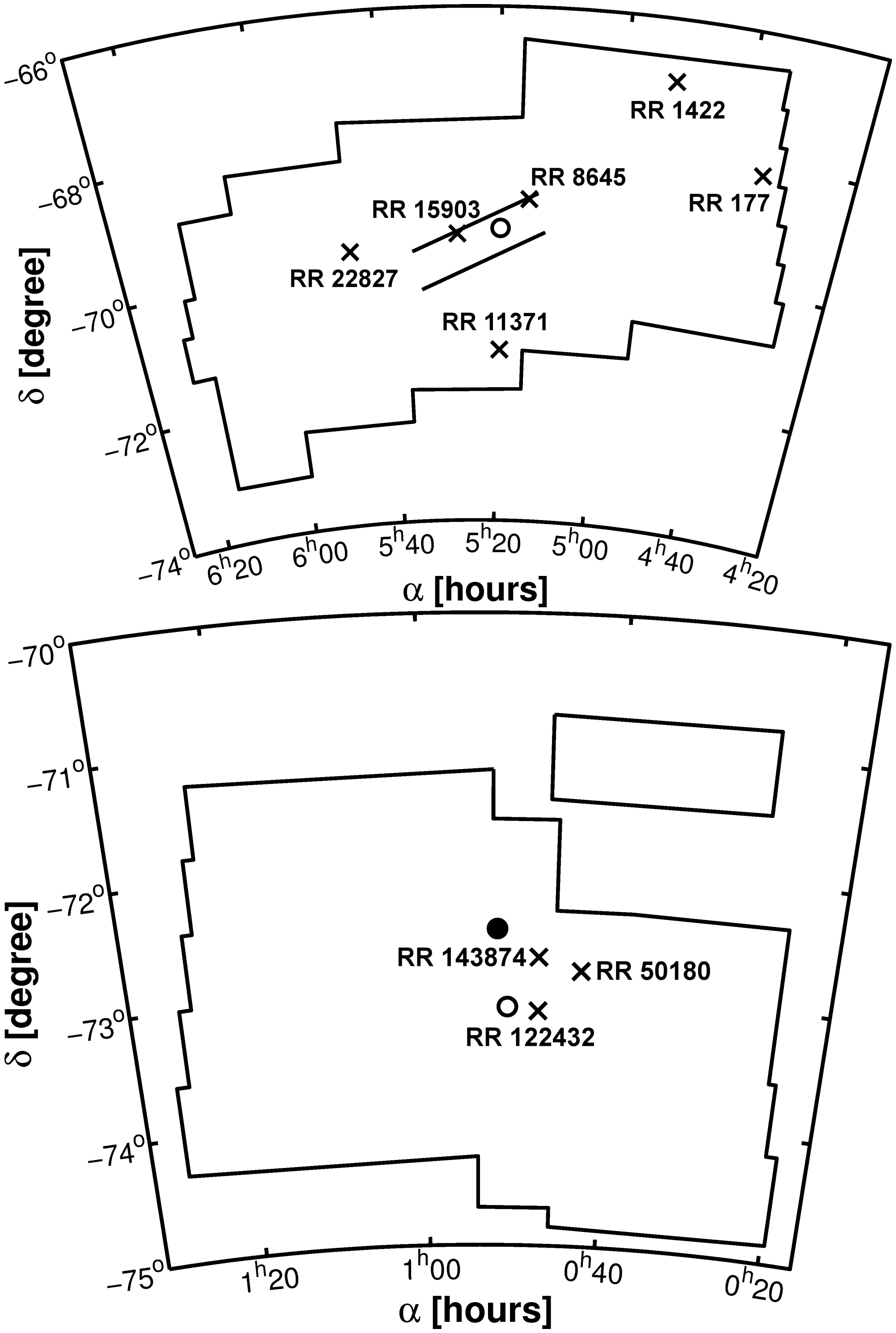

Figure 7.1: Location of the observed RR Lyrae stars within the OGLE III fields. The crosses illustrate the position of the RR Lyrae stars. While the open circle in the upper panel shows the optical center of the LMC (de Vaucouleurs & Freeman 1972), the open circle in the lower panel shows the center of the SMC as found by G09 from isophotes of giant stars and the filled circle the center comes from proper motion measurements as found by Piatek et al. (2008).

Table 7.2: This table summarizes the flat-field exposure times.

	Quartz			Xenon			ThAr			Skyflat			
slit width [″]	0.7	1.0	2.0	0.7	1.0	2.0	0.7	1.0	2.0	0.7	1.0	2.0	5.0
exposure time [s]	45	28	15	35	28	15	4	3	2	7.5	45	6	5

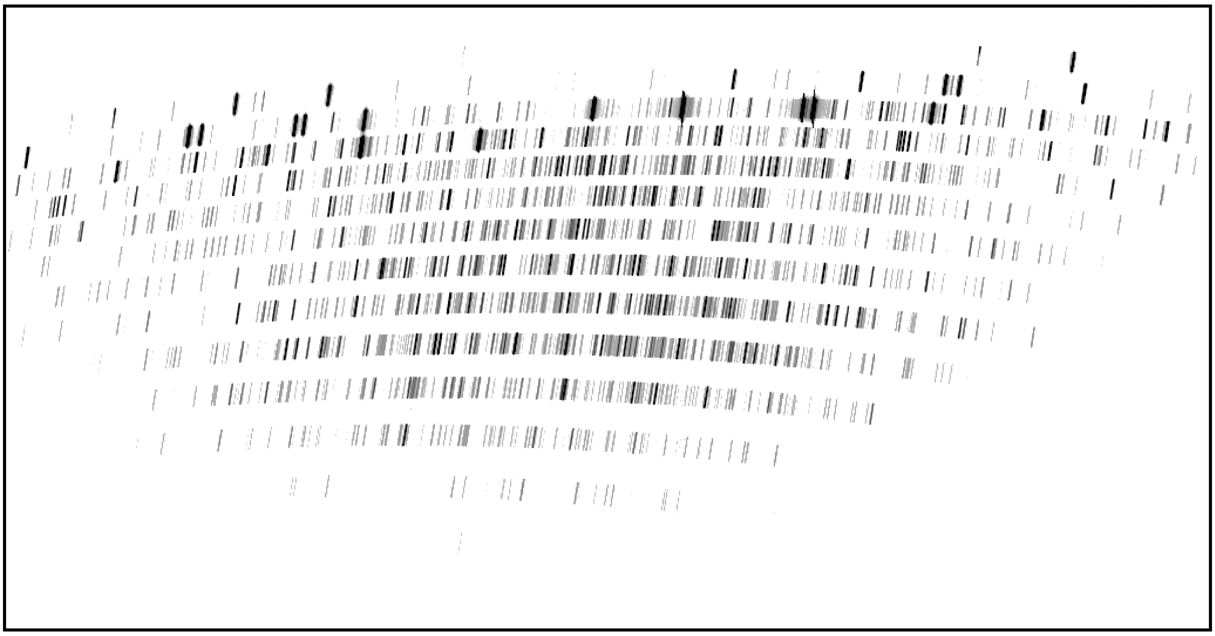

Figure 7.2: An example of an unreduced ThAr flat.

We started by taking flat-fields of the spectrograph. For this purpose we used a Quartz lamp and a Xenon lamp. While the Quartz lamp emits much more light in the red part of the spectrum covered by the spectrograph, the Xenon lamp is used to flat-field the bluer part of the spectrum. For each lamp ten exposures of each slit are taken. At dusk and dawn additional sky-flats were taken to flat-field the very blue part of the spectrum (see Table 7.2).

Thorium-Argon (ThAr) cathode tubes are very useful calibrators for the wavelength solution of a spectrum. As shown in Figure 7.2 the complete wavelength coverage of the spectrograph has a decent amount of lines at a well known wavelength. This allows to correlate the wavelength with the pixel positions of the lines measured by the spectrograph. In the afternoon several exposures are taken to compute the resolution of the spectrograph for different slitwidth. Ideally during the scientific operation a ThAr calibration frame should be taken after each exposure to have a decent wavelength calibration for the spectrum and to exclude errors due to changes in the telescope or CCD. In the first night ThAr frames were only taken at the beginning and end of the night, while in the other nights ThAr frames were taken after each science frame. We test if the calibration of the first night suffers from having only two calibration frames, but do not find any evidence in the reduced data.

The resolution of the spectrograph does not only change with the slit width, but also with the observed wavelength. Each pixel covers 0.33″which allows to calculate the pixel-size in Ångstrom [px Å^{-1}]. For the red part of the spectrograph at $\lambda \approx 8500$Å we find a pixel size of 1.488Å^{-1}, while in the blue at $\lambda \approx 4000$Å the scale increases to a pizel size of 3.210Å^{-1}. The resolution is then calculated as

$$\mathrm{R} = \frac{\lambda}{\mathrm{FWHM}} \frac{\mathrm{px}}{\text{Å}} \tag{7.1}$$

Table 7.3: This table summarizes the resolution of the spectrograph for different slit width.

	$\lambda = 8670$Å				$\lambda = 3950$Å			
slit width [″]	0.7	1.0	1.2	1.5	0.7	1.0	1.2	1.5
resolution	6400	4950	4160	3400	5780	4360	3720	2950

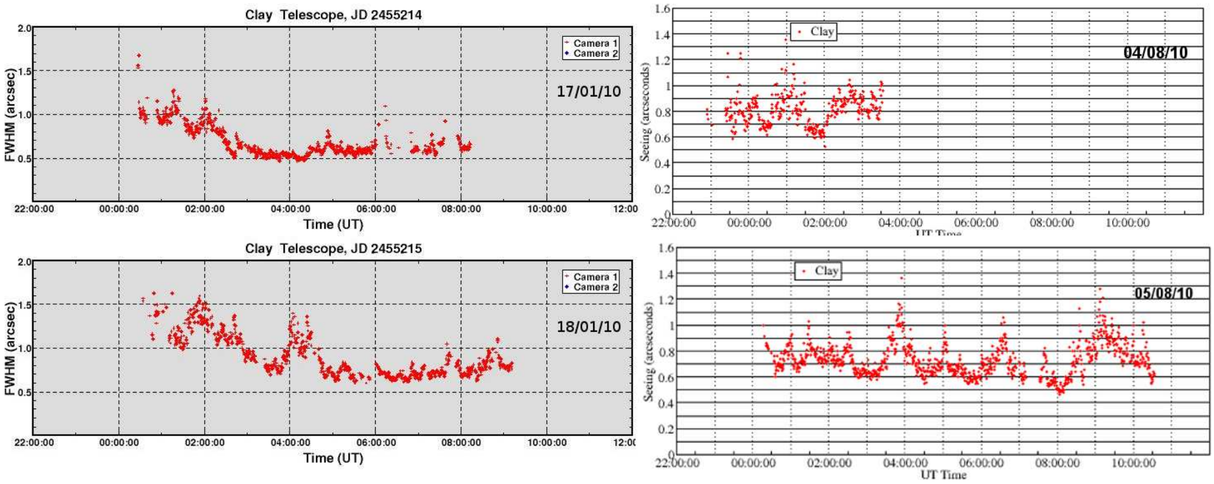

Figure 7.3: The seeing during the four nights of observations.

for different slits in the blue and in the red part of the spectrum. Table 7.3 summarizes the results.

For the observations we had two runs, both with non-optimal weather conditions. This is illustrated by the table of seeing shown in Figure 7.3. Thus, the slit width had to be increased drom 0.7″to 2.0″for some of the objects. These are noted in Table 7.1. The photometric metallicity estimates of the target stars, as well as the integration time of each object is also shown in Table 7.1.

During the observations several frames of standard stars were taken. We chose to observe the well investigated, very metal-poor RR Lyrae star X Arietis (X Ari) and the two non-variable, very metal-poor stars HD74000 and G64-12. All spectra were taken with the 0.7″slit. The stellar parameters of the bright standards are listed in Table 7.4

For two stars we experienced complications during the observation. The reduction of RR8645 needs special attention, because a second star was present in the slit during the observation. These might possibly contaminate the data. In the second half of the first night we observed a movement of the location of the spectra in the aperture. This affected RR1422. We want to classify the movement at the very end of the night and take many short exposures of standard stars. Remarkably this effect disappears until the next day and the origin for the shift remains unclear.

Table 7.4: Properties of standard stars observed with Magellan/MagE. The values listed are taken from the quoted literature.

star	V [mag]	RA (J2000) [hh:mm:ss]	Dec (J2000) [dd:mm:ss]	[Fe/H] [dex]	T_{eff} [K]	log g	Reference
HD74000	9.67	08:40:50.80	−16:20:42.52	−2.02	6166	4.19	Cenarro et al. (2007)
X Ari	9.63	03:08:30.88	+10:26:45.22	−2.50	6109	2.60	Cenarro et al. (2007)
GD64-12	11.49	13:40:02.49	−00:02:18.75	−3.28	6400	4.1	Primas et al. (2000)

7.2.3 Data Reduction

The data reduction was performed in two steps. Firstly the data were reduced with the echelle package of the IRAF distribution. W. Aoki wrote a comprehension[2] of the sequences of operation to reduce the echelle spectra obtained with the HDS instrument mounted on the Subaru telescope, Mauna Kea, Hawai'i, USA. This manual is with small modifications applicable to the spectra obtained from the MagE spectrograph. The second step was to use the *MagE-reduce* pipeline, written by G. Becker[3]. Finally it was decided that the results of the pipeline are better than the spectra from the IRAF procedure.

IRAF

We start the reduction with a bias correction of each individual frame. The median count value of the pixels located in the overscan region of the CCD is subtracted from each pixel of the science parts of the CCD.

Before a flat-field correction can be applied the location and size of the apertures in the spectra have to be determined. The location of the apertures on the CCD at an arbitrarily chosen vertical pixel position is automatically determined by IRAF. The limits are finetuned by hand and a multiorder polynomial fit identifies the curvature of each spectral order to trace the x-y positions of the apertures. This procedure is performed on a flat-field frame and the calibrated positions of the orders are applied later to all other frames.

Inspecting the different kind of flat-fields in detail it becomes obvious that each of them is only applicable to a certain range of the wavelength band. Therefore the Quartz-flats are used for the orders 6 to 13 ($4500Å < \lambda < 10500Å$), the Xenon-flats for the orders 14-17 ($3500Å < \lambda < 4700Å$) and the orders 18-20 ($3000Å < \lambda < 3600Å$) are covered by the sky-flats. While the Quartzlamp illuminates the spectra without any noticeable lines, many distinct features can be seen for the sky-flats and the Xenonlamps. Lines in the flat-field introduce additional noise. This effect has to be minimized (Bochanski et al. 2009). For every pixel the values of the 30 surrounding pixels in this column are averaged and assumed as value for this pixel. Inspection of the smoothed and unsmoothed flats reveal that for the Xenon- and sky-flats much better results are obtained, while the Quartz-flats seem to be better without smoothing.

The individual flat-fields of each type are merged together. Then a normalized flat-field is produced, however, all unusable orders mentioned above are cut. That leaves us with three normalized flat-fields covering all the different orders. These are finally merged together to obtain a master-flat-field. For every night a new master-flat-field is produced and all exposures of this night are flat-fielded using this master-flat-field.

To measure the background counts of the CCD we mask out the apertures of the spectra. This should leave us with a zero count image. However, scattering within the spectrograph and fluctuations of the CCD lead to non-zero values of the background. The distribution of counts is fitted with an multiorder polynom and crosschecked by visual inspection. Then we subtract the background of each individual frame from the spectra without masking the apertures.

The center and the limits of the apertures, as found by IRAF, are inspected by eye and changed if necessary. This is especially the case for the last observations in the first night, when the aperture had experienced displacements in comparison to the other frames. For RR8645 the aperture is limited such, that the second star in the slit is ignored. After applying these steps IRAF automatically extracts a 1-d spectra for each order of all science frames.

The spectral features in the 1-d spectra have to be wavelength calibrated. The wavelength of the lines of the ThAr lamp are well known and can easily be connected with the pixel positions in a 1-d spectra. Unfortunately, the calibration to connect the wavelength of the ThAr lamp with the actual pixel positions

---

[2] the manual is available at `http://optik2.mtk.nao.ac.jp/~waoki/QL/specana200810e.pdf`

[3] `ftp://ftp.ociw.edu/pub/gdb/mage\_reduce/mage\_reduce.tar.gz`

on our ThAr exposures of the MagE spectrograph are not available, with the argument of the science team at Las Campanas that a pipeline is available. Therefore, we have to adopt calibration frames from the NOAO[4] and crosscorrelate them with our observations. Using the ten to fiveteen most prominent ThAr lines of every order a wavelength solution is created and applied to all science spectra. The wavelength calibration is checked by comparing the position of the O III peak, which should be located at 5577Å, with its actual position in the spectrum.

We normalize the spectra by fitting a polynomial of order four to ten to the spectra. Furthermore the upper and lower limits of the fit are adjusted by eye to gain the best possible result. For the frames with two stars in the slit or with a moved aperture some orders show strange patterns which can not be fitted. These frames are rejected.

The last step is to combine the orders of each spectra. At the edges of each order the efficiencies of the CCD are reduced and a simple sum would introduce additional noise into the spectra. Therefore a weight function is introduced by dividing the non-normalized frame by the normalized. This reveals the shape of the count efficiency of the CCD in dependence of the wavelength. If two orders cover the same wavelength the orders are added together by using the weight function.

Finally the final reduced frames of each star are added together by using the median to get the best possible spectrum with a decent signal to noise (S/N) ratio and to eliminate the cosmics present. For the combined frames of the MC spectra a S/N of $10 - 25$ per pixel at a wavelength of 7500Å is achieved.

MagE-reduce pipeline

The IDL based pipeline MagE-reduce uses the raw observations of the MagE spectrograph to produce wavelength calibrated 1-d spectra.

We use the pipeline with the single frames and with the already added spectra. It turns out, that the spectra which are added together before processing through the pipeline return a better S/N.

Using the Xenon and Quartz flats a master-flat is produced by the pipeline. It turns out that the pipline master-flat has less variations and is in general closer to one than the IRAF master-flat. The tracing of the different orders is inspected by eye individually for every frame. If the tracing does not work well the order is interpolated by the pipeline using a spline function. However, all orders used for scientific purposes are always traced and never interpolated.

After using the pipeline we only have to normalize the orders and add them together as described in the last paragraphs of the previous section. The only difference to the IRAF procedure is that we use a polynom of order six for all orders instead of varying the order individually.

For the MC RR Lyrae stars a final S/N level of $10 - 25$ per pixel was achieved for the combined observations at a wavelength of 7500Å. For the standard stars, reduced in the same way, a S/N level of $150 - 200$ per pixel at $\lambda \approx 7500$Å is obtained. An exemplary spectrum is shown in Figure 7.4. The other spectra are shown in the Appendix.

7.2.4 Uncertainties

For the discussion of our uncertainties we will always quote the standard deviations

$$\sigma = \sqrt{\frac{1}{n}\Big(\sum_{n=1}^{i}(x_i - \mu)^2\Big)\frac{n}{n-1}} \tag{7.2}$$

where n is the number of measurements, x_i are the individual datapoints and μ is the mean of the sample. The last term $n/(n-1)$ corrects for the effects of small number statistics. We do not use the standard error $\sigma/\sqrt{n}$, unless not explicitly stated.

---

[4] `http://www.noao.edu/kpno/specatlas/thar/`

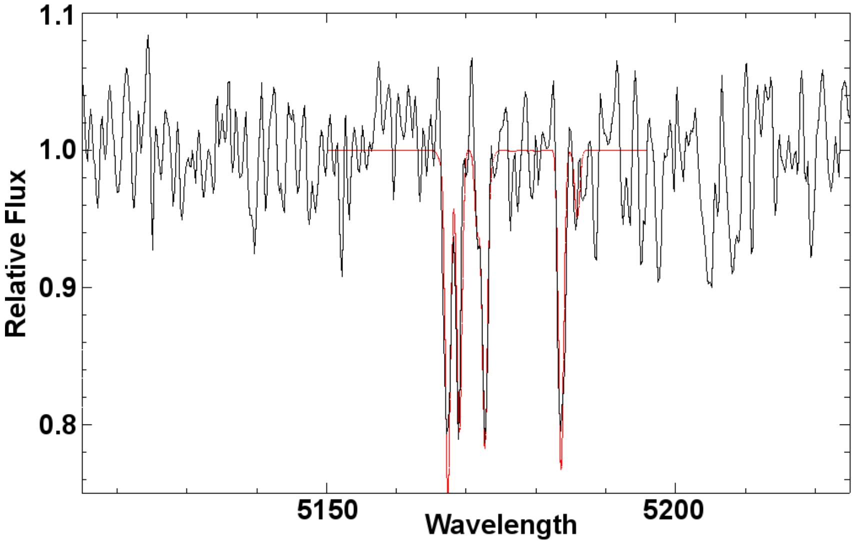

Figure 7.4: Spectrum of RR1422 at the Mg lines around 5170Å. The red line indicate the best fitting synthesized model.

7.3 Radial Velocities

The pulsation of an RR Lyrae star causes periodic changes in the observed spectra and hence of the measured radial velocity. For RR Lyrae type *ab* stars, the radial velocity changes by up to 60 – 70 km s^{-1} during a given period, with the lowest velocity around minimum light (Smith 2004). Moreover, the different layers of the stellar atmosphere move with a velocity that gradually increases towards the outer shells. Since metallic and Balmer lines originate at different optical depths in the atmospheres, the pulsation can introduce systematic velocity offsets in the lines used for the velocity estimate depending at which phase the spectra were taken.

We determine the radial velocities from the Doppler shift of the near-infrared Ca II-triplet lines between 8492Å and 8662Å and of the Balmer lines, Hγ, Hβ and Hα, between 4333Å and 6568Å. Taking all individual measurements, we compute the mean and median value of the radial velocity as well as the standard deviation.

Using the approach described in Vivas et al. (2005), we estimate the pulsational velocity of each target star to obtain the systemic velocity. The template pulsational velocity curve of X Ari, observed by Oke (1966) and parameterized by Layden (1994), is adopted for all target RR Lyrae stars. The velocity curve of X Ari is fitted at the observed phase of our targets to derive the corresponding pulsational velocity. However, for each star only measurements at one certain phase of the period are available and a fit to the radial velocity curve is rather uncertain. To calculate the uncertainties of the systemic velocities we adopt Equation 1 of Vivas et al. (2005)

$$\sigma_\gamma^2 = \sigma_r^2 + (119.5 \times 0.15)^2 + (23.9\Delta\Phi)^2, \tag{7.3}$$

where σ_γ is the uncertainty of the systemic velocity and σ_r the standard deviation of the radial velocity measurements. The second term reflects the duration of the observation of the spectra. This took usually about 15% of the target's phase. This duration of the observation is convolved with the slope of the velocity curve of 119.5 km s^{-1}. The third term reflects the 1σ star-to-star variation of the velocity amplitude of 23.9 km s^{-1}, as found by Vivas et al. (2005), combined with the difference of the observed phase of our target star to the phase with zero systemic velocity, which is found to occur at $\Phi = 0.5$ for X Ari.

Table 7.5: Various velocity estimates and uncertainties of all our target stars and X Ari

Star	$RV_{\mathrm{median/helio}}$ km s^{-1}	$RV_{\mathrm{median/LSR}}$ km s^{-1}	mean phase	σ_r	σ_γ
RR15903	320	304	0.64	5	19
RR8645	292	277	0.38	23	29
RR1422	325	309	0.57	11	21
RR177	287	271	0.18	20	27
RR11371	323	308	0.41	30	35
RR22827	295	279	0.81	33	38
RR122432	174	163	0.45	33	38
RR50180	133	122	0.66	18	25
RR143874	109	98	0.41	8	20
X Ari	−40	−51	0.51	15	23

In Table 7.5 we present the median heliocentric systemic radial velocities, as well as systemic radial velocities in the local standard of rest (LSR), using the IRAF task *rvcorrect*. The mean velocities are very similar to the median velocities in Table 7.5. Additionally the pulsational velocity of the star, the mean phase of the observation and the standard deviation of the radial velocity measurements as well as the uncertainty of the systemic velocity are shown.

The values for the heliocentric radial velocity of X Ari found by us are in very good agreement with the literature, for instance, Valdes et al. (2004) found a value of −40 km s^{-1}.

The mean systemic heliocentric velocity of our small sample of LMC RR Lyrae stars is found to be 307 ± 19 km s^{-1}. This value is more than 1 σ greater than the radial velocities of Gratton et al. (2004), who found 261 ± 40 km s^{-1}, of Borissova et al. (2004), who found 264 ± 19 km s^{-1}, or of Borissova et al. (2006) with 255 ± 65 km s^{-1}. However, these measurements were made in the most central parts of the LMC and it seems reasonable that the disk region may have a different velocities compared to the central regions in and close to the bar.

Velocities of the H I gas of the LMC are investigated in Staveley-Smith et al. (2003). Most of the gas has velocities between 186 km s^{-1} and 280 km s^{-1}. The velocities of the southern regions are in general a bit lower, while the northern parts are at the high end of the velocity distribution. For the intermediate velocities the gas is distributed like a barred spiral, however the 'bar' does not coincide with the stellar bar (compare Staveley-Smith et al. 2003, Figure 2). The overall mean velocity is in good agreement with the measurements from Gratton et al. (2004) and Borissova et al. (2004, 2006).

In the sample of Borissova et al. (2006), some high-velocity stars with radial velocities up to 399 km s^{-1} are present. We compare their metallicities of these high-velocity stars with their metallicities for the other stars. Both groups of stars have an indistinguishable mean metallicity and therefore we do not find any correlation between velocity and metallicity.

Moreover, the radial velocity of the LMC seems very similar for different stellar tracers. With a sample of 738 red supergiants distributed within several degrees from the center of the LMC, Olsen et al. (2011) found a systemic velocity of 263 ± 2 km s^{-1}. One possibility is that the differences to our mean value are an effect of small number statistics. Another possibility is that our metal-poor RR Lyrae stars trace an older, earlier population than the more metal-rich RR Lyrae stars studied before, possibly tracing a sparse, metal-poor halo.

For the RR Lyrae stars in the SMC we find a mean systemic velocity of 138 ± 40 km s^{-1}. In the literature no velocity estimates were carried out for RR Lyrae stars so far. Only samples of brighter SMC stars were used to determine the distribution of the radial velocity. With more than 2000 RGB stars, Harris & Zaritsky (2006) found a Gaussian distribution of the velocity with its maximum at 145.6 ±

Table 7.6: Equivalent width measurements for all target and standard stars. Only the first few lines and columns are shown. The full table is available electronically.

Element	λ [Å]	χ [eV]	log gf	HD 74000$_{\mathrm{H11}}$ [mÅ]
Na I	5889.97	0.00	0.108	175
Na I	5895.94	0.00	−0.194	130
Mg I	4057.52	4.34	−0.890	...
Mg I	4167.28	4.34	−1.010	31

0.6 km s^{-1} and a velocity dispersion of 27.6 ± 0.5 km s^{-1}. Our results are in good agreement with these values. De Propris et al. (2010) evaluated red giants in ten different fields with distances of 0.9 kpc to 5.1 kpc from the SMC center and found that the velocity distribution functions between the different fields are significantly different. Some fields show single peak distributions, while others seem to be bimodal. The mean radial velocity changes also between the fields and they find values between 147 ± 26 km s^{-1} and more than 200 km s^{-1} for the second peak in fields with a bimodal distribution. Overall, our velocity estimates are in good agreement with the velocities of De Propris et al. (2010). However, our stellar sample for the SMC needs to be enlarged first before more detailed conclusions can be drawn.

7.4 Equivalent Width Measurements

Our line list for the investigated RR Lyrae stars of the MCs is primarily based on the line list of C95. They investigated, among others, X Ari, which we use as a standard RR Lyrae star in our analysis. The line list of C95 is complemented by the lists of Peterson (1978, from now on P78) and Beveridge & Sneden (1994), who obtained abundances for HD 74000, the other standard star in our investigation. Before we employ the merged list, we test for blends by comparing our list with the line list extracted from the Vienna Atomic Line Database (VALD), set up by Piskunov et al. (1995). All blended lines are removed from the sample.

With the IRAF task *splot*, a Gaussian is fitted to the line profile of every unblended atomic line in our line list. We remove all lines that are obviously contaminated by noise or cosmic rays. For our science targets, very strong lines (EW $>$ 200 mÅ) as well as weak lines (EW $<$ 20 mÅ) were excluded from further analysis. The strong lines might be saturated, while for the weak lines the uncertainties of the EW measurements are too large due to the low S/N. The remaining values for the EWs of our target stars, together with the literature values for the standard stars, the excitation potential (χ) and the value for the oscillator strength (log gf), are given in Table 7.6.

Comparing our EW measurements of the standard star HD 74000 we find very similar results to the literature values by P78 with a mean difference of ΔEW = 5.9 mÅ and a standard deviation of 16.4 mÅ. Even better agreement is achieved by comparing the measurements to Beveridge & Sneden (1994). A mean difference of ΔEW = 3.5 mÅ with a standard deviation of 7.6 mÅ is obtained. The literature values of the EWs of X Ari obtained by C95 are generally higher by ΔEW = 38.6 mÅ than the measurements by us. We explain this rather large difference with a different observed phase of the variable RR Lyrae star X Ari. While C95 observed X Ari between $0.71 < \Phi < 0.82$, our observations were conducted between $0.47 < \Phi < 0.55$. The physical conditions, such as a temperature and surface gravity, are therefore altered.

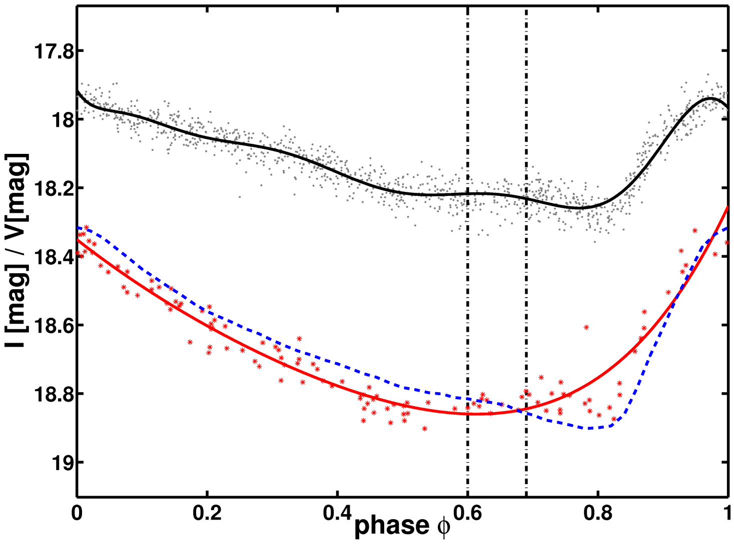

Figure 7.5: An exemplary light curve for our target stars, here RR 15903. The grey dots are the observed *I* band magnitudes, while the black line is the corresponding fit. *V* band magnitudes are shown with red asterisks. The red line is the polynomial fit. The best template of Layden (1998) is shown with the blue dotted line. The vertical black dash-dotted lines indicate the actually used observation window for RR15903.

7.5 Stellar Parameters

For the analysis of the chemical abundances of our nine RR Lyrae stars in the MCs as well as for the three standard stars, we use two independent approaches. In order to determine the stellar abundances, either from EWs or spectral synthesis, we need to know the following parameters: effective temperature ($T_{\rm eff}$), surface gravity (log g), metallicity ([Fe/H]) and microturbulence (ν_t). Interpolation of Kurucz's atmosphere model grid without convective overshooting (Castelli et al. 1997) is used to construct model atmospheres for the different stars. The local thermodynamic equilibrium (LTE) spectral line synthesis code MOOG[5] (Sneden 1973) is used, in its version from 2010, to derive the elemental abundances from the EW measurements and from the synthesis of the spectra. The code assumes the solar and meteoritic abundances from Anders & Grevesse (1989), except for the iron content of $\log \varepsilon(\mathrm{Fe}) = 7.52$, taken from the solar abundance catalogue of Grevesse & Sauval (1998).

7.5.1 Effective Temperature

C95 derived a relation to calculate the effective temperature $T_{\rm eff}$ of an RR Lyrae star from the differences of its brightness in different filters. Their Equation 4 summarizes the relations for four different colors. In OGLE III, the *V* and *I* filter are used. Therefore, we use

$$\begin{aligned} T_{\mathrm{eff/C95}} &= 753.906677(V-I)^2 \\ &-4836.16016(V-I) + 8801.4248. \end{aligned} \tag{7.4}$$

Investigating dwarfs and subgiants Casagrande et al. (2010, from now on C10) found a relation for the reciprocal effective temperature, $\theta_{\rm eff} \equiv 5040/T_{\rm eff}$, based on the color of the star and its metallicity

---

[5] http://www.as.utexas.edu/~chris/moog.html

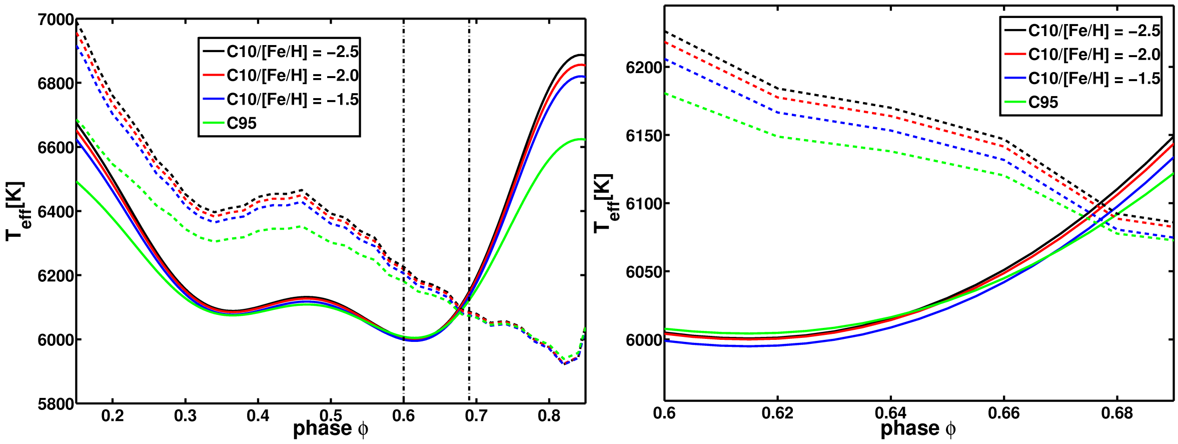

Figure 7.6: Using Equation 7.4 of Clementini et al. (1995) we obtain the green curves for the effective temperature of the target star RR 15903. The black, red and blue lines indicate the temperature curves of Equation 7.5 (C10) for three different metallicities. While the solid line shows the temperature obtained by using the polynomial fit of the *V* band measurements, the dashed lines are computed with the template *V* band light curve of Layden (1998). The upper panel shows the temperature for one period, while the lower panel is a blow-up of the observed phase enclosed by the two vertical black dash-dotted line in the upper panel.

[Fe/H]. This equation has not been tested for variable stars yet. We want to test whether the relation is applicable and adopt their Equation 3

$$\begin{aligned}\theta_{\mathrm{eff/C10}} &= 0.4033 + 0.8171(V-I) - 0.1987(V-I)^2 \\ &- 0.0409(V-I)[\mathrm{Fe/H}] + 0.0319[\mathrm{Fe/H}] + 0.0012[\mathrm{Fe/H}]^2.\end{aligned} \tag{7.5}$$

To calculate the effective temperature of each star at the phase of observation, we need the color information for this specific time. The lightcurve of the RR Lyrae star is recovered using the individual observations taken over several years by the OGLE III collaboration in the *V* and preferentially the *I* band. As a first approach, we fit the data points of the individual observations with a tenth order polynomial for the *I* band and a fifth order polynomial for the *V* band. The data in the *I* band are much better sampled because of the many repeat observations in this filter, while the fit of the *V* band is more susceptible to the influence of outliers. Especially the phase of rapid atmospheric change at $\Phi = 0.8 - 0.2$ is not very well sampled and therefore the fitted lightcurve is not reliable in this range.

As a second approach to determine the lightcurve in the *V* band, we use the six template light curves Layden (1998) introduced, based on his study of 103 Galactic RR Lyrae type *ab* stars. By using a χ^2 test, we find the template light curve fitting our target stars best.

Subtracting the *I* band light curve (black line in Figure 7.5) from the *V* band light curve from the polynomial fit (red line in Figure 7.5), as well as from the template light curve of Layden (1998) (blue dotted line in Figure 7.5), we obtain two sets of colors for the different phases of the RR Lyrae stars.

These colors are inserted into Equation 7.4 and the resulting temperature curve over the whole period of the star is shown with the green lines in Figure 7.6. For Equation 7.5 we use the obtained colors plus a set of metallicities to calculate the effective temperature curve of the RR Lyrae star. We decided to use three metallicity values, $[\mathrm{Fe/H}] = -2.5$, $[\mathrm{Fe/H}] = -2.0$ and $[\mathrm{Fe/H}] = -1.5$, to calculate effective temperatures. Figure 7.6 illustrates that the differences introduced by the metallicity are small and therefore the temperature curve of $[\mathrm{Fe/H}] = -2.0$ is used for all stars as a temperature estimate.

Table 7.7: Mean effective temperatures of the observed phase of our target stars from Equation 7.4 and Equation 7.5 with a metallicity of [Fe/H] = −2.0. The first two values show the temperature obtained from using the polynomial fits of the V band. For column 4 and column 5 the template light curves of Layden (1998) are used. Moreover, the effective temperature determined by the spectral analysis program MOOG is shown in column 6.

Star	phase	$T^{\text{poly fit}}_{\text{eff/C10}}$	$T^{\text{poly fit}}_{\text{eff/C95}}$	$T^{\text{templ. fit}}_{\text{eff/C10}}$	$T^{\text{templ. fit}}_{\text{eff/C95}}$	$\mathrm{T}_{\text{eff/spec}}$
RR 15903	0.60 – 0.69	6037	6035	6143	6121	6500
RR 8645	0.33 – 0.44	6529	6408	7755	7113	6500
RR 1422	0.52 – 0.62	6786	6579	6703	6525	6250
RR 177	0.14 – 0.22	6335	6269	6213	6176	6500
RR 11371	0.38 – 0.45	6203	6169	5937	5950	6250
RR 22827	0.78 – 0.85	6468	6360	5271	5288	6500
RR 122432	0.42 – 0.49	7675	7075	9084	7649	6000
RR 50180	0.64 – 0.69	6061	6053	6324	6259	6000
RR 143874	0.36 – 0.45	6898	6650	7175	6812	6500
X Ari	0.47 – 0.55	5915	6271	...	...	6700

Table 7.8: The mean and median differences as well as the standard deviation between the different photometric and the spectroscopic temperature estimates $T_{\text{eff/spec}}$.

$T^{\text{fit}} - T_{\text{spec}}$	$T^{\text{poly fit}}_{\text{eff/C10}}$	$T^{\text{poly fit}}_{\text{eff/C95}}$	$T^{\text{templ. fit}}_{\text{eff/C10}}$	$T^{\text{templ. fit}}_{\text{eff/C95}}$
mean [K]	39	−60	65	95
median [K]	−2	−87	19	−21
stdev σ [K]	312	264	768	597

For the relations of C95 and of C10, the solid line in Figure 7.6 represents the temperature obtained from the polynomial fit of the V band magnitudes. The temperature calculated with the V band template light curves of Layden (1998) are shown with the dotted line in Figure 7.6.

A color difference of $\Delta(\mathrm{V}-\mathrm{I}) = 0.01$ mag corresponds to a temperature difference of 50 K (C95) in T_{eff}. Our V band magnitudes are not as well sampled as for the I band. With individual uncertainties of 0.05 mag for each V band magnitude, our fit of the V band light curve becomes less certain than the I band fit, where each data point has a similar uncertainty as in the V-band. We thus have to assume an uncertainty of at least 300 K of the temperatures.

These temperatures are used as a first guess for spectroscopic temperature determinations with the spectral analysis program MOOG. To determine such a temperature estimate we force the abundance of the iron line not to change with the χ of the respective lines. Table 7.7 summarizes the temperatures found.

The comparison between photometric and spectroscopic temperature estimates reveals a good agreement for four of the stars, with differences smaller than 150 K between them (Table 7.7). For four other stars, we find deviations between 150 K and ~ 500 K, which can still be accounted for by the uncertainties due to the not very well-sampled V band light curves. In general, we find that a less good sampling of the observations in the V band introduces higher differences in the temperature estimates, while the sampling in the I band is always very good. This is especially the case for the V band light curve for RR 122432, where the temperatures deviate by more than 500 K. Therefore the fit to the light curve is rather uncertain and the temperature estimate, which is much too high for an RR Lyrae star, is rejected. Thus, this star is excluded from the further comparison of photometric and spectroscopic temperatures.

The mean, the median and the standard deviation for the differences between the photometric and

Table 7.9: The final set of parameters from the EW abundance determination.

Star	T_{eff}	log g	[Fe/H]	v_t
HD74000	6100	3.5	−2.08	1.5
X Ari	6700	2.1	−2.61	2.6
G64-12	6350	4.4	−3.13	1.5
RR 15903	6500	2.6	−2.24	3.5
RR 8645	6500	3.0	−1.97	5.0
RR 1422	6250	2.0	−2.49	4.0
RR 177	6500	2.6	−2.67	3.8
RR 11371	6250	2.6	−2.18	3.2
RR 22827	6500	1.5	−2.49	2.5
RR 122432	6000	2.6	−2.36	4.5
RR 50180	6000	2.0	−2.36	4.5
RR 143874	6500	2.0	−2.34	2.0

the spectroscopic temperatures are shown in Table 7.8. It turns out that the polynomial fit of the V band lightcurve is preferable to the use of the templates provided by Layden (1998). The templates of Layden are calibrated on RR Lyrae stars with higher metallicities than the our targets. The parameters of the lightcurves change with metallicity and it is therefore not surprising that deviations from the templates are found. The relation adopted from C95 leads to slightly better temperature estimates than the relation by C10, assuming that the spectroscopic temperatures are correct. We conclude that both relations are well suited for an estimate of the temperature of an RR Lyrae star.

7.5.2 Other stellar parameters

The other stellar parameters, such as the log g, metallicity ([Fe/H]) and $v_{mathrmt}$ are determined in an iterative procedure. For the metallicity, we assume the photometric estimate as a starting point for our stellar models. The surface gravity is set to log g = 2.6, a typical value for an RR Lyrae star at minimum light (e.g., Oke 1966). For the microturbulence we assume $v_t = 3\,\mathrm{km\,s^{-1}}$.

Fe II is much more sensitive to the surface gravity than Fe I. By varying the abundance of Fe I and Fe II until the different ionization states lead to a similar abundance the value of log g is estimated. The microturbulence is matched such that no abundance differences with the reduced width log(EW/λ) of the Fe I lines are found. After each iteration a new Kurucz model is used with the updated version of the parameters and the next iteration is started, until the final set of parameters is found. Owing to the low S/N for two stars the difference between Fe I and Fe II can only be reduced by assuming unphysical stellar parameters. Therefore we allow for differences of 0.2 dex for the LMC targets and 0.3 dex for the SMC RR Lyrae stars. Furthermore we test our log g values using photometrically derived gravities and find good agreement between both methods. The final set of stellar parameters is shown in Table 7.9.

7.5.3 Comparison of stellar parameters for the standard stars with literature values

For HD 74000, we found data on the stellar parameters in P78, Beveridge & Sneden (1994), and Fulbright (2000). Their estimates agree very well with ours. Only the log g value is higher by about 0.6 dex (see Table 7.10).

For X Ari, we estimate slightly higher temperature and lower log g values than found by C95 and Lambert et al. (1996) (see Table 7.10). However, this is an effect of observing X Ari at a different phase than the other authors. The metallicity is in very good agreement with the literature, while the microturbulence is a bit lower than the literature values.

Table 7.10: Stellar parameters of standard stars from the literature.

Star	T_{eff}	log g	[Fe/H]	v_t	Source
HD74000	6250	4.50	−1.80	...	P78
HD74000	6090	4.15	−2.07	1.30	Beveridge & Sneden (1994)
HD74000	6025	4.10	−2.00	1.20	Fulbright (2000)
X Ari	6100	2.60	−2.5	3.0	Lambert et al. (1996)$_{\mathrm{phot}}$
X Ari	6500	2.70	−2.5	4.4	Lambert et al. (1996)$_{\mathrm{spec}}$
X Ari	6109	2.60	−2.5	4.5	C95$_{\mathrm{spec}}$
G64-12	6350	4.40	−3.0	1.5	Boesgaard & Novicki (2006)

Table 7.11: Abundance differences due to parameter uncertainties, applied to X Ari as a proxy for all target stars

Element	$\Delta T = 300\,\mathrm{K}$	$\Delta \log g = 0.5$	$\Delta v_{\mathrm{t}} = 0.5$
Na I	−0.21	0.02	0.05
Mg I	−0.16	0.02	0.10
Al I	−0.24	0.02	0.01
Si I	−0.24	0.03	0.04
Ca I	−0.22	0.02	0.08
Sc II	−0.15	−0.16	0.07
Ti I	−0.15	0.03	0.02
Ti II	−0.18	−0.12	0.13
Cr I	−0.28	0.02	0.01
Cr II	−0.30	−0.01	0.19
Mn I	−0.30	0.03	0.01
Fe I	−0.28	0.03	0.08
Fe II	−0.06	−0.16	0.08
Co I	−0.29	0.02	0.02
Ni I	−0.51	0.17	0.15
Sr II	−0.21	−0.13	0.12
Ba II	−0.26	−0.08	0.01

For G64-12, the agreement of our estimates with the values by Boesgaard & Novicki (2006) is very good for all the parameters.

7.5.4 Systematic parameter uncertainties

We test the sensitivity of the abundances to the stellar parameters by altering one single parameter of X Ari at a time and calculating the abundance difference (Table 7.11). For the temperature we assume an uncertainty of $\Delta T = 300\,\mathrm{K}$, which corresponds to the uncertainty of our photometric temperature estimate. For the surface gravity we adopt an uncertainty of $\Delta \log g = 0.5$ dex, while for the microturbulence $\Delta v_{\mathrm{t}} = 0.5\,\mathrm{km/s}^{-1}$ is assumed. These differences are adopted as uncertainties for all RR Lyrae stars in our sample.

For neutral species the abundance ratios show the largest dependence on the estimated $\mathrm{T}_{\mathrm{eff}}$. These elements are rather insensitive to changes in the surface gravity or microturbulence. The surface gravity plays a much larger role for the ionized elements.

7.6 Results: abundance ratios

We use two independent approaches to determine the abundances of the nine target and three standard stars. First, we calculate the the abundances directly from the EWs using MOOG's *abfind* driver. For the second approach, we synthesize the spectral features of the stars. Both approaches are performed with the 2010 version of the spectral analysis program MOOG (Sneden 1973).

First the abundances are determined from the EW measurements. First, the set of model atmosphere parameters is iterated until the best possible solution for the iron content is found (see Section 7.5). These best model parameters are used to determine the abundances of up to 14 different elements (Na I, Mg I, Al I, Si I, Ca I, Sc II, Ti, Cr, Mn I, Fe, Co I, Ni I, Sr II, Ba II). For three of the elements (Ti, Cr, Fe) we are able to determine the abundances both for neutral and singly ionized line transitions.

We identify the spectral features that are significantly larger than the background noise. These lines are further investigated by spectral synthesis. All features close to the line of interest are fitted by the spectral synthesis model to determine abundance values for all features present and measureable. In this way we properly account for blended lines, which yield the correct abundance of the line of interest. The resulting mean abundances for [Fe/H] and [X/Fe] of the synthesis for the different elements are shown in Table 7.12. Here, X stands for all investigated elements except Fe.

For [X/Fe] we have computed a simple mean of the individual abundances. To compute the standard deviation σ these individual values, together with the mean value [X/Fe], are used as described in Section 7.2.4. The resulting values of σ are shown in Table 7.12. Additionally this table displays, for each species, the number N of lines we were able to determine abundances from.

Unfortunately the number of measurable lines is usually quite small. Therefore the standard deviations are not useable for uncertainty estimates. We rather use the values obtained in Table 7.11 to assign uncertainties to the abundances. For the standard stars we obtain $\sigma_{[X/Fe]} = 0.2$ dex, while for the science targets $\sigma_{[X/Fe]} = 0.3$ dex is found. We only publish the abundances from the spectral synthesis in Table 7.12 if the fitting of the model and the observed spectrum is unambiguous within this uncertainty range. Otherwise the abundance value of the line is rejected.

Due to the low S/N level of the target stars, we inspect the profiles of the features very carefully. The knowledge of the expected line profile of the feature leads to a more conservative abundance estimate using the spectral synthesis than the EW. While using the EW on low S/N data, it may sometimes be difficult to distinguish between real features and additional noise. If the abundances from the EW measurements agree within the uncertainties with the results obtained from the spectral synthesis we show them in Table 7.12 as well. The standard deviations σ of the EW abundances are computed in the same way as described for the spectral synthesis. For elements with only a few available lines, the spectral synthesis abundances are anyhow always taken as more reliable.

Our target stars have very similar stellar parameters as the RR Lyrae stars investigated in Hansen et al. (2011). Therefore, we adopt their NLTE corrections, which are larger than our uncertainties. For aluminum a correction of $\Delta_{\mathrm{NLTE}} = +0.7$ dex (Andrievsky et al. 2008) is found. The NLTE correction for strontium is adopted from Mashonkina & Gehren (2001) with a value of $\Delta_{\mathrm{NLTE}} = +0.6$ dex.

7.6.1 Iron

For the iron content of the stars, we adopt the data from the EWs as well as from the spectral synthesis. We are able to measure EWs for eight to 34 reliable iron lines per star. For the other elements we consider only the synthesized abundances since there are many fewer lines.

The extremely low photometric metallicity of some of the targets cannot be confirmed. For our target stars spectroscopic metallicities between -2.67 dex $\leq$ [Fe/H] ≤ -1.97 dex are found (see Table 7.12). The RR Lyrae star with [Fe/H] $= -2.67$ dex is the most metal-poor star found so far in the MCs (see Figure 8.2).

Table 7.12: Abundances from EW measurements and spectral synthesis of the lines.

star	[Fe/H]			[Fe I/H]			[Fe II/H]		
	synth	σ	N	EW	σ	N	EW	σ	N
HD74000	−2.15	0.15	10	−2.08	0.28	28	−2.12	0.31	6
X Ari	−2.58	0.10	9	−2.61	0.23	26	−2.62	0.28	5
G64-12	−3.06	0.20	6	−3.13	0.28	20	−3.02	0.36	2
RR 15903	−2.34	0.00	2	−2.24	0.26	11	−2.32	0.24	3
RR 8645	−1.72	0.33	4	−1.97	0.26	8	−1.94	0.41	3
RR 1422	−2.26	0.17	4	−2.49	0.32	13	−2.23	0.31	4
RR 177	−2.57	...	1	−2.67	0.33	10	−2.50	0.48	3
RR 11371	−2.10	...	1	−2.18	0.24	6	−2.16	0.48	2
RR 22827	−2.42	0.11	4	−2.50	0.24	14	−2.63	0.08	5
RR 122432	...	...	...	−2.36	0.12	9	−2.31	0.47	3
RR 50180	...	...	...	−2.36	0.33	13	−2.02	0.34	2
RR 143874	...	...	...	−2.34	0.17	8	−2.34	0.39	3

star	[Na I/Fe I]						[Mg I/Fe I]						[Al I/Fe I]					
	synth	σ	N	EW	σ	N	synth	σ	N	EW	σ	N	synth	σ	N	EW	σ	N
HD74000	0.70	...	1	0.57	0.23	2	0.60	0.00	2	0.68	0.71	4	0.50	...	1	...	...	...
X Ari	−0.05	...	1	0.17	0.24	2	0.35	0.10	2	...	...	...	−0.50	...	1	−0.65	0.37	2
G64-12	−0.40	...	1	−0.30	0.38	2	−0.03	0.06	2	0.14	...	1	−0.40	...	1	...	...	...
RR 15903	0.10	...	1	0.02	...	1	0.55	0.10	2	0.54	0.34	2	...	...	...	...	...	...
RR 8645	0.10	...	1	−0.05	...	1	0.75	0.49	2	0.93	...	1	...	...	...	...	...	...
RR 1422	...	...	...	...	...	...	0.50	0.00	2	...	...	...	0.50	...	1	...	...	...
RR 177	...	...	...	...	...	...	−0.50	...	1	...	...	...	...	...	...	...	...	...
RR 11371	...	...	...	...	...	...	...	...	...	...	...	...	...	...	...	...	...	...
RR 22827	...	...	...	...	...	...	0.35	0.10	2	...	...	...	0.40	...	1	...	...	...
RR 122432	...	...	...	...	...	...	...	...	...	...	...	...	...	...	...	...	...	...
RR 50180	...	...	...	...	...	...	0.10	...	1	0.03	0.35	2	...	...	...	...	...	...
RR 143874	...	...	...	...	...	...	...	...	...	...	...	...	...	...	...	...	...	...

star	[Ca I/Fe I]						[Sc II/Fe II]						[Ti II/Fe II]					
	synth	σ	N	EW	σ	N	synth	σ	N	EW	σ	N	synth	σ	N	EW	σ	N
HD74000	0.20	0.40	5	0.24	...	1	−0.05	...	1	−0.04	...	1	0.19	0.18	8	0.52	0.37	12
X Ari	0.33	0.22	4	0.50	0.51	3	0.50	...	1	0.36	...	1	0.16	0.23	6	0.70	0.24	14
G64-12	0.50	0.00	2	0.70	0.59	2	0.10	...	1	0.19	...	1	0.10	0.21	3	0.44	0.27	8
RR 15903	0.75	0.49	2	...	...	...	...	...	...	...	...	...	0.10	0.39	2	0.24	0.27	6
RR 8645	0.00	...	1	...	...	...	...	...	...	...	...	...	0.33	0.15	4	0.38	...	1
RR 1422	0.50	...	1	...	...	...	...	...	...	...	...	...	0.33	0.43	3	0.24	0.35	3
RR 177	...	...	...	...	...	...	0.30	...	1	0.34	...	1	0.00	...	1	−0.20	0.34	4
RR 11371	0.33	0.06	2	...	...	...	...	...	...	...	...	...	...	...	...	0.26	0.46	3
RR 22827	0.35	0.10	2	0.38	0.23	3	−0.20	...	1	...	...	...	0.20	...	1	0.00	0.45	4
RR 122432	...	...	...	...	...	...	...	...	...	...	...	...	...	...	...	−0.66	0.24	4
RR 50180	...	...	...	...	...	...	...	...	...	...	...	...	0.00	...	1	−0.01	0.63	2
RR 143874	0.20	...	1	...	...	...	...	...	...	...	...	...	...	...	...	0.05	0.24	4

star	[Cr I/Fe I]						[Sr II/Fe II]						[Ba II/Fe II]					
	synth	σ	N	EW	σ	N	synth	σ	N	EW	σ	N	synth	σ	N	EW	σ	N
HD74000	−0.20	0.39	2	−0.18	0.19	4	0.60	...	2	0.39	...	1	0.20	0.59	2	0.49	0.22	3
X Ari	0.05	0.39	2	−0.11	0.38	3	−0.40	0.20	2	−0.39	...	1	−0.30	...	1	−0.12	0.41	2
G64-12	0.00	...	1	...	...	...	...	...	...	...	...	...	...	...	...	0.81	0.35	2
RR 15903	...	...	...	...	...	...	0.40	...	1	...	...	...	0.20	...	1	0.08	0.42	4
RR 8645	...	...	...	...	...	...	...	...	...	...	...	...	0.50	0.00	2	0.30	0.16	2
RR 1422	0.10	0.20	2	−0.24	0.03	2	0.25	0.49	2	...	...	...	...	...	...	0.04	0.17	4
RR 177	0.30	...	1	0.02	0.02	2	−0.40	...	1	...	...	...	...	...	...	0.32	0.83	2
RR 11371	...	...	...	...	...	...	...	...	...	...	...	...	...	...	...	−0.50	0.37	2
RR 22827	0.50	...	1	0.38	...	1	0.10	0.20	2	...	...	...	...	...	...	0.35	0.89	2
RR 122432	...	...	...	...	...	...	...	...	...	...	...	...	...	...	...	−0.61	1.34	2
RR 50180	...	...	...	...	...	...	...	...	...	...	...	...	...	...	...	−0.20	0.54	4
RR 143874	...	...	...	...	...	...	...	...	...	...	...	...	...	...	...	0.15	0.85	3

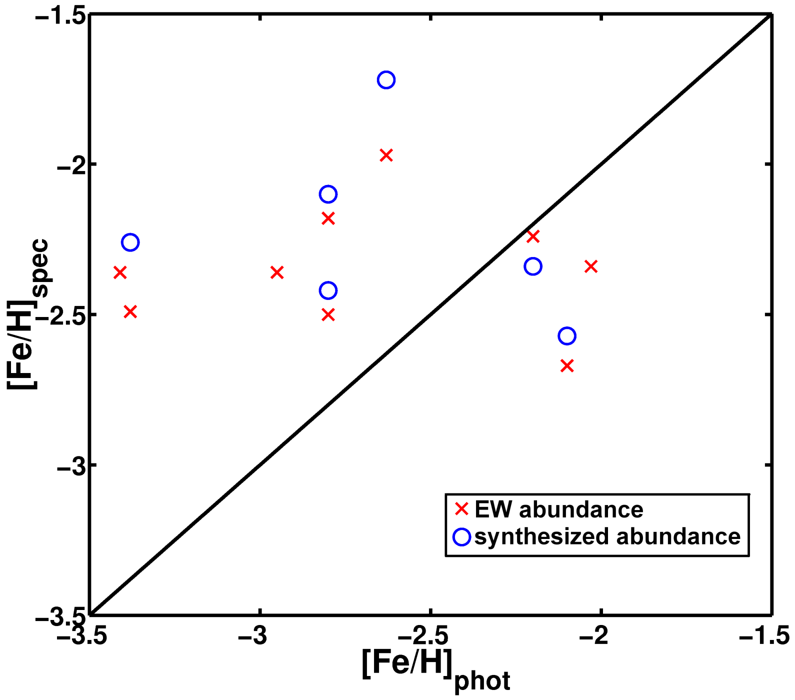

Figure 7.7: Photometric metallicity estimates versus spectroscopic measurements. The iron abundances from the EW measurements are labeled with the red crosses, while the synthesized abundances of iron are shown as blue circles. For the SMC RR Lyrae stars no synthesized value is available. Overall we see a trend for lower spectroscopic metallicities for stars with photometric metallicities around −2 dex. For $[\mathrm{Fe/H}]_{\mathrm{phot}} < -2.5$ dex the trend is reversed. Overall all target stars have similar spectroscopic metallicities.

Measuring the EW, we detect for all target stars several Fe I lines and at least two reliable Fe II lines. By construction the abundances of both ionisation states should be the same, but due to the low S/N of the data we allow for small differences to obtain reasonable stellar parameters (see Section 7.5.2). Therefore, a small difference of on average -0.07 ± 0.15 dex is found between the abundances of Fe I and Fe II from EW measurements for our target stars.

Some of the iron lines are weak and the synthesizing process did not provide a significant result within our uncertainty margins. However, for the lines that are synthesizable, very good agreement with the abundances from the EW measurements is obtained. We are therefore confident that the values obtained from the EW are reliable owing to the large number of lines used.

The low S/N is responsible that the synthesis of the iron lines in our SMC targets did not yield to any results within our error margins. We therefore rely on the EW measurements for the iron content of these stars. The individual measurements of the lines yield high uncertainties, but we were able to measure a large number of lines, which leads, within our error margins, to a reliable determination of the abundance.

Comparing the photometric metallicity of the RR Lyrae stars obtained from the Fourier parameters of the lightcurves (Chapter 3) with the iron abundances of our spectra, we find trends as shown in Figure 7.7. For the most metal-rich stars of our sample, i.e., the three stars with $[\mathrm{Fe/H}]_{\mathrm{phot/J95}} \geq -2.20$ dex, we find lower spectroscopic metallicities. These differences range from −0.04 dex to −0.57 dex. This discrepancy of too high photometric metallicity estimates for the metal-poor stars is a well known property for the *V* and *I* band calibration and was found to amount to 0.2 dex to 0.3 dex (e.g., Dékány & Kovács 2009; Arellano Ferro et al. 2011) for Galactic RR Lyrae stars. The offset is attributed to the low number of metal-poor calibration stars for the Fourier decomposition method. Papadakis et al. (2000) found that the metallicity scale of ZW84 is about 0.3 dex lower than that of J95. If we transform the photometric metallicities to the scale of ZW84 and compare them to our spectroscopic metallicities we find very good agreement between both values with a mean difference of 0.02 ± 0.14 dex.

However, for the RR Lyrae stars that may be even more metal-poor, we find a completely different picture. The stars with a photometric metallicity estimate of $[\mathrm{Fe/H}]_{\mathrm{phot/J95}} \leq -2.80$ dex turn out to be more metal-rich by 0.31 dex to 1.05 dex when analyzed spectroscopically. On the scale of ZW84 the differences between the photometric and spectroscopic metallicities are even larger by 0.3 dex.

Comparing the spectroscopic metallicities of these two groups, we find that they are indistinguishable. On average both groups have a mean value of $[\mathrm{Fe/H}]_{\mathrm{spec}} = -2.4$ dex. In the low metallicity regime another unknown factor appears to additionally alter the shape of the lightcurve to mimic extremely metal-poor stars. These extremely metal-poor candidates have never been followed up spectroscopically before, therefore with this limited sample of datapoints we cannot conclude whether this is a coincidence or a systematic trend.

7.6.2 α-elements

We now consider the abundance ratios of the α-elements magnesium, calcium and titanium. We note that we cannot synthesize any silicon line to a satisfying accuracy, because they are in the blue part of the spectrum where the low S/N makes abundance determinations particularly difficult.

Synthesized abundances for α-elements are derived for five LMC and one SMC RR Lyrae star (Table 7.12). For four of these LMC stars we find a mean value of $[\mathrm{Mg/Fe}] = 0.54 \pm 0.19$ dex. For one SMC RR Lyrae target a lower abundance value of $[\mathrm{Mg/Fe}] = 0.10$ dex is obtained. For RR 177 we obtain a quite low value of $[\mathrm{Mg/Fe}] = -0.50$ dex. We discuss this special case in detail below. The mean abundances for calcium and titanium are slightly lower. We find $[\mathrm{Ca/Fe}] = 0.39 \pm 0.30$ dex and $[\mathrm{Ti/Fe}] = 0.19 \pm 0.16$ dex. The corresponding abundances of the SMC star are $[\mathrm{Ca/Fe}] = 0.20$ dex and $[\mathrm{Ti/Fe}] = 0.00$ dex. We caution that the S/N of all SMC targets is considerably lower than that of the LMC objects.

A mean α-enhancement of $[\alpha/\mathrm{Fe}] = 0.36 \pm 0.25$ dex is found for the LMC stars. Due to the small number of measurements and the low S/N level of the SMC spectra a meaningful mean value cannot be computed. The tendency of lower α-enhancement seen from the three measurements is not significant within the uncertainties.

The LMC abundances are in very good agreement with the literature values for the MW RR Lyrae stars (For et al. 2011; Hansen et al. 2011) as well as with the HB stars of For & Sneden (2010) and Preston et al. (2006). Johnson et al. (2006) spectroscopically investigated four LMC GCs with metallicities between $-2.2 \leq [\mathrm{Fe/H}] \leq -1.2$ dex, while in Mucciarelli et al. (2009) the metallicity of three LMC GCs with was measured to be $-1.95 \leq [\mathrm{Fe/H}] \leq -1.65$ dex. The stars in these clusters show stronger α-enhancements with lower metallicities, but the α-enhancement is much weaker in the investigation by Johnson et al. (2006). The mean Mg-overabundance for the most metal-poor stars of Mucciarelli et al. (2009) is between $0.4 \leq [\mathrm{Mg/Fe}] \leq 0.5$ dex, in very good agreement with the RR Lyrae stars. Mucciarelli et al. (2010) obtained the abundances of calcium and titanium for these clusters. The overabundance of these elements is lower than for [Mg/Fe], similarly to our results. In Johnson et al. (2006) the α-enhancement is in general lower. The mean Mg-overabundance for the most metal-poor cluster is 0.2 dex. For the other α-elements, no or only slight enrichment was found for the metal-poor cluster stars.

For the metal-poor stars located in the MW halo and in the Galactic dSph galaxies a general trend of α-enhancement has been found. The spread of abundances between single stars is quite large, which may be due to localized, inhomogeneous enrichment, but might also partly be related to measurement uncertainties. However, the differences in abundance are in general much larger than for stars with metallicity $[\mathrm{Fe/H}] \geq -1$ dex, which are mainly located in the MW disk. Our investigated stars of the

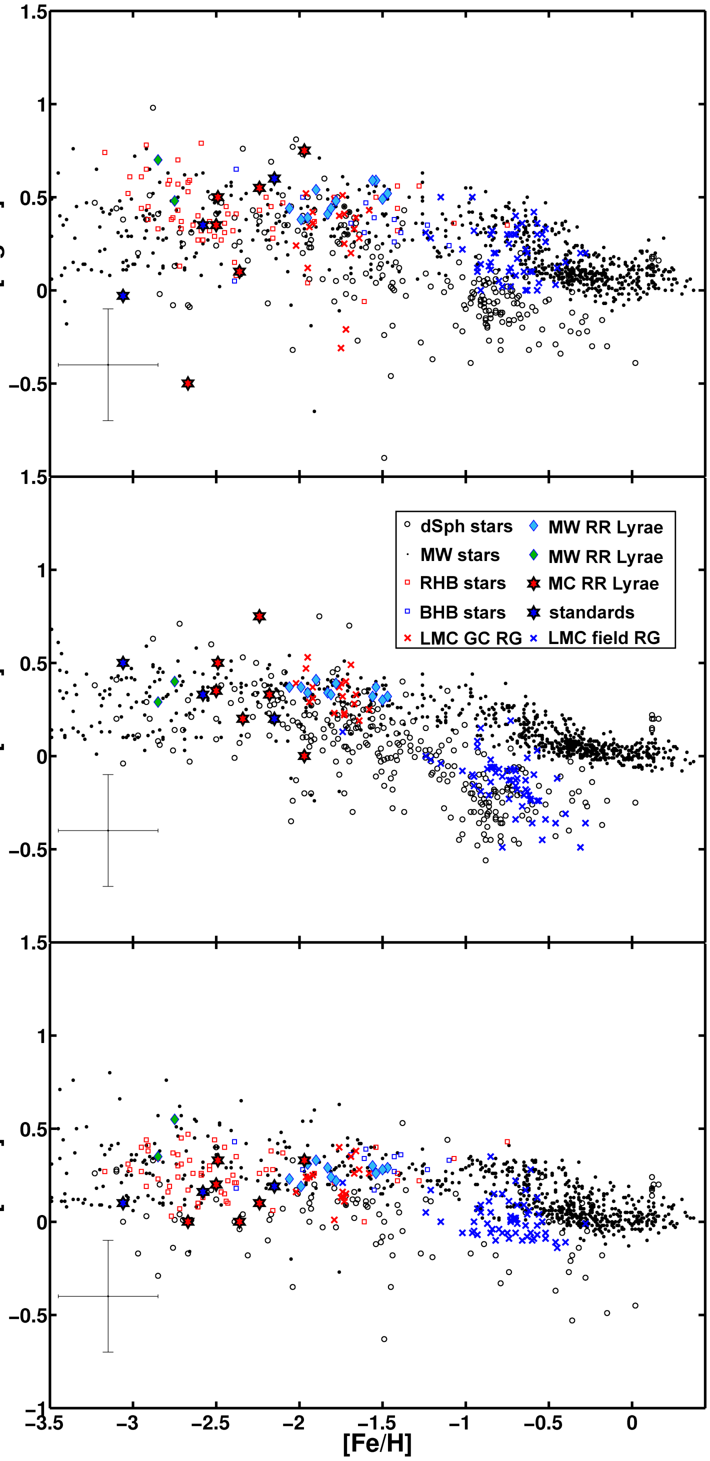

Figure 7.8: Synthesized abundances of the light α-elements Mg, Ca and Ti. We find good agreement with the abundances obtained for other stars at similar metallicity. Especially the MW RR Lyrae stars from For et al. (2011, cyan diamonds) and Hansen et al. (2011, green diamonds) show good agreement with our sample of RR Lyrae stars. Additionally we find good agreement with the BHB (blue squares) and RHB stars (red squares) of For & Sneden (2010); Preston et al. (2006), as well as with LMC GC RGs (red crosses) from Mucciarelli et al. (2010). For the LMC RR Lyrae stars a mean overabundance of $[\alpha/\mathrm{Fe}] = 0.36$ dex is found.

MCs fit quite well into the picture of α-enhancement, even though the actual abundances determined by us for the individual stars differ by several tenths of dex. Therefore no claim of RR Lyrae stars in the MCs being different from the stars in the MW halo and in the dSphs can be made and we suggest that the MCs underwent a similar early chemical evolution.

For metal-poor stars it has been known for a long time (e.g., Wallerstein et al. 1963) that they are enhanced in α-elements, typically by $[\alpha/\mathrm{Fe}] \sim 0.4$ dex. In Figure 7.8, we compare the abundances of our target stars with literature values for different samples. The black dots represent stars in the MW thin and thick disk as well as from the halo (Bonifacio et al. 2009; Cayrel et al. 2004; Lai et al. 2008; Venn et al. 2004, and references therein). The black open circles show the abundance of red giants from different MW dSph companions, namely Bootes I (Feltzing et al. 2009; Norris et al. 2010b), Carina (Koch et al. 2008a), Coma Berenices (Frebel et al. 2010b), Draco (Cohen & Huang 2009) Fornax (Letarte et al. 2010), Hercules (Adén et al. 2011; Koch et al. 2008b), Leo II (Shetrone et al. 2009), Sgr (Monaco et al. 2005; Sbordone et al. 2007), Sculptor (Frebel et al. 2010a), Sextans (Aoki et al. 2009), Ursa Major II (Frebel et al. 2010b) and Ursa Minor (Sadakane et al. 2004). RR Lyrae stars are on the horizontal branch (HB) and therefore we show the abundances of red horizontal branch (RHB) stars from For & Sneden (2010) and Preston et al. (2006) as well as the blue horizontal branch (BHB) stars from For & Sneden (2010) with red and blue squares, respectively. In For et al. (2011) eleven nearby Galactic field RR Lyrae stars were spectroscopically investigated. The analysis revealed a very similar elemental abundance for all RR Lyrae stars, shown with cyan diamonds, with a mean overabundance of $[\mathrm{Ca/Fe}] = 0.34$ dex and $[\mathrm{Mg/Fe}] = 0.48$ dex. In Hansen et al. (2011) two very metal-poor Galactic RR Lyrae stars were investigated. The α-enhancement for these two stars, illustrated by green diamonds, is similar to the results found by For et al. (2011).

The very metal-poor population of the MCs has not been extensively investigated yet. Therefore we include abundances of red giants from the LMC field (Pompéia et al. 2008, blue crosses) and LMC GCs (Mucciarelli et al. 2009, 2010, red crosses) in our comparison.

7.6.3 Light odd-Z elements

The light odd-Z elements are investigated via the resonance D-line doublet of sodium at 5889.9 Å and 5895.9 Å, as well as through the aluminum lines at 3944 Å and 3961 Å. For the sodium lines, the spectrum is carefully inspected for interstellar contamination. Fortunately, the radial velocity is high enough to avoid major contamination by interstellar lines. Regrettably we can obtain synthesized abundances for these two elements with acceptable uncertainties for two stars only (Table 7.12).

In Figure 7.9 the same literature sources are used as in Figure 7.8 and described in Section 7.6.2. In the low metallicity regime of our target stars the sodium abundances of the MW and the dSph stars are very similar. The two LMC RR Lyrae stars are slightly enhanced in their sodium abundance and are in good agreement with those stars of the MW and the dSphs. The stars in the old metal-poor GCs of the LMC have very similar sodium abundances as our RR Lyrae targets. Johnson et al. (2006) found solar mean ratios for their LMC clusters, while Mucciarelli et al. (2010) obtained sodium enhancement for most of the stars in the GCs.

A bimodal distribution of the aluminum abundances is observed investigating BHB, RHB and RR Lyrae stars in the MW. While the more metal-rich RR Lyrae and the BHB stars are enhanced in aluminum, the metal-poor RR Lyrae and the RHB stars show an underabundance in [Al/Fe]. There is no explanation for this phenomenon yet. However, we find that our two target stars have aluminum abundances similar to the Galactic RR Lyrae and the BHB stars, even though the LMC RR Lyrae stars of this study are more metal-poor than the other aluminum enhanced stars. We test if NLTE effects might be responsible, but applying the NLTE corrections of Andrievsky et al. (2008) increases the overabundance even more. It might be possible that (some of) the investigated RR Lyrae stars are underabundant in aluminum and therefore we were not able to detect the lines. Some of the LMC GC stars of Mucciarelli

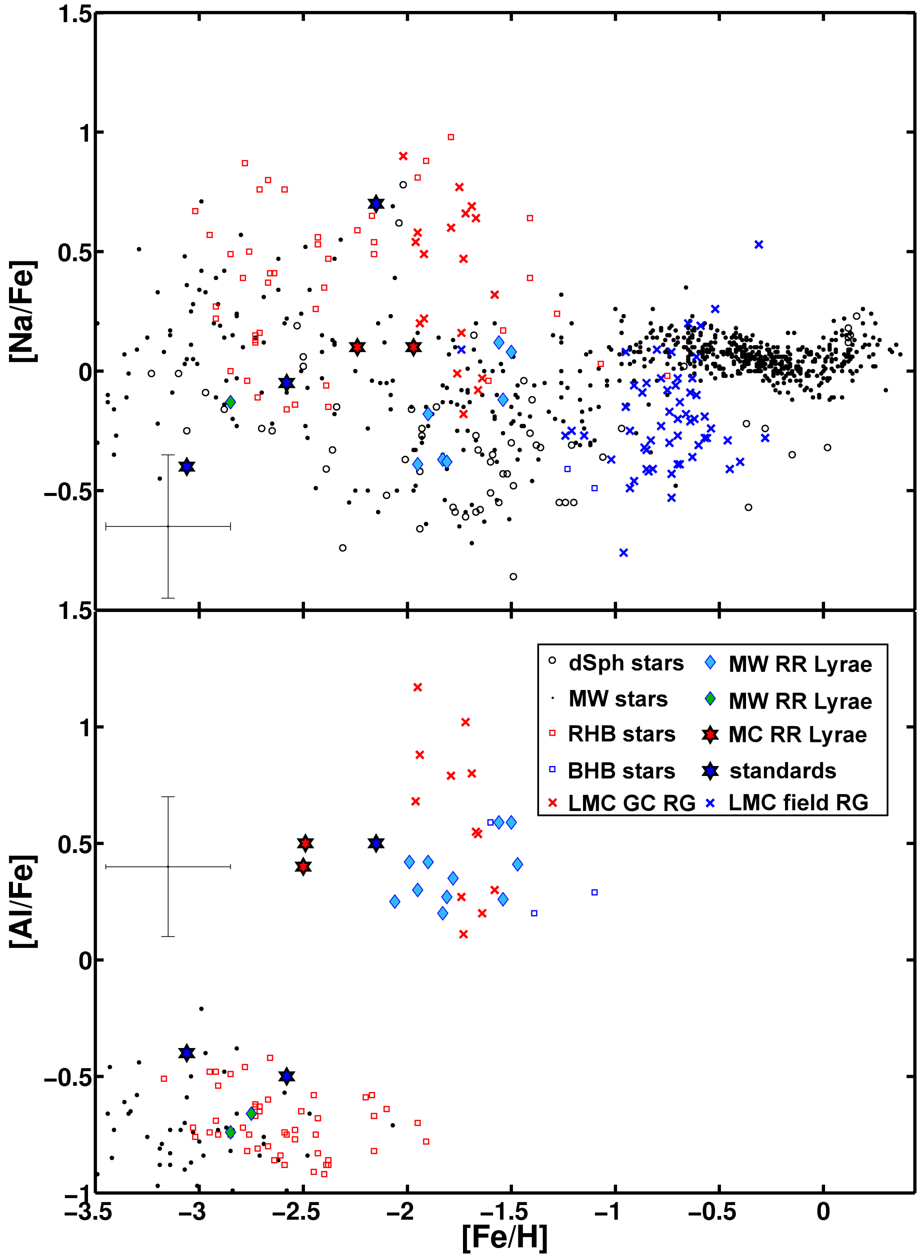

Figure 7.9: Abundance ratio of sodium to iron (upper panel) and aluminum to iron (lower panel) vs. [Fe/H]. The coding of the different types of stars is the same as in Figure 7.8. We see that the LMC RR Lyrae stars follow the trend of sodium enhancement with lower iron abundance. For the aluminum abundance a bimodal distribution is found. The RR Lyrae stars with measureable aluminum abundance belong to the group of aluminum enhanced stars, even though they are more metal-poor than the other stars of this group.

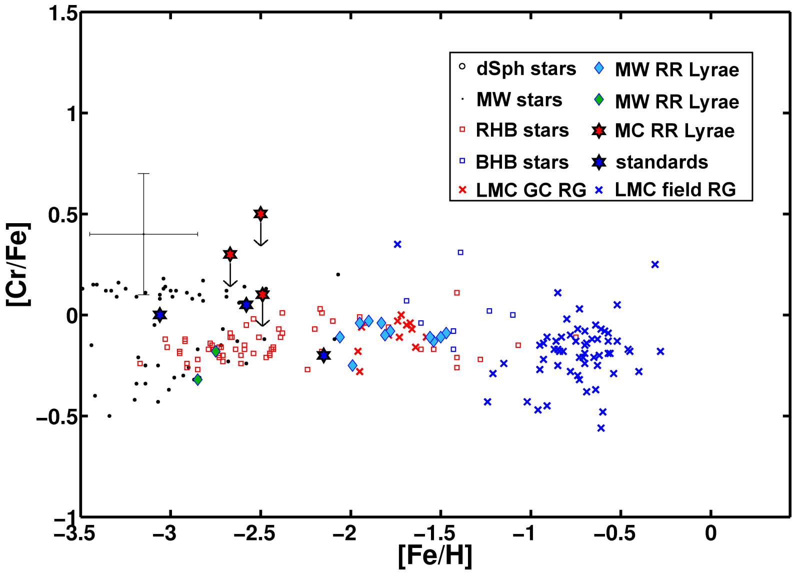

Figure 7.10: Chromium to iron ratio versus [Fe/H]. Only for three of our LMC RR Lyrae stars upper limits (indicated by the arrows) of chromium can be synthesized in our spectral synthesis analysis, but no other iron-peak elements. The abundances are in general a bit higher than the comparison values from MW RR Lyrae and HB stars. The color coding is the same as in Figure 7.8.

et al. (2010) have estimates for aluminum. These stars, with metallicities of the BHB stars, show abundance patterns similar to the Galactic RR Lyrae stars of For et al. (2011) and to the Galactic BHB stars. However, we cannot conclude that all RR Lyrae stars in the MCs are overabundant in [Al/Fe] and more stars need to be investigated.

7.6.4 Iron-peak elements

For the iron-peak elements we are only able to synthesize a few chromium lines for three LMC RR Lyrae stars to within acceptable error margins. In general these abundances are higher than the comparison MW RR Lyrae stars. However, the low S/N of our spectra does not allow us to identify the lines properly and we recommend to take these values as upper limits for these stars.

7.6.5 Neutron-capture elements

Neutron-capture elements are represented by synthesized abundance measurements of strontium for four of our LMC RR Lyrae stars and synthesized abundances of barium for two of our LMC RR Lyrae stars. In Figure 7.11 the abundances are compared with the literature datasets mentioned in Section 7.6.2.

For strontium a slight overabundance is found in most of the literature RR Lyrae and HB stars. However, there is no well defined trend and some stars are significantly underabundant. We find three RR Lyrae stars that are enhanced in strontium, while the abundance of one star deviates significantly from the other three. This is RR 177, the same star that showed a low abundance pattern in the α-elements. All stars are, however, in good agreement with the literature values, see Figure 7.11. Mashonkina & Gehren (2001) found that a NLTE correction of $\Delta_{\mathrm{NLTE}} = +0.6$ should be applied. Adding this value to our LTE measurements, the abundances of our RR Lyrae stars would still be in agreement with the abundances found for other Galactic RR Lyrae and RHB stars.

The barium content of our RR Lyrae stars is slightly overabundant. Comparing it to the MW RR Lyrae stars by For et al. (2011) and the RGs of the GCs (Johnson et al. 2006; Mucciarelli et al. 2010),

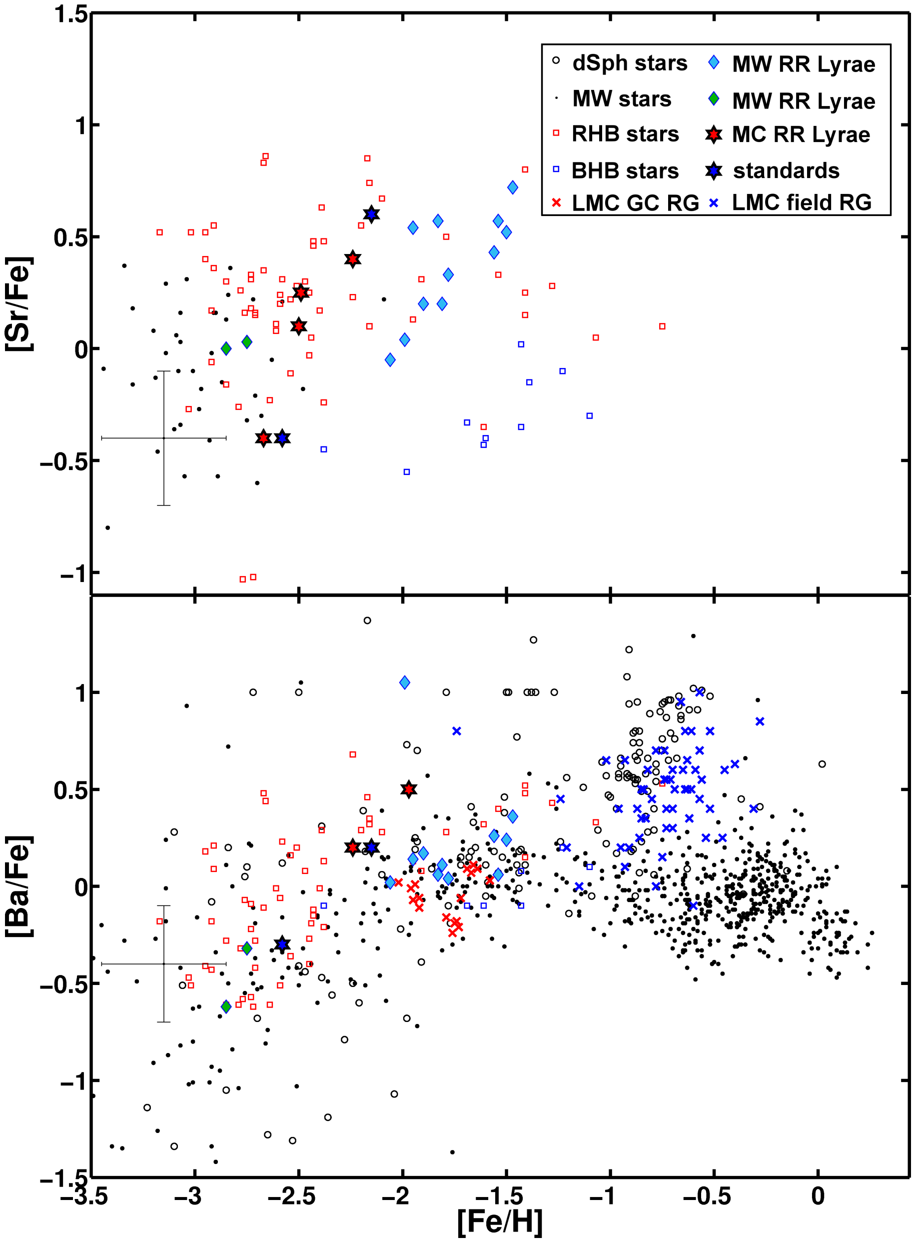

Figure 7.11: Strontium to iron and barium to iron ratios vs. [Fe/H]. There is good agreement with the literature data (see Figure 7.8). The strontium abundances of the LMC RR Lyrae stars fit well within the trend set by the MW RR Lyrae and HB stars (upper panel). For dSph and MW stars a significantly different trend of the barium to iron ratio is only observable at metallicities higher than those of our RR Lyrae sample (lower panel). Therefore we cannot distinguish whether the RR Lyrae stars follow the trend of the dSph or the MW stars.

we find that our abundances are a bit enhanced. However, within the uncertainties good agreement is found with these stars as well as with the RHB stars and the RGs of the dSphs (see Figure 7.11).

7.6.6 The α-poor star RR 177

For our most metal-poor star RR 177, we find unusual abundances of the other elements. With [Fe/H] = −2.7, this is the most metal-poor star currently known in the LMC. Therefore, we would expect the star to be similarly α-enhanced as most of the metal-poor stars. Instead, we find [Mg/Fe] = −0.5, with a signal well above the noise level. For [Ca/Fe] we do not find a conclusive value, but the spectral synthesis shows that the abundance has to be lower than [Ca/Fe] < 0. For the α-element titanium we find [Ti/Fe] = 0.0, a bit higher than the abundances for the other α-elements. However, as pointed out in Thielemann et al. (1996) the production of titanium can also happen through complete silicon burning with an α-rich freeze-out. The complete sequences inside a star that lead to the synthesis of titanium are not yet fully understood (e.g., Woosley & Weaver 1995).

The low abundance of the α-elements might be indicative for a single enrichment event without sufficient mixing of the supernova debris. In Argast et al. (2000, 2002), the mixing of the ejecta into a gas cloud of 10^4 $M_\odot$ may lead to an α-underabundance for individual stars. Following these models, the chromium abundance would appear rather normal, as observed for RR 177 (compare Figure 2 of Argast et al. 2000).

To date, Galactic field and dSph stars with such an amount of selective depletion in the α- (and possibly in some neutron-capture) elements have only been found at metallicities $\gtrsim -2$ dex (e.g., Carney et al. 1997; Ivans et al. 2003; Koch et al. 2008a).

7.7 Conclusions

We present the first detailed spectroscopic analysis of MC RR Lyrae stars, with six stars located in the LMC and three stars in the SMC. With metallicities as low as [Fe/H] = −2.7 dex, we find the most metal-poor stars yet known in the MCs. A mean metallicity of [Fe/H] = −2.4 dex for our nine objects allows us to probe the earliest currently available tracers of the chemical evolution of the MCs.

The candidates for the most metal-poor RR Lyrae stars were identified via photometric metallicity estimates (Chapter 3). These candidates generally turn out to be more metal-rich when using spectroscopic measures. Overall, the metallicities of our RR Lyrae stars are significantly higher than those of the extremely metal-poor RGB stars found in several dSphs (e.g., Frebel et al. 2010a; Norris et al. 2010c) or the most metal-poor stars of the Galactic halo (e.g., Frebel et al. 2005; Caffau et al. 2011). The reason for this lack of extremely metal-poor RR Lyrae stars are the evolutionary tracks of stars beyond the main sequence. As pointed out by Yoon & Lee (2002) extremely metal-poor stars do not enter the instability strip and therefore one would not expect to find RR Lyrae stars with [Fe/H] ≤ -3 dex.

For the α-enhancement an overabundance between $0.1 < [\alpha/\mathrm{Fe}] < 0.5$ dex is found for Galactic RR Lyrae stars (For et al. 2011; Hansen et al. 2011) as well as for red giants in the GCs of the MCs (Johnson et al. 2006; Mucciarelli et al. 2009, 2010), in dSphs (e.g., Koch et al. 2008a, and references mentioned above) and in the MW halo (e.g., Venn et al. 2004, and references therein). Our spectral synthesis of the α-elements in our metal-poor field RR Lyrae stars in the MCs reveals a mean α-enhancement of 0.36 ± 0.25 dex in very good agreement with these other sources.

For the odd-Z elements we find a small overabundance in sodium and a significant overabundance in aluminum in good agreement with the red giants of the MC GCs and the Galactic RR Lyrae stars. The upper limits for our measured iron-peak elements are consistent with the abundances determined for different types of Galactic stars of similar metallicity (e.g., Preston et al. 2006; For & Sneden 2010).

For the neutron capture elements we also find good agreement between our abundances and the values obtained for the different dSphs, the LMC GCs and the halo stars of the MW.

As members of the old population of the MC our metal-poor RR Lyrae stars were only or primarily enriched by supernovae of type II, with little or no contribution from supernovae of type Ia, as indicated by the abundance patterns that we derived. Our results are, therefore, consistent with the model of an invariant, massive star, initial mass function (IMF) for all environments at early times (e.g., Wyse et al. 2002).

The spread of abundances observed in our target stars and the α-element deficient star RR 177 are indicative of local star formation in bursts in an inhomogeneously enriched environment or even enrichment by single supernova events. Therefore we expect that star formation happened locally in a stochastical way and that the early MCs were not chemically well mixed. This is also consistent with the varying metallicities at any given age in the SMC (e.g., Glatt et al. 2008a) as well as in dSphs (e.g., Koch et al. 2008b).

In general we find that the abundances of the old and metal-poor MCs RR Lyrae stars are consistent with the abudnances measured in the MW halo. Recent numerical simulations (Font et al. 2006; Robertson et al. 2005) indicate that the halo was primarily built up from early mergers of the MW with MC-sized objects. From our results we can confirm that the abundance patterns of all investigated elements of the metal-poor, old MC stars and the MW halo are compatible. Therefore it is conceivable that early mergers of “proto-MCs” with the MW contributed to the build-up of its halo.

"It’s time to put an end to your trek through the stars"
Q - Star Trek: The Next Generation (All Good Things...)

8

Summary and Outlook

Summary

The main theme of this work is the evolution and structure of the MCs. Evaluating the chemical properties of large samples of variable RR Lyrae stars, using the archival data of the OGLE survey, allowed us to uncover aspects of the early history of both Clouds. The abundances of the most metal-poor, and presumably oldest, members of the RR Lyrae stars are investigated using spectroscopic measures. The three-dimensional structure of the old population, from the RR Lyrae stars, as well as for the young population, traced by Cepheid variable stars, was determined for the Clouds and conclusions about the evolutionary history were drawn. The knowledge and expertise is finally used on the OGLE dataset of the Galactic bulge region, which included also parts of the leading arm of the Sgr stream.

The first step in my thesis was the determination of detailed, spatially resolved reddening maps for both Clouds in Chapter 2. Two different approaches were used to determine an area-averaged reddening of the whole OGLE field of the MCs and to compute line-of-sight reddening estimates to individual stars. For the area-averaged reddening, the color of the RC of 3174 subfields in the LMC and 693 subfields in the SMC were evaluated and compared with a theoretical value for an unreddened field of the same metallicity. In both Clouds it was shown that most regions do not suffer from a large amount of reddening. However, some star-forming regions, especially 30 Doradus, experience heavy extinction and were clearly visible as highly reddened regions in the reddening maps. Since the reddening in the MCs is variable on small scales, for the determination of precise distances the extinction is a crucial factor. We therefore decided to calculate individual reddening estimates for each RR Lyrae star by subtracting the color computed from the calculated absolute magnitudes from the observed color in the same passband. The area-averaged reddening maps were compared with the individual reddening estimates from the RR Lyrae stars as well as with literature values of MC extinction maps. On large scales an overall very good agreement between all the different methods was found.

The MDF of the old population of the LMC and SMC was evaluated in Chapter 3. From the OGLE archive, the data of 16776 RR Lyrae stars were used to determine photometric metallicities of the LMC. For the SMC, photometric metallicities of 1831 RR Lyrae stars were evaluated. The OGLE collaboration already performed a Fourier decomposition of each light curve to determine the phase parameter ϕ_{31}. We repeated the process to test whether the data were reliable and to calculate uncertainty estimates for each phase parameter. Kovács & Zsoldos (1995) and Smolec (2005) introduced a method to use this parameter, and the period, to calculate photometric metallicity estimates for RR Lyrae stars on the scale of J95. These were transformed to the more widely used scale of ZW84. For the LMC a mean metallicity of $[Fe/H] = -1.50$ dex is found, while the SMC is more metal-poor with a mean value of $[Fe/H] = -1.70$ dex. The individual metallicity estimates were convolved assuming a Gaussian distribution, giving an intrinsic width of 0.24 dex for the metallicity distribution of the LMC and 0.27 dex for the SMC. These results suggest that the early evolutionary history of the MCs might be a bit different from each other and we took it as an indication that the enhancement of the initial material has taken place differently. For a subset of our RR Lyrae stars with photometric metallicities spectroscopic estimates were also available. The comparison between both revealed good agreement, even though some deviations were found at the metal-poor end of the calibration.

The three-dimensional structure of the LMC was investigated in Chapter 4 for the young and old stellar population traced by Cepheids and RR Lyrae stars. Exploiting the metallicities from Chapter 3, the absolute magnitudes were calculated using the relation by Clementini et al. (2003). Together with observed magnitudes by OGLE and the reddening estimates from Chapter 2, individual distances were calculated for 16776 RR Lyrae stars and 1849 Cepheids. It turned out that the individually dereddend populations have a better agreement with each other and we interpreted their reddening values and distances as more reliable. We find a mean distance of 53.1 ± 3.2 kpc to the RR Lyrae stars and a Cepheid mean distance of 53.9 ± 1.8 kpc. Thus, using individually dereddened distances appears to resolve the long-standing "long and short distance scale problem" for RR Lyrae stars and Cepheids. The same position angle ($\Theta = 115^\circ \pm 15^\circ$) and inclination angle ($i = 32^\circ \pm 4^\circ$) is found for both stellar tracers. The scale height is a bit larger for the RR Lyrae stars with 2.3 ± 0.2 kpc, in contrast to 1.9 ± 0.2 kpc for the Cepheids. The most interesting result, however, was that we could confirm the off-center bar suggest by several authors. The bar protrudes out of the disk towards us by up to ~ 5 kpc.

For the three-dimensional structure of the SMC we used the same approach as in Chapter 4. The results for 1494 RR Lyrae and 2522 Cepheids observed by OGLE were presented in Chapter 5. The structure of the old population is very different from the young stellar tracers. The RR Lyrae stars have a mean distance of 64.6 ± 3.4 kpc, a position angle of $\Theta = 81^\circ \pm 21^\circ$ and an inclination angle of $i = 7^\circ \pm 15^\circ$. A similar mean distance of 63.1 ± 3.0 kpc and position angle of $\Theta = 71^\circ \pm 15^\circ$ is found for the Cepheids. The inclination angle is, however, rather different with $i = 74^\circ \pm 9^\circ$. This difference may be the result of major interactions between the SMC, the LMC and/or the MW. These interactions disturbed the gas content and triggered intensive star formation. The large intrinsic depth of the SMC is observable in the RR Lyrae distribution with a scale height of 3.7 ± 0.4 kpc as well as for the Cepheids, where we find a scale height of 4.5 ± 0.3 kpc. The fact that the large scale height is evident in both populations showed that the SMC gas was disturbed by intensive interactions and that the stellar population of the SMC present before the encounter(s) between the galaxies has been tidally heated and therefore extended to larger scale heights.

In Chapter 6 we investigated the reddening, the metallicities and the three-dimensional distribution of 11534 RR Lyrae stars observed by the OGLE collaboration towards the Galactic bulge. The OGLE field was restricted to Galactic latitude below -3°, therefore the central region of the Galaxy was omitted. The techniques of the previous Chapters were used to calculate all the parameters needed to investigate the properties mentioned above. We find quite severe reddening, especially for the fields close to Galactic disk. A mean metallicity of $[Fe/H] = -1.25$ dex is obtained. Different reddening laws were applied to find the most reliable distance estimates, and the results were compared with the recent literature. The best agreement was found for the reddening laws by SFD98 and PUS11, which resulted in mean distances of 8.0 ± 1.7 kpc and 8.8 ± 1.7 kpc, respectively. The leading arm of the tidal stream from the Sgr dSph cuts through the OGLE field. Given the RR Lyrae distance estimates it is possible to disentangle which stars are likely to belong to the Sgr stream. For 251 RR Lyrae stars located in the distance suspected for the stream, we found a significantly lower mean metallicity of $[Fe/H] = -1.50$ dex. This metallicity is in very good agreement with the mean metallicity of the LMC, derived in Chapter 3, and mean distances of 24.0 ± 3.6 kpc and 25.2 ± 3.9 kpc were obtained for the Sgr stream using the two different extinction laws. Comparing the stream distances with the literature it appears that the stream is inclined.

The last part of this thesis was dedicated to the analysis of nine spectra of RR Lyrae stars observed in the MCs and is presented in Chapter 7. The RR Lyrae stars were among the most metal-poor candidates found in our analysis in Chapter 3. The spectra were observed by us with the MagE instrument at the Magellan telescopes, Las Campanas, Chile. First I reduced the low S/N data. The spectral analysis revealed that the derived metallicities for the most metal-poor candidates are more metal-rich than those found by the photometric estimate. Nevertheless, all of our candidates turned out to be quite metal-poor, and we found the most metal-poor star with an iron abundance of $[\mathrm{Fe/H}] = -2.7$ dex discovered in the MCs so far. For all the other target stars, metallicities below $[\mathrm{Fe/H}] \lesssim -2$ dex were obtained. Apart from iron, abundances for up to ten different elements were obtained for the target stars. We found that the abundances ratios are consistent with the estimates found for metal-poor stars in the dSph as well as in the MW halo. A formation scenario where a MC like galaxy had been accreted by the Galaxy to form (part of) the halo is therefore plausible.

Outlook

The field of OGLE III covers only the dense, central parts of the MCs. The new ongoing OGLE IV and VISTA surveys will increase the field to include the outskirts of the Clouds and cover the Magellanic Bridge. This will allow one the study of the structural parameters of the outskirts in unprecedented precision and to address how the Clouds have been altered by interactions between themselves as well as with the Galaxy. Tracing the RR Lyrae stars will allow the study of the early evolutionary history through MDFs and the identification of possible metallicity gradients. These will give insights how the MCs have been formed, and whether they have a common origin.

Future observations of the MCs by the Gaia satellite will allow the determination of parallaxes to the brighter stars of these galaxies. The distance calibration will solve the problem of the true distance modulus, the line-of-sight depth and other structural parameters of the Clouds. Calibrations of the absolute magnitude for the RR Lyrae stars will be tested and reliable new relations will become available. This will enable the use of data from the large survey telescopes, such as LSST, which will come online and fully operational within the next decade, to obtain lightcurves for RR Lyrae stars in galaxies outside our own MW and its companions. These lightcurves will provide additional information about the physical and chemical parameters of the exclusively old population.

Photometric metallicities are not well calibrated for very metal-poor RR Lyrae stars. It would be extremely valuable if a photometric survey could observe a large number of Galactic field RR Lyrae stars to get very well defined lightcurves in different bands, as planned for LSST. For an optimal calibration of the photometric metallicities all these stars should also be observed spectroscopically to determine homogeneous metallicities. Hopefully a metallicity range as wide as possible would be covered. This would allow us to extend the metallicity-period-ϕ_{31}-calibrations, especially for other passbands than V. Using only Galactic field RR Lyrae stars would allow to perform this task with a medium-sized telescopes, which are more readily accessible. If one does not want to wait for LSST, the observations for the lightcurve determination could even be performed by a non-professional astronomer.

Another aspect that has to be addressed in future work is a more extended survey of the very metal-poor stellar population of the MCs. Especially for the SMC, few stars with very low metallicities are known, primarily because no very metal-poor GC is present. It is, however, crucial for the understanding of the early phases of the evolution of a galaxy to find these type of stars. RR Lyrae stars might not be the best choice, because the observation time is limited due to their variability and extremely metal-poor RR Lyrae stars might not exist. Therefore, BHB stars were a logical choice to look for extremely metal-poor stars. However, it might still be worth to attempt it with the RR Lyrae. Otherwise, the planned large photometric surveys of the Clouds done by SkyMapper, for instance, could be used to find candidate extremely metal-poor stars, which could be followed up spectroscopically.

There are many more issues to tackle and a lot of ideas for interesting projects will hopefully come to your mind after reading this thesis.

Take-Home message

The analysis of archival data from the Optical Gravitational Lensing Experiment allowed us to draw conclusions about the distance, stellar structure and chemical history of the Magellanic Clouds. The depth extend of both Clouds is significant, with ~ 2 kpc for the Large Magellanic Cloud and a Small Magellanic Cloud depth of ~ 4 kpc. The depth has an influence on the reliability of mean distance estimates, which were found to be 53 kpc for the Large Magellanic Cloud and 63 kpc for the Small Magellanic Cloud. With our three-dimensional maps of both Clouds, we showed that the bar in the Large Magellanic Cloud protrudes out of the disk and is an off-center feature. The cause of this feature is still not understood, but might be connected to recent interactions between both Clouds. The significantly different metallicity distribution functions of the old populations are, however, an indication that the Clouds have a different early chemical history. It seems that considerable interaction have taken place between the Clouds. We found the most metal-poor star yet discovered in the Large Magellanic Cloud, which shows indications of being the result of local star formation with inhomogeneous enrichment. Nonetheless, the extremely metal-poor stellar population of the Magellanic Clouds still waits for its discovery. The individual element abundances of those old stars for which we obtained spectroscopy led to the conclusion that a build-up of the Milky Way halo from a merger with a Magellanic Cloud type galaxy is plausible.

"Oh, shit!!!"
Data - Star Trek 7: Generations

Appendix

Spectra of very metal-poor RR Lyrae stars in the Magellanic Clouds

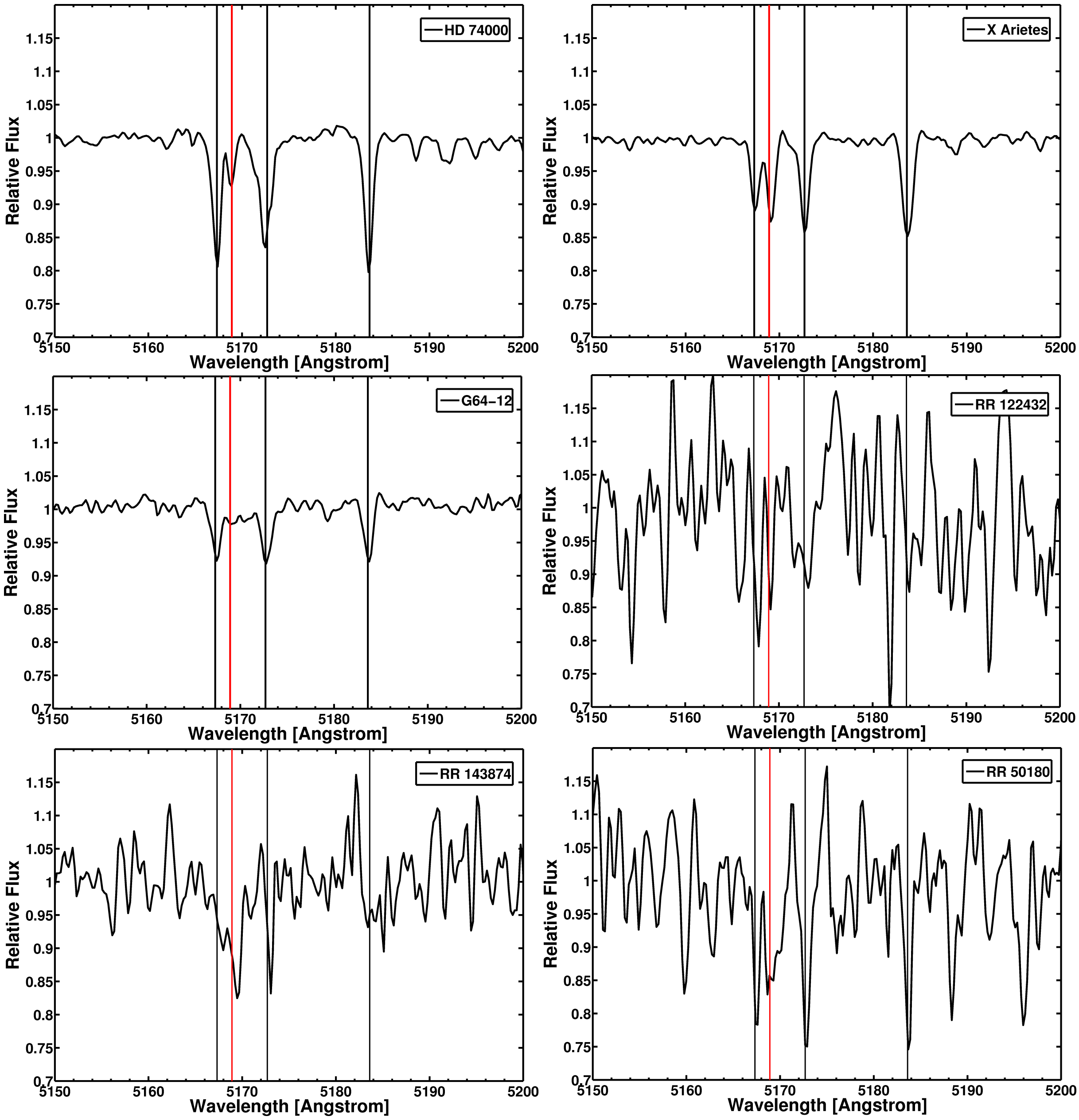

Figure 8.1: Spectra of the Mg lines between 5150Å and 5200Å. The black lines show the Mg lines, while the red lines show an Fe I line. The standard stars HD74000, G64-12 and X Arietes and our three SMC targets are shown.

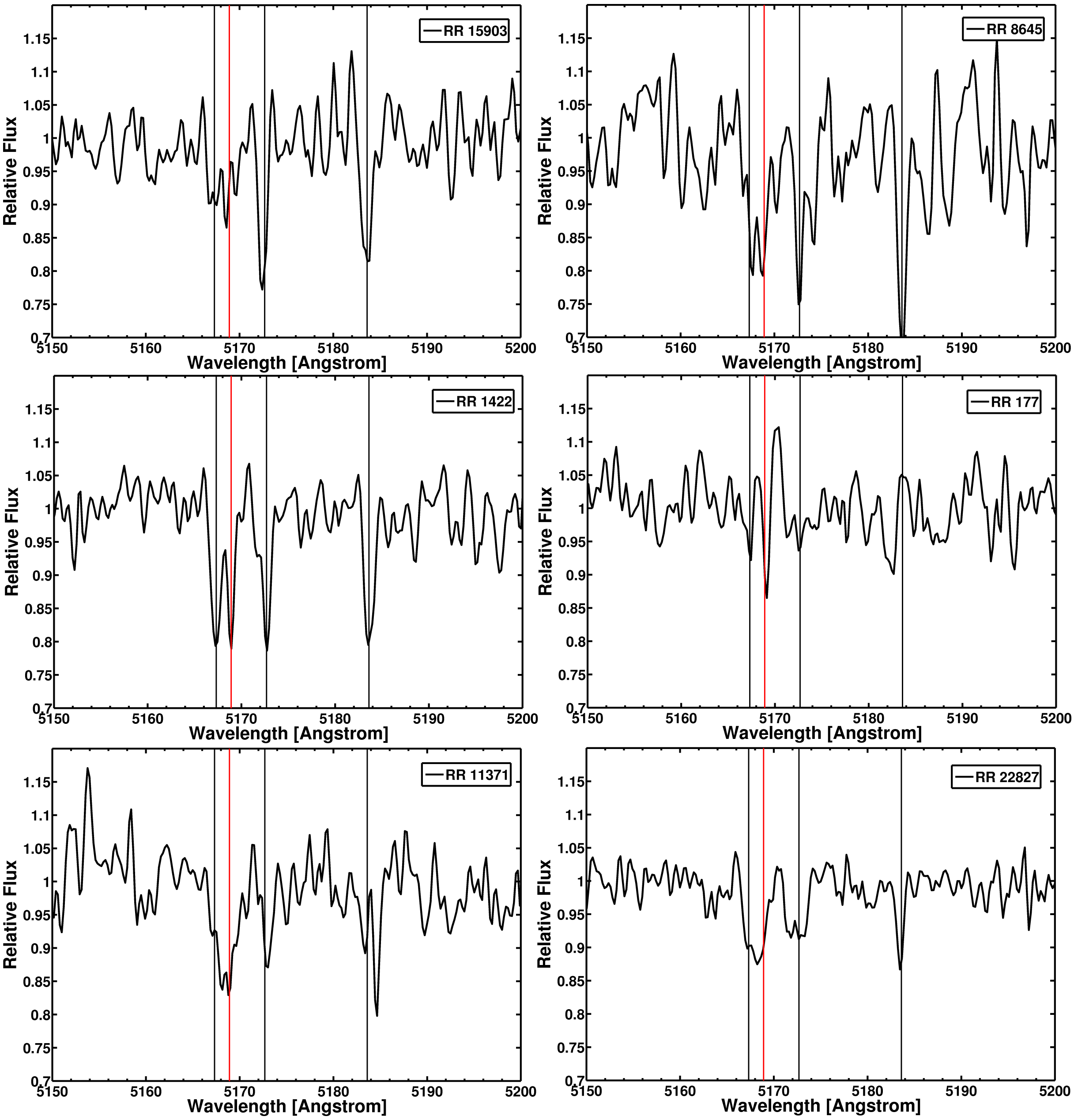

Figure 8.2: Spectra of the Mg lines between 5150Å and 5200Å. The black lines show the Mg lines, while the red lines show an Fe I line. All targets from the LMC are shown here.

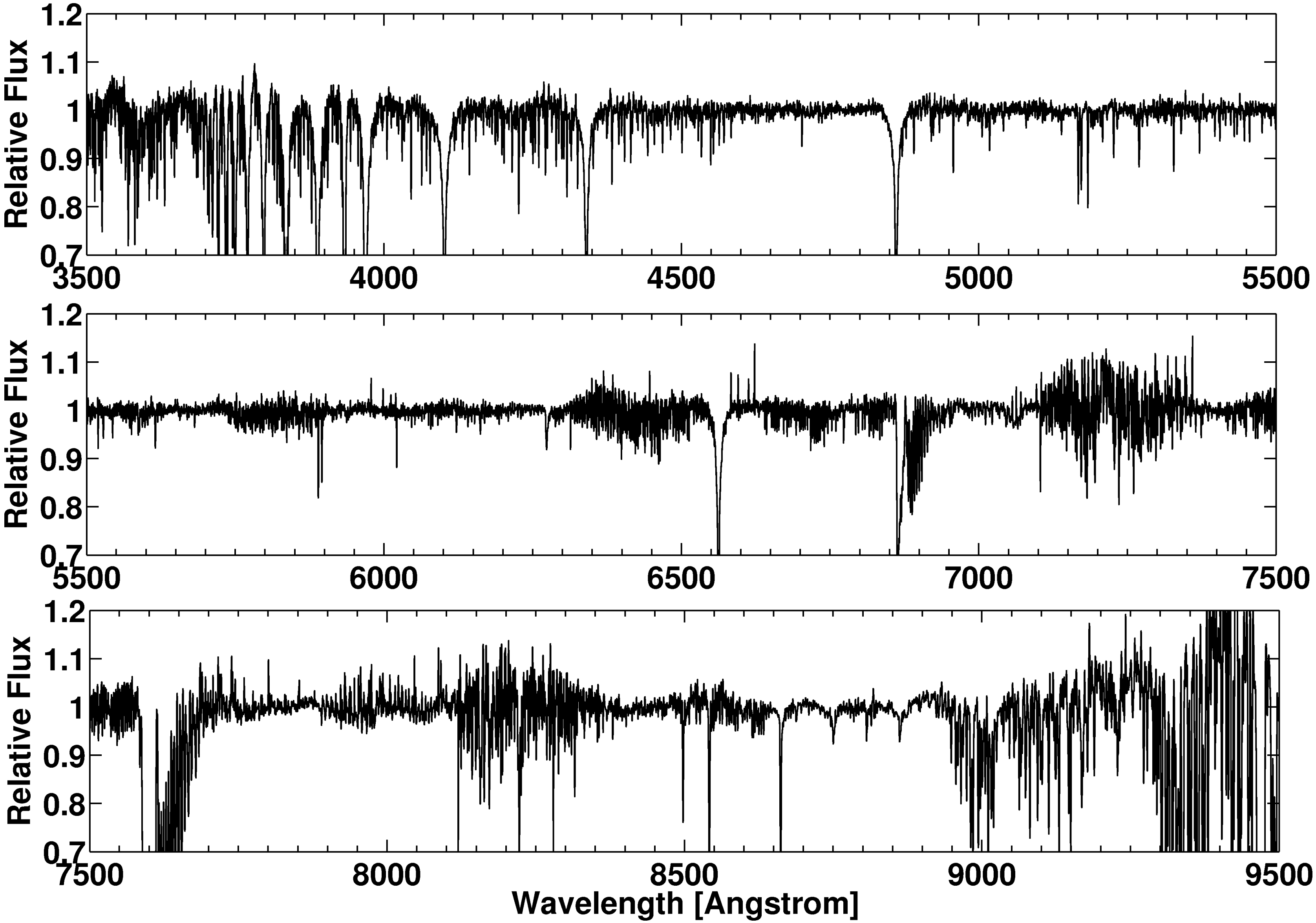

Figure 8.3: Spectra of HD74000

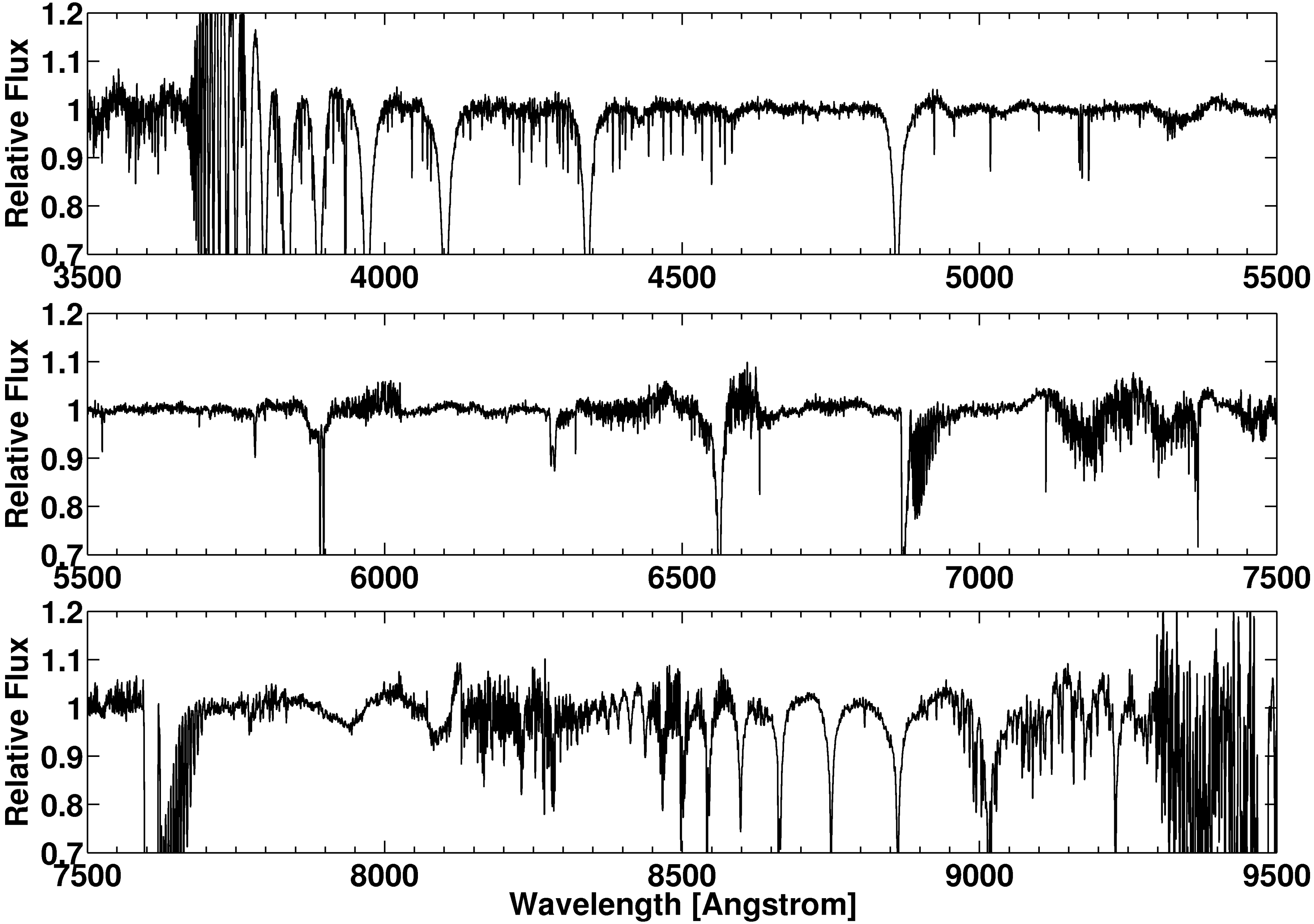

Figure 8.4: Spectra of X Arietes

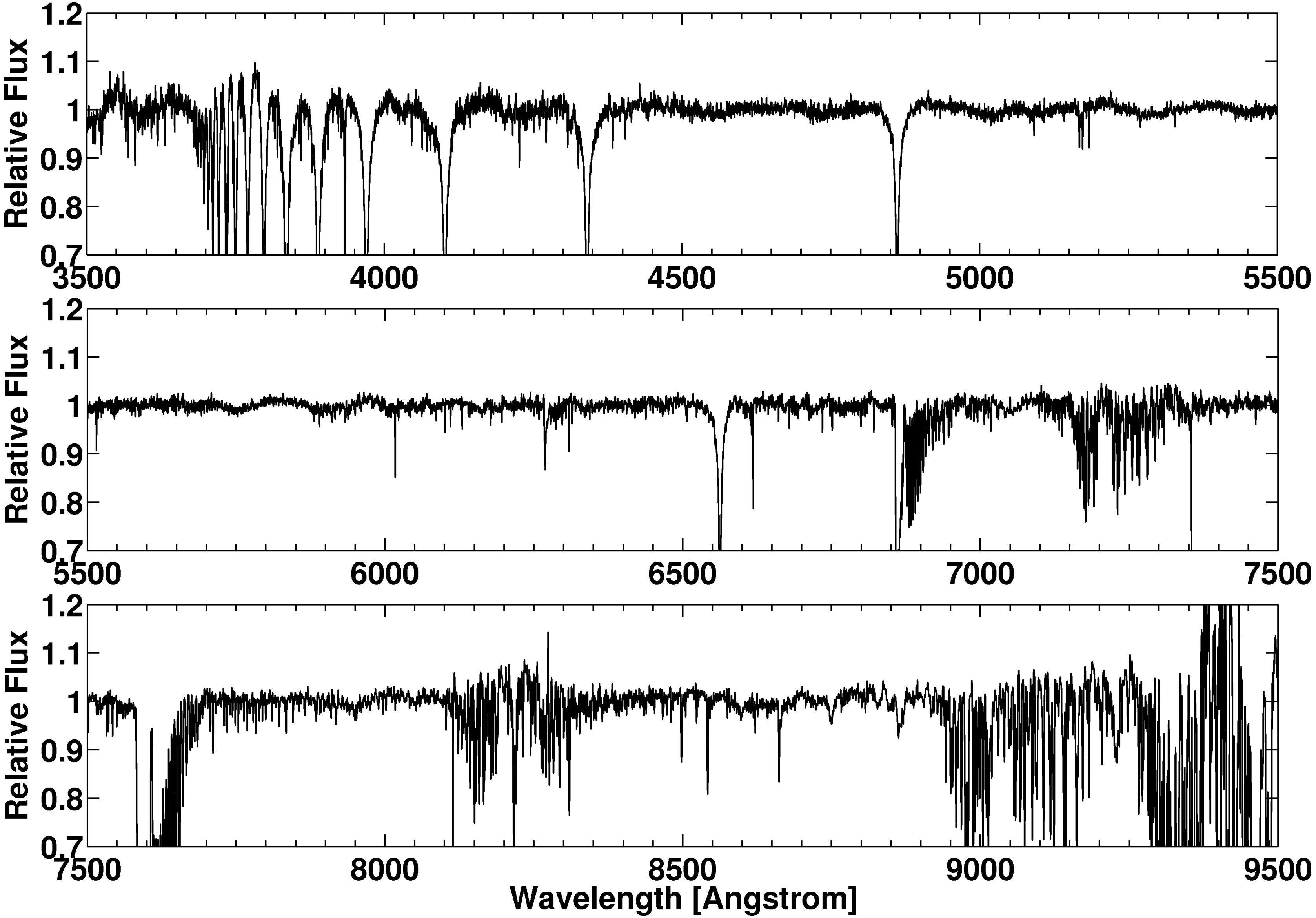

Figure 8.5: Spectra of G64-12

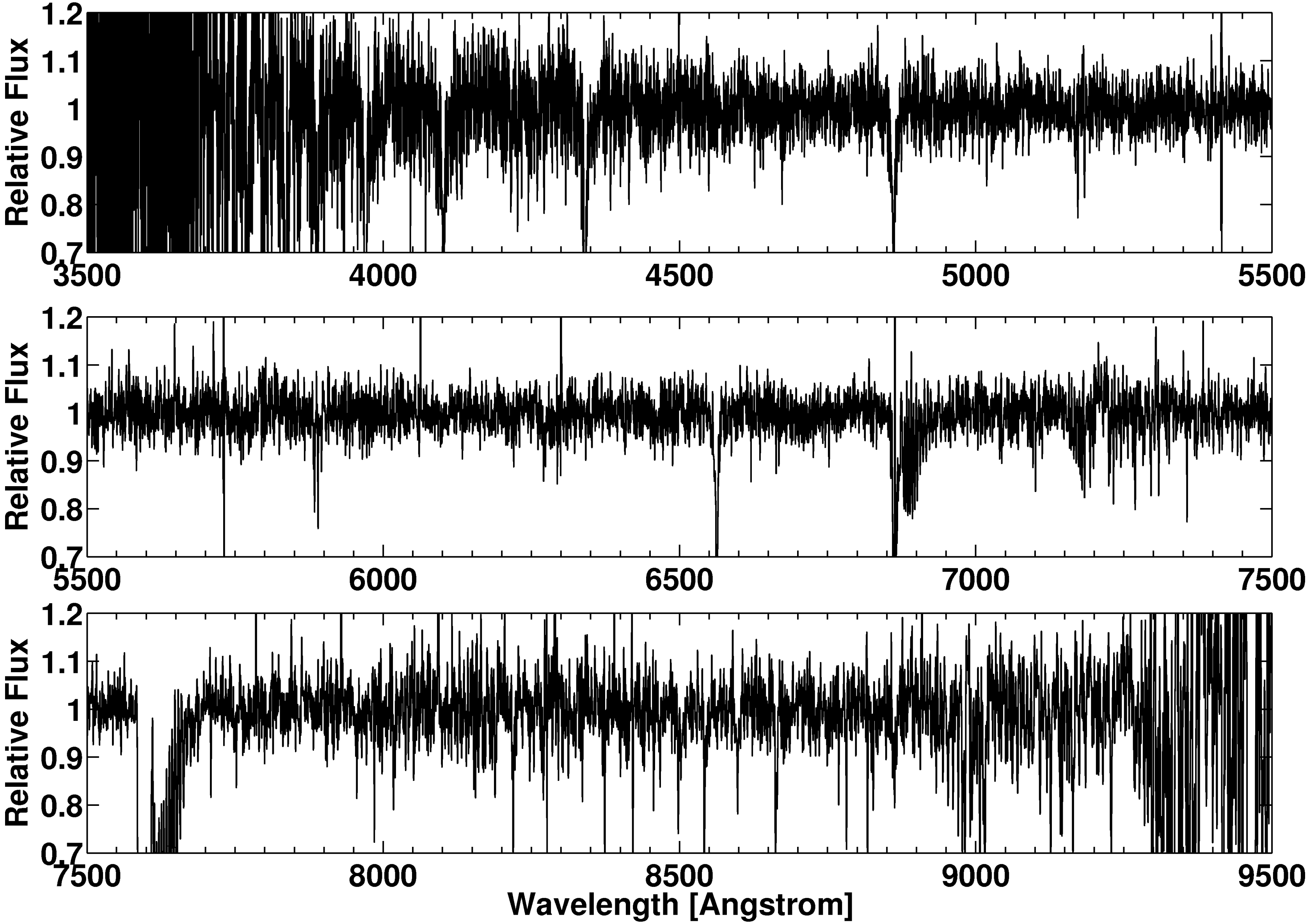

Figure 8.6: Spectra of RR 15903

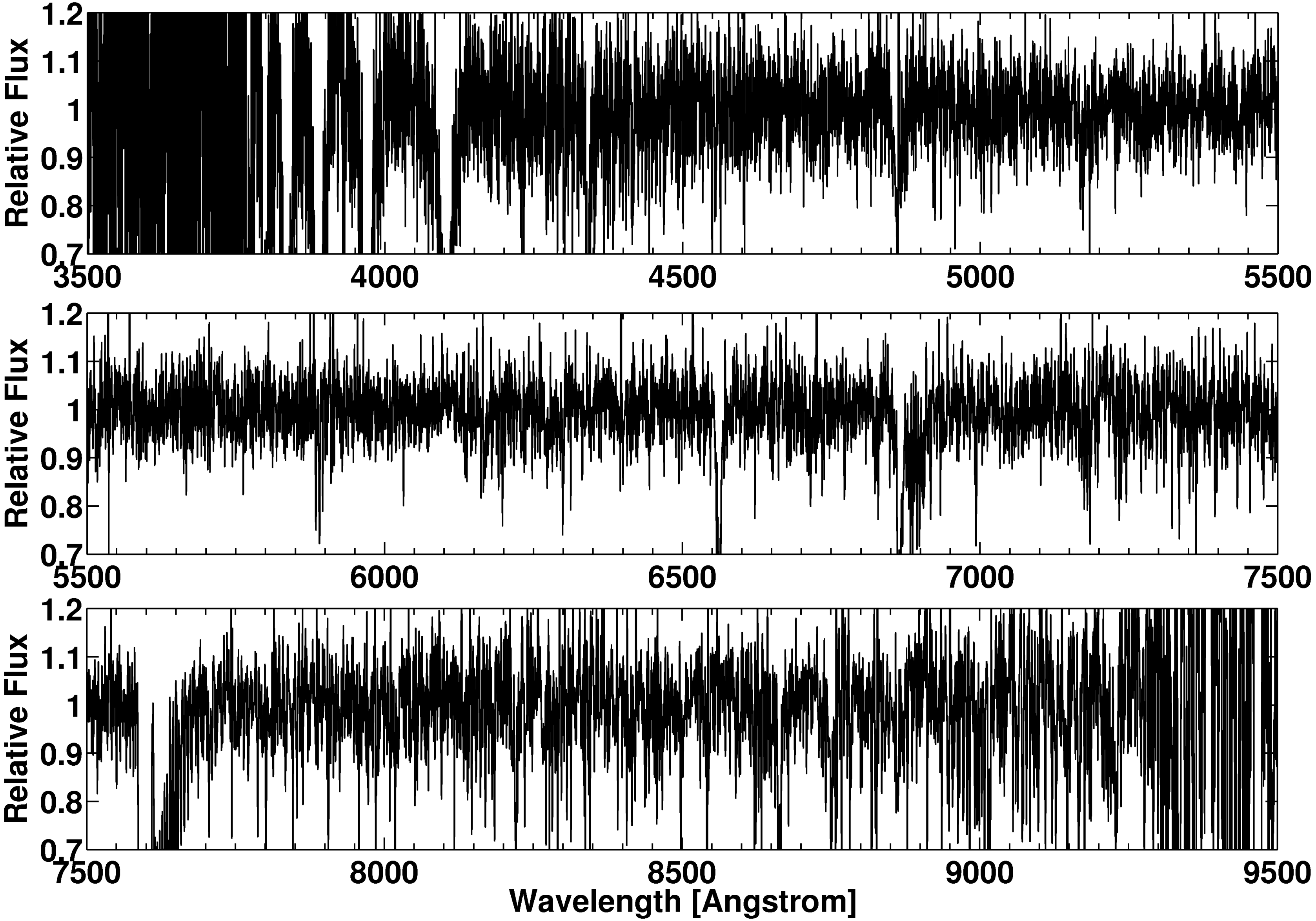

Figure 8.7: Spectra of RR 8645

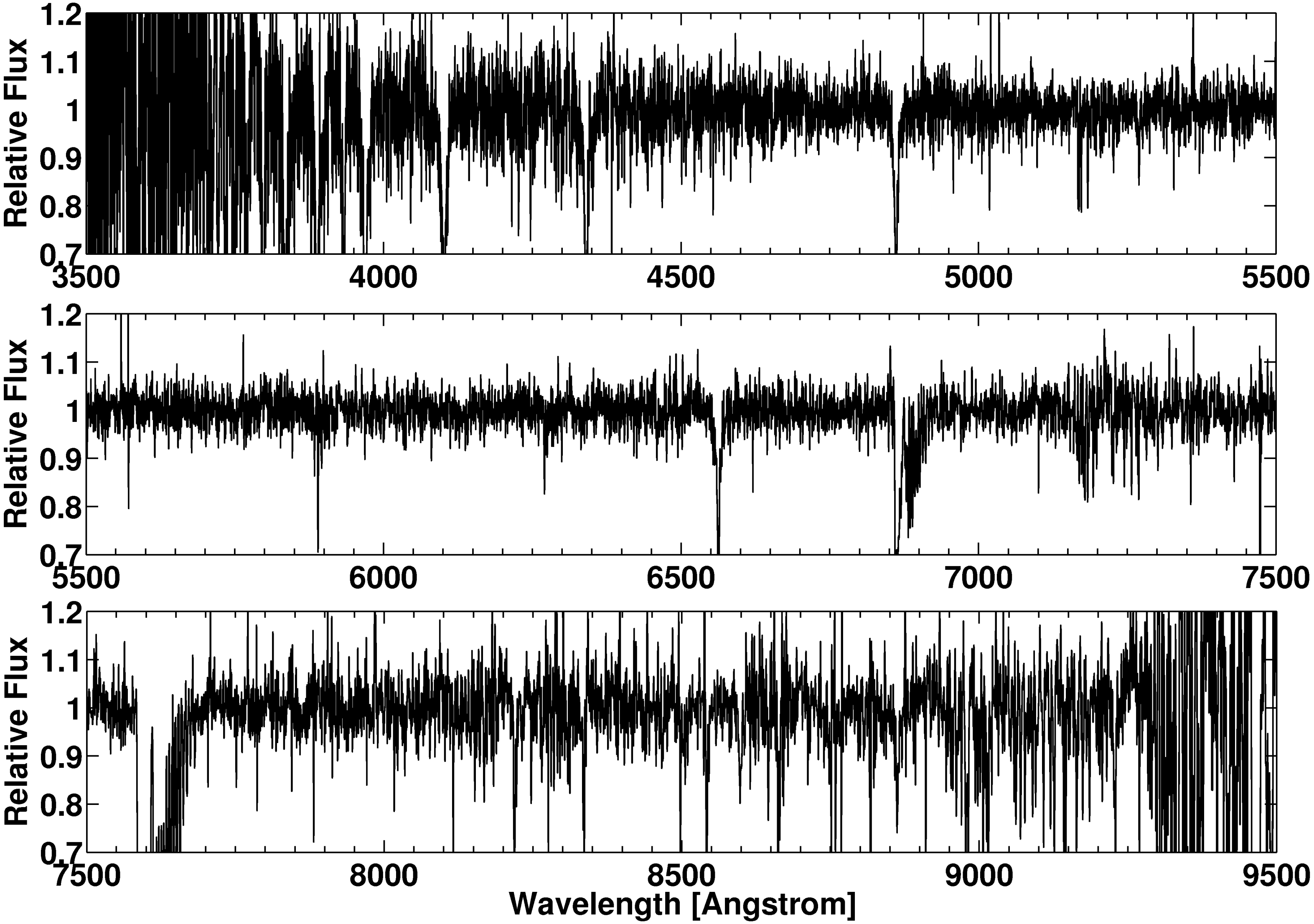

Figure 8.8: Spectra of RR 1422

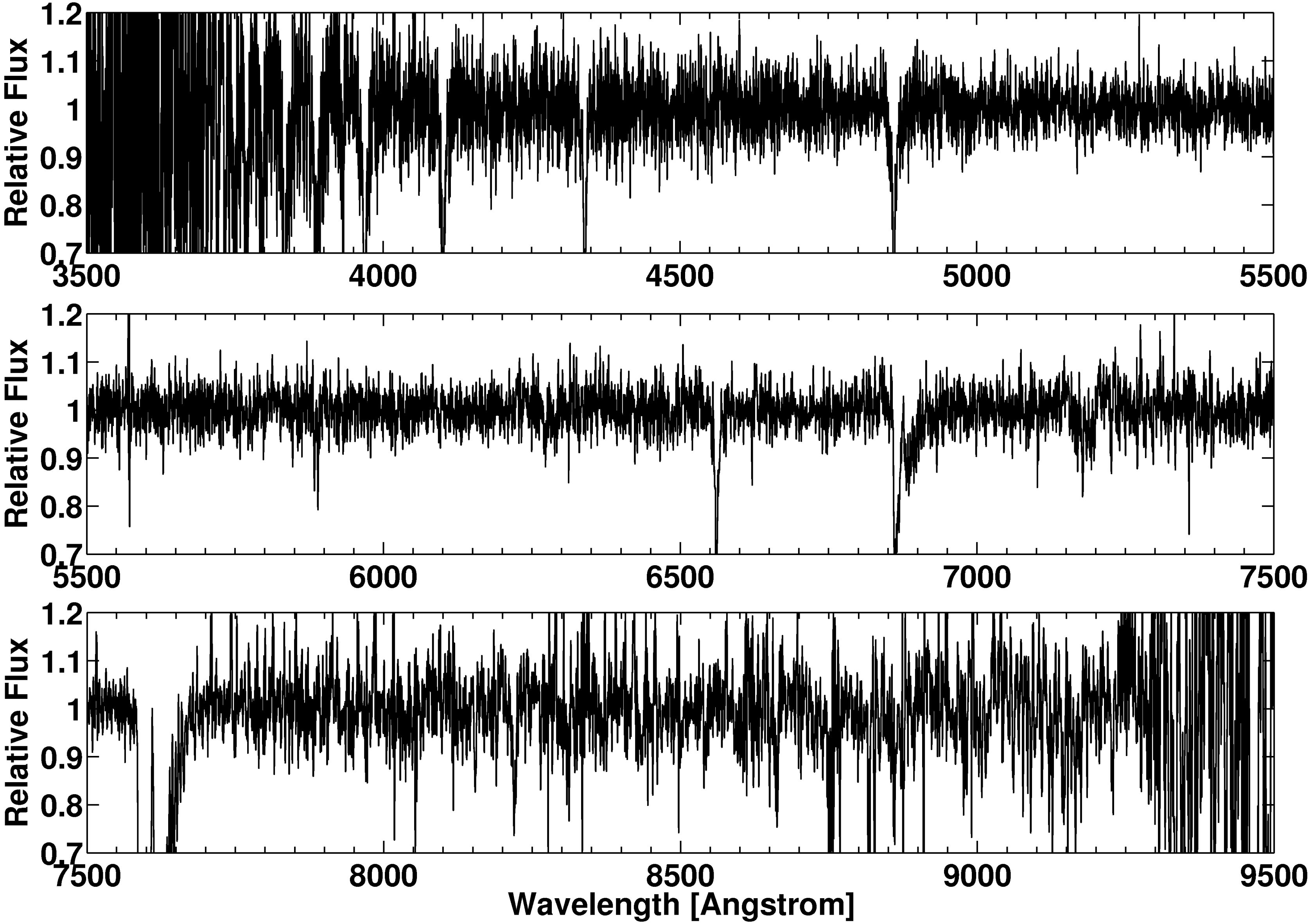

Figure 8.9: Spectra of RR 177

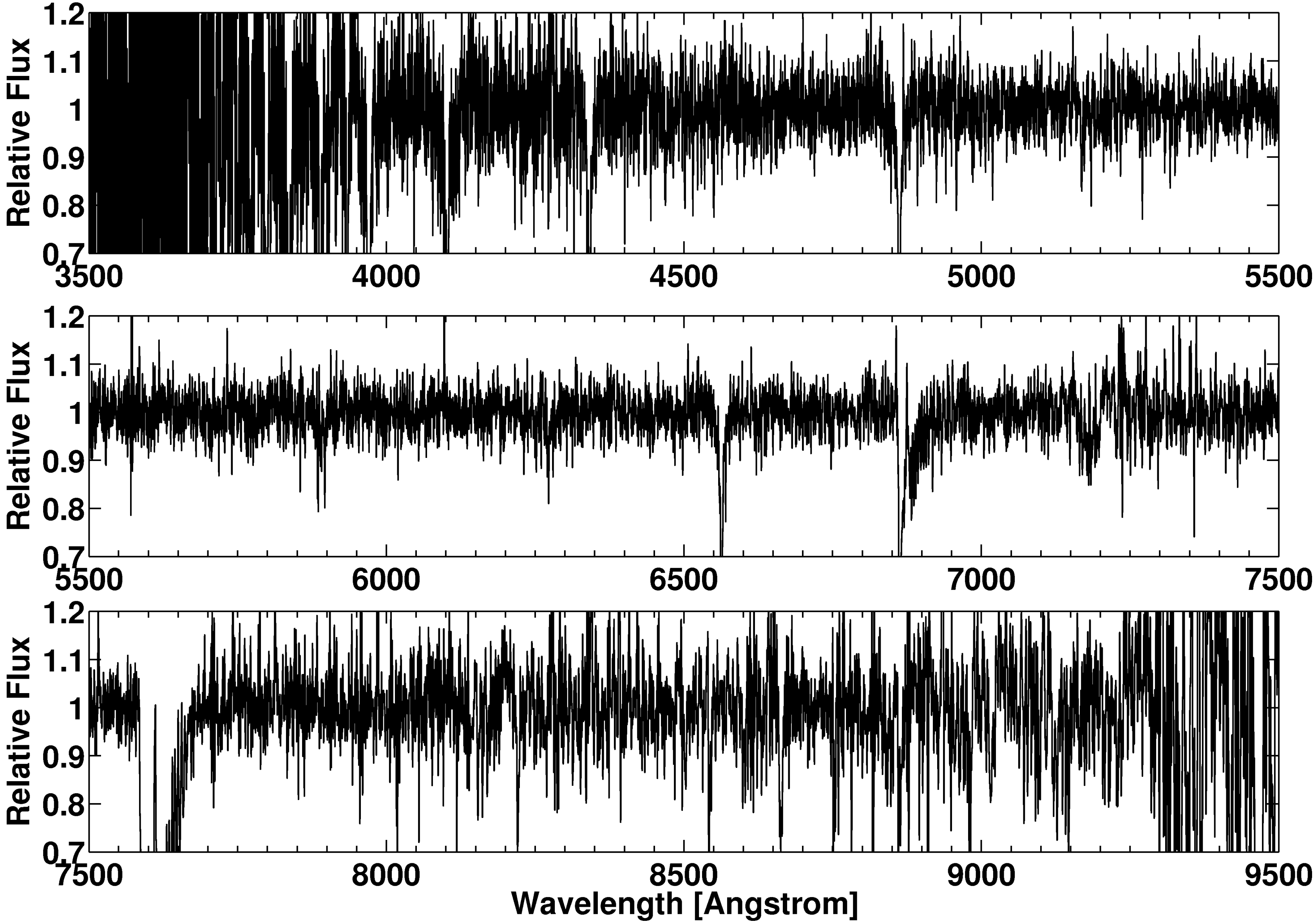

Figure 8.10: Spectra of RR 11371

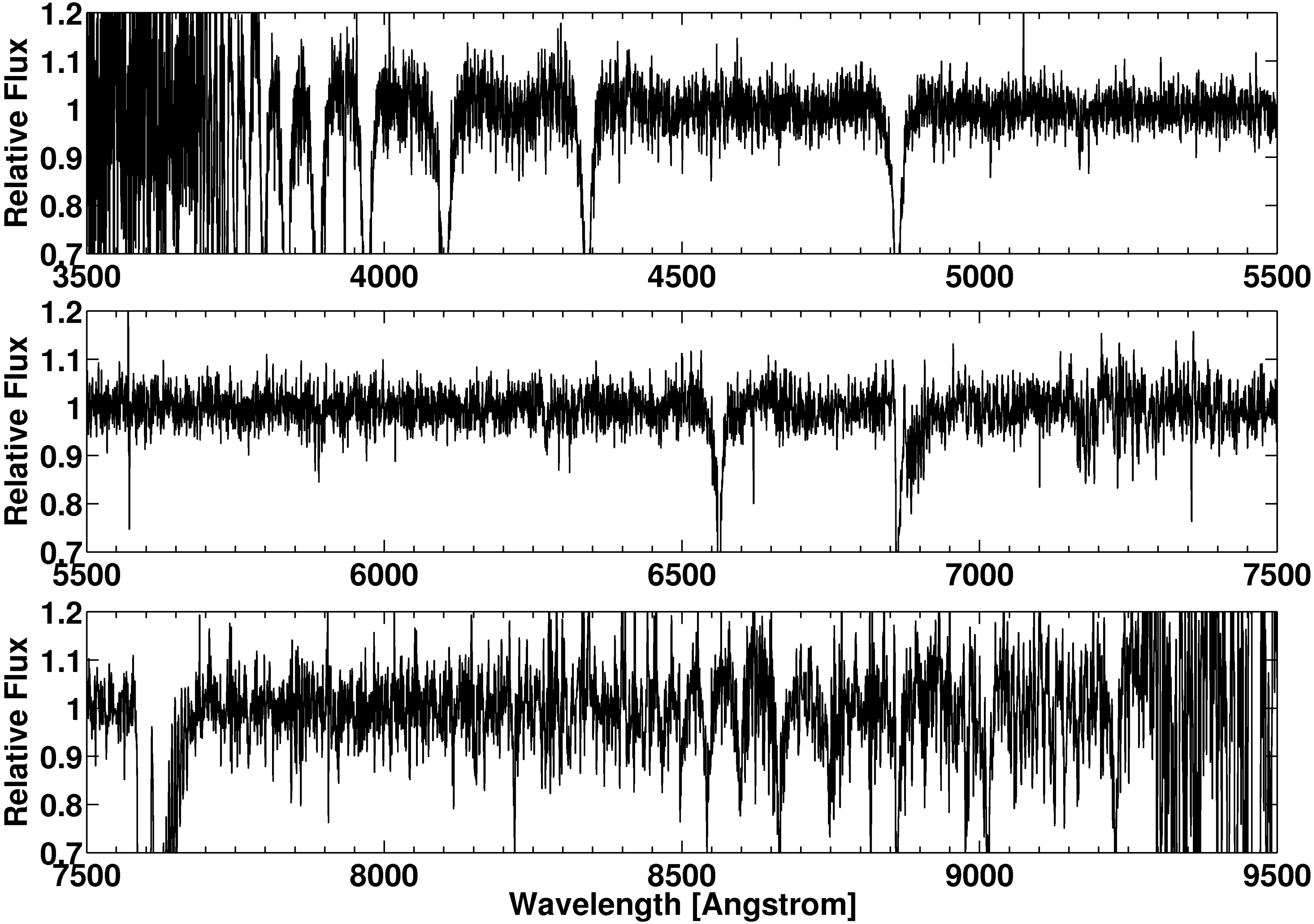

Figure 8.11: Spectra of RR 22827

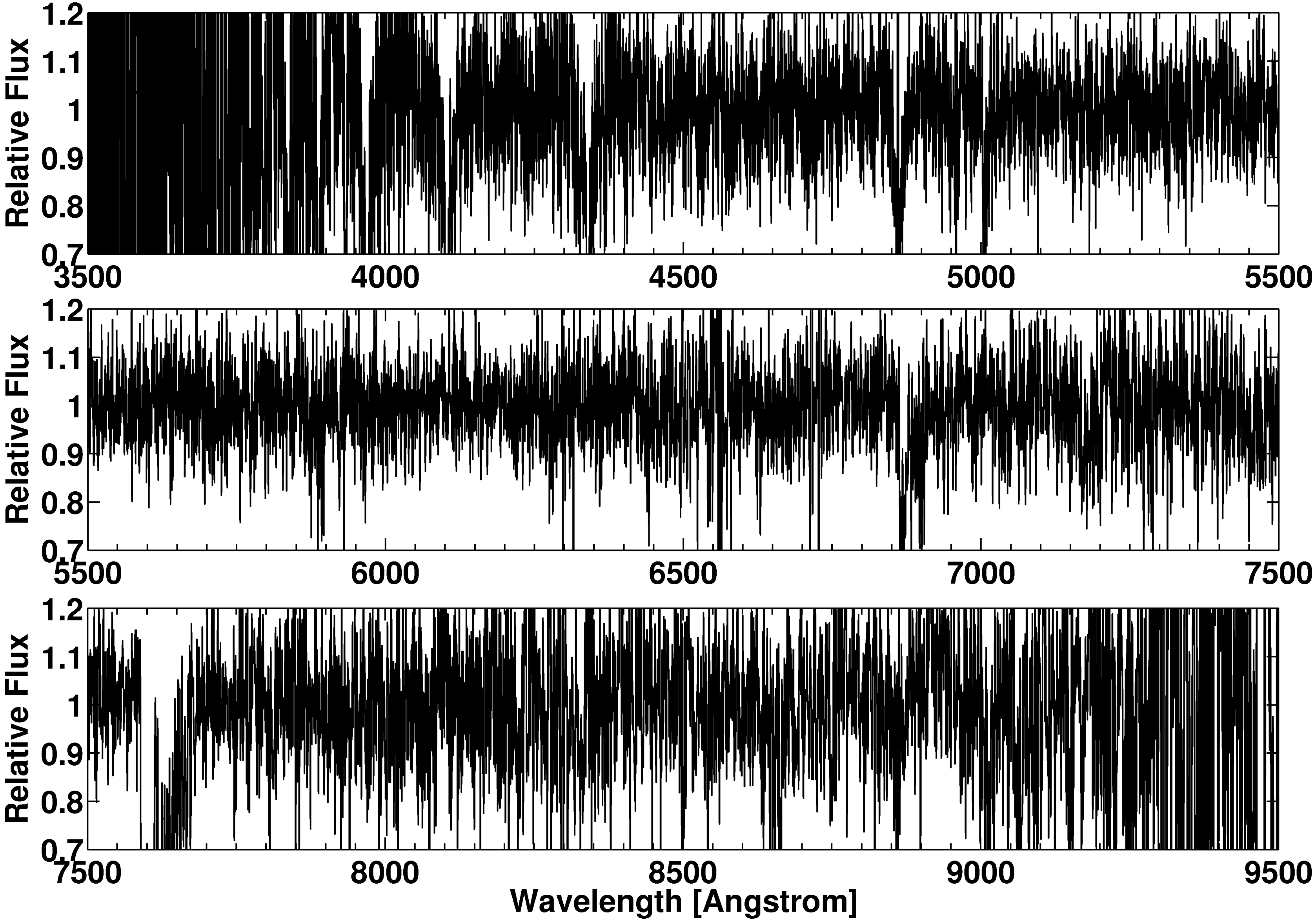

Figure 8.12: Spectra of RR 122432

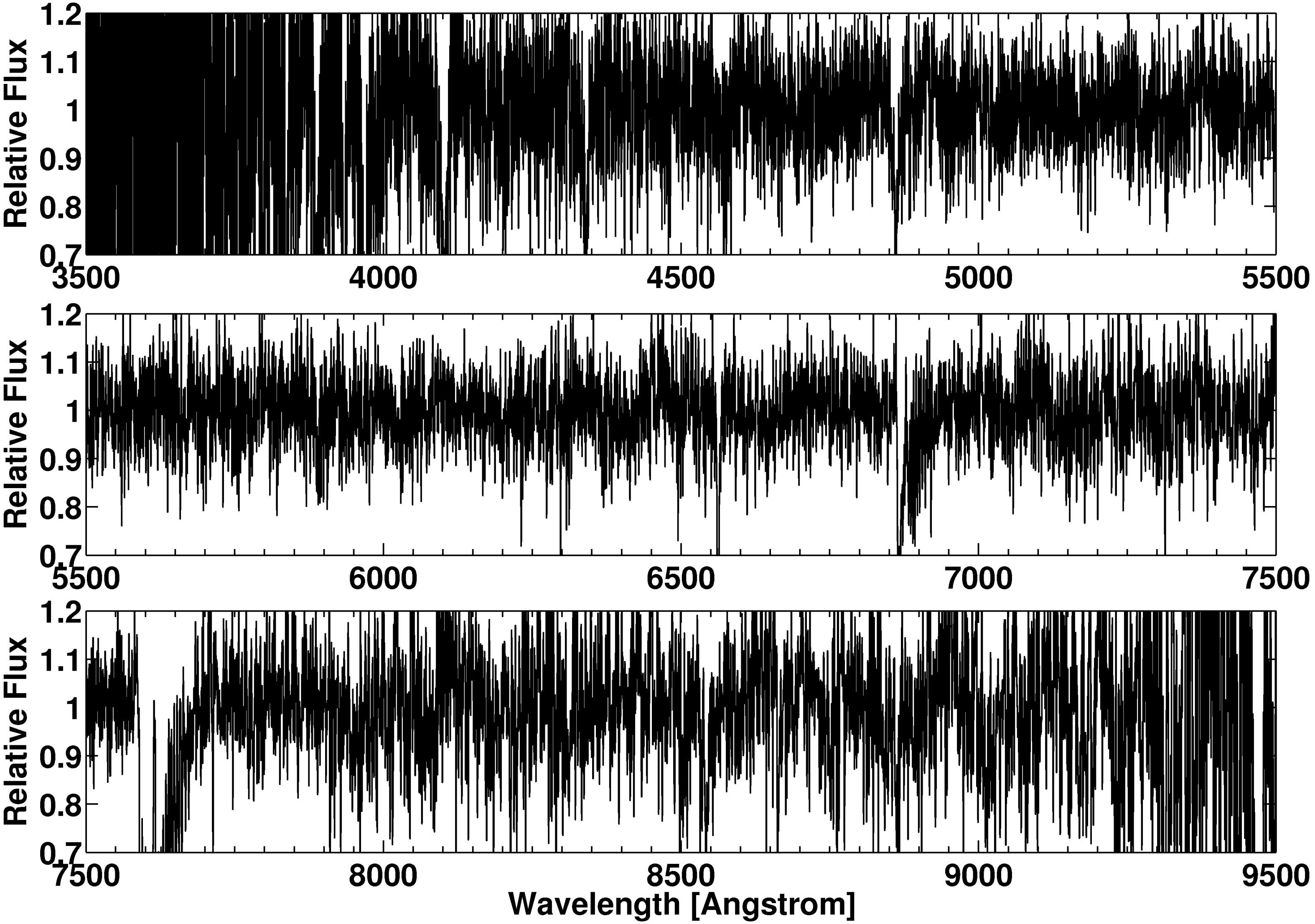

Figure 8.13: Spectra of RR 50180

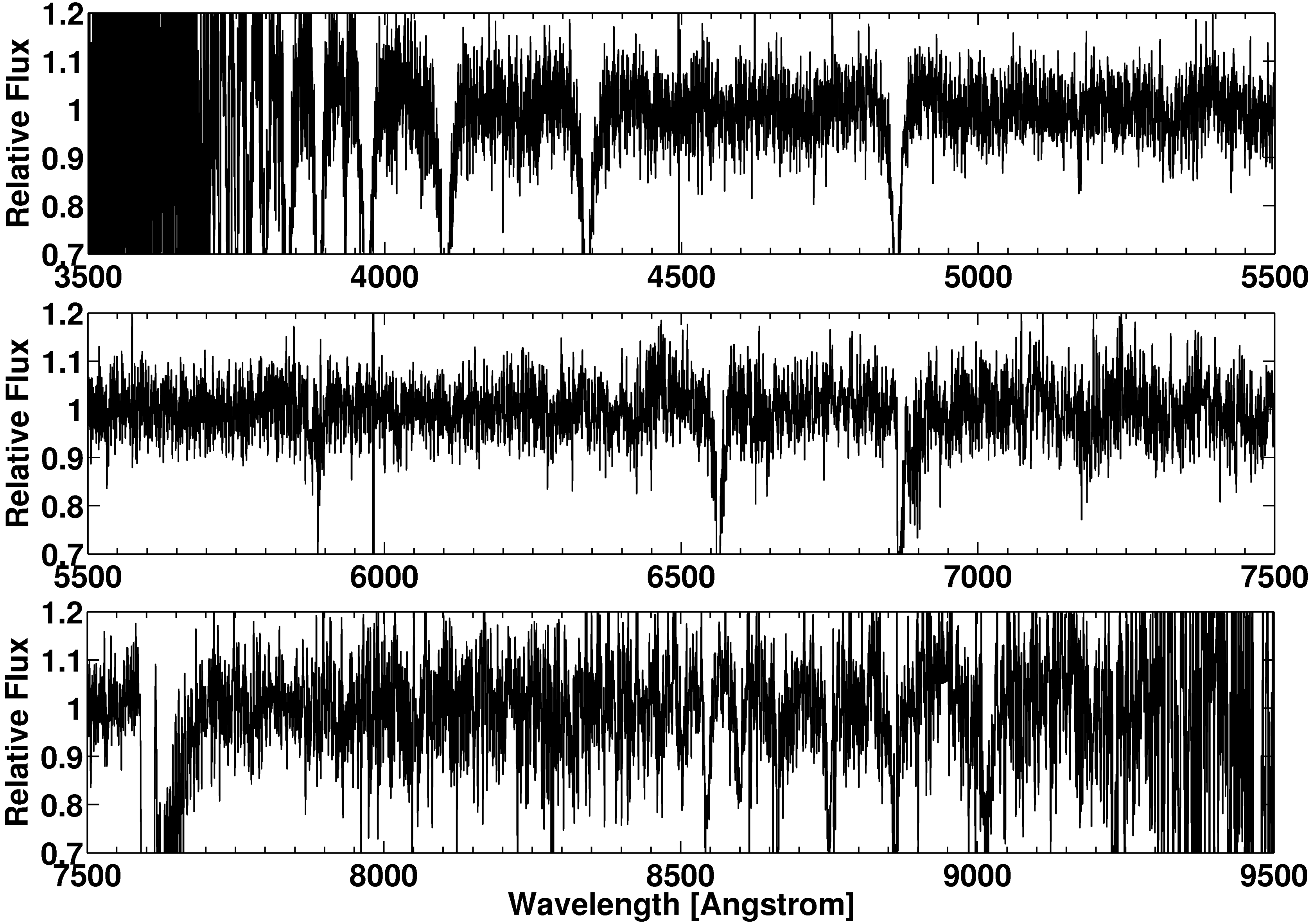

Figure 8.14: Spectra of RR 143874

Bibliography

Adam, J. 1978, Sterne und Weltraum, 17, 258

Adén, D., Eriksson, K., Feltzing, S., Grebel, E. K., Koch, A., & Wilkinson, M. I. 2011, A&A, 525, A153

Alard, C. 1996, ApJ, 458, L17

Alcock, C., et al. 2000, AJ, 119, 2194

Alexander, S. 1852, AJ, 2, 97

Alves, D. R. 2004, New Astronomy Review, 48, 659

Alves, D. R., & Nelson, C. A. 2000, ApJ, 542, 789

Anders, E., & Grevesse, N. 1989, GCA, 53, 197

Andrievsky, S. M., Spite, M., Korotin, S. A., Spite, F., Bonifacio, P., Cayrel, R., Hill, V., & François, P. 2008, A&A, 481, 481

Aoki, W., et al. 2009, A&A, 502, 569

Arellano Ferro, A., Figuera Jaimes, R., Giridhar, S., Bramich, D. M., Hernández Santisteban, J. V., & Kuppuswamy, K. 2011, MNRAS, 416, 2265

Arendt, R. G., et al. 2008, ApJ, 682, 384

Argast, D., Samland, M., Gerhard, O. E., & Thielemann, F.-K. 2000, A&A, 356, 873

Argast, D., Samland, M., Thielemann, F.-K., & Gerhard, O. E. 2002, A&A, 388, 842

Arp, H. C. 1955, AJ, 60, 317

Aubourg, E., et al. 1993, The Messenger, 72, 20

Baade, W. 1926, Astronomische Nachrichten, 228, 359

Bailey, S. I. 1902, Annals of Harvard College Observatory, 38, 1

Baker, N., & Kippenhahn, R. 1962, Zeitschrift für Astrophysik, 54, 114

Barcza, S. 2010, MNRAS, 406, 486

Barmby, P., Marengo, M., Evans, N. R., Bono, G., Huelsman, D., Su, K. Y. L., Welch, D. L., & Fazio, G. G. 2011, AJ, 141, 42

Bastian, N., Gieles, M., Ercolano, B., & Gutermuth, R. 2009, MNRAS, 392, 868

Bekki, K. 2009a, MNRAS, 393, L60

Bekki, K. 2009b, in The Magellanic System: Stars, Gas, and Galaxies, ed. J. T. van Loon & J. M. Oliveira, IAU Symp. 256 (Cambridge: CUP), 105

Bekki, K., & Chiba, M. 2009, PASA, 26, 48

Bell, E. F., et al. 2008, ApJ, 680, 295

Belokurov, V., et al. 2007, ApJ, 654, 897

Benedict, G. F., et al. 2011, AJ, 142, 187

Benkő, J. M., Bakos, G. Á., & Nuspl, J. 2006, MNRAS, 372, 1657

Benkő, J. M., Szabó, R., & Paparó, M. 2011, MNRAS, 417, 974

Besla, G., Kallivayalil, N., Hernquist, L., Robertson, B., Cox, T. J., van der Marel, R. P., & Alcock, C. 2007, ApJ, 668, 949

Besla, G., Kallivayalil, N., Hernquist, L., van der Marel, R. P., Cox, T. J., & Kereš, D. 2010, ApJ, 721, L97

Beveridge, R. C., & Sneden, C. 1994, AJ, 108, 285

Bica, E. L. D., & Schmitt, H. R. 1995, ApJS, 101, 41

Blažko, S. 1907, Astronomische Nachrichten, 175, 325

Bochanski, J. J., et al. 2009, PASP, 121, 1409

Boesgaard, A. M., & Novicki, M. C. 2006, ApJ, 641, 1122

Bolatto, A. D., et al. 2007, ApJ, 655, 212

Bonatto, C., & Bica, E. 2010, MNRAS, 403, 996

Bonifacio, P., et al. 2009, A&A, 501, 519

Bono, G., Caputo, F., Castellani, V., & Marconi, M. 1997, A&AS, 121, 327

Bono, G., Caputo, F., & Di Criscienzo, M. 2007, A&A, 476, 779

Bono, G., Caputo, F., & Marconi, M. 2001, MNRAS, 325, 1353

Book, L. G., Chu, Y., & Gruendl, R. A. 2008, ApJS, 175, 165

Book, L. G., Chu, Y., Gruendl, R. A., & Fukui, Y. 2009, AJ, 137, 3599

Borissova, J., Minniti, D., Rejkuba, M., & Alves, D. 2006, A&A, 460, 459

Borissova, J., Minniti, D., Rejkuba, M., Alves, D., Cook, K. H., & Freeman, K. C. 2004, A&A, 423, 97

Borissova, J., Rejkuba, M., Minniti, D., Catelan, M., & Ivanov, V. D. 2009, A&A, 502, 505

Bragaglia, A., et al. 2001, AJ, 121, 327

Brocato, E., Castellani, V., Ferraro, F. R., Piersimoni, A. M., & Testa, V. 1996, MNRAS, 282, 614

Brown, T. M., Ferguson, H. C., Smith, E., Kimble, R. A., Sweigart, A. V., Renzini, A., & Rich, R. M. 2004, AJ, 127, 2738

Butler, D., Demarque, P., & Smith, H. A. 1982, ApJ, 257, 592

Cabrera-Lavers, A., Hammersley, P. L., González-Fernández, C., López-Corredoira, M., Garzón, F., & Mahoney, T. J. 2007, A&A, 465, 825

Caffau, E., et al. 2011, Nature, 477, 67

Caldwell, J. A. R., & Coulson, I. M. 1986, MNRAS, 218, 223

Caldwell, N., Schiavon, R., Morrison, H., Rose, J. A., & Harding, P. 2011, AJ, 141, 61

Cardelli, J. A., Clayton, G. C., & Mathis, J. S. 1989, ApJ, 345, 245

Carlin, J. L., Majewski, S. R., Casetti-Dinescu, D. I., Law, D. R., Girard, T. M., & Patterson, R. J. 2012, ApJ, 744, 25

Carney, B. W., Wright, J. S., Sneden, C., Laird, J. B., Aguilar, L. A., & Latham, D. W. 1997, AJ, 114, 363

Carollo, D., et al. 2007, Nature, 450, 1020

Carrera, R., Gallart, C., Aparicio, A., Costa, E., Méndez, R. A., & Noël, N. E. D. 2008a, AJ, 136, 1039

Carrera, R., Gallart, C., Aparicio, A., & Hardy, E. 2011, AJ, 142, 61

Carrera, R., Gallart, C., Hardy, E., Aparicio, A., & Zinn, R. 2008b, AJ, 135, 836

Carretta, E., Bragaglia, A., Gratton, R., D'Orazi, V., & Lucatello, S. 2009, A&A, 508, 695

Carretta, E., & Gratton, R. G. 1997, A&AS, 121, 95

Carretta, E., Gratton, R. G., & Clementini, G. 2000a, MNRAS, 316, 721

Carretta, E., Gratton, R. G., Clementini, G., & Fusi Pecci, F. 2000b, ApJ, 533, 215

Carretta, E., et al. 2010, ApJ, 722, 1

Casagrande, L., Ramírez, I., Meléndez, J., Bessell, M., & Asplund, M. 2010, A&A, 512, 54, (C10)

Castelli, F., Gratton, R. G., & Kurucz, R. L. 1997, A&A, 318, 841

Catelan, M. 2009, Ap&SS, 320, 261

Catelan, M., & Cortés, C. 2008, ApJ, 676, L135

Catelan, M., Pritzl, B. J., & Smith, H. A. 2004, ApJS, 154, 633

Cayrel, R., et al. 2004, A&A, 416, 1117

Cenarro, A. J., et al. 2007, MNRAS, 374, 664

Chou, M.-Y., et al. 2007, ApJ, 670, 346

Christy, R. F. 1966, ARAA, 4, 353

Ciechanowska, A., Pietrzyński, G., Szewczyk, O., Gieren, W., & Soszyński, I. 2010, Acta Astronomica, 60, 233

Cignoni, M., et al. 2009, AJ, 137, 3668

Cioni, M. 2009, A&A, 506, 1137

Cioni, M., Girardi, L., Marigo, P., & Habing, H. J. 2006, A&A, 448, 77

Cioni, M., van der Marel, R. P., Loup, C., & Habing, H. J. 2000, A&A, 359, 601

Clayton, G. C., & Cardelli, J. A. 1988, AJ, 96, 695

Clement, C. M., & Shelton, I. 1999, ApJ, 515, L85

Clementini, G., Carretta, E., Gratton, R., Merighi, R., Mould, J. R., & McCarthy, J. K. 1995, AJ, 110, 2319, (C95)

Clementini, G., Gratton, R., Bragaglia, A., Carretta, E., Di Fabrizio, L., & Maio, M. 2003, AJ, 125, 1309

Clementini, G., Gratton, R. G., Bragaglia, A., Ripepi, V., Martinez Fiorenzano, A. F., Held, E. V., & Carretta, E. 2005, ApJ, 630, L145

Cohen, J. G., & Huang, W. 2009, ApJ, 701, 1053

—. 2010, ApJ, 719, 931

Cohen, J. G., & Meléndez, J. 2005, AJ, 129, 303

Cole, A. A. 1998, ApJ, 500, L137

Cole, A. A., Grocholski, A. J., Geisler, D., Sarajedini, A., Smith, V. V., & Tolstoy, E. 2009, in IAU Symposium 256, ed. J. T. van Loon & J. M. Oliveira (Cambridge University Press, Cambridge), 263

Cole, A. A., Tolstoy, E., Gallagher, III, J. S., & Smecker-Hane, T. A. 2005, AJ, 129, 1465

Cole, N., et al. 2008, ApJ, 683, 750

Colucci, J. E., Bernstein, R. A., Cameron, S. A., & McWilliam, A. 2011, ApJ, 735, 55

Cook, K., et al. 1992, in Bulletin of the American Astronomical Society, Vol. 24, 1179

Correnti, M., Bellazzini, M., Ibata, R. A., Ferraro, F. R., & Varghese, A. 2010, ApJ, 721, 329

Costa, E., Méndez, R. A., Pedreros, M. H., Moyano, M., Gallart, C., & Noël, N. 2011, AJ, 141, 136

Costa, E., Méndez, R. A., Pedreros, M. H., Moyano, M., Gallart, C., Noël, N., Baume, G., & Carraro, G. 2009, AJ, 137, 4339

Cox, J. P., & Olsen, K. H. 1963, AJ, 68, 276

Crowl, H. H., Sarajedini, A., Piatti, A. E., Geisler, D., Bica, E., Clariá, J. J., & Santos, Jr., J. F. C. 2001, AJ, 122, 220

Da Costa, G. S., & Hatzidimitriou, D. 1998, AJ, 115, 1934

Davies, R. D., Elliott, K. H., & Meaburn, J. 1976, MmRAS, 81, 89

De Propris, R., Rich, R. M., Mallery, R. C., & Howard, C. D. 2010, ApJ, 714, L249

de Vaucouleurs, G. 1955a, AJ, 60, 126

—. 1955b, AJ, 60, 219

—. 1955c, PASP, 67, 350

de Vaucouleurs, G., de Vaucouleurs, A., Corwin, Jr., H. G., Buta, R. J., Paturel, G., & Fouqué, P. 1991, Third Reference Catalogue of Bright Galaxies. Volume I: Explanations and references. Volume II: Data for galaxies between 0^h and 12^h. Volume III: Data for galaxies between 12^h and 24^h., ed. de Vaucouleurs, G., de Vaucouleurs, A., Corwin, H. G., Jr., Buta, R. J., Paturel, G., & Fouqué, P.

de Vaucouleurs, G., & Freeman, K. C. 1972, Vistas in Astronomy, 14, 163

Deb, S., & Singh, H. P. 2010, MNRAS, 402, 691, (DS10)

Dékány, I., & Kovács, G. 2009, A&A, 507, 803

Dekel, A., Shaham, J., & Lecar, M. 1980, ApJ, 241, 946

Diaz, J., & Bekki, K. 2011, MNRAS, 413, 2015

Dobashi, K., Bernard, J.-P., Hughes, A., Paradis, D., Reach, W. T., & Kawamura, A. 2008, A&A, 484, 205, (D08)

Dobashi, K., Bernard, J.-P., Kawamura, A., Egusa, F., Hughes, A., Paradis, D., Bot, C., & Reach, W. T. 2009, AJ, 137, 5099, (D09)

Dolphin, A. E., Walker, A. R., Hodge, P. W., Mateo, M., Olszewski, E. W., Schommer, R. A., & Suntzeff, N. B. 2001, ApJ, 562, 303

Dorfi, E. A., & Feuchtinger, M. U. 1999, A&A, 348, 815, (DF99)

Dotter, A., Chaboyer, B., Jevremović, D., Baron, E., Ferguson, J. W., Sarajedini, A., & Anderson, J. 2007, AJ, 134, 376

Draine, B. T. 2003, ARAA, 41, 241

Duffau, S., Zinn, R., Vivas, A. K., Carraro, G., Méndez, R. A., Winnick, R., & Gallart, C. 2006, ApJ, 636, L97

Eggen, O. J., Lynden-Bell, D., & Sandage, A. R. 1962, ApJ, 136, 748

Epchtein, N., et al. 1997, The Messenger, 87, 27

Feast, M. W., Abedigamba, O. P., & Whitelock, P. A. 2010, MNRAS, 408, L76, (FAW10)

Feltzing, S., Eriksson, K., Kleyna, J., & Wilkinson, M. I. 2009, A&A, 508, L1

Fernley, J., & Barnes, T. G. 1996, A&A, 312, 957

Fernley, J., Skillen, I., Carney, B. W., Cacciari, C., & Janes, K. 1998, MNRAS, 293, L61

Font, A. S., Johnston, K. V., Bullock, J. S., & Robertson, B. E. 2006, ApJ, 638, 585

Font, A. S., Johnston, K. V., Ferguson, A. M. N., Bullock, J. S., Robertson, B. E., Tumlinson, J., & Guhathakurta, P. 2008, ApJ, 673, 215

For, B.-Q., & Sneden, C. 2010, AJ, 140, 1694

For, B.-Q., Sneden, C., & Preston, G. W. 2011, ApJS, 197, 29

Frebel, A., Kirby, E. N., & Simon, J. D. 2010a, Nature, 464, 72

Frebel, A., Simon, J. D., Geha, M., & Willman, B. 2010b, ApJ, 708, 560

Frebel, A., et al. 2005, Nature, 434, 871

Freedman, W. L., et al. 2001, ApJ, 553, 47

Fritz, T. K., et al. 2011, ApJ, 737, 73

Fukui, Y., et al. 2008, ApJS, 178, 56

Fulbright, J. P. 2000, AJ, 120, 1841

Gallart, C., Stetson, P. B., Meschin, I. P., Pont, F., & Hardy, E. 2008, ApJ, 682, 89

Geisler, D., Wallerstein, G., Smith, V. V., & Casetti-Dinescu, D. I. 2007, PASP, 119, 939

Ghez, A. M., et al. 2008, ApJ, 689, 1044

Gilbert, K. M., Font, A. S., Johnston, K. V., & Guhathakurta, P. 2009, ApJ, 701, 776

Gillessen, S., Eisenhauer, F., Trippe, S., Alexander, T., Genzel, R., Martins, F., & Ott, T. 2009, ApJ, 692, 1075

Girardi, L., & Salaris, M. 2001, MNRAS, 323, 109

Glatt, K., Grebel, E. K., & Koch, A. 2010, A&A, 517, 50

Glatt, K., et al. 2008a, AJ, 136, 1703

—. 2008b, AJ, 135, 1106

Gonidakis, I., Livanou, E., Kontizas, E., Klein, U., Kontizas, M., Belcheva, M., Tsalmantza, P., & Karampelas, A. 2009, A&A, 496, 375, (G09)

Gordon, K. D., Clayton, G. C., Misselt, K. A., Landolt, A. U., & Wolff, M. J. 2003, ApJ, 594, 279

Gratton, R. G., Bragaglia, A., Clementini, G., Carretta, E., Di Fabrizio, L., Maio, M., & Taribello, E. 2004, A&A, 421, 937

Grebel, E. K. 1997, in Reviews in Modern Astronomy, ed. R. E. Schielicke, Vol. 10, 29

Grebel, E. K. 2001, Astrophysics and Space Science Supplement, 277, 231

Grebel, E. K., & Brandner, W. 1998, in Magellanic Clouds and Other Dwarf Galaxies, ed. T. Richtler & J. M. Braun (Shaker Verlag), 151

Grebel, E. K., & Gallagher, III, J. S. 2004, ApJ, 610, 89

Grebel, E. K., Gallagher, III, J. S., & Harbeck, D. 2003, AJ, 125, 1926

Grebel, E. K., & Roberts, W. J. 1995, A&AS, 109, 293

Grevesse, N., & Sauval, A. J. 1998, Space Science Reviews, 85, 161

Grillmair, C. J. 2009, ApJ, 693, 1118

Grocholski, A. J., Cole, A. A., Sarajedini, A., Geisler, D., & Smith, V. V. 2006, AJ, 132, 1630

Grocholski, A. J., Sarajedini, A., Olsen, K. A. G., Tiede, G. P., & Mancone, C. L. 2007, AJ, 134, 680

Groenewegen, M. A. T. 2000, A&A, 363, 901

Groenewegen, M. A. T., & Oudmaijer, R. D. 2000, A&A, 356, 849

Groenewegen, M. A. T., Udalski, A., & Bono, G. 2008, A&A, 481, 441

Grosse, E., & Schorr, R. R. E. 1932, Astronomische Abhandlungen der Hamburger Sternwarte, 4, 39

Guedes, J., Callegari, S., Madau, P., & Mayer, L. 2011, ApJ, 742, 76

Guldenschuh, K. A., et al. 2005, PASP, 117, 721

Gunn, J. E. 1977, ApJ, 218, 592

Gunn, J. E., & Gott, III, J. R. 1972, ApJ, 176, 1

Hankey, W. J., & Cole, A. A. 2011, MNRAS, 411, 1536

Hansen, C. J., et al. 2011, A&A, 527, A65

Harries, T. J., Hilditch, R. W., & Howarth, I. D. 2003, MNRAS, 339, 157

Harris, J. 2007, ApJ, 658, 345

Harris, J., & Zaritsky, D. 2004, AJ, 127, 1531

—. 2006, AJ, 131, 2514

—. 2009, AJ, 138, 1243

Harris, W. E. 1996, AJ, 112, 1487

Haschke, R., & Grebel, E. K. in prep.

Haschke, R., Grebel, E. K., & Duffau, S. 2011, AJ, 141, 158

—. in prep.a

—. submitted

Haschke, R., Grebel, E. K., Duffau, S., & Jin, S. 2012, AJ, 143, 48

Haschke, R., Grebel, E. K., Frebel, A., Duffau, S., Hansen, C. J., & Koch, A. in prep.b

Hernquist, L., & Mihos, J. C. 1995, ApJ, 448, 41

Hertzsprung, E. 1924, BAN, 2, 109

Hidalgo, S. L., Aparicio, A., Martínez-Delgado, D., & Gallart, C. 2009, ApJ, 705, 704

Hilditch, R. W., Howarth, I. D., & Harries, T. J. 2005, MNRAS, 357, 304

Hindman, J. V., Kerr, F. J., & McGee, R. X. 1963, Australian Journal of Physics, 16, 570

Høg, E., et al. 2000, A&A, 355, L27

Holtzman, J. A., et al. 1999, AJ, 118, 2262

Hoskin, M. A. 1976, Journal for the History of Astronomy, 7, 169

Hubble, E. P. 1925a, Popular Astronomy, 33, 252

—. 1925b, ApJ, 62, 409

Ibata, R., Mouhcine, M., & Rejkuba, M. 2009, MNRAS, 395, 126

Ibata, R. A., Gilmore, G., & Irwin, M. J. 1994, Nature, 370, 194

Irwin, M. J., Kunkel, W. E., & Demers, S. 1985, Nature, 318, 160

Ivans, I. I., Sneden, C., James, C. R., Preston, G. W., Fulbright, J. P., Höflich, P. A., Carney, B. W., & Wheeler, J. C. 2003, ApJ, 592, 906

Ivezić, Ž., et al. 2008, ApJ, 684, 287

James, P. A., & Ivory, C. F. 2011, MNRAS, 411, 495

Johnson, H. M. 1961, PASP, 73, 20

Johnson, J. A., Ivans, I. I., & Stetson, P. B. 2006, ApJ, 640, 801

Johnston, K. V., Hernquist, L., & Bolte, M. 1996, ApJ, 465, 278

Joy, A. H. 1938, ApJ, 88, 408

Jurcsik, J. 1995, Acta Astronomica, 45, 653, (J95)

Jurcsik, J., & Kovács, G. 1996, A&A, 312, 111

Jurcsik, J., et al. 2009, MNRAS, 400, 1006

Kallivayalil, N., van der Marel, R. P., & Alcock, C. 2006a, ApJ, 652, 1213

Kallivayalil, N., van der Marel, R. P., Alcock, C., Axelrod, T., Cook, K. H., Drake, A. J., & Geha, M. 2006b, ApJ, 638, 772

Kant, I. 1755, Allgemeine Naturgeschichte und Theorie des Himmels, ed. Kant, I.

Kapakos, E., Hatzidimitriou, D., & Soszyński, I. 2011, MNRAS, 415, 1366

Kayser, A., Grebel, E. K., Harbeck, D. R., Cole, A. A., Koch, A., Glatt, K., Gallagher, J. S., & da Costa, G. S. 2007, in IAU Symposium 241, ed. A. Vazdekis & R. F. Peletier (Cambridge University Press, Cambridge), 351

Keller, S. C., & Wood, P. R. 2006, ApJ, 642, 834

Kerber, L. O., Santiago, B. X., & Brocato, E. 2007, A&A, 462, 139

Kiess, C. C. 1913, Lick Observatory Bulletin, 7, 140

Kim, S., Staveley-Smith, L., Dopita, M. A., Freeman, K. C., Sault, R. J., Kesteven, M. J., & McConnell, D. 1998a, ApJ, 503, 674

Kim, S., Staveley-Smith, L., Sault, R. J., Kesteven, M. J., McConnell, D., Dopita, M. A., & Bessell, M. 1998b, PASA, 15, 132

Kirby, E. N., Lanfranchi, G. A., Simon, J. D., Cohen, J. G., & Guhathakurta, P. 2011, ApJ, 727, 78

Koch, A., Grebel, E. K., Gilmore, G. F., Wyse, R. F. G., Kleyna, J. T., Harbeck, D. R., Wilkinson, M. I., & Wyn Evans, N. 2008a, AJ, 135, 1580

Koch, A., Grebel, E. K., Kleyna, J. T., Wilkinson, M. I., Harbeck, D. R., Gilmore, G. F., Wyse, R. F. G., & Evans, N. W. 2007a, AJ, 133, 270

Koch, A., Grebel, E. K., Wyse, R. F. G., Kleyna, J. T., Wilkinson, M. I., Harbeck, D. R., Gilmore, G. F., & Evans, N. W. 2006, AJ, 131, 895

Koch, A., McWilliam, A., Grebel, E. K., Zucker, D. B., & Belokurov, V. 2008b, ApJ, 688, L13

Koch, A., Wilkinson, M. I., Kleyna, J. T., Gilmore, G. F., Grebel, E. K., Mackey, A. D., Evans, N. W., & Wyse, R. F. G. 2007b, ApJ, 657, 241

Koerwer, J. F. 2009, AJ, 138, 1

Kolenberg, K. 2011, in RR Lyrae Stars, Metal-Poor Stars, and the Galaxy, ed. A. McWilliam (Pasadena: Carnegie Observatories), 100

Kovács, G., & Jurcsik, J. 1996, ApJ, 466, L17

Kovács, G., & Zsoldos, E. 1995, A&A, 293, L57

Kunder, A., & Chaboyer, B. 2008, AJ, 136, 2441

—. 2009, AJ, 137, 4478

Lah, P., Kiss, L. L., & Bedding, T. R. 2005, MNRAS, 359, L42

Lai, D. K., Bolte, M., Johnson, J. A., Lucatello, S., Heger, A., & Woosley, S. E. 2008, ApJ, 681, 1524

Lambert, D. L., Heath, J. E., Lemke, M., & Drake, J. 1996, ApJS, 103, 183

Laney, C. D., & Stobie, R. S. 1986, MNRAS, 222, 449

Lanfranchi, G. A., & Matteucci, F. 2004, MNRAS, 351, 1338

Law, D. R., & Majewski, S. R. 2010, ApJ, 714, 229

Layden, A. C. 1994, AJ, 108, 1016

—. 1998, AJ, 115, 193

Leavitt, H. S. 1908, Annals of Harvard College Observatory, 60, 87

Leavitt, H. S., & Pickering, E. C. 1912, Harvard College Observatory Circular, 173, 1

Lee, J., Carney, B. W., & Habgood, M. J. 2005, AJ, 129, 251

Lejeune, T., Cuisinier, F., & Buser, R. 1997, A&AS, 125, 229

Lemaître, G. 1931, Nature, 127, 706

Letarte, B., et al. 2010, A&A, 523, A17

Libeskind, N. I., Cole, S., Frenk, C. S., Okamoto, T., & Jenkins, A. 2007, MNRAS, 374, 16

Liu, L., Gerke, B. F., Wechsler, R. H., Behroozi, P. S., & Busha, M. T. 2011, ApJ, 733, 62

Livanou, E., et al. 2007, AJ, 133, 2179

Lorimer, D. R., Bailes, M., McLaughlin, M. A., Narkevic, D. J., & Crawford, F. 2007, Science, 318, 777

Luck, R. E., Gieren, W. P., Andrievsky, S. M., Kovtyukh, V. V., Fouqué, P., Pont, F., & Kienzle, F. 2003, A&A, 401, 939

Lundmark, K. 1924, The Observatory, 47, 276

Luri, X., Gomez, A. E., Torra, J., Figueras, F., & Mennessier, M. O. 1998, A&A, 335, L81

Lux, H., Read, J. I., & Lake, G. 2010, MNRAS, 406, 2312

Lynden-Bell, D. 1975, Vistas in Astronomy, 19, 299

Mackey, A. D., & Gilmore, G. F. 2004, MNRAS, 355, 504

Majewski, S. R., Skrutskie, M. F., Weinberg, M. D., & Ostheimer, J. C. 2003, ApJ, 599, 1082

Majewski, S. R., et al. 2004, AJ, 128, 245

Mancini, L., Calchi Novati, S., Jetzer, P., & Scarpetta, G. 2004, A&A, 427, 61

Marcolini, A., D’Ercole, A., Battaglia, G., & Gibson, B. K. 2008, MNRAS, 386, 2173

Marconi, M., & Clementini, G. 2005, AJ, 129, 2257

Marshall, J. L., et al. 2008, in Society of Photo-Optical Instrumentation Engineers (SPIE) Conference Series, ed. Ian S. McLean & Mark M. Casali, Vol. 7014, 169

Martell, S. L., Smolinski, J. P., Beers, T. C., & Grebel, E. K. 2011, A&A, 534, A136

Martin, N. F., & Jin, S. 2010, ApJ, 721, 1333

Mashonkina, L., & Gehren, T. 2001, A&A, 376, 232

Mathewson, D. S., Ford, V. L., & Visvanathan, N. 1986, ApJ, 301, 664

—. 1988, ApJ, 333, 617

Matsunaga, N., Kawadu, T., Nishiyama, S., Nagayama, T., Hatano, H., Tamura, M., Glass, I. S., & Nagata, T. 2009, MNRAS, 399, 1709

Matsunaga, N., et al. 2011, Nature, 477, 188

Matteucci, A., Ripepi, V., Brocato, E., & Castellani, V. 2002, A&A, 387, 861

McCumber, M. P., Garnett, D. R., & Dufour, R. J. 2005, AJ, 130, 1083

Meixner, M., et al. 2006, AJ, 132, 2268

Monaco, L., Bellazzini, M., Bonifacio, P., Ferraro, F. R., Marconi, G., Pancino, E., Sbordone, L., & Zaggia, S. 2005, A&A, 441, 141

Morgan, S. M., Simet, M., & Bargenquast, S. 1998, Acta Astronomica, 48, 341

Morris, M., & Serabyn, E. 1996, ARAA, 34, 645

Mucciarelli, A., Origlia, L., & Ferraro, F. R. 2010, ApJ, 717, 277

Mucciarelli, A., Origlia, L., Ferraro, F. R., & Pancino, E. 2009, ApJ, 695, L134

Muller, E., Stanimirović, S., Rosolowsky, E., & Staveley-Smith, L. 2004, ApJ, 616, 845

Muller, E., Staveley-Smith, L., Zealey, W., & Stanimirović, S. 2003, MNRAS, 339, 105

Myers, J. M., Snyder, B., Rusthoven, M., The, L.-S., & Hartmann, D. H. 2010, ApJ, 723, 1057

Navarro, J. F., Frenk, C. S., & White, S. D. M. 1994, MNRAS, 267, L1

Newberg, H. J., et al. 2002, ApJ, 569, 245

Ngeow, C., & Kanbur, S. M. 2008, in Galaxies in the Local Volume, ed. Koribalski, B. S. & Jerjen, H., Astrophysics and Space Science Proceedings (Springer Netherlands), 317

Nidever, D. L., Majewski, S. R., Butler Burton, W., & Nigra, L. 2010, ApJ, 723, 1618

Nidever, D. L., Majewski, S. R., Muñoz, R. R., Beaton, R. L., Patterson, R. J., & Kunkel, W. E. 2011, ApJ, 733, L10

Niederste-Ostholt, M., Belokurov, V., Evans, N. W., & Peñarrubia, J. 2010, ApJ, 712, 516

Nikolaev, S., Drake, A. J., Keller, S. C., Cook, K. H., Dalal, N., Griest, K., Welch, D. L., & Kanbur, S. M. 2004, ApJ, 601, 260

Nishiyama, S., Nagata, T., Tamura, M., Kandori, R., Hatano, H., Sato, S., & Sugitani, K. 2008, ApJ, 680, 1174

Noël, N. E. D., & Gallart, C. 2007, ApJ, 665, L23

Norris, J. E., Gilmore, G., Wyse, R. F. G., Yong, D., & Frebel, A. 2010a, ApJ, 722, L104

Norris, J. E., Wyse, R. F. G., Gilmore, G., Yong, D., Frebel, A., Wilkinson, M. I., Belokurov, V., & Zucker, D. B. 2010b, ApJ, 723, 1632

Norris, J. E., Yong, D., Gilmore, G., & Wyse, R. F. G. 2010c, ApJ, 711, 350

North, P., Gauderon, R., Barblan, F., & Royer, F. 2010, A&A, 520, A74

Oke, J. B. 1966, ApJ, 145, 468

Olech, A., Kaluzny, J., Thompson, I. B., Pych, W., Krzemiński, W., & Schwarzenberg-Czerny, A. 2000, in Astronomical Society of the Pacific Conference Series, Vol. 203, IAU Colloq. 176: The Impact of Large-Scale Surveys on Pulsating Star Research, ed. L. Szabados & D. Kurtz (Astronomical Society of the Pacific), 317

Olsen, K. A. G., Hodge, P. W., Mateo, M., Olszewski, E. W., Schommer, R. A., Suntzeff, N. B., & Walker, A. R. 1998, MNRAS, 300, 665

Olsen, K. A. G., & Massey, P. 2007, ApJ, 656, L61

Olsen, K. A. G., & Salyk, C. 2002, AJ, 124, 2045

Olsen, K. A. G., Zaritsky, D., Blum, R. D., Boyer, M. L., & Gordon, K. D. 2011, ApJ, 737, 29

Oosterhoff, P. T. 1939, The Observatory, 62, 104

—. 1944, BAN, 10, 55

Pagel, B. E. J. 1997, Nucleosynthesis and Chemical Evolution of Galaxies (Cambridge University Press)

Papadakis, I., Hatzidimitriou, D., Croke, B. F. W., & Papamastorakis, I. 2000, AJ, 119, 851

Parisi, M. C., Geisler, D., Grocholski, A. J., Clariá, J. J., & Sarajedini, A. 2010, AJ, 139, 1168

Parisi, M. C., Grocholski, A. J., Geisler, D., Sarajedini, A., & Clariá, J. J. 2009, AJ, 138, 517

Peñarrubia, J., et al. 2011, ApJ, 727, L2

Pejcha, O., & Stanek, K. Z. 2009, ApJ, 704, 1730, (PS09)

Perrine, C. D. 1927, MNRAS, 87, 426

Peterson, R. 1978, ApJ, 222, 181, (P78)

Piatek, S., Pryor, C., & Olszewski, E. W. 2008, AJ, 135, 1024

Pickering, E. C. 1903, Annals of Harvard College Observatory, 48, 91

Piersimoni, A. M., Bono, G., & Ripepi, V. 2002, AJ, 124, 1528

Pietrukowicz, P., et al. 2011, ArXiv e-prints, (PUS11)

Piskunov, N. E., Kupka, F., Ryabchikova, T. A., Weiss, W. W., & Jeffery, C. S. 1995, A&AS, 112, 525

Pompéia, L., et al. 2008, A&A, 480, 379

Popowski, P. 2000, ApJ, 528, L9

Preston, G. W. 1959, ApJ, 130, 507

Preston, G. W., Sneden, C., Thompson, I. B., Shectman, S. A., & Burley, G. S. 2006, AJ, 132, 85

Primas, F., Asplund, M., Nissen, P. E., & Hill, V. 2000, A&A, 364, L42

Puzeras, E., Tautvaišienė, G., Cohen, J. G., Gray, D. F., Adelman, S. J., Ilyin, I., & Chorniy, Y. 2010, MNRAS, 408, 1225

Quinn, P. J., & Goodman, J. 1986, ApJ, 309, 472

Revnivtsev, M., van den Berg, M., Burenin, R., Grindlay, J. E., Karasev, D., & Forman, W. 2010, A&A, 515, A49

Richardson, J. C., et al. 2009, MNRAS, 396, 1842

Robertson, B., Bullock, J. S., Font, A. S., Johnston, K. V., & Hernquist, L. 2005, ApJ, 632, 872

Röck, B., & Grebel, E. K. priv. comm.

Růžička, A., Theis, C., & Palouš, J. 2010, ApJ, 725, 369

Rubele, S., et al. 2012, A&A, 537, A106

Sabbi, E., et al. 2009, ApJ, 703, 721

Sadakane, K., Arimoto, N., Ikuta, C., Aoki, W., Jablonka, P., & Tajitsu, A. 2004, PASJ, 56, 1041

Salaris, M., & Cassisi, S. 2005, Evolution of Stars and Stellar Populations (Wiley)

Sandage, A. 1958, AJ, 127, 513

—. 2004, AJ, 128, 858

—. 2006, AJ, 131, 1750

Sandage, A., Katem, B., & Sandage, M. 1981, ApJS, 46, 41

Sandage, A., & Tammann, G. A. 1968, ApJ, 151, 531

—. 2006, ARAA, 44, 93

Sandage, A., Tammann, G. A., & Reindl, B. 2004, A&A, 424, 43

—. 2009, A&A, 493, 471

Sandstrom, K., Pilachowski, C. A., & Saha, A. 2001, AJ, 122, 3212

Sarajedini, A., Barker, M. K., Geisler, D., Harding, P., & Schommer, R. 2006, AJ, 132, 1361

Sbordone, L., Bonifacio, P., Buonanno, R., Marconi, G., Monaco, L., & Zaggia, S. 2007, A&A, 465, 815

Schlegel, D. J., Finkbeiner, D. P., & Davis, M. 1998, ApJ, 500, 525, (SFD98)

Schönrich, R., Asplund, M., & Casagrande, L. 2011, MNRAS, 415, 3807

Schwarzschild, M. 1940, Harvard College Observatory Circular, 437, 1

Searle, L., & Zinn, R. 1978, ApJ, 225, 357

Sesar, B., et al. 2010, ApJ, 708, 717

Shapley, H. 1916, ApJ, 43, 217

—. 1924, Harvard College Observatory Circular, 268, 1

—. 1953, AJ, 58, 47

Sharma, S., Borissova, J., Kurtev, R., Ivanov, V. D., & Geisler, D. 2010, AJ, 139, 878

Shetrone, M. D., Siegel, M. H., Cook, D. O., & Bosler, T. 2009, AJ, 137, 62

Simon, N. R. 1985, ApJ, 299, 723

—. 1988, ApJ, 328, 747

Simon, N. R., & Clement, C. M. 1993, ApJ, 410, 526

Simon, N. R., & Lee, A. S. 1981, ApJ, 248, 291

Simon, N. R., & Teays, T. J. 1981, PASP, 93, 550

Skrutskie, M. F., et al. 2006, AJ, 131, 1163

Smith, H. A. 2004, RR Lyrae Stars

Smith, H. A., Catelan, M., & Kuehn, C. 2011, in RR Lyrae Stars, Metal-Poor Stars, and the Galaxy, ed. A. McWilliam (Pasadena: Carnegie Observatories), 17

Smolec, R. 2005, Acta Astronomica, 55, 59

Sneden, C. A. 1973, PhD thesis, The University of Texas at Austin

Sollima, A., Cacciari, C., Bellazzini, M., & Colucci, S. 2010, MNRAS, 406, 329

Soszyński, I., Udalski, A., Szymański, M. K., Kubiak, J., Pietrzyński, G., Wyrzykowski, Ł., Ulaczyk, K., & Poleski, R. 2010a, Acta Astronomica, 60, 165

Soszyński, I., et al. 2003, Acta Astronomica, 53, 93

—. 2008, Acta Astronomica, 58, 163

—. 2009, Acta Astronomica, 59, 1

—. 2010b, Acta Astronomica, 60, 17

—. 2011, Acta Astronomica, 61, 1

Soszynski, I., et al. 2011, ArXiv e-prints

Springel, V., et al. 2005, Nature, 435, 629

Stanimirović, S., Staveley-Smith, L., Dickey, J. M., Sault, R. J., & Snowden, S. L. 1999, MNRAS, 302, 417

Stanimirović, S., Staveley-Smith, L., & Jones, P. A. 2004, ApJ, 604, 176

Staveley-Smith, L., Kim, S., Calabretta, M. R., Haynes, R. F., & Kesteven, M. J. 2003, MNRAS, 339, 87

Stellingwerf, R. F., & Dickens, R. J. 1987, ApJ, 322, 133

Stothers, R. B. 1988, ApJ, 329, 712

Sturch, C. 1966, ApJ, 143, 774

Subramaniam, A. 2003, ApJ, 598, L19

—. 2004, ApJ, 604, L41

—. 2005, A&A, 430, 421, (S05)

Subramaniam, A., & Subramanian, S. 2009a, A&A, 503, L9

—. 2009b, ApJ, 703, L37

Subramanian, S., & Subramaniam, A. 2009, A&A, 496, 399, (S09)

—. 2012, ApJ, 744, 128

Sumi, T. 2004, MNRAS, 349, 193

Szewczyk, O., Pietrzyński, G., Gieren, W., Ciechanowska, A., Bresolin, F., & Kudritzki, R. 2009, AJ, 138, 1661

Szewczyk, O., et al. 2008, AJ, 136, 272

Szymański, M. K., Udalski, A., Soszyński, I., Kubiak, M., Pietrzyński, G., Poleski, R., Wyrzykowski, Ł., & Ulaczyk, I. 2011, Acta Astronomica, 61, 83

Tafelmeyer, M., et al. 2010, A&A, 524, A58

Tammann, G. A. 1977, Mitteilungen der Astronomischen Gesellschaft Hamburg, 42, 42

Thackeray, A. D., & Wesselink, A. J. 1953, Nature, 171, 693

—. 1955, The Observatory, 75, 33

Thielemann, F.-K., Nomoto, K., & Hashimoto, M.-A. 1996, ApJ, 460, 408

Tikhonov, N. A. 2005, Astronomy Reports, 49, 501

Tsujimoto, T., & Bekki, K. 2009, ApJ, 700, 69

Tumlinson, J. 2010, ApJ, 708, 1398

Udalski, A. 2000, Acta Astronomica, 50, 279

—. 2003a, ApJ, 590, 284

—. 2003b, Acta Astronomica, 53, 291

Udalski, A., Kubiak, M., & Szymanski, M. 1997, Acta Astronomica, 47, 319

Udalski, A., Soszyński, I., Szymanski, M., Kubiak, M., Pietrzynski, G., Wozniak, P., & Zebrun, K. 1999a, Acta Astronomica, 49, 223

—. 1999b, Acta Astronomica, 49, 437

Udalski, A., Szymanski, M., Kaluzny, J., Kubiak, M., & Mateo, M. 1992, Acta Astronomica, 42, 253

Udalski, A., Szymanski, M., Kubiak, M., Pietrzynski, G., Wozniak, P., & Zebrun, K. 1998, Acta Astronomica, 48, 1

Udalski, A., et al. 2008a, Acta Astronomica, 58, 89

—. 2008b, Acta Astronomica, 58, 329

Valdes, F., Gupta, R., Rose, J. A., Singh, H. P., & Bell, D. J. 2004, ApJS, 152, 251

van der Marel, R. P. 2001, AJ, 122, 1827

van der Marel, R. P. 2006, in Proc. Space Telescope Science Institute Symp.17, ed. M. Livio & T. M. Brown, The Local Group as an Astrophysical Laboratory (Cambridge: Cambridge Univ. Press), 47 van der Marel, R. P., Alves, D. R., Hardy, E., & Suntzeff, N. B. 2002, AJ, 124, 2639

van der Marel, R. P., & Cioni, M.-R. L. 2001, AJ, 122, 1807

Venn, K. A., Irwin, M., Shetrone, M. D., Tout, C. A., Hill, V., & Tolstoy, E. 2004, AJ, 128, 1177

Vieira, K., et al. 2010, AJ, 140, 1934

Vivas, A. K., Zinn, R., & Gallart, C. 2005, AJ, 129, 189

Walker, A. R. 2011, ArXiv e-prints

Wallerstein, G., Greenstein, J. L., Parker, R., Helfer, H. L., & Aller, L. H. 1963, ApJ, 137, 280

Watkins, L. L., et al. 2009, MNRAS, 398, 1757

Weinberg, M. D. 2000, ApJ, 532, 922

Weinberg, M. D., & Nikolaev, S. 2001, ApJ, 548, 712

Wesselink, A. J. 1946, BAN, 10, 91

Westerlund, B. E. 1997, The Magellanic Clouds, ed. Westerlund, B. E.

Wilcots, E. M. 2009, in IAU Symposium 256, ed. J. T. van Loon & J. M. Oliveira (Cambridge: Cambridge University Press), 461

Wilke, K., Stickel, M., Haas, M., Herbstmeier, U., Klaas, U., & Lemke, D. 2003, A&A, 401, 873

Wilson, R. E. 1924, AJ, 35, 183

Woosley, S. E., & Weaver, T. A. 1995, ApJS, 101, 181

Wozniak, P. R., & Stanek, K. Z. 1996, ApJ, 464, 233

Wyse, R. F. G., Gilmore, G., Houdashelt, M. L., Feltzing, S., Hebb, L., Gallagher, III, J. S., & Smecker-Hane, T. A. 2002, New Astronomy, 7, 395

Yang, Y., & Hammer, F. 2010, ApJ, 725, L24

Yanny, B., et al. 2003, ApJ, 588, 824

Yoon, S.-J., & Lee, Y.-W. 2002, Science, 297, 578

Yoshizawa, A. M., & Noguchi, M. 2003, MNRAS, 339, 1135

Zagury, F. 2007, Ap&SS, 312, 113

Zaritsky, D. 1999, AJ, 118, 2824

—. 2004, ApJ, 614, L37

Zaritsky, D., Harris, J., Grebel, E. K., & Thompson, I. B. 2000, ApJ, 534, L53

Zaritsky, D., Harris, J., & Thompson, I. 1997, AJ, 114, 1002

Zaritsky, D., Harris, J., Thompson, I. B., & Grebel, E. K. 2004, AJ, 128, 1606, (Z04)

Zaritsky, D., Harris, J., Thompson, I. B., Grebel, E. K., & Massey, P. 2002, AJ, 123, 855, (Z02)

Zasowski, G., et al. 2009, ApJ, 707, 510

Zhao, H., & Evans, N. W. 2000, ApJ, 545, L35

Zinn, R., & West, M. J. 1984, ApJS, 55, 45, (ZW84)

Zwicky, F. 1933, Helvetica Physica Acta, 6, 110

List of Abbreviations

χ	excitation potential
ν_{t}	microturbulence
θ	position angle
i	inclination angle
2MASS	Two Micron All Sky Survey
AGB	asymptotic giant branch
BHB	blue horizontal branch
CMD	colour magnitude diagram
DENIS	Deep Near-Infrared Southern Sky Survey
dSph	dwarf spheroidal galaxies
EW	Equivalent Width
FWHM	Full Width Half Maximum
GAVO	German Astrophysical Virtual Observatory
GC	globular cluster
Gyr	Gigayear
HB	horizontal branch
IMF	initial mass function
ISRF	interstellar radiation field
K-S test	Kolmogorov-Smirnov test
kpc	kiloparsec $\equiv 3.08568025 \times 10^{16}$ km
LMC	Large Magellanic Cloud
log g	surface gravity
log gf	oscillator strength
LSR	local standard of rest
LSST	Large Synoptic Survey Telescope

LTE	local thermodynamic equilibrium
MACHO	Massive Compact Halo Objects
MagE	Magellan Echellette
MCPS	Magellanic Clouds Photometric Survey
MCs	Magellanic Clouds
MDF	metallicity distribution function
MW	Milky Way
Myr	Megayear
OGLE	Optical Gravitational Lensing Experiment
OGLE III	third phase of the Optical Gravitational Lensing Experiment
PAHs	polycyclic aromatic hydrocarbons
RC	red clump
RGB	red giant branch
RHB	red horizontal branch
S/N	signal to noise
SAGE	Surveying the Agents of Galaxy Evolution
SDSS	Sloan Digital Sky Survey
SFH	star formation history
Sgr	Sagittarius
SMC	Small Magellanic Cloud
T_{eff}	effective temperature
ThAr	Thorium-Argon
VALD	Vienna Atomic Line Database
VISTA	Visible and Infrared Survey Telescope for Astronomy
X Ari	X Arietis

List of Figures

List of Tables

"Believing oneself to be perfect is often the sign of a delusional mind."

Data - Star Trek 8: First Contact

Acknowledgements

There are many people who I would like to thank for their contributions throughout the last three years. Hopefully I have not forgotten anybody, but I do want to stress that the order of appearance might not in all cases reflect how important someone has been to me. Everybody contributed in his or her own way and it is impossible to grade that appropriately. Therefore do not interpret it as being more or less important.

First of all I want to express my gratitude to Eva Grebel, who offered me the opportunity to do this PhD. During our long and intensive 'scientific' discussions you provided me with the skills and expertise needed to fulfill the requirements for a doctoral degree. The use of, at least multiple, of your red pens helped me in many ways to learn what scientific work really means. I am also very grateful for the freedom you gave me to be active in non-scientific areas of my life, which were very important for me.

I have to state my warmest thank to Sonia Duffau, 'my postdoc'. You have accompanied me through these three years with a lot of patience and always with good advice. You always took your time to help me with all your power to solve the problems that have occurred during my PhD. I will miss your 'significant voice', that made it unnecessary to get out of my chair to see if you are around.

A big thank you to Shoko Jin, for many scientific discussions and helpful comments on very different topics and issues. Speaking to you was always a very appreciated break, with many fruitful results. Especially your continuous efforts to improve my English skills are highly valued.

Special thanks go to Andreas Koch, Camilla Hansen and Anna Frebel for their support throughout the spectroscopic part of my thesis. Anna's help in accessing telescope time at a suitable spectroscopic instrument and in performing the observing run was highly valuable. My gratitude goes to all of you for helping me to get scientific significant results out of my 'crappy' spectra. Your help significantly improved this part of my thesis and now I can tell the spectra: "Resistance is futile!".

For agreeing to be the second referee of my thesis I am very grateful to Norbert Christlieb. I also thank him for being a member of my thesis committee. In this regard, I want to thank Andreas Just for being the other member of the thesis committee. The meetings and discussions with the committee always led to new scientific projects and was very helpful in the course of my PhD.

As members of my disputation committee I thank Norbert Christlieb, Cornelius Dullemond and Markus Oberthaler. I am very confident that this will not change in the near future.

I would like to acknowledge the support and funding that was given to me by the Heidelberg Graduate School for Fundamental Physics and from its astronomy branch, the International Max Planck Research School for Astronomy and Cosmic Physics at the University of Heidelberg.

The 'Grebelgroup' has supported me in many different ways and occasions. Special thank goes to Johannes Ludwig, my office mate and fellow sufferer relating to football issues. I enjoyed our conversations and benefited a lot from our scientific discussions. For the communistic point of views and the discussions about how to change the (political) system, as well as for the Star Trek nights, I want to thank Baybars Külebi. You taught me patience and calmness. Important to mention is Denija Crnojevic, I will always profit from learning what it means to be really mean. Even though I will probably never understand the Swiss people, Katharina Glatt and Katrin Jordi played an essential part during my PhD, until they unfortunately had to leave. Even though one of you always said, "Don't ask me!", your help, support and courtesy in the process of learning how a real scientist should work remains important to me. Every member of the group had his or her own influence on my work or behavior and I am thankful to have worked with all of them: André Herling, Anna Pasquali, Avon Huxor, Benjamin Röck, Christina Hennig, Corrado Boeche, Frederik Schönebeck, Jan Rybizki, John Vickers, Matthias Frank, Mohamad Abbas, Oleksiy Golubov, Sarah Martell, Shuang Gao, Sophia Lianou, Stefan Schmeja, Stefano Pasetto, Veronica Lora, Xiaoying Pang. For helping me with many organizational issues and for the nice discussions that we had every now and then, I want to thank 'our coordinator' Guido Thimm.

For proof reading of paper and thesis drafts, proposals and applications, special thanks go to Andreas Koch, Anna Frebel, Avon Huxor, Benjamin Röck, Camilla Hansen, Johannes Ludwig, Katharina Glatt, Katrin Jordi, Shoko Jin, Sonia Duffau and, of course, Eva Grebel.

In my 'normal' life, the Café Botanik and its people gave me a lot of support and, even more important, friends. My boss Andreas Krauth taught me very important lessons for my life and I am very grateful to have worked with him. From my numerous colleagues, I especially want to mention Frank Kondziella, Julia Schmid, Marina Koch, Nadine Kaupa and Sarah Hüthwohl. You make my time extremely special and I hope that our friendships will last for a long time. This support gives me the strength to do many things that life demands, even though I might not like them.

Most of what I am today is based on the education of my parents Michael and Dafna Haschke. I am very very thankful that you have supported me in so many ways and situations over the last 28 years. That you are always available and that you care so much about how I am doing. Even though I might not always show my appreciation of your care, I have no idea, and I do not want to know, what I would be without it. This thesis was only possible because you always give me the feeling that I am able to do (more or less) whatever I want.

There are no words to describe my gratitude for the most important person in my life. Katharina Anhalt provides me with the support needed to survive in this fast-developing and ruthless world. It is impossible for me to imagine a life without you. Your faith in me provides me the security and strength that I need. Your generosity and thoughtfulness, your ... – in brief your love, makes me what I am. If I had one free wish, I would choose to stay with you forever!